Theoretical rotational-vibrational and rotational-vibrational-electronic spectroscopy of triatomic molecules

Emil J. Żak

A dissertation submitted in partial fulfillment

of the requirements for the degree of

Doctor of Philosophy

of

University College London.

Department of Physics & Astronomy

University College London

October 27, 2017

I, Emil J. Żak, confirm that the work presented in this thesis is my own. Where information has been derived from other sources, I confirm that this has been indicated in the work.

Complete list of publications

1. **Zak E. J.**, Tennyson J. (2017); Ro-vibronic transition intensities for triatomic molecules from the exact kinetic energy operator; electronic spectrum for the $\tilde{C}^1B_2 \leftarrow \tilde{X}^1A_1$ transition in SO_2. In press: The Journal of Chemical Physics

2. Gordon I. E., Rothman L. S. *et al.*, **Zak E. J.** (2017); The HITRAN2016 molecular spectroscopic database. In press: Journal of Quantitative Spectroscopy and Radiative Transfer

3. **Zak E. J.**, Tennyson J., Polyansky O. L., Lodi L., Zobov N. F., Tashkun S. A., Perevalov V. I. (2017); Room temperature line lists for CO_2 asymmetric isotopologues with ab initio computed intensities. In press: Journal of Quantitative Spectroscopy and Radiative Transfer

4. Szczepanik D. W., **Zak E. J.** and Mrozek J. (2017); From quantum superposition to orbital communications. Computational and Theoretical Chemistry, 1115, 8087

5. Odintsova T., Fasci E., Moretti L., **Zak E. J.** , Polyansky O. L., Tennyson J., Gianfrani L., Castrillo A. (2017); Highly-accurate intensity factors of pure CO_2 lines near 2 μm. The Journal of Chemical Physics 146, 244309

6. Owens A., **Zak E. J.**, Chubb K. L., Yurchenko S. N., Tennyson J., Yachmenev A. (2017); Simulating electric field interactions of polar molecules using spectroscopic databases. Scientific Reports 7:45068

7. **Zak E. J.**, Tennyson J., Polyansky O. L., Lodi L., Zobov N. F., Tashkun S. A., Perevalov V. I. (2017); Room temperature line lists for CO_2 symmetric isotopologues with ab initio computed intensities. Journal of Quantitative Spectroscopy and Radiative Transfer; 189, 267-280

8. Tennyson J., Yurchenko S. N., Al-Refaie A. F., Barton E. J., Chubb K. L., Coles P. A., Diamantopoulou S., Gorman M. N., Hill C., Lam A. Z., Lodi

L., McKemmish L. K., Na Y., Owens A., Polyansky O. L., Rivlin T., Sousa-Silva C., Underwood D. S., Yachmenev A., **Zak E. J.** (2016); The ExoMol database: Molecular line lists for exoplanet and other hot atmospheres. Journal of Molecular Spectroscopy 327, 73-94

9. **Zak E. J.**, Tennyson J., Polyansky O. L., Lodi L., Zobov N. F., Tashkun S. A., Perevalov V. I. (2016); A room temperature CO_2 line list with ab initio computed intensities. Journal of Quantitative Spectroscopy and Radiative Transfer; 177, 31-42

10. Petelenz P., **Zak E. J.** (2014); Quasiperiodic Energy Dependence of Exciton Relaxation Kinetics in the Sexithiophene Crystal. Journal of Physical Chemistry A, 118, 41, 9653–9660

11. Szczepanik D. W., Andrzejak M., Dyduch K., **Zak E. J.**, Makowski M., Mazur G., Mrozek J. (2014); A uniform approach to the description of multicenter bonding. Physical Chemistry Chemical Physics 16, 38, 20514–20523

12. Szczepanik D. W., **Zak E. J.**, Dyduch K., Mrozek J. (2014); Electron delocalization index based on bond order orbitals. Chemical Physics Letters, 593, 154–159

List of associated publications

Chapter 3:

- Zak E. J., Tennyson J., Polyansky O. L., Lodi L., Zobov N. F., Tashkun S. A., Perevalov V. I. (2017); Room temperature line lists for CO_2 asymmetric isotopologues with ab initio computed intensities. In press: Journal of Quantitative Spectroscopy and Radiative Transfer

- Zak E. J., Tennyson J., Polyansky O. L., Lodi L., Zobov N. F., Tashkun S. A., Perevalov V. I. (2017); Room temperature line lists for CO_2 symmetric isotopologues with ab initio computed intensities. Journal of Quantitative Spectroscopy and Radiative Transfer; 189, 267-280

- Zak E. J., Tennyson J., Polyansky O. L., Lodi L., Zobov N. F., Tashkun S. A., Perevalov V. I. (2016); A room temperature CO_2 line list with ab initio computed intensities. Journal of Quantitative Spectroscopy and Radiative Transfer; 177, 31-42

Chapter 4:

- Zak E. J., Tennyson J. (2017); Ro-vibronic transition intensities for triatomic molecules from the exact kinetic energy operator; electronic spectrum for the $\tilde{C}^1B_2 \leftarrow \tilde{X}^1A_1$ transition in SO_2. In press: The Journal of Chemical Physics

Abstract

The major part of this work is construction of 54 room-temperature infrared absorption line lists for isotopologues of carbon dioxide. In accurate nuclear motion calculations an exact nuclear kinetic energy operator is used in the Born-Oppenheimer approximation and three *ab initio* and semi-empirical potential energy surfaces for generation of rotational-vibrational wavefunctions and energy levels. Transition intensities are calculated with two different high quality *ab initio* dipole moment surfaces. The generated line lists are comprehensively compared to state-of-the-art measurements, spectroscopic databases and other theoretical studies. As a result, uncertainties in calculated transition intensities in several vibrational CO_2 bands are shown below 1%, which is sufficient for use in remote sensing measurements of carbon dioxide in the Earth's atmosphere. Results of the present calculations set a new state-of-the-art and have been included in the 2016 release of the HITRAN database.

A theoretical procedure for estimating reliability of computed transition intensities is presented and applied to CO_2 line lists. As a result, each transition intensity received a reliability factor, a particularly useful descriptor for detecting resonance interactions between rotational-vibrational energy levels, as well as a good measure quantifying the strength of such interactions.

The theoretical procedure used for CO_2 is extended to electronic transitions in the Born-Oppenheimer approximation. In this extended framework rotational-vibrational-electronic line lists for SO_2 and CaOCa molecules are generated. For this purpose appropriate *ab initio* potential energy surfaces and a transition dipole moment surface are generated. Absolute transition intensities are then calculated

both in the Franck-Condon approximation and with a full transition dipole moment surface. Resulting line lists are compared with available experimental and theoretical data. The unprecedented accuracy of the model used in these calculations and the rotational resolution of transition lines renders the present approach as promising for future uses in atmospheric science.

Finally a theoretical framework for fully non-adiabatically coupled Hamiltonian is derived and discussed. A proposition for computer implementation of this theoretical scheme is also given.

Acknowledgements

I would like to thank my supervisor Prof. Jonathan Tennyson for his kind support during my time at UCL.

Because a complete list of persons for which I would like to express my gratitude is long, I wish to thank every individual I have met on my way, because you cannot deny, that reading these words right now, would not be possible without each and every one of them.

Contents

List of Figures

List of Tables

Chapter 1

Introduction

Monitoring of the Earth's atmospheric composition has been one of the grand challenges since the early days of molecular spectroscopy. In fact, understanding the processes in the Earth's atmosphere and the impact of humans on it, represents a fundamental motivation on which modern science is founded. Thus undeniably, it is of vital importance for us, humans, to understand and responsibly asses our impact on the environment. This thesis is an attempt to propagate towards this goal.

Among a number of molecules detected in the Earth's atmosphere, the triatomic molecules represent a major group containing primarily water, carbon dioxide, sulphur dioxide, nitrous oxide and ozone [1]. Identifying sources, sinks and migration mechanisms of these gases is the key to understanding the processes observed in the Earth's atmosphere. This, in turn, requires acquisition of highly accurate molecular absorption spectra from ground based or remote sensing measurements. Carbon dioxide (CO_2) is one of the main greenhouse gases and has been monitored over the years by several government and private funded projects [2–11]. For determination of the concentration of CO_2 in the Earth's atmosphere, both satellite and ground based measurements use infrared transitions between rotational-vibrational states of this molecule [6, 12–15]. Very often, the measured spectrum is compared against a laboratory measurement convolved with a supporting spectroscopic model, by means of which the information about the concentration is gained. The accuracy of such schemes relies on the accuracy of the reference data, and the transition intensities in particular.

For responsible conclusions on the impact of human activity on the CO_2 levels in the Earth's atmosphere 1-ppm resolution in retrieved concentration is needed [16, 17]. This concentration could be determined in the laboratory from atmospheric samples [18, 19]. Such an approach however is incapable of providing the global maps of CO_2 concentration, whereas understanding mechanisms for migration and depletion of carbon dioxide on the global scale is essential for climate science [20–23]. For this reason, a number of continuous detection methods on the global scale have been developed, one of which is remote sensing [2–6]. In such measurements, it would be ideal to have several isotopologues of carbon dioxide quantified simultaneously, to learn about the sources of this gas [23]. For example, the unstable $^{14}CO_2$ isotopologue containing radioactive ^{14}C is a key trace species used as a marker for industrial activities [21, 24–26]. Thus, maps of this isotopologue of CO_2 could deliver information about pollution sources.

At the end of the day, all remote sensing measurements require accurate transition intensities and line shapes for several isotopologues, which can be used in the retrieval procedure [6, 16]. The 1-ppm resolution requirement imposes levels of accuracy on reference spectra (0.3% for transition intensities [16]) which have been, until recently, beyond the reach of the experiment [27, 28], mainly due to low natural abundance of isotopologues of CO_2 containing ^{13}C, ^{17}O or ^{18}O. Even for the main isotopologue $^{12}C^{16}O_2$, the very recent highly sophisticated measurements reached 0.3%–1% accuracy for a limited number of transitions [28–33].

Spectroscopic databases such as HITRAN [196], HITEMP [34] and GEISA [35] are partly dedicated for use in the atmospheric retrieval models. These databases contain mainly, but not only, line-by-line spectra with quantum number assignments and a number of other spectroscopic parameters, which together are called a *line list*. However, for successful ppm-level retrieval of molar fractions of molecules in the atmospheric measurements, all absorption lines in a given spectral region have to be characterized, requiring high-resolution supporting data and this currently represents a major challenge. In fact, for some molecules, such as SO_2 in the ultraviolet region, only cross-sections at few given temperatures and pressures

are supplied by the present versions of spectroscopic databases. In addition to that, these databases still have issues with completeness of the data as well as insufficient quality of line intensities, which have been so far taken only from measurements.

Thus, a significant portion of the results presented in this thesis is motivated by the need for high accuracy CO_2 infrared transition intensities for remote sensing purposes. For this reason, in the first instance, this thesis presents theoretical line lists for 13 isotopologues of carbon dioxide, which are dedicated to meet the requirements by the remote sensing, thereby designed to redefine the old paradigm of solely empirical sourcing of reference data in the atmospheric science. The line lists are generated by large scale first principles quantum mechanical calculations. In the first step the rotational-vibrational Schrödinger equation is solved to provide energy levels and nuclear wavefunctions, and subsequently the transition intensities between different rotational-vibrational (ro-vibrational) states of the molecule are calculated. The final calculated transition line positions, transition intensities, energy levels and appropriate quantum numbers are stored in the form of a line list, which serves as a comprehensive data source for various purposes [36]. The accuracy of transition intensities in these line lists for carbon dioxide, which were generated with an *ab initio* dipole moment surface (DMS), has reached and arguably exceeded experimental accuracy [28,32,37–39]. As a result, for 12 isotopologues of carbon dioxide in the 0 – 8000 cm^{-1} wavenumber range, the theoretical transition intensities calculated and presented in this thesis were included in the 2016 release of the HITRAN spectroscopic database [196].

Detection and quantification of other very important, but less abundant molecules in the Earth's atmosphere, such as SO_2 or O_3 relies on absorption of ultraviolet (UV) radiation [40–43], which is accompanied by transition between rotational-vibrational-electronic (ro-vibronic) states of the molecule. For this reason, as a logical follow up to modelling the infrared spectra of carbon dioxide, we focus on molecular spectra in the UV, associated with ro-vibronic transitions. The SO_2 molecule is chosen as a case study, mainly because of the relatively rich experimental data available, but also due to its role in measurements of volcanic

activity [44, 45]. Again, similar to the case of CO_2, a molecular line list for SO_2 in the UV is calculated, analysed and compared with experiment. The computation is done within the Born-Oppenheimer (BO) approximation in the ro-vibronic resolution, which is the first reported high-accuracy *ab initio* line list of this type. From the theoretical point of view a major problem with the calculation of accurate UV spectra of molecules, associated with an electronic transition, is the breakdown of the Born-Oppenheimer approximation [46, 47]. In many cases, line lists generated using the BO approximation are of little use [48–53], especially when crossing between electronic states occurs. On such occasions, an appropriate ro-vibronic model needs to be constructed. Thus, to continue from the Born-Oppenheimer UV absorption calculations presented for SO_2, we present a general ro-vibronic theory for the nuclear motion of triatomic molecules, which if implemented, can be used to generate accurate spectra for any triatomic molecule, regardless of the complexity of its electronic structure. The thesis concludes on perspective applications of the methodology used for the calculation of ro-vibrational CO_2 and ro-vibronic SO_2 spectra to other triatomic molecules.

Chapter 2 gives a theoretical background for calculations of ro-vibrational and ro-vibronic line lists for triatomic molecules based on methodology given by Tennyson *et al.* [54, 55].

Chapter 3 presents 54 theoretical infrared line lists calculated for 13 isotopologues of carbon dioxide. This chapter opens with a discussion of the motivation for calculations on CO_2 in the context of atmospheric science. Next, computational details and a summary of all line lists are given, which is followed by comparisons of the calculated line lists (line positions and line intensities) to recent high accuracy measurements. Two CO_2 absorption bands, which are currently used in remote sensing measurements are selected and analysed in detail in section 3.3. This analysis, which is done against the most recent and the most accurate intensity measurements available serves as a quality check for the calculations and indicates the very high accuracy of calculated transition intensities. As a benchmark supporting the findings of section 3.3, a more comprehensive comparison to popular spectroscopic

databases is given for all isotopologues. Although each isotopologue of carbon dioxide is treated in this thesis separately, all isotopologues can be grouped into the symmetric ones ($^{x}O^{y}C^{x}O$) and asymmetric ones ($^{x}O^{y}C^{z}O$), which explains the organisation of chapter 3. The isotopologue containing the radioactive nuclei ^{14}C is discussed separately, because of its special role in monitoring of the industrial activity and extremely low natural abundance.

Along with calculations of ro-vibrational line lists for isotopologues of CO_2, in chapter 3, we present a theoretical procedure for estimation of uncertainty of calculated transition intensities. This procedure has been found useful in detection and quantification of the strength of resonance interactions between ro-vibrational energy levels. In section 3.4 in chapter 3, a theory for ro-vibrational resonance interactions is developed and utilized to derive the quantities on which the theoretical transition intensity reliability analysis, originally introduced by Lodi and Tennyson [56], operates.

Chapter 4 contains the description of the theoretical procedure, the potential energy surface and the transition dipole moment surface used to produce the Born-Oppenheimer line list for the $\tilde{C}\ ^1B_2 \leftarrow \tilde{X}\ ^1A_1$ electronic transition in SO_2. The computed line list is then compared against other theoretical approaches as well as available state-of-the-art measurements, with a perspective for further developments beyond the Born-Oppenheimer approximation.

Finally, following the demands sparked in chapter 4, the fifth chapter aims at formulation of the nuclear motion theory for triatomic molecules, which accounts for all ro-vibronic interactions. This theory builds upon the general nuclear motion formalism introduced by Sutcliffe and Tennyson [57, 58]. A tentative proposition for the computational implementation of this theory is also presented, with listing of necessary molecular input functions.

Chapter 2

Theoretical background

The aim of this section is to introduce key elements of the theory implemented in the DVR3D program [59] used in generation of the infrared line lists for carbon dioxide and the ultraviolet line list for sulphur dioxide. First, a general ro-vibrational Hamiltonian for a triatomic molecule is derived and expressed in the chosen ro-vibrational basis set. Next in section 2.4 details of a solution strategy to the stationary Schrödinger equation (SE) are given. This strategy mainly relies on a multi-step diagonalisation-truncation procedure with the use of the discrete variable representation technique, details of which are also outlined in subsection 2.4.1. Finally, we show how solutions to the ro-vibrational SE obtained with DVR3D can be used in transition line strength and transition intensity calculations, for which appropriate expressions are derived in section 2.6.

2.1 General ro-vibrational Hamiltonian for a triatomic molecule

A general Hamiltonian for the motion of nuclei of a triatomic molecule within the Born-Oppenheimer approximation is given (in atomic units) by:

$$\hat{H}(\mathbf{x}_1,\mathbf{x}_2,\mathbf{x}_3) = -\frac{1}{2}\sum_{i=1}^{3}\frac{1}{m_i}\nabla_i^2(\mathbf{x}_i) + V(\mathbf{x}_1,\mathbf{x}_2,\mathbf{x}_3) \tag{2.1}$$

where $\mathbf{x}_i$ is a vector representing three Cartesian coordinates of nucleus i with mass m_i and $V(\mathbf{x}_1,\mathbf{x}_2,\mathbf{x}_3)$ is the potential energy of the system. In computational prac-

tice, a direct solution to the stationary Schrödinger equation with the Hamiltonian from eq. 2.1 is very inconvenient, especially when a large number of solutions is needed. This is because the Cartesian representation of the Hamiltonian does not make any use of symmetries of the system. For this reason, it is more convenient to use a coordinate system in which the internal energy of the system can be at least approximately decomposed into contributions from individual translational, vibrational and rotational degrees of freedom. Here, this goal is achieved in a number of steps.

In the first step, the translational motion of the centre-of-mass of the system is separated. Such separation is possible because of the translational symmetry of the system in free 3D space, which corresponds to the conservation of linear momentum [60]. Following Sutcliffe [61], and Sutcliffe and Tennyson [57], the Cartesian coordinates of nuclei can be transformed into a translationally-invariant form, by means of relations:

$$\mathbf{t}_i = \sum_{j=1}^{3} \mathbf{x}_j V_{ji} \qquad i = 1,2 \tag{2.2}$$

where V_{ji} is a transformation matrix element satisfying the condition: $\sum_{j=1}^{3} V_{ji} = 0$ for $i = 1,2$. This condition ensures the translational invariance in the set of $\mathbf{t}_i$ coordinates, which can now be called the *space-fixed coordinate system*, i.e. the coordinate system which moves along with the centre-of-mass of the molecule. In this new frame, the three translational degrees of freedom of the centre of mass are fixed and the corresponding kinetic energy operator can be removed, thus one can focus on the remaining six internal degrees of freedom only. The transformed Hamiltonian expressed in terms of the $\mathbf{t}_i$ coordinates reads:

$$\hat{H}(\mathbf{t}_1, \mathbf{t}_2) = -\frac{1}{2} \sum_{i,j=1}^{2} \frac{1}{\mu_{ij}} \vec{\nabla}(\mathbf{t}_i) \cdot \vec{\nabla}(\mathbf{t}_j) + V(\mathbf{t}_1, \mathbf{t}_2) \tag{2.3}$$

where $\vec{\nabla}(\mathbf{t}_i)$ is simply the Nabla operator in $\mathbf{t}_i$ coordinate and $\mu_{ij}^{-1} = \sum_{k=1}^{3} m_k^{-1} V_{ki} V_{kj}$. Transformation 2.2 can be uniquely characterized by two independent parameters,

g_1 and g_2 in the following way:

$$\mathbf{V} = \begin{pmatrix} -g_2 & 1 \\ 1 & -g_1 \\ g_2 - 1 & g_1 - 1 \end{pmatrix} \tag{2.4}$$

which are determined from the geometric definition of the internal coordinate system [57], as displayed in Figure 2.1.

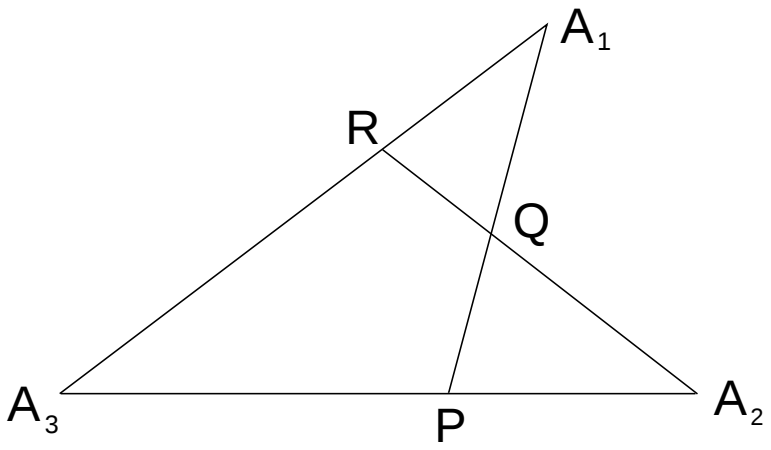

Figure 2.1: A generalized coordinate system for a triatomic system introduced by Sutcliffe and Tennyson [57]. A_i represents the point at which atom i is positioned.

With this definition, the geometric parameters g_1 and g_2 can be written as:

$$g_1 = \frac{A_3P}{A_3A_2} \qquad g_2 = \frac{A_3R}{A_3A_1} \tag{2.5}$$

and $0 \leq g_1, g_2 \leq 1$. A_3P stands for length of the segment connecting points A_3 and P. Different choices of g_1 and g_2 yield different popular types of internal coordinates: $g_1 = \frac{m_1}{m_2+m_3}, g_2 = 0$ gives Jacobi (scattering) coordinates [59], $g_1 = 0, g_2 = 0$ gives bond-length-bond-angle coordinates and $g_1 = 1 - \frac{\alpha}{\alpha+\beta-\alpha\beta}, g_2 = 1 - \frac{\alpha}{1-\beta+\alpha\beta}$ defines Radau coordinates [62], with $\alpha = \left(\frac{m_3}{m_1+m_2+m_3}\right)^{\frac{1}{2}}$ and $\beta = \frac{m_2}{m_1+m_2}$.

The choice of internal nuclear coordinates is primarily dictated by the geometry, mass distribution and perhaps symmetries of the system. Appropriately chosen internal coordinates can significantly reduce the computational cost of calculations, by ensuring fast convergence of the variational procedure [58,63–66]. However, an-

other yet equally important factor which has to be taken into account when choosing internal coordinates is the location of singularities, which appear inevitably [58] in the ro-vibrational Hamiltonian for any choice of the internal curvilinear coordinates. Thus, it is reasonable to choose coordinates for which these singularities can be appropriately dealt with or occur at geometries with very high internal potential energy, so that the wavefunction can be considered as vanishing in these regions. Otherwise, expectation values of observables and scalar products can be obscured by a large magnitude numerical noise originating from the singular regions. In this work we use Radau coordinates [62], which are suitable for a tightly bonded, semi-rigid triatomic molecule, such as the CO_2 molecule. In these coordinates, it is possible to restrict the singularities in the Hamiltonian to the very high energetic C–O–O configuration or even, in some cases, eliminate these singularities with an appropriate choice of the basis set [67].

The length and the mutual orientation of the $\mathbf{t}_1$ and $\mathbf{t}_2$ vectors determine the three internal coordinates of the system, whereas directions of $\mathbf{t}_1, \mathbf{t}_2$ in space define the orientation of the molecule with respect to the laboratory (LAB) frame. The internal coordinates will be denoted as follows: $r_1 = |\mathbf{t}_1|$, $r_2 = |\mathbf{t}_2|$ and $\theta = arccos\left(\frac{\mathbf{t}_1 \cdot \mathbf{t}_2}{|\mathbf{t}_1| \cdot |\mathbf{t}_2|}\right)$. Then, the translation-free Hamiltonian from eq. 2.3 can be transformed into a Hamiltonian, which is a function of r_1, r_2, θ and three angles (α, β, γ) determining the orientation of the $\mathbf{t}_1, \mathbf{t}_2$ vectors with respect to the space-fixed coordinate system. This can be achieved by means of embedding of the molecule-fixed coordinate frame, which is mathematically realised by an orthogonal transformation $\mathbf{C}$ of vectors in the space-fixed coordinate frame to a molecule-fixed coordinate frame:

$$\mathbf{t}_i = \mathbf{C} \cdot \mathbf{z}_i \qquad i = 1, 2. \tag{2.6}$$

The transformation matrix $\mathbf{C}(\alpha, \beta, \gamma)$ can be expressed in terms of *Euler angles* only [60, 68, 69], which define the three rotational degrees of freedom of the molecule. Here the zyz' convention for the choice of Euler angles is used [60].

With the transformation in eq. 2.6, it is possible to express the Hamiltonian

from eq. 2.3 in a form which depends on the internal coordinates r_1, r_2, θ and the total angular momentum operators $\hat{J}_x, \hat{J}_y, \hat{J}_z$. These operators generate rotations associated with the x, y and z axis of the molecule-fixed coordinate frame, respectively, and can be expressed analytically in terms of the three Euler angles: α, β, γ [60,68,69]. Now, with the use of the *chain-rule* the space-fixed Hamiltonian (eq. 2.3) can be transformed into the molecule-fixed Hamiltonian, with algebraic methods presented in refs. [57, 58, 61]. The final molecule-fixed Hamiltonian is given by:

$$\hat{H}(r_1,r_2,\theta,\alpha,\beta,\gamma) = \hat{K}_V^{(1)}(r_1,r_2,\theta) + \mu_{12}^{-1}\hat{K}_V^{(2)}(r_1,r_2,\theta) + \hat{K}_{VR}(r_1,r_2,\theta,\alpha,\beta,\gamma) + V(r_1,r_2,\theta) \tag{2.7}$$

where:

$$\begin{aligned}\hat{K}_V^{(1)}(r_1,r_2,\theta) = -\frac{1}{2}\Bigg[&\frac{1}{\mu_1 r_1^2}\left(\frac{\partial}{\partial r_1} r_1^2 \frac{\partial}{\partial r_1} + \frac{1}{\sin\theta}\frac{\partial}{\partial\theta}\sin\theta\frac{\partial}{\partial\theta}\right) + \\ &+\frac{1}{\mu_2 r_2^2}\left(\frac{\partial}{\partial r_2} r_2^2 \frac{\partial}{\partial r_2} + \frac{1}{\sin\theta}\frac{\partial}{\partial\theta}\sin\theta\frac{\partial}{\partial\theta}\right)\Bigg]\end{aligned} \tag{2.8}$$

$$\begin{aligned}\hat{K}_V^{(2)}(r_1,r_2,\theta) = &-\cos\theta\frac{\partial^2}{\partial r_1\partial r_2} + \frac{\cos\theta}{r_1 r_2}\left(\frac{1}{\sin\theta}\frac{\partial}{\partial\theta}\sin\theta\frac{\partial}{\partial\theta}\right) + \\ &+\sin\theta\left(\frac{1}{r_1}\frac{\partial}{\partial r_2} + \frac{1}{r_2}\frac{\partial}{\partial r_1} + \frac{1}{r_1 r_2}\right)\frac{\partial}{\partial\theta}\end{aligned} \tag{2.9}$$

$$\begin{aligned}\hat{K}_{VR}(r_1,r_2,\theta,\alpha,\beta,\gamma) = &\frac{1}{2}\left[M_{xx}\hat{J}_x^2 + M_{yy}\hat{J}_y^2 + M_{zz}\hat{J}_z^2 + M_{xz}\left(\hat{J}_x\hat{J}_z + \hat{J}_z\hat{J}_x\right)\right] + \\ &+\frac{1}{i}\Bigg[\left(\frac{1-a}{\mu_1 r_1^2} - \frac{a}{\mu_2 r_2^2}\right)\left(\frac{\partial}{\partial\theta} + \frac{\cot}{2}\right) + \frac{2a-1}{\mu_{12} r_1 r_2}\left(\cos\theta\frac{\partial}{\partial\theta} + \frac{1}{2\sin\theta}\right) + \\ &+\frac{\sin\theta}{\mu_{12}}\left(\frac{a}{r_2}\frac{\partial}{\partial r_1} - \frac{(1-a)}{r_1}\frac{\partial}{\partial r_2}\right)\Bigg]\hat{J}_y\end{aligned} \tag{2.10}$$

here $\hat{J}_i$ are the molecule-fixed angular momentum operators, obeying the standard commutation relations $\left[\hat{J}_i, \hat{J}_j\right] = i\varepsilon_{ijk}\hat{J}_k$ (where ε_{ijk} is the totally antisymmetric Levi-

Civita tensor). $M_{\alpha\beta}$ are the elements of the inverse generalized moment of inertia tensor, given explicitly in ref. [70]. In derivation of eqs. 2.8 - 2.10, it was assumed that the molecule is located in the x–z plane of the right-handed ($\det(\mathbf{C}) = +1$) molecule-fixed coordinate system. The Jacobian associated with the space-fixed to molecule-fixed transformation is given by $r_1^2 r_2^2 \sin\theta$. Here $a \in [0,1]$ determines the orientation of the molecule-fixed z-axis with respect to the direction of r_1 (more specifically r_1 makes an $a\theta$ angle with the z-axis). In this work, we are using *orthogonal coordinates* only, which by definition give $\mu_{12}^{-1} = 0$ [57]. This causes the second term in eq. 2.7 to vanish. The last term in eq. 2.7, $V(r_1, r_2, \theta)$ is the potential energy surface (PES) for a given electronic state, defined as the total electronic energy in this state for a given configuration of clamped-nuclei.

With the ro-vibrational Hamiltonian in hand, let us write down an Ansatz for the eigenfunction of the ro-vibrational SE:

$$|\Psi_{rv}^{(h)}\rangle = \sum_{i,l} c_{i,l}^{(h)} |\Phi_{rot,i}\rangle |\Phi_{vib,l,i}\rangle \tag{2.11}$$

where index h enumerates solutions to the stationary SE and i, l stand for general indices characterizing the rotational and vibrational basis states, respectively. Note that in the DVR3D procedure the vibrational wavefunction is also indexed with quantum numbers referring to rotational basis states. Such a rotation-vibration coupling scheme was chosen to ensure proper handling of singularities appearing in the ro-vibrational Hamiltonian. Below, we are going to show how DVR3D solves the stationary SE with the Hamiltonian given in eq. 2.7 and the variational wavefunction given in eq. 2.11. First, let us inspect the rotational degrees of freedom in the wavefunction.

In general, the rotational degrees of freedom cannot be separated out from the internal degrees of freedom of the molecule, as shown in eq. 2.10. But because the angular momentum operators $\hat{J}_i$ depend on the Euler angles alone [71], it is feasible to employ a spectral representation of the symmetric-top model Hamiltonian [60] for the rotational degrees of freedom (eigenfunctions of $\hat{J}^2$ and $\hat{J}_z$). In the position representation of the Euler angles the symmetric-top Hamiltonian eigenvectors can

be expressed as follows[1]

$$|J,k,M\rangle = \sqrt{\frac{2J+1}{8\pi^2}}(-1)^k \mathscr{D}^{J*}_{M,-k}(\alpha,\beta,\gamma) \tag{2.12}$$

where $\mathscr{D}^{J}_{M,k}(\alpha,\beta,\gamma)$ is the Wigner rotation matrix [72]. Here J stands for the total angular momentum quantum number, $k = -J,-J+1,...,J-1,J$ is the projection of the total angular momentum on the z-axis in the molecule-fixed coordinate frame and M is the projection of the total angular momentum on the z-axis in the space-fixed coordinate frame. The rotational symmetry (O(3), which with the choice of orientation of the coordinate system becomes SO(3)) of the ro-vibrational Hamiltonian guarantees independence of the ro-vibrational energy levels of the M quantum number. For this reason, a shorthand notation for the rotational basis function will be used $|J,k,M\rangle \equiv |J,k\rangle$. The complete basis set of $2J+1$ functions: $\{|J,k\rangle\}_{k=-J,...,J}$ is used to perform analytical integration over the rotational degrees of freedom α,β,γ in the ro-vibrational Hamiltonian given in eq. 2.7, yielding a set of effective Hamiltonians depending only on three internal coordinates describing the vibrational degrees of freedom, and parametrized by the J and k quantum numbers:

$$\hat{H}^{J'J}_{k'k}(r_1,r_2,\theta)\delta_{J'J} = \langle J',k'|\hat{H}(r_1,r_2,\theta,\alpha,\beta,\gamma)|J,k\rangle_{\alpha,\beta,\gamma} \tag{2.13}$$

here J is a good quantum number associated with the invariance of the ro-vibrational Hamiltonian to 3D-space rotations, but k in general is not a good quantum number for a triatomic molecule. k only becomes a good quantum number, associated with the $\hat{J}_z$ operator, when the molecule is in its linear geometry (symmetric-top) or all Coriolis-couplings ($\hat{K}_{VR}$) are neglected. Without utilizing any further symmetries, one arrives with the effective vibrational Hamiltonian in the form:

$$\hat{H}^{J}_{k'k}(r_1,r_2,\theta) = \delta_{k'k}\left(\hat{K}_V(r_1,r_2,\theta)+V(r_1,r_2,\theta)\right)+\hat{K}_{VR}(r_1,r_2,\theta) \tag{2.14}$$

[1] note that the "=" in equation 2.12 is informal, as we are equating an object from the *Hilbert* vector space $\mathscr{H}$ to a function from $\mathscr{L}^2$. These distinct spaces are are isomorphic, and in this sense equation 2.12 should be understood.

where

$$\hat{K}_V(r_1,r_2,\theta) = -\frac{1}{2}\left[\frac{1}{\mu_1 r_1^2}\frac{\partial^2}{\partial r_1^2} + \frac{1}{\mu_2 r_2^2}\frac{\partial^2}{\partial r_2^2} + \left(\frac{1}{\mu_1 r_1^2} + \frac{1}{\mu_2 r_2^2}\right)\frac{1}{\sin\theta}\frac{\partial}{\partial\theta}\sin\theta\frac{\partial}{\partial\theta}\right] \tag{2.15}$$

$$\hat{K}_{VR}(r_1,r_2,\theta) = \delta_{k'k\pm2}\frac{1}{4}C^{\pm}_{Jk\pm1}C^{\pm}_{Jk}b_- + \delta_{k'k\pm1}\frac{1}{2}C^{\pm}_{Jk}\lambda^{\pm} + \delta_{k'k}\frac{1}{2}\left(b_+(J(J+1)-k^2)+b_0k^2\right) \tag{2.16}$$

with

$$\begin{aligned}\lambda^{\pm} = \frac{1}{\mu_1 r_1^2}&\left[\mp(1-a)\left(\frac{\partial}{\partial\theta}+\frac{\cot\theta}{2}\right)+\left(k\pm\frac{1}{2}\right)\frac{z_{x2}z_{z2}}{r_2^2\sin^2\theta}\right]+\\ &+\frac{1}{\mu_2 r_2^2}\left[\pm a\left(\frac{\partial}{\partial\theta}+\frac{\cot\theta}{2}\right)+\left(k\pm\frac{1}{2}\right)\frac{z_{x1}z_{z1}}{r_1^2\sin^2\theta}\right]\end{aligned} \tag{2.17}$$

and

$$C^{\pm}_{Jk} = \left[J(J+1)-k(k\pm1)\right]^{\frac{1}{2}}, \tag{2.18}$$

$$b_{\pm} = \frac{M_{xx}\pm M_{yy}}{2}, \qquad b_0 = M_{zz}$$

the z_{x1} type terms are elements of the molecule-fixed coordinates matrix defined in eq. 2.6. The ro-vibrational Hamiltonian in the present form takes infinite values for $\theta = 0,\pi$, due to $\frac{1}{\sin\theta}$ terms appearing in both its vibrational and ro-vibrational part. Sutcliffe and Tennyson suggested [58] that these singularities can be, at least partially, eliminated with the use of the associated Legendre polynomial basis $|jk\rangle = P_j^{(|k|)}(\cos\theta)$ for the bending motion. Additionally, this basis couples the rotational motion through the k quantum number. Indeed, such effectively rotation-vibration coupled basis results in cancelling of the singular terms in the ro-vibrational Hamiltonian for certain embedding types. Integration over the bending coordinate, with the chosen basis in the phase convention of Condon and Shortley [73] further simplifies the effective operators to the radial-vibrational form:

$$\hat{H}(r_1,r_2) = \delta_{k'k}\left(\hat{K}_V(r_1,r_2) + V^k_{j'j}(r_1,r_2)\right) + \hat{K}_{VR}(r_1,r_2) \tag{2.19}$$

$$\hat{K}_V(r_1,r_2) = -\delta_{j'j}\left[-\frac{1}{2\mu_1}\frac{\partial^2}{\partial r_1^2} - \frac{1}{2\mu_2}\frac{\partial^2}{\partial r_2^2} + \frac{1}{2}j(j+1)\left(\frac{1}{\mu_1 r_1^2} + \frac{1}{\mu_2 r_2^2}\right)\right] - \\ -\frac{k^2}{2}\left(\frac{1}{\mu_1 r_1^2} + \frac{1}{\mu_2 r_2^2}\right)\langle j'k'|\frac{1}{\sin^2\theta}|jk\rangle. \tag{2.20}$$

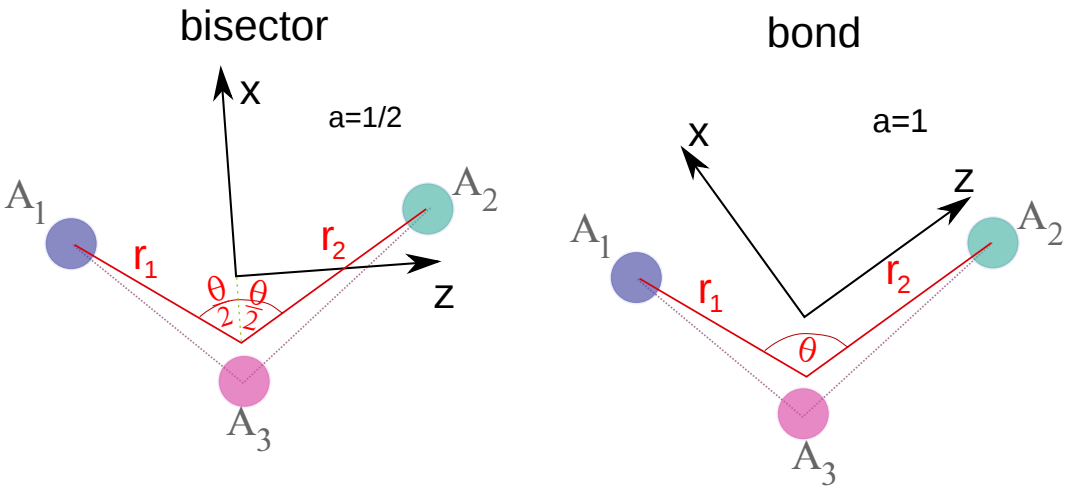

Figure 2.2: Two types of embedding of the molecule-fixed coordinate frame used in DVR3D calculations. A_1, A_2, A_3 stand for labels of atom 1, 2 and 3, respectively. r_1, r_2, θ are Radau coordinates. The molecule-fixed axis system is centred at the nuclear centre of mass of the triatomic system. However the point at which Radau coordinates originate is a geometric mean between the distance from atom A_3 and the centre of mass for atoms A_1 and A_2 and the distance from the nuclear centre of mass to the centre of mass for atoms A_1 and A_2. In the bisector embedding the x-axis bisects the θ angle, whereas in bond embeddings the z-axis is parallel to the r_1 or r_2 coordinate.

The form of the rotation-vibration operator $\hat{K}_{VR}(r_1,r_2)$ depends on the embedding chosen. Here two cases are considered: bond embedding ($a = 0, 1$) and bisector embedding ($a = \frac{1}{2}$). Both types of embeddings are depicted in Figure 2.2. From now on we are going to use Radau internal coordinates [62], which are also displayed in Figure 2.2. The bisector embedding of the molecule-fixed frame will be used to calculate ro-vibrational line lists for the symmetric isotopologues of CO_2

whereas the bond embedding will be used for the asymmetric isotopologues of CO_2 and for calculation of ro-vibronic spectra for SO_2.

Bond embedding. In bond embedding the z-axis in the molecule-fixed coordinate frame lies along $\mathbf{t}_1$ ($a = 0$) or $\mathbf{t}_2$ ($a = 1$). The vibration-rotation part of the KEO is then given by

$$\hat{K}_{VR}(r_1, r_2) = -\delta_{j'j}\delta_{k'k}\frac{1}{2\mu_1 r_1^2}(J(J+1) - 2k^2) - \delta_{j'j}\delta_{k'k\pm1}\frac{1}{2\mu_1 r_1^2}C_{Jk}^{\pm}C_{jk}^{\pm} \quad (2.21)$$

Bisector embedding. In the bisector embedding the x-axis of the molecule-fixed coordinate frame bisects the angle between $\mathbf{t}_1$ and $\mathbf{t}_2$ ($a = \frac{1}{2}$). In such case, the rotation-vibration KEO couples states with $k' = k \pm 1$ and $k' = k \pm 2$ and can be split into three parts:

$$\begin{aligned}\hat{K}_{VR}^{(1)}(r_1, r_2) = \delta_{k'k}\frac{1}{8}(J(J+1) - 3k^2)\left(\frac{1}{\mu_1 r_1^2} + \frac{1}{\mu_2 r_2^2}\right) I_{j'k'jk}^{(1)} + \\ + \delta_{k'k}\delta_{j'j}\frac{1}{16}(J(J+1) - k^2)\left(\frac{1}{\mu_1 r_1^2} + \frac{1}{\mu_2 r_2^2}\right)\end{aligned} \quad (2.22)$$

$$\hat{K}_{VR}^{(2)}(r_1, r_2) = \delta_{k'k\pm1}\frac{C_{jk}^{\pm}}{4}\left(\frac{1}{\mu_2 r_2^2} - \frac{1}{\mu_1 r_1^2}\right)\left(\delta_{j'j}C_{jk}^{\pm} + \left(k \pm \frac{1}{2}\right) I_{j'k'jk}^{(2)}\right) \quad (2.23)$$

$$\hat{K}_{VR}^{(3)}(r_1, r_2) = \delta_{k'k\pm2}C_{Jk\pm1}^{\pm}C_{Jk}\left(\frac{1}{\mu_2 r_2^2} + \frac{1}{\mu_1 r_1^2}\right)\left(2I_{j'k'jk}^{(1)} - I_{j'k'jk}^{(3)}\right) \quad (2.24)$$

where

$$I_{j'k'jk}^{(1)} = \langle j'k'|\frac{1}{1-\cos\theta}|jk\rangle \quad (2.25)$$

$$I_{j'k'jk}^{(2)} = \langle j'k'|\frac{1+\cos\theta}{\sin\theta}|jk\rangle \quad (2.26)$$

$$I^{(3)}_{j'k'jk} = \langle j'k'|jk\rangle \tag{2.27}$$

Coming back to the general embedding, both operator matrices 2.15 and 2.16 are diagonal in J, and the rotation-vibration coupling operator in eq. 2.16 have a strip-pentadiagonal structure in k, meaning that it can have non-zero elements only two rows or two columns away from the diagonal. Such structure allows for an efficient computer implementation, which will be described in section 2.4. The final form of the rotation-vibration operator depends on the embedding chosen, which is reasonable, because individual moments of inertia and the magnitude of the rotation-vibration coupling strongly depend on where the molecule-fixed axis is placed. A common choice for the molecule-fixed embedding is the so called *Eckart frame* [60], which by definition minimizes the coupling between rotations and vibrations. Here however, only embeddings fixed to a chosen set of internal coordinates will be used; these have been shown to be sufficient for highly accurate nuclear motion calculations [32, 37–39, 67, 74–77]. Of course, one could be concerned that a fixed embedding of the molecule-fixed frame will result in poor convergence of energy level calculations. The Eckart embedding comes to mind naturally. However, first of all, with the Eckart embedding the form of the kinetic energy operator becomes complicated [78–81]. Secondly, the Eckart frame is not suitable for very floppy systems and no advantage could be gained over the fixed embeddings for such systems [82, 83]. Finally, an efficient algorithm by Tennyson *et al.* [59], for solution to the ro-vibrational SE, presented in the following sections, diminishes the drawback of the non-minimal rotation-vibration coupling. All in all, a good level of convergence can be achieved with the fixed embeddings too.

Having the effective vibrational Hamiltonian derived, the next step is to choose a vibrational radial basis, for calculation of the matrix elements of the operators in eqs. 2.21–2.24. The next section gives a brief description of available radial basis sets in DVR3D, as well as summarizes on the total ro-vibrational basis. After the choice of the vibrational radial basis, the resulting Hamiltonian matrix needs to be diagonalised, to obtain expansion coefficients in eq. 2.11 and ro-vibrational energy

levels. Details of the diagonalisation step are given in section 2.4.

From the computational perspective, the reduction in the number of degrees of freedom, from 9 Cartesian degrees of freedom to three effective vibrational degrees of freedom labelled by rotational quantum numbers is a huge improvement. This improvement however comes at a cost of singularities arising in the ro-vibrational Hamiltonian and the complicated form of the kinetic energy operator. On the other hand, as we expected, in the internal coordinates framework it is easy to identify vibrational, rotational and rotational-vibrational parts of the Hamiltonian, thus physically motivated approximations can be made at hand.

2.2 Ro-vibrational basis set

Following the previous section (cf. eq. 2.11), the trial variational wavefunction for DVR3D can be generally written as:

$$|\Psi_{rv}^{(h)}\rangle = \sum_{i,l} c_{i,l}^{(h)} |\Phi_{rot,i}\rangle |\Phi_{vib,l,i}\rangle \tag{2.28}$$

For the rotational degrees of freedom the complete symmetric-top eigenbasis was chosen $|\Phi_{rot,i}\rangle = |J,k\rangle$. Each vibrational basis wavefunction $|\Phi_{vib,l,i}\rangle$ is factorized into three independent sets of primitives, each depending on a single vibrational coordinate: $|\Phi_{vib,l,i}\rangle = |m\rangle|n\rangle|jk\rangle$. Then $l = m,n,j, i = J,k$. For the bending vibrational motion the associated Legendre polynomial basis is used $|jk\rangle = P_j^{(k)}(\cos\theta)$. The combined angular-bending basis set $|\Phi_{rot-bend}\rangle = |J,k\rangle|jk\rangle$ is an eigenbasis for the $\hat{J}^2$ and $\hat{J}_z$ operator. For the product radial-vibrational basis $|m\rangle|n\rangle$ (where $|m\rangle$ refers to the r_1 coordinate and $|n\rangle$ refers to the r_2 coordinate) two types of functions will be considered: the Spherical oscillator basis [59, 84] and the Morse oscillator-like basis [59, 84]. The Morse oscillator-like basis is defined as:

$$|n\rangle = N_{n\alpha}\beta^{\frac{1}{2}} L_n^{\alpha}(x(r))x(r)^{\frac{\alpha+1}{2}} e^{-\frac{x(r)}{2}} \tag{2.29}$$

with

$$x(r) = Ae^{-\beta(r-r_e)} \tag{2.30}$$

where

$$A = \frac{4D_e}{\beta} \qquad \beta = \omega_0 \left(\frac{\mu}{2D_e} \right)^{\frac{1}{2}}; \tag{2.31}$$

α has been defined by Tennyson and Sutcliffe as the integer part of A [59, 84, 85]. With this definition, the Morse oscillator-like functions $|n\rangle$ constitute a complete orthonormal basis set, a property which is missing in the 'standard' Morse oscillator eigenbasis. Here $N_{n\alpha}L_n^{\alpha}(x(r))$ is a normalised associated Laguerre polynomial and μ is the reduced mass related to a vibrational coordinate. ω_0 and D_e are standard Morse potential parameters, related to the width and depth of the potential well, respectively. The number of bound states for the Morse oscillator is the integer part of $\frac{A-1}{2}$.

Note that the Morse oscillator and Morse oscillator-like basis do not vanish at $r = 0$ ($x(0) = Ae^{\beta r_e}$), as one may expect. Nonetheless, in the $r = 0$ region the Morse potential increases rapidly, making it almost un-explorable for the wavefuncion. Moreover, the value $Ae^{\beta r_e}$ is typically large enough for the exponent factor in eq.(2.29) to damp other factors almost to 0. Hence, without significant loss in accuracy it is possible to replace the finite boundary value $Ae^{\beta r_e}$ with $+\infty$ in integrations, making them analytically feasible. Thus, the Morse oscillator-like basis is applicable for $r \neq 0$. Whenever a vibrational coordinate has a chance to penetrate regions near $r = 0$, the Morse basis set can give inaccurate results; is it then more suitable to use the Spherical oscillator basis set defined as:

$$|n\rangle = N_{n\alpha+\frac{1}{2}} 2^{\frac{1}{2}} \beta^{\frac{3}{4}} L_n^{\alpha+\frac{1}{2}}(x(r)) x^{\frac{\alpha+1}{2}} e^{-\frac{x(r)}{2}} \tag{2.32}$$

with

$$x(r) = \beta r^2 \tag{2.33}$$

where

$$\beta = (\mu\omega_0)^{\frac{1}{2}} \tag{2.34}$$

The Morse-like oscillator basis set depends on three parameters: D_e, ω_0 and r_e and the Spherical oscillator basis set depends on parameters: α, ω_0. These pa-

rameters can be considered as non-linear variational parameters, and should be optimized. Such optimization is performed for CO_2 in section 3.3.3 in chapter 3. At this stage, the full Hamiltonian matrix is labelled by the following indices: J,k,m,n,j, meaning that for a chosen J, the Hamiltonian has the dimension of $(2J+1)\times N_{r_1}\times N_{r_2}\times N_\theta$, where N_{r_1},N_{r_2} and N_θ are sizes of 1D vibrational basis sets associated with coordinates r_1,r_2 and θ, respectively. The size of the vibrational basis set is system-specific and is chosen to ensure an appropriate level of convergence of energy levels. Further reduction in the vibrational basis set size can be made with the use of symmetries of the system.

2.3 Additional symmetries

From the perspective of computational efficiency one usually should utilize all relevant physical symmetries of the system, so that the Hamiltonian operator acts acts irreducibly in *Hilbert space* spanned by the ro-vibrational the basis functions: $|J,k\rangle|m\rangle|n\rangle|jk\rangle$. In other words, we want to find a complete set of observables commuting with the Hamiltonian. Such an operation is also usable from the point of view of spectroscopic assignments, which are based on all good quantum numbers of the system. It is thus convenient to have the ro-vibrational wavefunctions labelled by all good quantum numbers of the system. The variational basis set defined in the previous section can be written as:

$$|J,h\rangle = \sum_{k=-J}^{J}\sum_{m,n,j} c^{J(h)}_{k,m,n,j}|J,k\rangle|m\rangle|n\rangle|jk\rangle \tag{2.35}$$

The parity operation E^*, which is a feasible symmetry operation for all molecules [2], can be used to construct a symmetry-adapted basis, which further factorizes the Hamiltonian matrix and introduces spectroscopically an important symmetry label. The parity symmetry operation transforms states with k quantum number into states with $-k$, and *vice versa*: which in the classical picture means that the clockwise and anti-clockwise rotation of the molecule around the molecule-fixed z-axis is energetically equivalent. For this reason, it is convenient to symmetry-adapt

[2] if 'weak nuclear interactions' are neglected.

the rotational-bending basis, by means of the following unitary transformation:

$$|J,K,j,p\rangle = \frac{1}{\sqrt{2(1+\delta_{k0})}}|jk\rangle \otimes (|J,k\rangle + (-1)^p|J,-k\rangle)^* \qquad (2.36)$$

where the new quantum number $p = 0,1$ is associated with the *parity* symmetry of the ro-vibrational state and determines the e/f Wang labels ($p = 0$ for the e state and $p = 1$ for the f state); now $K = |k|$ takes integer values from p to J. In such a basis, only positive values of k can be considered and the full Hamiltonian is factorized into independent blocks with $p = 0$ and $p = 1$ of dimension $J+1$ and J, respectively.

For triatomic symmetric XY_2 molecules for which the molecule-fixed axis system is chosen so that the x-axis (or z-axis) bisects the Y–X–Y angle [67], an additional symmetry can be utilized to simplify the Hamiltonian matrix: the permutation symmetry of identical nuclei P_{12}. The permutation operator interchanges r_1 and r_2 coordinates, hence effectively acts on radial vibrational basis functions. For this reason, the radial-vibrational basis set can be unitarily transformed into its symmetry-adapted form:

$$|m,n,q\rangle = \frac{1}{\sqrt{2(1+\delta_{mn})}}\left(|m\rangle \otimes |n\rangle + (-1)^q|n\rangle \otimes |m\rangle\right), \qquad m \geq n \qquad (2.37)$$

where $|m\rangle \otimes |n\rangle$ stands for the tensor product of vibrational basis states associated with the first r_1 and the second r_2 stretching Radau coordinate, respectively. m and n label the 1D basis states. The new vibrational parity quantum number takes two values: $q = 0$ for 'even' vibrational states and $q = 1$ for 'odd' vibrational states. Note that the character of the permutation P_{12} of identical nuclei acting on the basis state in eq. (2.37) is $(-1)^{q+k}$ and the character of the parity E^* operation acting on the basis state in eq. (2.36) is $(-1)^{p+J}$.

Utilization of the rotational parity and the vibrational parity decomposes the *Hilbert space* of the problem into simple sum of four independent sub-spaces for each J: $\mathscr{H}^J_{p,q} \bigoplus \mathscr{H}^J_{p,1-q} \bigoplus \mathscr{H}^J_{1-p,q} \bigoplus \mathscr{H}^J_{1-p,1-q}$. This allows to run calculations in-

dependently in each of these reduced subspaces. Mixing of these reduced *Hilbert spaces* occurs when we consider the electronic dipole moment operator $\hat{\mu}_{el}$ in transition intensities calculations. Then, $\hat{\mu}_{el}$ mixes subspaces according to rigorous selection rules: $|\Delta q| = 1$ and for $\Delta J = 0$: $|\Delta p| = 1$ and $\Delta J = \pm 1$: $|\Delta p| = 0$.

With the above transformations, the final ro-vibrational basis set used in the present implementation of DVR3D is given by the expression:

$$|J,h,p,q\rangle = \sum_{K=p}^{J} \sum_{m,n,j} C_{mnjK}^{J,(h),p,q} |m,n,q\rangle \otimes |J,K,j,p\rangle \tag{2.38}$$

This basis will be used to calculated matrix elements of the Hamiltonian in eq. 2.7.

2.4 Strategy for solution

As we could see in the preceding sections, the total ro-vibrational Hamiltonian matrix is constructed gradually by integrating over rotational, bending and radial stretching degrees of freedom. Direct calculation of the matrix elements of the KEO and the PES in the basis presented in eq. 2.38 is impractical, and becomes prohibitive for higher J values. For this reason Sutcliffe and Tennyson proposed a two-step procedure of diagonalizing the ro-vibrational Hamiltonian matrix [67, 86, 87]. In the first step a Coriolis-decoupled Hamiltonian is considered:

$$\hat{H}_K = \delta_{K,K'} \hat{K}_V + \delta_{K,K'} \hat{K}_{rv} + \delta_{K,K'} V \tag{2.39}$$

and the respective SE is solved with $K = |k| = p, p+1, ..., J$ as a good quantum number for each J separately. This approximation is valid for any system with negligible Coriolis coupling, which mixes states with different K. With these assumptions, the solutions to the SE in the first step can be written as:

$$|J,p,q,K,h\rangle = \sum_{m,n,j} d_{mnj}^{J,(h),K,p,q} |m,n,q\rangle \otimes |J,K,j,p\rangle \tag{2.40}$$

with the corresponding energy levels $\varepsilon^{J,(h),K,p,q}$. For a chosen J it is necessary to solve only $J+p$ nuclear motion problems for $K = p, 1, ..., J$.

In the second step, solutions to the first step are used as the variational basis. Typically, good convergence is achieved with even very contracted basis set from the first step, because the Coriolis-decoupled basis captures the majority of physical information about the vibrational motion, hence becomes an excellent basis. For this reason, one can usually choose only a small percentage of solutions from the first step to achieve a good convergence level. The final wavefunction mixes states with different K's, as suggested by the form of the K_{VR} operators:

$$|J,h,p,q\rangle = \sum_{K=p}^{J} f_K^{J,h,p,q} |J,p,q,K,h\rangle = \sum_{K=p}^{J} \sum_{m,n,j} C_{mnjK}^{J,(h),p,q} |m,n,q\rangle \otimes |J,K,j,p\rangle \tag{2.41}$$

where in the last equality we retained the form of the wavefunction from eq. 2.38.

The first step of solving the ro-vibrational SE sketched above is implemented in the "DVR3DRJZ" program [59, 67]. It uses a discrete variable representation (DVR) to obtain values of the matrix elements of the Coriolis-decoupled Hamiltonian. Below, in a nutshell, we will therefore introduce the essential basics of the DVR theory. Next, we shall discuss the second variational step implemented in programs Rotlev3, Rotlev3b or Rotlev3z, depending on embedding used.

2.4.1 The DVR technique

The discrete variable representation (DVR) is a technique originally developed by Harris *et al.* [88] which was later implemented by Light *et al.* [89, 90] to solve quantum-mechanical problems in the nuclear motion theory. In this technique the physical space is discritized and respective quantum-mechanical quantities are defined on a finite grid of points.

The reason for using DVR, in a nutshell, is that the DVR technique produces sparse matrices, which can be efficiently diagonalised by iterative algorithms. Alternatively, if one utilizes a two-step procedure like the one proposed by Sutcliffe and Tennyson [67, 86, 87], it has been shown by Lee *et al.* [91] and Bramley *et al.* [92] that a DVR can provide an optimal contracted basis, such as the one presented in subsection 2.4. It is a matter of choice, whether to choose the former

or the latter convenience coming from DVR [92]. Combining the DVR technique with a two-step variational procedure gives much better convergence than in the standard single-step variational approach. In addition to that, with DVR, there is no need for calculating $N(N+1)/2$ matrix elements in the potential energy part of the Hamiltonian matrix. Below, given is an introduction to the DVR, oriented for the purposes of use in DVR3D. Here we shall not follow any textbook derivation of DVR, but rather introduce a natural, in author's opinion, way of defining it in terms of quantum mechanical transformations.

Historically, the first discrete variable representations were based on orthogonal polynomials used in solutions to the SE for model systems, e.g. Harmonic oscillator (Hermite polynomials) [93], Hydrogen atom (Laguerre polynomials), Morse oscillator (associated Laguerre polynomials) [94,95], particle in the square potential well (Chebyszev polynomials) or Legendre Polynomials for problems with spherical symmetry. Nonetheless, there are many more types of DVRs and their use is currently much broader than molecular spectroscopy, see reviews by Light and Bacic [89], and Light and Carrington [90] or Szalay [96].

In the variational basis representation (VBR), matrix elements of the potential energy operator are given by

$$\left(\mathbf{V}^{\mathbf{VBR}}\right)_{ij} = \int_a^b \phi_i(x) V(x) \phi_j(x) dx \tag{2.42}$$

where an orthonormal basis set $\{\phi_i\}_{i=1,\ldots,N}$ was chosen. Let us transform this variational basis into a new basis, which we will be calling the 'Exact Discrete Variable Representation' (EDVR). The word *exact* suggests here complete equivalence of EDVR to the original variational representation. The VBR-EDVR basis change is defined as follows:

$$(d_0(x), d_1(x), \ldots, d_{N-1}(x)) = (\phi_0(x), \phi_1(x), \ldots, \phi_{N-1}(x))\,\mathbf{T} \tag{2.43}$$

where $d_i(x)$ is the EDVR basis, which contains functions localized in space around certain points. We are aiming at transformation from a usually diffuse variational

basis to a basis which is highly localized around given points in space, and in the limit of the complete basis set, these highly localized functions become Dirac deltas. With this target in mind, now let us postulate a general form for the transformation T, by means of some chosen N coordinate points, $\{x_i\}_{i=0,...,N-1}$:

$$T_{ik} = t_k \phi_i(x_k), \qquad i,k = 0,1,...,N-1 \tag{2.44}$$

where t_k is yet to be determined and $\phi_i(x_k)$ is the value of the basis function $\phi_i(x)$ at point x_k. Note that up to now all functions are defined over the continuous variable space. A physical requirement of the equivalence of the EDVR and VBR basis sets means that we demand quantum mechanical scalar products to be identical in both representations. This is achieved by imposing the condition thath the transformation 2.44 is unitary:

$$\mathbf{T}\mathbf{T}^\dagger = \mathbf{1} \Rightarrow \left(\mathbf{T}\mathbf{T}^\dagger\right)_{ij} = \sum_{k=0}^{N-1} t_k^2 \phi_i(x_k)\phi_j(x_k) = \delta_{ij} \tag{2.45}$$

Because $\mathbf{T}\mathbf{T}^\dagger = \mathbf{1}$ and we assume *a priori* the existence of the inverse of $\mathbf{T}$, we have $\mathbf{T}^\dagger = \mathbf{T}^{-\mathbf{1}}$, hence the relation $\mathbf{T}^\dagger\mathbf{T} = \mathbf{1}$ appears as a corollary. In other words, if the relation 2.45 holds, 'the other' relation must be satisfied as well, for transformation T to be unitary:

$$\mathbf{T}^\dagger\mathbf{T} = \mathbf{1} \Rightarrow \left(\mathbf{T}^\dagger\mathbf{T}\right)_{ij} = \sum_{k=0}^{N-1} t_i t_j \phi_k(x_i)\phi_k(x_j) = \delta_{ij} \tag{2.46}$$

The next step is to find a complete set of functions satisfying eq. 2.45. There are probably infinitely many possible solutions to this equation. Historically, Gaussian quadratures were first associated with DVR by Harris *et al.* [88], Dickinson *et al.* [97] and Light *et al.* [98]. The DVR3D procedure uses only Gaussian quadrature-based discretization schemes (DVRs), thus here we only discuss Gaussian-type quadratures. For further reading refer to [89, 90]. In this light, it is useful to regard the sum in eq. 2.46 as a Gaussian quadrature. The sum in eq. 2.46 a has similar form to the Gaussian quadrature associated with integral $\int \phi_i(x)\phi_j(x)dx$.

Such N-point quadrature is exact for polynomials up to degree $2N-1$. Therefore, it is natural to define ϕ as a product of some orthogonal polynomial $p(x)$ and an associated positive weight function $\omega(x)$, imposing the relations 2.45–2.46 to be exact.

$$\phi_i(x) = \sqrt{\omega(x)}p_i(x) \tag{2.47}$$

The square root of the weight function $\omega(x)$ is to ensure the proper orthogonality relations[3] for ϕ. The form of t_i can be now easily guessed: $t_i = \sqrt{\frac{A_i}{\omega(x_i)}}$, which entails

$$\left(\mathbf{T}\mathbf{T}^{\dagger}\right)_{ij} = \sum_{k=0}^{N-1} A_i p_i(x_k) p_j(x_k) = \int_a^b \omega(x) p_i(x) p_j(x) dx = \delta_{ij} \tag{2.48}$$

where A_i are weights associated with the N-point Gaussian quadrature based on orthogonal polynomials $p(x)$. The above sum represents a Gaussian quadrature for the overlap integral (scalar product) of orthogonal polynomials, and is computed exactly. The second orthogonality relation then reads

$$\left(\mathbf{T}^{\dagger}\mathbf{T}\right)_{ij} = \sum_{k=0}^{N-1} \sqrt{A_i A_j} p_k(x_i) p_k(x_j) = \delta_{ij} \tag{2.49}$$

which yields the following sum rule:

$$\sum_{k=0}^{N-1} p_k(x_i) p_k(x_j) = \frac{\delta_{ij}}{\sqrt{A_i A_j}} \tag{2.50}$$

At this stage we have fully defined a unitary basis transformation in N-element space over the continuous variable physical space (function space). Formally, for a chosen operator $\hat{V}$ the EDVR-VBR transformation can be written in the matrix form [4]:

$$\mathbf{V}^{\mathbf{EDVR}} = \mathbf{T}^{\mathbf{T}}\mathbf{V}^{\mathbf{VBR}}\mathbf{T} \tag{2.51}$$

[3] Note that by definition $\int_a^b \omega(x) p_i(x) p_j(x) dx = \delta_{ij}$

[4] Because the basis transformation is defined as $d_i = \sum_k \phi_k T_{ki}$ and $\langle d_i|V|d_j\rangle = V_{ij}^{DVR} = \sum_{k,t} T_{ki}\langle\phi_i|V|\phi_j\rangle T_{kj} = \left(T^T V^{VBR} T\right)_{ij}$

The EDVR basis functions are localized around the associated quadrature points. The type of quadrature is dictated by the choice of the orthogonal polynomial $p(x)$ and the exact location of points is given by the order of the quadrature N. Localization is more effective as the number of basis functions (quadrature points N) increases, and in the limit of the infinite basis EDVR functions become *Dirac delta* distributions [99]:

$$\begin{aligned}\left(\mathbf{V}^{\mathbf{EDVR}}\right)_{ij} = \int d_i(x)V(x)d_j(x)dx \longrightarrow \int \delta(x-x_i)V(x)\delta(x-x_j)dx = \\ = \int V(x_i)\delta(x_i-x_j)dx = V(x_i)\delta_{ij}\end{aligned} \tag{2.52}$$

here the $d_i(x)$ basis functions are defined over continuous domain, localized in discrete points and packed infinitely densely one next to another. All above relations between DVR and VBR are exact, since we operate within a limit of infinitely dense quadrature nodes (i.e. continuous representation). Because the EDVR and VBR basis sets are unitarily connected, they are quantum-mechanically equivalent (i.e. all scalar products and expectation values of observables are equal in both basis sets). Truncations in the VBR basis implies non-perfect-localization of the corresponding EDVR basis. For this reason, in computational practice, when a finite set of variational basis functions is used, eq. 2.52 is satisfied only approximately: $\left(\mathbf{V}^{\mathbf{DVR}}\right)_{ij} \approx V(x_i)\delta_{ij}$. The matrix of the potential energy operator in 'finite basis EDVR', which is simply called 'DVR', is not exactly diagonal, however the off-diagonal elements are assumed to 'be small' (smaller and smaller for larger basis size). In computational practice, the physical space is always discretized. For this reason, it is usually necessary to choose a discrete set of points in physical space over which scalar products are computed. In DVR, for this purpose the set of Gaussian quadrature nodes $\{x_i\}_{i=0,\ldots,N-1}$ is used.

Recall the EDVR-VBR transformation:

$$d_i(x) = \sum_{j=0}^{N-1} T_{ji}\phi_j(x) \tag{2.53}$$

In discrete coordinate space, for $x_k \neq x_i$ we have

$$d_i(x_k) = \sum_{j=0}^{N-1} \sqrt{A_i \omega(x_k)} p_j(x_i) p_j(x_k) \tag{2.54}$$

and on account of relation 2.49 we find

$$d_i(x_k) = \sqrt{\frac{\omega(x_k)}{A_i}} \delta_{ik} \tag{2.55}$$

It means that the DVR basis vanish everywhere except in one quadrature node, where it takes a non-zero value determined by the type and size of the quadrature. We shall take advantage of this fact by defining the physical space spanned over those quadrature points. In a continuous representation, basis functions generally take non-zero values between discrete points, however they tend to be smaller with increasing distance to the central point. Such choice of grid points justifies the following approximation to the matrix elements of the potential energy function:

$$V_{ij}^{EDVR} = \langle d_i(x)|V(x)|d_j(x)\rangle = \int_a^b d_i(x) V(x) d_j(x) dx \approx V_{ij}^{DVR} =$$
$$\sum_{k=0}^{N-1} \frac{A_k}{\omega(x_k)} d_i(x_k) V(x_k) d_j(x_k) = \sum_{k=0}^{N-1} \frac{A_k}{\omega(x_k)} \sqrt{\frac{\omega(x_k)}{A_i}} \delta_{ik} V(x_k) \sqrt{\frac{\omega(x_k)}{A_j}} \delta_{jk} = V(x_i) \delta_{ij} \tag{2.56}$$

Because the definition of DVR, given in eq. 2.44, mixes the coordinates space and functions space, the discretization of space can be viewed from two perspectives. One of them is to look at the VBR integrals as finite sums, exactly as the Gaussian quadrature does. In this sense, the finite number of elements in the sum representing the VBR integral is associated with discretization of space in the corresponding DVR:

$$\left(\mathbf{V}^{\mathbf{VBR}}\right)_{ij} \approx V_{ij}^{FBR} = \sum_{k=0}^{N-1} \frac{A_k}{\omega(x_k)} \phi_i(x_k) V(x_k) \phi_j(x_k) = \sum_{k=0}^{N-1} \mathbf{T}_{ik} V(x_k) \mathbf{T}_{kj}^T \tag{2.57}$$

and the last sum is equivalent to matrix element of product of three matrices:

$$\left(\mathbf{V}^{\mathbf{FBR}}\right)_{ij} = \sum_{k=0}^{N-1} \mathbf{T}_{ik} V(x_k) \mathbf{T}^{\dagger}_{kj} = \left(\mathbf{T}\mathbf{V}^{\mathbf{DVR}}\mathbf{T}^{\dagger}\right)_{ij} \tag{2.58}$$

Such a representation of the potential energy operator matrix is called *Finite basis representation* - ***FBR***. Finite basis representation changes integral representation of the inner product into discrete inner product deified by corresponding quadrature nodes. The FBR is totally equivalent to the DVR, because the two are related by a unitary transformation, which preserves the inner product, hence do not change the mean values of observables of a system. Of course, $\mathbf{V}^{\mathbf{DVR}}$ remains diagonal

$$\mathbf{V}^{\mathbf{DVR}} = diag(V(x_0), ..., V(x_{N-1})) \tag{2.59}$$

hence $\mathbf{T}$ is a unitary transformation matrix from the finite basis representation to the discrete variable representation basis, where the potential energy (and all local operators) matrix is diagonal. Note that after diagonalization the quadrature points often need to be scaled to represent physical quantities.

To sum up, we postulated the form of VBR – DVR basis transformation, with the requirement of unitarity, which led to the appropriate transformation of operator matrices. Orthogonal polynomials were chosen as trial VBR functions, for which the Gaussian quadrature integration could be performed exactly. Thus, for functions of the position operator which are in the form of sufficiently low order polynomial (N or lower), the FBR integrals are exact, which entails that the DVR pointwise representation of these operators will also give the exact result. When this condition is fulfilled the DVR can be considered variational. However, matrix elements of non-local operators and non-polynomial position operators can be evaluated only approximately, which renders the DVR technique as non-variational. Whenever the FBR or DVR matrix elements are non-exact, it is possible that the variational principle (MacDonald's theorem [100]) is not satisfied. A FBR usually uses extra quadrature points to ensure variational behaviour. A summary of this section is displayed in Figure 2.3, where a scheme is given relating EDVR, FBR, VBR and

DVR.

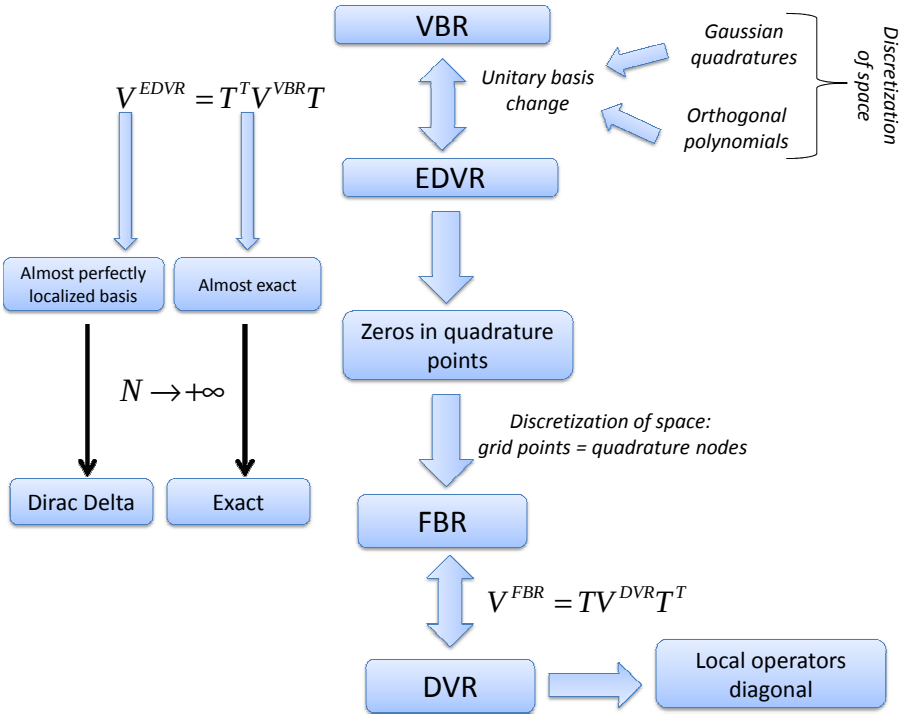

Figure 2.3: A general scheme for the VBR-DVR transformation.

2.4.2 Product approximation

The DVR-FBR transformation can be derived from yet another, more practical point of view. This approach is called *product approximation* [90] and it provides a procedure for generating the DVR-FBR transformation matrices by means of diagonalisation of the position operator matrix.

In general, the position operator matrix is of infinite size, as the position operator X is unbounded and acts irreducibly on the Hilbert space (in other words the largest invariant subspace of the Hilbert space for the position operator is the full space). In the VBR the matrix elements of X are written as:

$$\left(\mathbf{X}^{\mathbf{VBR}}\right)_{ij} = \int_a^b \phi_i(x) x \phi_j(x) dx \approx \sum_{k=0}^{N-1} \frac{A_k}{\omega(x_k)} \phi_i(x_k) x_k \phi_j(x_k) = \mathbf{T}_{ik} x_k \mathbf{T}^T_{kj} \qquad (2.60)$$

As long the $\left(\mathbf{X}^{\mathbf{VBR}}\right)_{ij}$ matrix is truncated to size $N \times N$ and the basis functions are orthogonal polynomials of degree $N-1$, the integrand is of degree $2N-1$, and can be evaluated exactly by a Gaussian quadrature. It means that $\mathbf{T}$ matrix diagonalizes position operator matrix in the orthogonal polynomials basis. As a result, eigenvalues of X in this basis correspond to quadrature points and the diagonalising transformation matrix is related to the quadrature weights. Diagonalisation of $\mathbf{X}^{\mathbf{VBR}}$ unambiguously defines the DVR.

$$\mathbf{X}^{\mathbf{DVR}} = \mathbf{T}^{\mathbf{T}}\mathbf{X}^{\mathbf{VBR}}\mathbf{T} \tag{2.61}$$

The VBR representation of the position matrix in the orthogonal polynomials basis is straightforward to derive, on account of three-term recurrence relations for orthogonal polynomials and the position operator matrix is tridiagonal. In practice, diagonalising this matrix is the most efficient way of finding a DVR.

At this stage a few obvious questions arise: how does the Gaussian quadrature (FBR) approximation refer to the present position operator derived basis? Are these approaches equivalent? Is there any advantage of using one over another?

Following Harris *et al.* [88] $\mathbf{V}^{\mathbf{VBR}}$ can be approximated with:

$$\mathbf{V}^{\mathbf{VBR}} \approx \mathbf{V}\left(\mathbf{X}^{\mathbf{VBR}}\right) \tag{2.62}$$

It is postulated that such approximation is equivalent to the FBR approximation:

$$\mathbf{V}\left(\mathbf{X}^{\mathbf{VBR}}\right) = \mathbf{V}^{\mathbf{FBR}} \tag{2.63}$$

In other words, we replace the matrix element of a function of the position operator with the same function of the matrix element of the position operator:

$$\langle \psi_i(x)|V(x)|\psi_j(x)\rangle \approx V\left(\langle \psi_i(x)|X|\psi_j(x)\rangle\right) \tag{2.64}$$

If we assume that the potential energy function is expandable in a power series, then

within a given radius of convergence we may write:

$$V(x) = \sum_{n=0}^{+\infty} c_n x^n \tag{2.65}$$

and in the postulated FBR approximation matrix elements of potential energy read:

$$V(\mathbf{X}^{\mathbf{VBR}}) = \sum_{n=0}^{+\infty} c_n \left(\mathbf{X}^{\mathbf{VBR}}\right)^n \tag{2.66}$$

On account of relation 2.61 the VBR monomials in the position operator take the form:

$$\left(\mathbf{X}^{\mathbf{VBR}}\right)^n = \left(\mathbf{T}\mathbf{X}^{\mathbf{VBR}}\mathbf{T}^{\mathbf{T}}\right)^n = \mathbf{T}\left(\mathbf{X}^{\mathbf{DVR}}\right)^n \mathbf{T}^{\mathbf{T}} \tag{2.67}$$

where orthogonality of $\mathbf{T}$ matrix was used. As long as $\mathbf{X}^{\mathbf{DVR}}$ is diagonal, so is its $n-$th power. Finally,

$$\mathbf{V}\left(\mathbf{X}^{\mathbf{VBR}}\right) = \mathbf{T}\left(\sum_{n=0}^{+\infty} c_n \left(\mathbf{X}^{\mathbf{VBR}}\right)^n\right)\mathbf{T}^{\mathbf{T}} \tag{2.68}$$

proves the equivalence of the product approximation with the Gaussian quadrature approach. The inherent error of DVR(FBR) approximation lies within the approximation from eq. 2.64. To show it more explicitly, let us point that matrix elements of the potential energy function are built from terms containing powers of the position operator. As the Hilbert space is complete (as well as our orthogonal polynomial basis set) it is possible to decompose the matrix elements of n-th power of the position operator into a sum of products of n matrices:

$$\begin{aligned} &\langle \psi_i(x)|x^n|\psi_j(x)\rangle = \sum_{k=0}^{+\infty} \langle \psi_i(x)|x^{n-1}|\alpha_k(x)\rangle\langle \alpha_k(x)|x|\psi_j(x)\rangle = \ldots \\ &\sum_{k_1=0}^{+\infty} \ldots \sum_{k_n=0}^{+\infty} \langle \psi_i(x)|x|\alpha_{k_n}(x)\rangle \ldots \langle \alpha_{k_s}(x)|x|\alpha_{k_s}(x)\rangle \ldots \langle \alpha_{k_1}(x)|x|\psi_j(x)\rangle \end{aligned} \tag{2.69}$$

Now by truncating the resolutions of identity inserted in between the position operators we formally conduct an approximation equivalent to the Gaussian quadrature approximation. Infinite matrices in eq. 2.69 are replaced with truncated matrices,

and the product approximation is retrieved:

$$\begin{aligned} \sum_{k_s=0}^{+\infty} |\alpha_{k_s}(x)\rangle\langle\alpha_{k_s}(x)| &\approx \sum_{k_s=0}^{n} |\alpha_{k_s}(x)\rangle\langle\alpha_{k_s}(x)| \\ \langle\psi_i(x)|x^n|\psi_j(x)\rangle &\approx \prod_{l=1}^{n} \mathbf{X}^{\mathbf{VBR}} = \left(\mathbf{X}^{\mathbf{VBR}}\right)^n \end{aligned} \tag{2.70}$$

Note a close relation to eq. (2.57), where the infinite dimensional scalar product (integral) is being replaced by a finite dimensional one.

To conclude, diagonalization of the position operator matrix is equivalent to applying a Gaussian quadrature to VBR integrals. In other words Gaussian quadratures and the product approach are operating at exactly the same level of approximation and can be used interchangeably.

2.5 The Hamiltonian operator

In an ideal case, the ro-vibrational Hamiltonian can be represented in the VBR, with its matrix elements evaluated exactly. In computational practice, the error in variational calculations is due to truncation of the matrix and approximate calculation of the matrix elements.

Diagonalisation of the VBR Hamiltonian gives energy levels and wavefunctions in the form of expansion coefficients

$$\mathbf{H}^{\mathbf{VBR}}_{\mathbf{diag}} = \beta^{\mathbf{T}} \mathbf{H}^{\mathbf{VBR}} \beta \tag{2.71}$$

where the transformation matrix β diagonalizes $\mathbf{H}^{VBR}$. The kinetic energy operator for a triatomic molecule, as discussed in section 2.1, contains first and second derivatives with respect to internal coordinates, as well as functions of these coordinates. In this case, matrix elements of the KEO can be calculated analytically in the VBR, which is discussed in detail by Szalay [101]. Then why not to use the VBR for solving the whole nuclear motion problem? First of all, a very efficient basis set contraction is possible with combination of DVR and a two-step variational procedure discussed in subsection 2.4. Secondly, in the VBR one is required to calculate

$(N+1)N/2$ matrix elements of the potential energy function, which is sometimes a formidable task. In the DVR on the other hand, one needs to calculate the values of the potential function at many different grid points.

With the above motivation, the VBR Hamiltonian is transformed into a DVR, which can be formally written as

$$\mathbf{H}^{\mathbf{DVR}} = \mathbf{T}^{\mathbf{T}}\mathbf{K}^{\mathbf{VBR}}\mathbf{T} + \mathbf{V}^{\mathbf{DVR}} \tag{2.72}$$

where $\mathbf{V}^{\mathbf{DVR}} = diag(V(x_0), ..., V(x_{N-1}))$. Thus, whenever the matrix elements of the KEO can be computed analytically in the VBR, the only action needed is transformation of this matrix into the DVR representation. Finally the DVR Hamiltonian needs to be diagonalised. The procedure for multi-step construction of solutions to the stationary SE and sequential diagonalisation in DVR3D is described in the next two sections. We conclude this section with a sum-up equation relating the VBR, FBR and DVR Hamiltonian:

$$\mathbf{H}^{\mathbf{VBR}} \approx \mathbf{H}^{\mathbf{FBR}} = \mathbf{T}^{\mathbf{T}}\mathbf{H}^{\mathbf{DVR}}\mathbf{T} \tag{2.73}$$

2.5.1 The DVR Hamiltonian

Purely vibrational energy levels ($J = 0$). In this section, we derive formally the matrix elements of the effective vibrational Hamiltonian given in eq. 2.14, which is used in the DVR3DRJZ program. First, we start with the $J = 0$ Hamiltonian in the VBR. After that we are going to consider Coriolis-decoupled Hamiltonians for $J > 0$ also in VBR. Next, an appropriate FBR-DVR transformation will be exploited to arrive in a pointwise representation for the Hamiltonian. With a DVR Hamiltonian a three-step diagonalisation-truncation solution strategy is presented. The resulting wavefunctions serve as a basis for the full Coriolis-coupled problem discussed in section 2.5.2.

Matrix elements of $J = 0$ effective radial Hamiltonian are given by

$$\langle m', n', j' | \hat{H}^{J=0}(r_1, r_2, \theta) | m, n, j \rangle \tag{2.74}$$

The form of the effective vibrational Hamiltonian in eq. 2.14 indicates five types of VBR matrix elements [59]

$$\begin{aligned}
h^{(1)}_{m'mn'nj'j} &= \langle m'| -\frac{1}{2\mu_1}\frac{\partial^2}{\partial r_1^2}|m\rangle \delta_{j'j}\delta_{n'n} \\
h^{(2)}_{m'mn'nj'j} &= \langle n'| -\frac{1}{2\mu_2}\frac{\partial^2}{\partial r_2^2}|n\rangle \delta_{j'j}\delta_{m'm} \\
g^{(1)}_{m'mn'nj'j} &= \langle m'|\frac{1}{2\mu_1 r_1^2}|m\rangle j(j+1)\delta_{j'j}\delta_{n'n} \\
g^{(2)}_{m'mn'nj'j} &= \langle n'|\frac{1}{2\mu_2 r_2^2}|n\rangle j(j+1)\delta_{j'j}\delta_{m'm} \\
V_{m'mn'nj'j} &= \langle m',n',j'|V(r_1,r_2,\theta)|m,n,j\rangle
\end{aligned} \tag{2.75}$$

in terms of which the Hamiltonian in eq. 2.74 reads:

$$\begin{aligned}
\langle m',n',j'|\hat{H}^{J=0}(r_1,r_2,\theta)|m,n,j\rangle = h^{(1)}_{m'mn'nj'j} + h^{(2)}_{m'mn'nj'j} + g^{(1)}_{m'mn'nj'j} + \\
+ g^{(2)}_{m'mn'nj'j} + V_{m'mn'nj'j}
\end{aligned} \tag{2.76}$$

Rotational excitation (J>0) in DVR. For $J > 0$, in the first step of the two-step Sutcliffe-Tennyson procedure K is treated as a good quantum number. For this reason all off-diagonal matrix elements in K', K are neglected, which leaves the purely vibrational Hamiltonian from eq.2.76 plus terms diagonal in K from the K_{VR} operator given in eq. 2.21 and 2.22. Thus for $J > 0$ the Coriolis-decoupled Hamiltonian in the VBR is given as

$$\begin{aligned}
\langle m',n',j'|\delta_{k'k}\hat{H}^J_{k'k}(r_1,r_2,\theta)|m,n,j\rangle = \langle m',n',j'|\hat{H}^{J=0}(r_1,r_2,\theta)|m,n,j\rangle + \\
+ g^{(s)}_{m'mn'nj'j}\left(J(J+1) - 2k^2\right)
\end{aligned} \tag{2.77}$$

for bond embedding ($s = 1$ for the bond embedding along r_1), and

$$\langle m',n',j'|\delta_{k'k}\hat{H}^J_{k'k}(r_1,r_2,\theta)|m,n,j\rangle = \langle m',n',j'|\hat{H}^{J=0}(r_1,r_2,\theta)|m,n,j\rangle + \\ +\langle m',n'|K^{(1)}_{VR}(r_1,r_2)|m,n\rangle \tag{2.78}$$

for the bisector embedding. These Hamiltonians need to be transformed into the DVR. Note that here the molecule-fixed z-axis is a quantization axis, thus for a given J, a set of Hamiltonians for $K = p, p+1, ..., J$ is considered.

The 3D VBR (FBR) to DVR transformation of the Hamiltonian, formally written in eq. 2.73, can be expressed as a product of 1D transformation matrices:

$$\mathbf{T} = \mathbf{T}^{(r_1)}\mathbf{T}^{(r_2)}\mathbf{T}^{(\theta)}; \tag{2.79}$$

each 1D transformation refers to a single vibrational coordinate. In DVR3D [59], Gauss-Laguerre quadrature scheme is used for DVR in radial coordinates r_1, r_2 and Gauss-Legendre quadrature scheme for the bending coordinate θ:

$$\begin{aligned} T^{(r_1)}_{m\gamma} &= N^{(1)}_m \left(\omega^{(1)}_m\right)^{\frac{1}{2}} H_m(r_{1\gamma}) \\ T^{(r_2)}_{n\beta} &= N^{(2)}_n \left(\omega^{(2)}_n\right)^{\frac{1}{2}} \tilde{H}_n(r_{2\beta}) \\ T^{(\theta)}_{jk\alpha} &= N^{(\theta)}_m \left(\omega^{(\theta)}_{jk}\right)^{\frac{1}{2}} P^{(k)}_j(\theta_\alpha) \end{aligned} \tag{2.80}$$

where $H_m(r_{1\gamma})$ are Hermite polynomials of degree m and $P^{(k)}_j(\theta_\alpha)$ are associated Legendre polynomials. $N^{(1)}_m, N^{(2)}_n, N^{(\theta)}_m$ are normalisation factors for respective transformations. With these transformation matrices, the DVR Hamiltonian can be written as:

$$H_{\alpha'\alpha\beta'\beta\gamma'\gamma} = K^{(1)}_{\gamma'\gamma}\delta_{\alpha'\alpha}\delta_{\beta'\beta} + K^{(2)}_{\beta'\beta}\delta_{\alpha'\alpha}\delta_{\gamma'\gamma} + L^{(1)}_{\alpha'\alpha}\delta_{\gamma'\gamma}\delta_{\beta'\beta} + L^{(2)}_{\alpha'\alpha}\delta_{\gamma'\gamma}\delta_{\beta'\beta} + \\ +\delta_{k'k}K_{VR\gamma'\gamma\beta'\beta\alpha'\alpha} + V(r_{1\gamma}, r_{2\beta}, \theta_\alpha)\delta_{\gamma'\gamma}\delta_{\beta'\beta}\delta_{\alpha'\alpha} \tag{2.81}$$

where $K^{(1)}_{\gamma'\gamma}$, $K^{(2)}_{\beta'\beta}$, $L^{(1)}_{\alpha'\alpha}$, $L^{(2)}_{\alpha'\alpha}$ are matrix elements of respective parts of the VBR Hamiltonian given in eq. 2.76 transformed into DVR by means of transformation in eq. 2.79. For bond embedding $K_{VR\gamma'\gamma\beta'\beta\alpha'\alpha}$ then reads:

$$K_{VR\gamma'\gamma\beta'\beta\alpha'\alpha} = L^{(1)}_{\alpha'\alpha}\delta_{\gamma'\gamma}\delta_{\beta'\beta}\left(J(J+1)-2k^2\right) \tag{2.82}$$

and for the bisector $K_{VR\gamma'\gamma\beta'\beta\alpha'\alpha}$ it is

$$K_{VR\gamma'\gamma\beta'\beta\alpha'\alpha} = \delta_{\gamma'\gamma}\frac{1}{8}\left(M^{(1)}_{\gamma'\gamma}+M^{(2)}_{\beta'\beta}\right)\left(\frac{1}{8}\left(J(J+1)-k^2\right)+\delta_{k1}\right), \tag{2.83}$$

with $M^{(1)}_{\gamma'\gamma} = \delta_{\gamma'\gamma}\frac{1}{2\mu_1 r^2_{1\gamma}}$ and $M^{(2)}_{\beta'\beta} = \delta_{\beta'\beta}\frac{1}{2\mu_2 r^2_{2\beta}}$.

Solution strategy. Having the DVR matrix elements of the ro-vibrational Hamiltonian in hand, a diagonalisation scheme can be applied. For the largest saving in the computer time, and for keeping as much information as possible in the form of a contracted wavefunction, a three-step diagonalisation-truncation procedure has been used by Tennyson *et al.* [59, 102]. From the DVR point of view there are three independent variables: $r_{1\gamma}, r_{2\beta}, \theta_\alpha$. The order, in which solution to the SE is constructed is important from the computational point of view. In general, the last coordinate in the order, should be associated with the highest density of states [103]. For this reason, it has been decided that $r_{2\beta} \to r_{1\gamma} \to \theta_\alpha$ ordering (θ comes last) is the most appropriate.

In the first step, for each α and γ, 1D Hamiltonian matrices $\mathbf{H}^{1D}$ are constructed and indexed by $\beta'\beta$:

$$\left(H^{1D}\right)^{(\gamma,\alpha)}_{\beta'\beta} = K^{(2)}_{\beta'\beta} + V(r_{1\gamma}, r_{2\beta}, \theta_\alpha)\delta_{\beta'\beta} \tag{2.84}$$

where we used a general form of the DVR Coriolis-decoupled Hamiltonian from eq. 2.81. Diagonalisation of $\left(H^{1D}\right)^{(\gamma,\alpha)}_{\beta'\beta}$ gives eigenvalues $\left(E^{1D}\right)^{(\gamma,\alpha)}_{h}$ and eigenvectors $\left(C^{1D}\right)^{(\gamma,\alpha)}_{h\beta}$. Then a user-controlled-truncated (parameter E^{1D}_{MAX}) 1D eigenbasis is used in solution to the 2D problem, defined by the Hamiltonian:

$$\left(H^{2D}\right)^{(\alpha)}_{\beta'\beta\gamma'\gamma} = \left(H^{1D}\right)^{(\gamma,\alpha)}_{\beta'\beta} + K^{(1)}_{\gamma'\gamma}\delta_{\beta'\beta} \tag{2.85}$$

which is indexed by $\beta'\beta$ and $\gamma'\gamma$ and needs to be calculated for all α values. In the eigenbasis of the 1D problem the 2D Hamiltonian can be rewritten as:

$$\left(H^{2D}\right)^{(\alpha)}_{h'h\gamma'\gamma} = \left(E^{1D}\right)^{(\gamma,\alpha)}_{h}\delta_{h'h}\delta_{\gamma'\gamma} + K^{(1)}_{\gamma'\gamma}\sum_{\beta}\left(C^{1D}\right)^{\gamma\alpha,h}_{\beta}\left(C^{1D}\right)^{\gamma'\alpha,h'}_{\beta} \tag{2.86}$$

For Y–X–Y systems, for which r_1 - r_2 symmetrization is possible, the computer time can be further reduced [59, 102, 104] by constructing and diagonalising the 2D Hamiltonian matrices in one step. The memory and time requirements needed to diagonalise all 2D matrices is usually negligible in comparison with the full 3D problem [102]. After diagonalisation of these 2D Hamiltonian matrices, only solutions $\left(C^{2D}\right)^{\alpha l}_{\gamma h}$ with energies $\left(E^{2D}\right)^{\alpha}_{l}$ lower than E^{2D}_{MAX} are chosen for the final step, with the 3D Hamiltonian:

$$\begin{aligned}\left(H^{3D}\right)^{(\alpha)}_{l'l\gamma'\gamma} &= \left(E^{2D}\right)^{(\alpha)}_{l}\delta_{l'l}\delta_{\alpha'\alpha} + \\ &+\sum_{\gamma\beta}\left(L^{(1)}_{\alpha'\alpha} + L^{(2)}_{\alpha'\alpha}\right)\sum_{s}\left(C^{2D}\right)^{\alpha l}_{\gamma s}\left(C^{1D}\right)^{\gamma\alpha s}_{\beta}\sum_{s'}\left(C^{2D}\right)^{\alpha' l'}_{\gamma s}\left(C^{1D}\right)^{\gamma\alpha' s}_{\beta}\end{aligned} \tag{2.87}$$

The $MAX3D$ and $MAX2D$ parameters in the DVR program additionally control the size of the 2D and 3D Hamiltonians, respectively. Diagonalisation of the Hamiltonian in eq. 2.87 yields final energy levels E_h and wavefunction coefficients $\left(C^{3D}\right)_{\beta hl}$. At the end of the day, the DVR output wavefunction is defined on a 3D grid and labelled by J, k and h quantum numbers:

$$|J,h,k\rangle = \psi^{Jkh}_{\gamma\beta\alpha} = \sum_{l}\left(C^{3D}\right)_{\beta hl}\sum_{s}\left(C^{2D}\right)^{\alpha l}_{\gamma s}\left(C^{1D}\right)^{\gamma\alpha s}_{\beta} \tag{2.88}$$

Note that in DVR the K-dependence of solutions is encoded in both the Hamiltonian and the bending basis set. Note that any symmetries are here neglected for simplicity. Extension to the p-symmetry labelled problem is straightforward. Fi-

nally, the DVR wavefunctions and energy levels are passed to the second step of the full solution procedure, where Coriolis-couplings are taken into account.

2.5.2 The Coriolis-coupled Hamiltonians: Rotlev3 and Rotlev3b

Rotlev3. In the bond embedding the Rotlev3 program is used for solving the Coriolis-coupled nuclear motion problem. The Hamiltonian for this system in the representation of eigenfunctions from the first step can be written as [59]:

$$\begin{aligned}\langle h',k',p'|\hat{H}^J_{k'k}|h,k,p\rangle = E^{J,k}_h \delta_{h'h}\delta_{k'k} + \\ -(1+\delta_{k0}+\delta_{k'0})^{-\frac{1}{2}}\,\delta_{k',k\pm1}\sum_{\gamma,\beta,j}\psi^{Jk'h'}_{\gamma\beta j}\psi^{Jkh}_{\gamma\beta j}C^{\pm}_{J,k'}C^{\pm}_{j,k'}M^{(i)}_{\alpha\alpha\beta\beta}\end{aligned} \tag{2.89}$$

where a symmetry adapted form of the wavefunction from DVR is used, and the DVR wavefunction has been transformed into FBR ($\psi^{Jkh}_{\gamma\beta j} = \sum_\alpha T^\alpha_j \psi^{Jkh}_{\gamma\beta\alpha}$) where the angular contribution to the full Hamiltonian is diagonal. Here $k = p, p+1, ..., J, \quad p = 0, 1$. Similarly as in DVR, in Rotlev3 user is given control over the size of the variational basis set (parameter IBASS). The $p = 1$ matrix is simply a submatrix of the $p = 0$ matrix. For this reason only the $p = 0$ matrix needs to be constructed.

Rotlev3b. In the bisector embedding the Rotlev3b program is used to solve the Coriolis-coupled nuclear motion problem. Eigenbasis from the first step is used in DVR in all three coordinates. With the vibrational and the parity symmetries used, the full Hamiltonian reads:

$$\begin{aligned}\langle h',k',p',q'|\hat{H}^J_{k'k}|h,k,p,q\rangle = E^{J,k}_h \delta_{h'h}\delta_{k'k} + \\ -(1+\delta_{k0}+\delta_{k'0})^{-\frac{1}{2}}\,\delta_{k',k\pm1}C^{\pm}_{J,k'}\sum_{\gamma,\beta,j}\psi^{Jkh}_{\gamma\beta\alpha}\psi^{Jkh}_{\gamma\beta\alpha'}\left(M^{(1)}_{\alpha\alpha\beta\beta} - M^{(2)}_{\alpha\alpha\beta\beta}\right)J(1)_{k\pm1,k,\alpha',\alpha} \\ -(1+\delta_{k0}+\delta_{k'0})^{-\frac{1}{2}}\,\delta_{k',k\pm2}C^{\pm}_{J,k'\pm1}C^{\pm}_{J,k'}\sum_{\gamma,\beta,j}\psi^{Jk'h'}_{\gamma\beta\alpha}\psi^{Jkh}_{\gamma\beta\alpha'}\left(M^{(1)}_{\alpha\alpha\beta\beta} + M^{(2)}_{\alpha\alpha\beta\beta}\right)J(2)_{k\pm2,k,\alpha',\alpha}\end{aligned} \tag{2.90}$$

where,

$$
\begin{aligned}
J^{(1)}_{k',k,\alpha',\alpha} &= \sum_{j'j} T^{\alpha'(k')}_{j'} \left(\delta_{j'j} + \left(\frac{k'+k}{2} \right) I^{(2)}_{j'k'jk} \right) T^{\alpha(k)}_{j} \\
J^{(2)}_{k',k,\alpha',\alpha} &= \sum_{j'j} T^{\alpha'(k')}_{j'} \left(\delta_{j'j} + \left(\frac{k'+k}{2} \right) \langle j'k' | \frac{1+\cos\theta}{1-\cos\theta} | jk \rangle \right) T^{\alpha(k)}_{j}
\end{aligned}
\tag{2.91}
$$

Direct diagonalisation of this Hamiltonian generates final wavefunctions and energy levels. Next, the final wavefunctions are transformed to FBR in the angular coordinate and can be further passed to a program for transition intensity calculations:

$$
|J,h,p,q\rangle = \psi^{Jhpq}_{\gamma\beta j} \tag{2.92}
$$

2.6 Line intensities

In this section we derive and inspect a general expression for the transition line strength in terms of wavefunctions provided by the Rotlev programs. In the derivation, transitions between different Born-Oppenheimer electronic states will be considered, for the sake of generality and for future use in Chapter 4. Thus, in this section we will be discussing rotational-vibrational-electronic or ro-vibronic transitions. The effective formula for the line strength in the Franck-Condon approximation is also discussed below. The final expressions for the transition line strength given below are used in the DIPOLE program, which is a part of the DVR3D suite for calculating transition intensities. Following the theory developed in this section, for the purposes of this work, the original version of the DIPOLE program [59] has been adopted to include transitions between different electronic states within the Born-Oppenheimer approximation.

First, we shall make an excursion to discuss the general form of the total internal wavefunction for a triatomic molecule. The total internal wavefunction of the molecule must contain information about the electronic, nuclear and all spin degrees of freedom. For the majority infrared spectroscopic purposes it is sufficient to assume independence of the spin degrees of freedom from the dynamical degrees of freedom. As a consequence, the total internal wavefunction for the molecule is

separable into the nuclear spin part, the electronic part (Born-Oppenheimer approximation) and the ro-vibrational part, as written below:

$$|\Phi_{int}\rangle = |\Phi_{nspin}\rangle|\Phi_{elec,(i)}\rangle|J,h,p,q\rangle \tag{2.93}$$

where $\Phi_{elec,(i)}$ is the wavefunction for the i-th electronic state and can be obtained from quantum chemistry calculations, Φ_{nspin} is easily construed in a finite-dimensional Hilbert space with a chosen standard spin basis. The ro-vibrational part of the wavefunction is provided in our case by the Rotlev routines. From now on, we are going to focus on the ro-vibronic part of the total internal wavefunction : $|\Phi_{elec,(i')}\rangle|J',h',p',q'\rangle \equiv |J',h',i',p',q',\vec{D}'\rangle$, where the additional label $\vec{D}'$ has been given to denote all quantum numbers which not affect the energy of the state (degeneracy labels).

The quantum probability for the $|i\rangle \equiv |J'',h'',i'',p'',q'',\vec{D}''\rangle \rightarrow |f\rangle \equiv |J',h',i',p',q',\vec{D}'\rangle$ ro-vibronic transition is given in the dipole approximation by the square modulus of the electric transition dipole moment vector $\sum_{A=X,Y,Z}\left|T_{if}^{A,\vec{D}'',\vec{D}'}\right|^2$ [60], where the summation is carried out over three Cartesian components of the electric dipole moment of the molecule in the laboratory frame $A = X,Y,Z$. Individual transition probabilities are then summed over all degenerate states, labelled by vector $\vec{D}$:

$$S_{if} = \sum_{A=X,Y,Z}\sum_{\vec{D}'',\vec{D}'}\left|T_{if}^{A,\vec{D}'',\vec{D}'}\right|^2 \tag{2.94}$$

giving a quantity called the *line strength*, which can be directly related to experimentally measured integral line intensity [60]:

$$I(\tilde{\nu}_{if}) = \frac{8\pi^2 N_A}{12\varepsilon_0 hc}\,\frac{\tilde{\nu}_{if}}{Q(T)}\,g_{ns}\exp\left(\frac{-E_i}{k_b T}\right)\left[1-\exp\left(-\frac{\tilde{\nu}_{if}}{k_b T}\right)\right]S_{if} \tag{2.95}$$

where $\tilde{\nu}_{if}$ is the transition wavenumber between the i'th and f'th ro-vibronic state and $Q(T)$ is the partition function at temperature T. N_A is the Avogadro number, k_b is the Boltzmann constant, h is the Planck constant, c is the speed of light in vacuum

and ε_0 is the permittivity of vacuum. g_{ns} is the spin statistical weight for the initial state *i* resulting from summation over degenerate nuclear spin functions. The values of spin statistical weights depend on the ro-vibronic symmetry of the state. Thus, the measured transition line strength is directly related to the total internal state of the molecule, including nuclear spin states. Units for integral line intensity are cm/molecule.

The electric transition dipole moment is defined as

$$T_{if}^{A,\vec{D}'',\vec{D}'} = \langle J'', h'', i'', p'', q'', \vec{D}'' \left| \hat{\mu}_{el}^{A,space} \right| J', h', i', p', q', \vec{D}' \rangle \tag{2.96}$$

and its value is identical for all components of $\vec{D}$ except the projection M of the total angular momentum on the space-fixed Z-axis. The space-fixed transition dipole moment can be transformed into a *spherical tensor form* [105], which transforms irreducibly in the 3D rotations group:

$$\vec{\mu}_{el,sph}^{space} = \mathbf{K}\vec{\mu}_{el}^{space} \tag{2.97}$$

where,

$$\mathbf{K} = \begin{pmatrix} -\frac{1}{\sqrt{2}} & \frac{i}{\sqrt{2}} & 0 \\ \frac{1}{\sqrt{2}} & \frac{i}{\sqrt{2}} & 0 \\ 0 & 0 & 1 \end{pmatrix} \tag{2.98}$$

is a unitary ($|\det(\mathbf{K})| = 1$, $\mathbf{K}^{\dagger}\mathbf{K} = \mathbf{1}$) transformation matrix between the Cartesian operator and *rank 1 spherical tensor operator* [105]. The electric dipole moment for a neutral molecule is invariant under translations in free space, so the 'LAB' components (X, Y, Z) of the transition dipole moments can be rewritten in terms of Cartesian components in the space-fixed coordinate system (ξ, η, ζ) with the origin at the nuclear center of mass [60]. In what follows, the transition dipole moment can be expressed as

$$T_{if}^{A} = \sum_{A=\xi,\eta,\zeta} \sum_{\sigma=-1}^{1} \mathbf{K}_{A\sigma}^{\dagger} \sum_{\vec{D},\vec{D}'} \tilde{T}_{if}^{\sigma,M,M'} \tag{2.99}$$

As a result of new transformation properties of the transition dipole vector, a straightforward transformation to the molecule-fixed coordinate system can be achieved with Wigner D-matrices:

$$\vec{\mu}_{\sigma}^{space} = \sum_{\sigma'=-1}^{1} \mathbf{D}^{(1)}_{\sigma\sigma'}(\alpha,\beta,\gamma)\vec{\mu}_{\sigma'}^{mol} \tag{2.100}$$

where α,β,γ denote Euler angles and subscripts 'el' and 'sph' have been dropped for clarity of presentation. After rather lengthy algebra with extensive use of properties of 3-j symbols, the line strength takes the form [106–108]:

$$S_{if} = \frac{1}{4}\left(2S''+1\right)\left(2S'+1\right)\left(2J''+1\right)\left(2J'+1\right)\left[(-1)^{J''+J'+1}+(-1)^{p''+p'}\right]^2$$
$$\times\left|\sum_{\sigma=-1}^{+1}\sum_{\substack{K'=p'\\K''=p''}}^{J',J''}(-1)^{K''}b^{\sigma}_{q'q''}\begin{pmatrix}1 & J' & J''\\ \sigma & K' & K''\end{pmatrix}\sum_{\substack{m',n',j'\\m'',n'',j''}} C^{J',i',h',p',q'}_{m'n'j'K'}C^{J'',i'',h'',p'',q''}_{m''n''j''K''}M^{\sigma,i'',i'}_{m'm''n'n''j'j''K'K''}\right|^2 \tag{2.101}$$

The $(2S'+1)(2S''+1)$ prefactor in eq. (2.101) comes from summation over all combinations of degenerate electron spin functions, as the electronic spin is preserved in a transition within the present model, $S''=S'$. Similarly, the $(2J'+1)(2J''+1)$ prefactor comes from summation over all combinations of degenerate rotational basis functions, characterized by the M quantum number. $b_{q'q''}$ is a symmetry dependent numerical factor defined in ref. [59]. The coefficients $C^{J',i',h',p',q'}_{m'n'j'K'}$ denote variational coefficients for the ro-vibrational wavefunction in a given electronic state (i'). $M^{\sigma,i'',i'}_{m'm''n'n''j'j''K'K''}$ is the matrix element of the electric dipole moment operator in the primitive vibrational basis defined in section 2.3,

$$M^{\sigma,i'',i'}_{m'm''n'n''j'j''K'K''} = \langle j''K''|\langle m''|\langle n''|\mu_{\sigma}^{i'',i'}(r_1,r_2,\theta)|n'\rangle|m'\rangle|j'K'\rangle, \tag{2.102}$$

where

$$\mu_{\sigma}^{i''i'}(r_1,r_2,\theta) = \langle\Phi_{elec,(i'')}\left|\hat{\mu}_{\sigma}^{mol}\right|\Phi_{elec,(i')}\rangle \tag{2.103}$$

is the σ-th spherical tensor component of the molecule-fixed electronic transition dipole moment surface between electronic states i'' and i'. In eq. (2.103) integration is carried over electronic coordinates only, leaving dependence on three internal (Radau) coordinates r_1, r_2, θ. This function is called the *electronic transition dipole moment surface* (TDMS) and can be obtained, for example, by fitting a predefined functional form to points calculated from a quantum chemistry package. For many molecules, the dependence of TDMS on internal coordinates is weak, and it is often replaced by a constant value of the transition dipole at equilibrium geometry $\mu_\sigma^{eq} \equiv \mu_\sigma^{ge}\left(r_1^{eq}, r_2^{eq}, \theta^{eq}\right)$. In such case we talk about the *Condon approximation* [60] to the electronic transition dipole moment:

$$M^{\sigma,i'',i'}_{m'm''n'n''j'j''K'K''} = \mu_\sigma^{i'',i'}\left(r_1^{eq}, r_2^{eq}, \theta^{eq}\right)\langle m''|m'\rangle\langle n''|n'\rangle\langle j''K''|j'K'\rangle \tag{2.104}$$

due to the choice of the identical orthonormal basis in the ground and the excited electronic state, the integrals in eq. (2.104) become Kronocker's deltas:

$$M^{\sigma,i'',i'}_{m'm''n'n''j'j''K'K''} = \mu_\sigma^{i''i'}\left(r_1^{eq}, r_2^{eq}, \theta^{eq}\right)\delta_{m''m'}\delta_{n''n'}\delta_{j''j'} \tag{2.105}$$

which significantly reduces the number of summed terms in the expression for the line strength, so that only the elements with the same indices in the coefficients vectors $C^{J'',M'',i'',h'',p'',q''}_{m'n'j'K'}$ are needed. This simplification compensates the extra computational time needed for wavefunction calculations when using identical grid for all electronic states. Note that identical basis sets are assumed for all electronic states.

$$S_{if} = \frac{1}{4}\left(2S''+1\right)^2\left(2J''+1\right)\left(2J'+1\right)\left[(-1)^{J''+J'+1}+(-1)^{p''+p'}\right]^2$$
$$\times\left|\sum_{\sigma=-1}^{+1}\mu_\sigma^{eq}\sum_{\substack{K'=p'\\K''=p''}}^{J',J''}(-1)^{K''}b^{\sigma}_{q'q''}\begin{pmatrix}1 & J' & J''\\ \sigma & k' & k''\end{pmatrix}\sum_{m'',n'',j''}C^{J',i',h',p',q'}_{m'n'j'K'}C^{J'',i'',h'',p'',q''}_{m''n''j''K''}\right|^2 \tag{2.106}$$

Expression given in eq. 2.106 comprises rotational and vibrational degrees of freedom. Traditional vibrational Franck-Condon approximation operates only on vibrational wavefunctions, with the Franck-Condon factors defined as the square modulus of the overlap integral between two vibrational wavefunctions [109] $F_{ij} = \left|\langle\phi^i_{vib}|\phi^j_{vib}\rangle\right|^2$. Then the vibrational band strength is proportional to the vibrational Franck-Condon factor. Here this definition is generalized onto ro-vibrational transitions.

The 3-j symbol [105] appearing in eq. (trans:strength) and (2.106) and the $\left[(-1)^{J''+J'+1}+(-1)^{p''+p'}\right]^2$ factor are responsible for selection rules. From the former, it follows that in order for the line strength not to vanish the following conditions must be satisfied: $|J''-J'|=0,1$, $J''+J'\geq 1$ and $\Delta K=0,\pm 1$. Selection rules for J quantum number define P,Q,R branches for $\Delta J=J''-J'=+1,0,-1$, respectively. Selection rules for the $K=|k|$ quantum number allow transitions of type $k\rightarrow -k$, which reflects the time-reversal symmetry of the system. For $\Delta K=0$ only the z-component of the molecule-fixed electronic transition dipole moment contributes to the overall line intensity, and because z-axis is chosen here as the axis of quantization, we call these transitions *parallel*. Accordingly $\Delta K=\pm 1$ corresponds to *perpendicular* transitions, as both x components of the electronic transition dipole moment contribute to the total intensity. For the Q branch ($\Delta J=0$) only transitions which change the p quantum number are allowed, i.e. $e\leftrightarrow f, e\nleftrightarrow e, f\nleftrightarrow f$. Conversely, P and R branches allow transitions conserving p, i.e. $e\nleftrightarrow f, e\leftrightarrow e, f\leftrightarrow f$. Neglecting the dependence of the TDMS on nuclear coordinates does not affect the rotational selection rules, but it can however make the vibrational selection rules stronger for example by forbidding vibrational overtone transitions.

The DIPOLE3 code, which we use for calculation of intensities in the present work, uses a mixed DVR-FBR representation for ro-vibrational wavefunctions, as given by eq. 2.92. Radial integrals in the ro-vibronic transition dipole moment in eq. 2.102 are carried out in the DVR representation, but the integral over the bending coordinate, which is formally in FBR, is evaluated using a Gauss-Legendre quadrature scheme with $k=0$. This means, that the final expression for the tran-

sition line strength contains coefficients defined over a 3D DVR grid, however, the angular grid is different than the original grid used in DVR program, due to back transformation to FBR (in Rotlev) and re-transformation to DVR in DIPOLE:

$$C^{J'',i'',h'',p'',q''}_{m''n''j''k''} = \sum_{\alpha,\beta,\gamma} (T)^{k''=0}_{j\gamma} (T)_{m\alpha} (T)_{n\beta} C^{J'',i'',h'',p'',q''}_{\alpha\beta\gamma k''} \tag{2.107}$$

where the unitary transformation matrix for the bending coordinate $(T)^{k=0}_{j\gamma}$ is defined on a Gauss-Legendre quadrature grid for $k = 0$ and the unitary transformation matrices for stretching coordinates $(T)_{m\alpha}$ and $(T)_{n\beta}$ are defined over the Gauss-Laguerre quadrature grid.

From the line strength, it is straightforward to calculate the integral transition intensity I given in eq. 2.95, which is directly related to the intensity of the attenuated incident radiation for a given wavelength, as in the Beer-Lambert law [60]

$$\frac{I}{I_0} = e^{-\sigma(\tilde{\nu})\cdot N\cdot L} \tag{2.108}$$

which relates the intensity of the absorbed radiation I, the reference radiation intensity I_0, the path length L and the the absorption cross-section $\sigma(\tilde{\nu})$ to N - the concentration of molecules. Absorption cross section depends on the wavenumber $\tilde{\nu}$ and is related to the integral line intensity by the relation:

$$\sigma(\tilde{\nu}) = \int I(\tilde{\nu}' - \tilde{\nu}) f(\tilde{\nu}') d\tilde{\nu} \tag{2.109}$$

In order to obtain absorption cross sections [31, 110, 111] the integral line intensity function (combined line intensities for a range of wavelengths) needs to be convoluted with a line shape function $f(\tilde{\nu}')$. This aspect of producing molecular spectra is particularly relevant for atmospheric science in determining concentrations of molecules from remote sensing and ground based telescope measurements. In this thesis, the main focus is on the step of accurate calculation of integral transition intensities.

Chapter 3

Room temperature infrared rotational-vibrational line lists for 13 isotopologues of carbon dioxide

This chapter discusses the theoretical procedure for generating infrared, rovibrational line lists for 13 isotopologues of CO_2. The importance of carbon dioxide and its isotopologues is outlined the next section, which focuses particularly on the need for accurate transition intensities required by remote sensing experiments. This is followed by a description of the procedure for generating theoretical line lists, which involved the use of the DVR3D suite and a sensitivity analysis of transition intensities. Finally, results of calculations are comprehensively compared to recent accurate measurements, semi-empirical databases and other theoretical approaches. The chapter is summarized in the context of meeting the requirements for remote sensing measurements of CO_2 in the Earth's atmosphere.

3.1 Motivation

Carbon dioxide is an inert gas in the Earth's atmosphere, therefore it can be relatively easily traced for studying the atmospheric circulation. Monitoring the concentration of carbon dioxide in the Earth's atmosphere remains a priority task for

a constantly growing number of government funded projects. This greenhouse gas has been a fingerprint of anthropogenic activity since the industrial revolution, by which time its atmospheric concentration is estimated to have risen from 280 ppm to over 380 ppm [112]. A 20% increase in the CO_2 atmospheric concentration has been observed over the past half-century - the most dramatic change in human history [113]. Mapping the circulation of the CO_2 gas in the troposphere is clearly vital to understanding and hopefully controlling the CO_2 content and hence the climate change [114, 115]. Several space missions are dedicated to explicitly monitor the atmospheric CO_2 molar fraction in high geographic resolution: GOSAT [2], ASCENDS [3], AIRS [4], CarbonSat [5] and recently launched NASA's OCO-2 mission [6–9]. Remote sensing measurements are cross-compared with ground based projects, such as Total Carbon Column Observing Network (TCCON) [10, 116] or Network for Detection of Atmospheric Composition Change (NDACC) [11], to look at the overall CO_2 concentration and its time variation, but more importantly to pinpoint where CO_2 is being produced (sources) and where it is going (sinks). Future missions, such as UK's Twinkle [117], ARIEL [118] and NASA's JWST [119], are designed to probe atmospheres of exoplanets, many of which are believed to have carbon dioxide as its major component [120–122].

Infrared absorption spectroscopy is the leading technique for precise determination of molar fractions of gases in atmospheres [3, 5, 10, 123, 124]. A major aim of these measurements is to establish carbon dioxide concentration at 1 ppm level or better [16, 27]. The uncertainty budget, which results from apparatus imperfections and random noise is estimated to be from 0.5 ppm to 1.5 ppm for the OCO-2 mission [17]. A major source of the systematic error in CO_2 concentration retrievals are reference line intensities and line profiles provided from experiment or theory [9, 31, 125, 126]. The accuracy requirement for transition intensities for remote sensing experiments is 0.3 –1%, which translates into 1-3 ppm resolution in CO_2 concentration [16]. Because some level of control over this error is possible, significant efforts have been made to minimize the uncertainty of the reference parameters, especially line intensities (see [27] and references therein). The CO_2

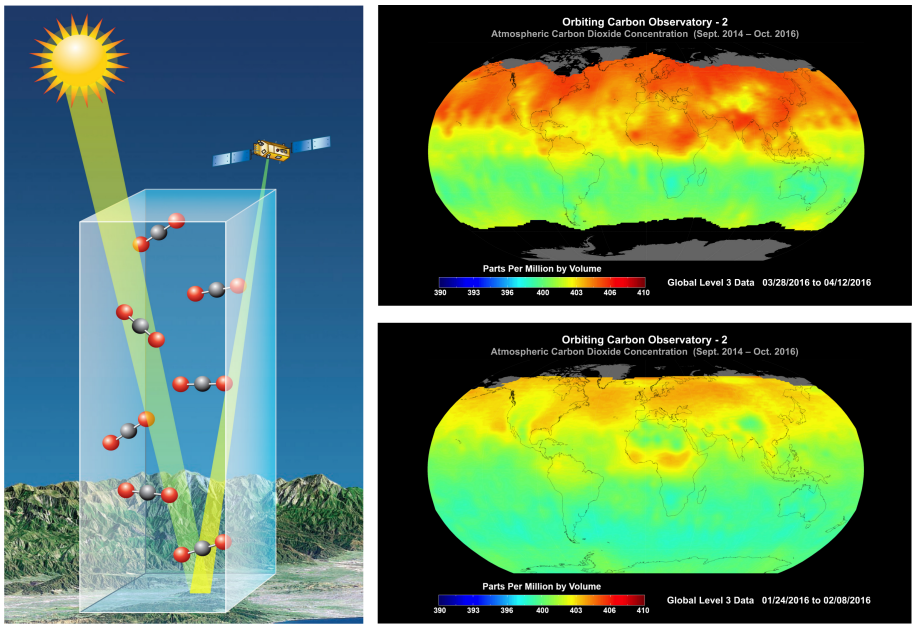

Figure 3.1: Schematic illustration of the working principle behind the OCO-2 mission (left panel). Global concentration maps (in ppm) of carbon dioxide from OCO-2 measurements taken in April 2016 (upper map) and in February 2016 (lower map). Courtesy of NASA/JPL-Caltech.

concentration retrieval process for the OCO-2 mission is currently (2017) under way [6]. The need for accurate transition intensities for remote sensing, particularly the OCO-2 mission, had prompted a number of theoretical and experimental studies devoted to calculation or measurement of transition intensities for the CO_2 'weak band' (1.6 μm) and the 'strong band' (2.06 μm), which are typically used in space-based measurements [27,31,127–129]. Detailed comparisons given in the following sections reveal that the present state-of-the-art measurements and calculations still do not meet requirements for remote sensing. For this reason, the present study is a response to the demand for more accurate models for transition intensities.

Other isotopologues. Up to 75% increase in the atmospheric CO_2 over recent decades have been associated with industrial fossil fuel combustion. For differentiation between different CO_2 pollution sources, a method for measuring isotopic ratios $^{14}C/^{13}C/^{12}C$ and $^{16}O/^{17}O/^{18}O$ can be employed. These ratios remain crucial for modelling Earth's geophysical processes [130–134], but also for example, in investigating processes of formation of radiation fields in the Martian atmosphere [23],

which is 96% rich in carbon dioxide [23]. Accurate knowledge of high resolution IR spectra for all isotopologues of carbon dioxide is essential in techniques for real-time monitoring of $^{13}C/^{12}C$ isotope ratios [131, 135, 136]. Such measurements are often used in identification of bio-geo-chemical origins of carbon dioxide emissions from the soil-air interface [137]. Spectra of CO_2 isotopologues are being increasingly considered for application in medical diagnosis, such as the recent suggestion that observations of infrared absorptions by $^{13}C^{16}O_2$ in breath provides a non-invasive means of diagnosing gastrointestinal cancers [138].

The low natural abundances (see Table 3.4) of ^{13}C, ^{14}C, ^{17}O and ^{18}O usually inhibit high accuracy measurements of integral line intensities on minor CO_2 isotopologues. Spectral congestion from more abundant carbon dioxide isotopologues and other molecules is the main problem when attempting to integrate the area under the peak, to obtain the integral intensity for a line. Therefore experimental accuracies of line intensities for trace abundant isotopologues of carbon dioxide are in general lower than for the main isotopologue. Theoretical line lists come to rescue in such cases.

The unstable $^{14}C^{16}O_2$ isotopologue is of special importance among other isotopologues because of its usage in dating of bio-samples and, more recently, in monitoring emissions, migrations and sinks of fossil fuel combustion products [20, 139, 140] as well as in assessment of contamination from nuclear power plants [25]. Until recently, monitoring fossil fuel emission relied mostly on β-decay count measurements [141] or mass spectrometry [142], both of which are high cost, invasive methods. Despite its low natural atmospheric abundance, radiocarbon dioxide has been probed via optical spectroscopy methods [26, 143–145]. Recent advances in absorption laser spectroscopy provided an unprecedented tool for detection of species containing radiocarbon of ratios $^{14}C/^{12}C$ down to parts per quadrillion. These measurements exploit a new spectroscopic technique called *saturated-absorption cavity ring down* (SCAR) [146] for measurements of the strongest lines in fundamental bands of $^{14}CO_2$ [26,144]. The knowledge of accurate line intensities for several isotopologues at the same time is therefore a necessity for

eliminating the unwanted noise sourced in traces of different isotopic carbon dioxide representatives. For instance the $P(20)$ line of the 00011 – 00001 band (00011 means $v_1 = 0, v_2 = 0, l = 0, v_3 = 1, n = 1$, i.e. asymmetric stretching fundamental band) in $^{14}CO_2$, which is used in radiocarbon measurements, above certain temperatures, interferes heavily with the Lorentzian tail of the $P(19)$ line in the 05511 – 05501 band of the $^{13}C^{16}O_2$ ('636') isotopologue [147]. This raises difficulties in retrieving unbiased concentrations of the radioactive isotopologue. Similar problems occurred in measurements based on the $P(40)$ line of the v_3 band of $^{14}CO_2$ [148]. In both cases accurate values of line intensities are required. Otherwise, as shown in [148], calculation of the fraction of ^{14}C in measured samples that employed a line strength taken from a theoretical approach, led to over 35 % error in retrieved concentrations (as later confirmed by alternative experiments (AMS) [142]). These observations were explained in terms of both inaccuracies of the line intensity and drawbacks of the spectroscopic fit model used, which fuels the need for reliable line intensity sources. Another successful technique further supporting this need was recently introduced by Genoud *et al.* [143], cavity ring-down spectroscopy with quantum cascade laser for monitoring of emissions from nuclear power plants.

One of the reasons for calculating a new set of infrared line lists for all important isotopologues of carbon dioxide was still the insufficient accuracy of theoretical approaches and experiments available at that time (three years ago). The newly published dipole moment surface (DMS) of Huang *et al.* [149] from NASA Ames Research Center (which was claimed to be the most accurate DMS available) revealed some discrepancies in comparisons to experiment and the the HITRAN 2012 database, which led to a general conclusion that the 'Ames' DMS still does not meet the requirements for remote sensing measurements. In this chapter, we show how present calculations meet the requirement of sub-percent accuracy in transition intensities, proving to be more accurate than other theoretical models and arguably some state-of-the art measurements.

3.2 Review of theoretical works on high resolution IR spectroscopy of CO_2

This section reports on the most notable works aimed at computation of accurate line lists for carbon dioxide. Apart from the most widespread method of fitting experimental data to a predefined quantum mechanical model for transition frequencies and transition intensities, a number of first principles theoretical approaches have been developed over the years, which were dedicated to calculating transition frequencies, transition intensities and line shapes for small molecules. CO_2 is one of the best studied molecules in terms of molecular spectroscopy, yet still it presents some unsolved issues.

3.2.1 Variational approaches

The variational method [60] is becoming more popular in solving the nuclear motion problem for triatomic molecules [150–154]. The main source of error in variational calculations is attributed to inaccuracies in the potential energy surface and the dipole moment surface [152]. Line positions are influenced by the quality of the PES. *Ab initio* PESs usually give energy levels with 1 cm^{-1} accuracy or worse [65,75,155,156]. This is because a number of components contributes to the overall uncertainty budget in *ab initio* calculations: finite basis set error, truncated CI expansion, non-Born-Oppenheimer corrections, relativistic or even quantum-electrodynamical effects for electrons [156]. Empirical refinement is one the most straightforward way of improving this accuracy to the level of 0.01 – 0.5 cm^{-1} for systems like CO_2 [157] or H_2O [75,158]. The situation is not the norm for transition intensities [154]. It has been shown that a fully *ab initio* dipole moment surface is capable of providing sub-percent accuracy in transition intensities [28]. Only specialist experiments are capable of providing parameters at this level of accuracy.

Early theoretical works on CO_2 were however far from meeting requirements for comparisons with high resolution measurements. In fact, spectroscopic accuracy in line positions has not been hitherto reached by variational methods.

Wattson *et al.* [159,160] produced the first comprehensive line lists using vari-

ational nuclear motion calculations with the use of a potential energy surface (PES). A major step toward more accurate line positions and intensities was made by the NASA Ames Research Center in a series of papers by Huang *et al.* [149, 157, 161]. Line lists from Huang *et al.* , called "Ames-1", provide both line positions and intensities covering the infrared and visible spectral region ($J = 0 - 150$) for room temperature (296 K) and 1000 K. Line positions, derived from a variational approach and based on semi-empirical mass-independent potential energy surface (PES), are accurate to 0.01 – 0.1 cm^{-1} for the main isotopologue of CO_2. Line intensities calculated with the *ab initio* Ames DMS are estimated to be 1-10% accurate for the main isotopologue.

Although the Ames line lists have been proven to be very accurate for the main isotopologue of carbon dioxide, a question remained about transferability of this high accuracy into other isotopologues. For line positions the accuracy of Ames line lists, based on a mass-independent PES, was shown nearly constant in all 13 isotopologues [157]. For line intensities however the limited experimental data on rare isotopologues did not give a definite answer to whether or not non-Born-Oppenheimer effects play any significant role in CO_2's infrared spectra. Very recently new experimental studies shown that line intensities calculated from Ames PES and Ames DMS are indeed reasonably accurate for both the symmetric and asymmetric isotopologues of CO_2 [31, 128, 162–164]. This important observation supports the thesis that line intensities can be computed variationally using mass-independent PES for all isotopologues with little loss in accuracy. This means that the non-Born-Oppenheimer corrections give negligible, possibly mutually cancelling effects, which enter the stipulated uncertainty budget.

3.2.2 Effective Hamiltonians

A widely-used alternative theoretical approach to variational calculations is based on effective operators for the Hamiltonian and the spectroscopic dipole moment [165–167]. Currently, the effective Hamiltonian approach achieves at least one order of magnitude better accuracy for $^{12}C^{16}O_2$ transition frequencies than the best-available PES [157]. Within this framework, the calculation of intensities re-

quires eigenfunctions of an effective Hamiltonian whose parameters were fitted to observed positions of rotation-vibration lines as well as dipole moment operators tuned to observed transition intensities. This approach has been used to create dedicated versions of the carbon dioxide spectroscopic databank (CDSD) for room-temperature [168] and high-temperature [169,170] applications. On the other hand, effective Hamiltonian models strongly depend on the quality of the input data, thus the accuracy and completeness of this technique are limited by experiment.

3.2.3 Discrete Variable Representation

Since early 1990's the discrete variable representation (DVR) schemes have begun gaining growing attention [59,67,103,104,171,172], as holding potential for being computationally more efficient [55, 67] than standard basis set variational implementations, which means savings in the CPU time, hence lowering the total computational cost. For large scale calculations, such as theoretical line lists for CO_2, any improvement in the computational efficiency is of great value. For these reasons, the present project uses the DVR technique for calculating line lists for CO_2. The DVR methods are not strictly variational, but can give results very close to variational ones, when appropriate convergence of integrals is maintained. It was reasonably decided to use the Ames-1 PES in the present DVR calculations of energy levels and ro-vibrational wavefunctions for all 13 isotopologues of CO_2 considered. For transition intensities, isotopologue-independent *ab initio* dipole moment surfaces are used, described in detail in section 3.3.2. It is believed that the error in neglecting non-Born-Oppenheimer effects introduces uncertainty in line intensities very much smaller than 1%. This assumption will be confirmed by comparisons with the latest high accuracy infrared absorption measurements in section 3.8.

To summarize, the key advantage of theoretical approach to IR line lists lies in its completeness within a given spectral region, as well as possible transferability between different isotopologues of the same molecule. Low natural abundance of a species is not a problem for a theoretical method, thus similar accuracy is expected from line lists for all 13 isotopologues of CO_2 considered in this work.

3.3 Computational details

3.3.1 General procedure for DVR3D calculations

This section provides details of calculations of infrared line lists for 13 isotopologues of CO_2 using the DVR3D program [59]. Theoretical details were already presented in chapter 2.

In a nutshell, the process of generation of theoretical line list is as follows: the potential energy surface in an analytical form serves as an input function for the first step of the ro-vibrational calculation with the DVR3DRJZ program, as displayed in Figure 3.2. Coriolis-decoupled energy levels and ro-vibrational wavefunctions are computed in the first step. In the second step a fully coupled ro-vibrational Hamiltonian is constructed in a truncated basis from the first step. Diagonalisation of this Hamiltonian in the Rotlev3b (or Rotlev3 for asymmetric isotopologues) program gives the final ro-vibrational energy levels and wavefunctions. The wavefunctions are then passed into the DIPOLE3 program, which also takes the dipole moment surface as an input. Calculated line strengths are then converted into transition intensities given in cm/molecule units. Combined: lower energy levels, transition frequencies, transition intensities and quantum numbers form a line list.

3.3.2 The potential energy and the dipole moment surfaces

In the first instance let us focus on details of the potential energy and the electric dipole moment surfaces used in the present work. The procedure proposed by Tennyson and Sutcliffe [57, 58, 67, 173] implemented in the DVR3D suite [59] requires a potential energy surface as an input function for the calculation (program DVR3DRJZ) of energy levels and rotational-vibrational wavefunctions. Because an exact nuclear kinetic energy operator in the Born-Oppenheimer approximation is used, the only significant source of errors comes from the PES and non-Born-Oppenheimer (NBO) effects. Errors introduced by non-Born-Oppenheimer effects have been shown to be marginally small in the electronic ground state of CO_2 [157, 161]. Thus, the quality of the electronic PES provided is of primary importance. Energy levels and rotational-vibrational wavefunctions obtained in the

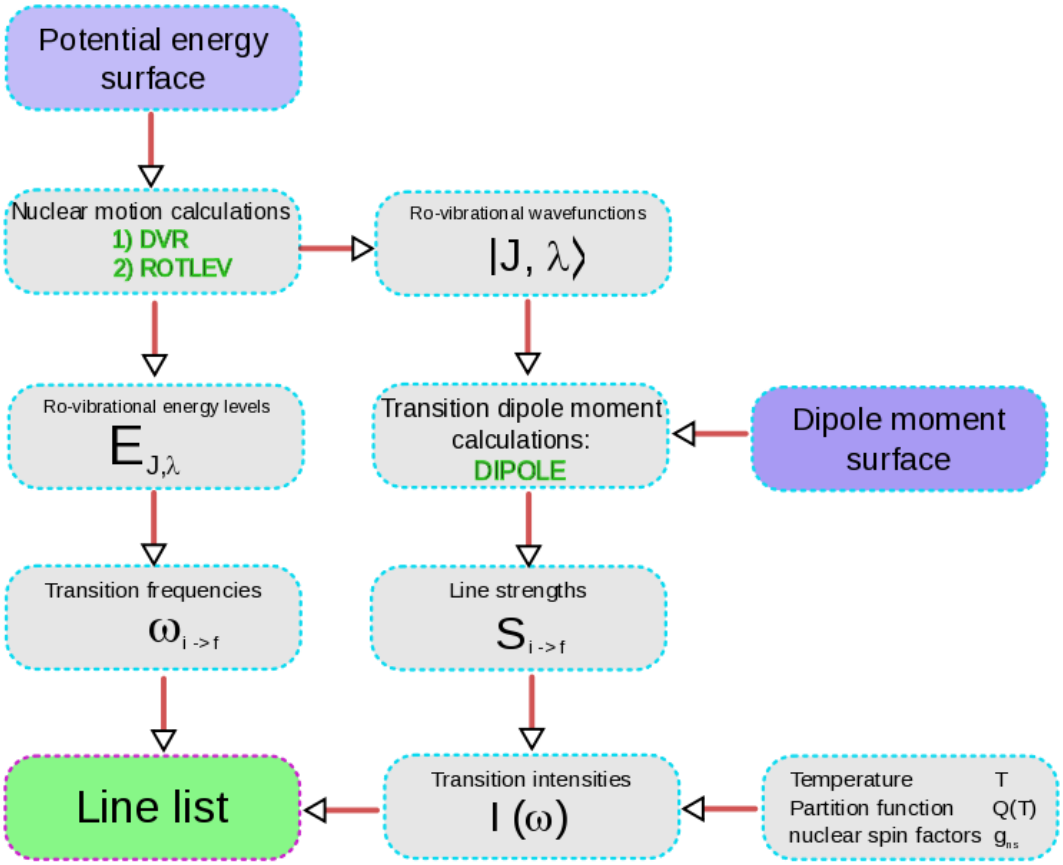

Figure 3.2: A general computational scheme for calculating ro-vibrational spectra from first principles with the DVR3D suite.

two step DVR-variational procedure, described in sections 3.3.1 and 2.4, are further used in intensity calculations, requiring additionally a DMS function as an input. The transition dipole moment elements depend both on the ro-vibrational wavefunctions and the DMS, therefore the quality of line intensities depends both on the PES and DMS. For this reason, in order to generate high accuracy line intensities, it is necessary to provide those two essential functions with the highest possible accuracy. The present state-of-the-art *ab initio* PESs are capable of reproducing experimental energy levels to 1 cm^{-1} accuracy [65, 75, 155, 156], which still remains insufficient for high resolution spectroscopy purposes. Hence empirical fitting of *ab initio* surfaces has become a standard procedure. This semi-empirical approach is much less successful in the case of DMSs, partly due to technical difficulties in obtaining accurate experimental data, suggesting the use of *ab initio* DMSs is a better choice [174]. The forthcoming section gives a brief description of the PESs and

DMSs used in the calculation of room temperature infrared line lists of CO_2. The most accurate PES and DMS were used to produce the final line list and the other two PESs and the other DMS were employed in a sensitivity analysis of transition intensities, a method for detecting resonance interactions between ro-vibrational energy levels (see section 3.5).

Ames-1 PES

Probably the most accurate semi-empirical PES for the electronic ground state of CO_2 was provided by Huang *et al.* [157]. In their approach 528 *ab initio* points were calculated with the CCSD(T) method. A three-point extrapolation of the basis set was based on cc-aug-pCVT/Q/5Z calculations. To account for higher-order electron correlation the scaled averaged coupled-pair functional (ACPF) method was used. Relativistic correction based on the Douglas-Kroll Hamiltonian was also added. No non-Born-Oppenheimer effects were included, resulting in an isotope-independent PES. The fit was performed to a functional form of Taylor expansion in Morse coordinates $(1-e^{-\beta\cdot(r_i-r_i^e)})$ for the C–O stretching and $\cos\theta$ for the O–C–O angle. 297 coefficients were finally used in the fit. Next, a two-step empirical refinement was performed: first using a subset of HITRAN2008 [175] $J=0-4$ energy levels, second with the use of purely experimental energy levels compiled for this purpose by Huang *et al.* [157], for chosen J's up to 85. The resultant PES was later rigorously tested against HITRAN2008 and HITRAN2012 databases as well as against more recent experiments [157, 161]. The best fit gave root-mean-square-deviation (RMSD) of 0.0156 cm^{-1} in $J=0-117$ range, with respect to purely experimental energy levels for the final Ames-1 PES for the CO_2 main isotopologue. Comparison with line positions from the HITRAN2012 database [176] gave an average shift of -0.0456 cm^{-1} and a spread (RMSD) of 0.0712 cm^{-1}. As a consistency test for the present calculations, energy levels computed with DVR3D and the Ames-1 PES were compared to the published Ames energy levels [157], giving excellent agreement (RMSD=0.04 cm^{-1} below 6000 $cm^{-1}$and RMSD=0.08 cm^{-1} below 10000 cm^{-1}).

Ab initio PES

A fully *ab initio* CO_2 PES was constructed by Polyansky *et al.* [28]. MOLPRO [177] multi-reference configuration interaction theory (MRCI) calculations with the aug-cc-pCVQZ basis were augmented by relativistic corrections at the one-electron mass-velocity Darwin (MVD1) level. The functional form was a Taylor expansion of symmetry-adapted bond-length and bond angle coordinates. A fit with 50 constants to the MRCI grid points gave an RMSD of 1.54 cm^{-1}. The relativistic correction surface was fitted separately with 31 constants to yield a RMSD of 0.56 cm^{-1}. A comparison with the Ames-1 PES shows a 1.5 cm^{-1} average discrepancy between the energy levels computed with the two surfaces for levels below 4000 cm^{-1}. Above this value some energy levels spoil this relatively good agreement to give a RMSD of 6.2 cm^{-1} for states below 11 000 cm^{-1}, with 200 (0.5% total) levels unmatched. However, for a fully *ab initio* procedure this PES represents roughly the state-of-the-art for CO_2. It was therefore used as part of the theoretical error estimation procedure.

Fitted PES

In the course of the sensitivity analysis for transition intensities, presented in section 3.5, it became clear that the *ab initio* PES is not accurate enough. The sensitivity analysis measures the response in transition intensities to very small distortions in the PES. The differences between the *ab initio* and the Ames-1 PES were sometimes too large to unambiguously match the corresponding energy levels. In addition to that, the insufficient quality of the *ab initio* PES sporadically caused detection of resonances, which turned out to be false positives. For this reason, a more accurate surface was needed. Higher quality can be achieved by refining the *ab initio* PES with Ames energy levels. This was done for levels with $J = 0, 1$ and 2. This fit resulted in a RMSD of 0.2 cm^{-1} between respective low J energy levels (Ames-1 PES vs. Fitted PES) and 1.4 cm^{-1} RMSD for states including all J's (0-129) below 11 000 cm^{-1}, leaving only 30 levels above 10 000 cm^{-1} (0.1% total) unmatched.

Ames DMS

The Ames dipole moment surface 'DMS-N2' of Huang *et al.* [149] was based on 2531 CCSD(T)/aug-cc-pVQZ dipole vectors. The linear least-squares fits were performed with 30 000 cm^{-1} energy cut-off and polynomial expansion up to 16-th order with 969 coefficients, which gave a RMSD of 3.2×10^{-6} a.u. and 8.0×10^{-6} a.u. for the parallel and the perpendicular components of the dipole vector, respectively.

UCL DMS

UCL dipole moment surface was calculated by Polyansky *et al.* [28] using the finite field method. In this method, the dipole moment is computed as first derivative of electronic energy with respect to a weak uniform external electric field. Both positive and negative electric field vector directions were considered for the *x* (perpendicular to molecular long axis) and *y* (along molecular long axis) components of the dipole moment, requiring 4 independent runs for each *ab initio* point. To evaluate the derivative of electronic energy with respect to the electric field a two-point numerical finite difference approximation was used:

$$E'(0) = \frac{E(\lambda) - E(-\lambda)}{2\lambda} + \mathscr{O}(\lambda^2) \tag{3.1}$$

where $E'(0)$ is the derivative of electronic energy with respect to electric field strength λ taken at zero-field. Previous research [28, 55] suggests that in general the derivative method yields more reliable dipole moments than those obtained from simple expectation value evaluation. In the calculation of the present *ab initio* DMS a two-point central difference formula from eq. 3.1 was used, with 3×10^{-4} a.u. electric field. Computationally more expensive four point finite difference formulas did not improve noticeably the accuracy of the dipole.

Electronic structure calculations were performed in the range 1.1 Å$< (r_1, r_2) <$ 1.45 Å, for C-O bond-lengths and 135 $^\circ < \theta <$ 180 $^\circ$ for the bond-angle coordinate [28]. Multi-reference configuration-interaction (MRCI) calculations were performed with the MOLPRO2012 package [177] in the aug-cc-pwCVQZ basis with one-electron mass-velocity Darwin (MVD1) relativistic correction included.

In the CASSCF calculations preceding the MRCI stage six core $1s$ electrons were frozen and the remaining 16 were distributed in the active space amongst the 12 $2s$ and $2p$ orbitals.

Randomly distributed *ab initio* dipole moment points corresponding to geometries with energies below 15 000 cm^{-1} were fitted to a Taylor expansion in symmetry adapted bond-lengths ($S_1 = (r_1 + r_2)/2 - r_e$, $S_2 = (r_1 - r_2)/2 - r_e$) and bond angle ($S_3 = 180 - \theta$) coordinates ($S_1^m S_2^n S_3^l$). The expansion was truncated at fifth order in S_1, S_2 and the x component of the dipole moment was fitted to 1963 points with 17 constants giving a RMSD of 2.25×10^{-5} a.u.; and 1433 points for the y component fitted with 19 constants giving RMSD of 1.85×10^{-5} a.u. The low RMSD of the fit and very high level of theory used to construct the UCL DMS allowed to ascribe an estimated 0.5% uncertainty to the DMS [28]. This high-accuracy DMS was expected to provide transition intensities at sub-percent accuracy level and therefore was the main reason for which the infrared line lists for CO_2 were computed.

3.3.3 Parameters for nuclear motion calculations

The task of computing ro-vibrational line lists for 13 isotopologues of CO_2, with at least 4 line lists per isotopologue is a major computational challenge. For this reason, it is desirable to pre-optimize the parameters of the DVR3D calculations, in order to reduce the computational time, memory and achieve the highest possible accuracy at lowest possible cost.

First, appropriate coordinates for the nuclear motion calculations need to be chosen, as well as an embedding type of the molecule-fixed frame. DVR offers two types of coordinates: Jacobi (scattering) coordinates and Radau coordinates (see chapter 2). High convergence of energy levels required by the nuclear motion calculations should imply nearly no dependence of energy levels on the choice of coordinates. Indeed, comparison of DVR3D calculated intensities with the Jacobi [28] coordinates and Radau [37] coordinates for a band located near CO_2's 2μm showed less than 0.1% discrepancy between independent studies. The choice of coordinates does however influence the convergence rate. After appropriate convergence tests with DVR program, it was concluded that Radau coordinates are the

most suitable for CO_2.

There are three available choices of embedding of the molecule-fixed coordinate frame in DVR3D: bisector (where, the z-axis bisects the angle between two atoms), bond (where the z-axis is aligned with one of the bonds in the molecule) and perpendicular (where the z-axis is embedded perpendicular to the plane of the molecule). For symmetric isotopologues of CO_2 the bisector embedding was chosen, which reflects the natural symmetry of the molecule. Moreover, the bisector embedding allows for symmetry factorisation of the Hamiltonian matrix, thus allows for faster calculations [67]. For asymmetric isotopologues of CO_2 the bond embedding was chosen.

Following the choice of coordinates and embedding, the vibrational basis set needs to be specified. DVR3D has two built-in radial basis set types: Morse oscillator-like basis functions [59, 85] and 3D Spherical oscillator basis functions [93]. Both basis set were tested for convergence of energy levels. The Morse-Oscillator-like basis functions gave faster convergence of $J = 0$ energy levels than the Spherical-Oscillator basis of the same size, thus the Morse-Oscillator basis was chosen for calculations.

The next step was to optimize the parameters of the chosen vibrational basis. By doing so, it is possible to significantly reduce the number of basis functions needed to achieve a satisfactory convergence of energy levels. The Morse oscillator-like basis function has three independent parameters: D_e - the dissociation energy of the Morse potential, r_0 - the equilibrium bond length and ω_0 - the width of the Morse potential. Preliminary tests showed that DVR energy levels only weakly depend on the value of D_e, which was set to 0.3 Hartree (E_h) for further calculations. This leaves a 2-dimensional parameters space, which needs to be optimized.

In the DVR program four parameters are relevant for energy levels calculation: NPNT - the number of vibrational stretching basis functions, NALF - the number of vibrational bending functions, MAX2D and MAX3D - truncation limits for the 2D and 3D DVR Hamiltonians, respectively. In practise, the MAX2D parameter neither influence the computation time nor the accuracy of energy levels, provided

that it is greater than MAX3D. MAX2D was therefore set to 10000. The NPNT, NALF and MAX3D parameters were optimized independently.

In the first step of the optimization procedure, a grid of (r_0, ω_0) values was created and for each grid point $J = 0$ DVR calculations were performed with NPNT= $20, 30, 40, 50, 60, 70, 80, 90$. NALF= 120 and MAX3D= 9000 were kept constant. Then, average deviation between respective energy levels calculated with NPNT and NPNT+10 was calculated. Such comparison allows to find the number of basis functions needed to assure a convenient level of convergence. Results of this procedure are displayed in Figures 3.3 and 3.4.

A preliminary sparse scan over a wide range of r_0 and ω_0 parameters identified the approximate region of 'quick convergence' for r_0 and ω_0, as shown in Figure 3.3. After narrowing the set of acceptable parameters with the low-resolution scan, a scan at a denser grid was performed, displayed in Figure 3.4. This allowed to elucidate r_0 and ω_0 parameters, for which only 20 vibrational stretching basis functions was needed to reach 0.001 cm^{-1} convergence of energy levels below 13000 cm^{-1} : $r_0 = 2.95$,a_0 $\omega_0 = 0.0085$ E_h. Similar analysis was performed with NALF and MAX3D as a subject to convergence test. In both cases, the optimal r_0 and ω_0 parameters for NPNT occurred to be also optimal for NALF and MAX3D. With these parameters, NALF = 120 and MAX3D= 1000 were found optimal and sufficient for good convergence of energy levels below 13 000 cm^{-1} . This efficiently contracted basis set reduced the memory and time cost, hence speeded up calculations. An identical set of basis set parameters was used for calculations with the *ab initio* and the Fitted PESs.

Figure 3.5 presents the total DVR3DRJZ calculation time and the total ROTLEV3b calculation time as a function of J quantum number. As expected, the computation time in DVR scales linearly with J. This is because in DVR3DRJZ $|k| = p, p+1, ..., J$ is a good quantum number, and for a given J, the code must solve $J + 2 - p$ problems of identical size (see 2.2). Scaling laws presented in Figure 3.5 reveal the importance of basis set optimization. The maximum J value considered (in the HITRAN2012 database) for a room temperature line list for the

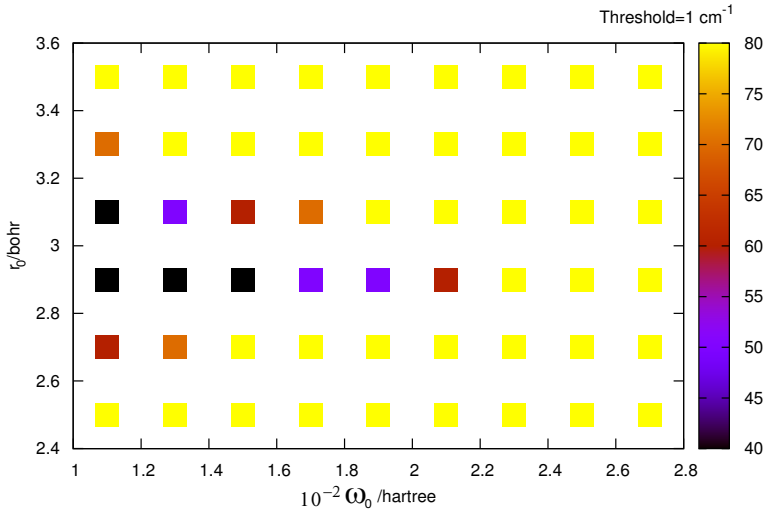

Figure 3.3: Low-resolution convergence map for DVR calculations. Colour code denotes the number of vibrational stretching basis functions (NPNT) needed to achieve mean convergence of energy $J = 0$ levels below 13 000 cm^{-1} better than the given 1 cm^{-1} threshold value. Optimized are ω_0 and r_0 parameters of the Morse-oscillator basis functions. The D_e parameter was set to 0.3 Hartree.

main isotopologue of CO_2 is $J = 130$. As shown in Figure 3.5, this corresponds to ≈ 5000 seconds of computation time. For comparison, the corresponding computation time for an unoptimized basis set, which requires NPNT $= 80$, NALF $= 120$ and MAX3D $= 9000$, is a few hundred times longer, making high-J calculations nearly prohibitive. To put things in perspective, for completion of fully converged $J = 0$ calculations with an un-optimized basis set requires 2500 seconds, whereas the $J = 0$ calculations with the optimized basis set are complete in 10 seconds. For example, previous DVR3D calculations of CO_2 energy levels and wavefunctions with Jacobi coordinates reported in ref. [28], for a good level of convergence required 80 radial basis functions and 120 bending basis functions. With this basis set size, computation of a single room temperature line list ($J < 130$) for CO_2 would take many months. With the basis set optimized here for Radau coordinates, this time could be reduced to one week.

In nuclear motion calculations the choice of masses is dictated by the masses used to fit the PES. In accordance with the NASA Ames-1 PES [157], in DVR calculations nuclear masses were used [178] in Dalton units (Da) for isotopologues

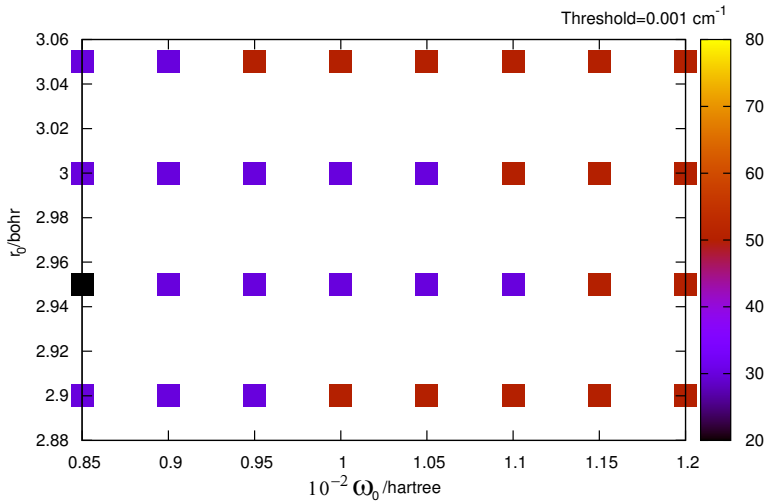

Figure 3.4: High-resolution convergence map for DVR calculations. Colour code denotes the number of vibrational stretching basis functions (NPNT) needed to achieve mean convergence of energy $J = 0$ levels below 13 000 cm^{-1} better than the given 0.001 cm^{-1} threshold value. Optimized are ω_0 and r_0 parameters of the Morse-oscillator basis functions. The D_e parameter was set to 0.3 Hartree.

of carbon dioxide: 11.996709 Da (^{12}C), 13.000439 Da (^{13}C), 15.990525 Da (^{16}O), 16.995245 Da (^{17}O) and 17.995275 Da (^{18}O).

Previous research [179,180] shows however, that often a better agreement with experiment is achieved when some intermediate mass between atomic and nuclear is used in the Hamiltonian. In addition to that, different masses are sometimes used for the rotational part of the Hamiltonian and the vibrational part of the Hamiltonian. Such a trick can account for non-adiabatic effects and reduce the observed minus calculated difference by tenths of a cm^{-1} in H_3^+ [179]. Although the present study operates within the Born-Oppenheimer approximation, it should be checked whether change from nuclear masses to atomic masses in the nuclear Hamiltonian has any significant effect on energy levels. Let us take an example of the ^{12}C atom, for which the mass fraction of electrons to nucleus is the largest. The effect of the nuclear-atomic mass interchange for other isotopes of carbon and oxygen atom should be only smaller. In the two-body Harmonic approximation the mass shift of the energy levels is inversely proportional to the reduced nuclear mass μ_0. Thus, the heavier the nuclei, the lower the energy levels should be. The effect of change

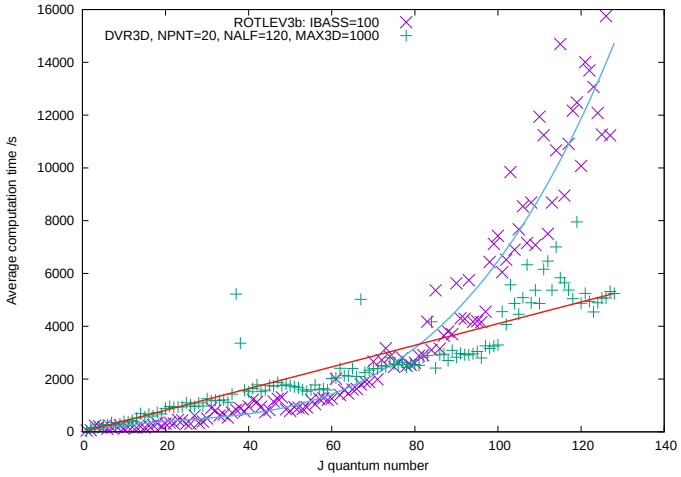

Figure 3.5: Computation time for DVR3DRJZ and ROTLEV3b runs for $^{12}C^{16}O_2$ as a function of J quantum number. For the DVR3DRJZ runs the optimized basis set was chosen and for ROTLEV3b a 100 element ro-vibrational basis was chosen (IBASS=100). Linear and quadratic fits are also displayed for DVR3DRJZ and ROTLEV3b runs, respectively. Test computations were performed with UCL's high-performance computer facility 'Legion'.

from nuclear to atomic mass in the nuclear Hamiltonian can be estimated by expanding the vibrational energy of the Harmonic oscillator in the mass difference $\Delta\mu = \mu - \mu_0$, which is a small parameter:

$$E(\mu) = E(\mu_0)\left(1 - \frac{1}{2}\frac{\Delta\mu}{\mu}\right) + \mathscr{O}\left((\Delta\mu)^2\right) \tag{3.2}$$

where μ is the atomic mass. By inserting for μ the atomic mass of ^{12}C and for m_0 the nuclear mass of ^{12}C we can estimate that the energy shift due to electron mass and electron-nucleus binding energy is 0.014%, which means that for energy levels at 10000 cm^{-1} the shift will be around 1.4 cm^{-1} and at 5000 cm^{-1} will be around 0.7 cm^{-1}. Full $J = 0$ DVR calculations for 626 CO_2 with nuclear and atomic masses for the same sets of other parameters show that: the lowest energy level (1285.398 cm^{-1}) shifts by 0.17 cm^{-1}, the energy level at 5022.328 cm^{-1} shifts by 0.67 cm^{-1} and the energy level at 10056.625 cm^{-1} shifts by 1.4 cm^{-1}, which confirms the estimates. Comparison to experimental energy levels shows that closer agreement

to experiment is observed when using nuclear masses, as expected from theory. This observation confirmed the choice of nuclear masses in DVR3DRJZ.

Prior to full scale calculations of line lists it is necessary to estimate ranges for the rotational quantum number J, for which ro-vibrational states are significantly populated at given temperature. This can be done in the first instance for the main isotopologue, whereas approximate J ranges for other isotopologues can be calculated by taking into account their abundances. First, a 10^{-30} cm/molecule intensity cut-off is established, which is the standard value employed by the HITRAN database. Then, informed by reliability limits of accuracy of the UCL DMS, the spectral region of interest for transition frequencies is chosen: 0 – 8000 cm^{-1}. From an estimate based on the Boltzmann law we infer that at room temperature (296 K) the highest initial ro-vibrational energy level that can be populated enough to give a transition above the 10^{-30} cm/molecule intensity threshold is roughly 6000 cm^{-1} and $J = 130$. Therefore we could potentially be interested in upper energy levels up to 14 000 cm^{-1} to cover the 0 – 8000 cm^{-1} wavenumber region. DVR3DRJZ calculations show that keeping only energy levels below 11 500 cm^{-1} is enough for the given frequency and intensity cut-off values. 70 lowest vibrational states are located below 11 500 cm^{-1}. For this reason, the Hamiltonian matrix in the first (vibrational) step of the calculation (program DVR3DRJZ) could be truncated at 1000 without the loss of accuracy in the energy levels of interest. Indeed, the $J = 0$ energy levels below 10 000 cm^{-1} were converged at the 10^{-6} cm^{-1} level and energy levels around 12 000 cm^{-1} at the 10^{-5} cm^{-1} level with MAX3D= 1000.

The ro-vibrational part of the computation (program ROTLEV3b) uses the Coriolis-decoupled ro-vibrational basis from the first step (program DVR3DRJZ). The number of the basis functions used in this second step depends on J: at $600 \times (J+1)$ for $J = 0-50$, $300 \times (J+1)$ for $J = 51-85$ and $200 \times (J+1)$ for $J = 86-130$. Fortunately, for higher J's smaller basis sets can be used, because less energy levels are needed, due to the upper energy level 11 500 cm^{-1} cut-off. As Figure 3.5 shows, the time cost of ROTLEV3b calculations depends quadratically on J. As long as the number of needed energy levels decreases with J, the pre-factor

in this quadratic dependence can be gradually reduced, which saves computational time.

Transition line strength calculations with the DIPOLE program used all states provided by ROTLEV3b. Separate calculations were performed for each J quantum number and for each separable block of the transition dipole moment matrix displayed in Figure 3.6. The number of Gauss-Legendre quadrature points required for integration over vibrational bending functions in the expression for the line strength (cf. eq. 2.101) was set to 250, which guaranteed good convergence.

For each isotopologue and for each pair of PES and DMS, the calculations were organized as shown in Figure 3.6. The figure represents a general scheme for DVR3D calculations with the full use of symmetry: the permutation symmetry of identical nuclei (even/odd) and the parity symmetry (e/f).

Parallel calculation of separable symmetry blocks in the transition dipole moment matrix for P,R and Q branches significantly speeds up the calculation. Selection rules given in chapter 2 constrain allowed transitions between states with different permutation parities and different p quantum numbers when J does not change (Q branch) and identical p quantum numbers when J does change (P and R branch). Transition frequencies and line strengths computed at the DIPOLE stage serve as an input to the SPECTRA program [59], which calculates integral transition intensities given by eq. 3.3.

$$I(\tilde{\nu}_{if}) = \frac{8\pi^2 N_A}{12\varepsilon_0 hc}\,\frac{\tilde{\nu}_{if}}{Q(T)}\,g_{ns}\exp\left(\frac{-E_i}{k_b T}\right)\left[1-\exp\left(-\frac{\tilde{\nu}_{if}}{k_b T}\right)\right]S_{if} \tag{3.3}$$

where $\tilde{\nu}_{if}$ is the transition wavenumber between the i'th and f'th ro-vibronic state and $Q(T)$ is the partition function at temperature T. N_A is the Avogadro number, k_b is the Boltzmann constant, h is the Planck constant, c is the speed of light in vacuum and ε_0 is the permittivity of vacuum. Units for integral line intensity are cm/molecule. Partition functions at 296 K given in table 3.4 were computed from eq. (3.4) using DVR3D energy levels obtained with the Ames-1 PES,

$$Q(T) = \sum_i g_i e^{-\frac{E_i}{k_b T}} \tag{3.4}$$

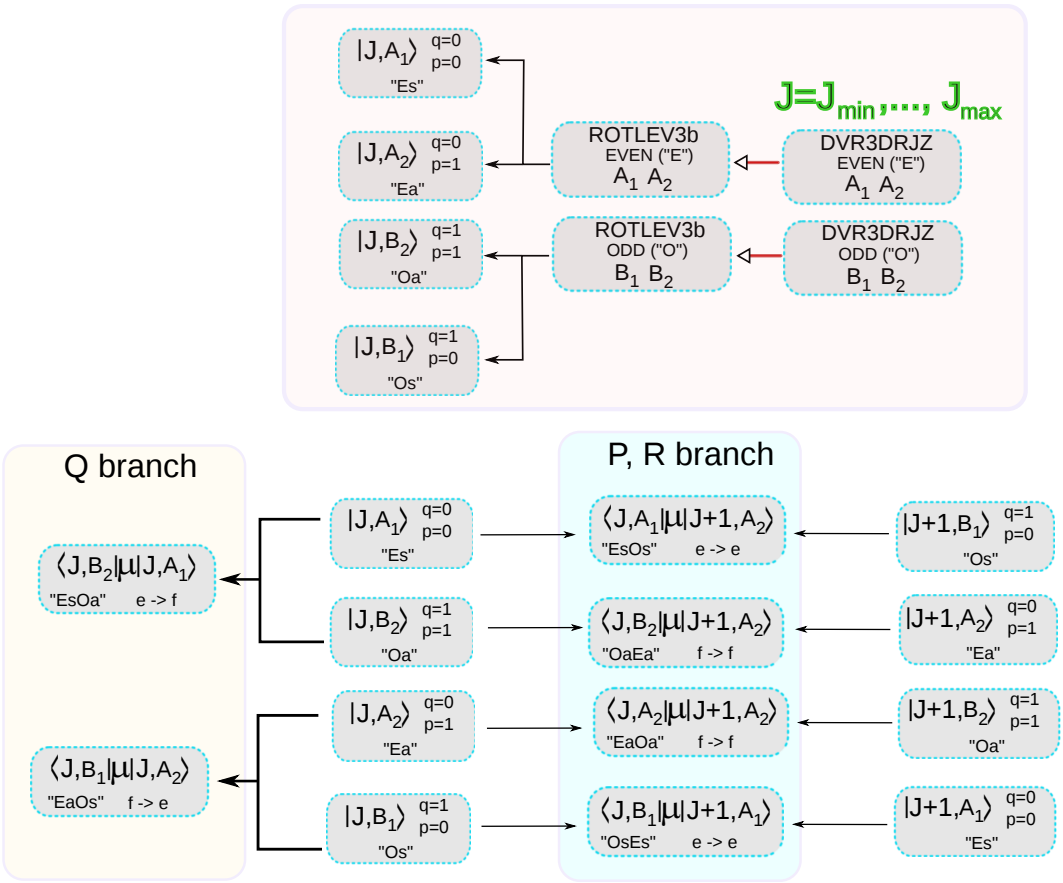

Figure 3.6: A general scheme for DVR3D calculations with the full use of symmetry: the permutation symmetry of identical nuclei (even/odd) and the parity symmetry (e/f). The upper panel depicts generation of ro-vibrational energy levels and wavefunctions with DVR3DRJZ and ROTLEV3b programs. The lower panel represents transition intensity calculations with DIPOLE. Each symmetry block of the transition dipole moment matrix for P,R and Q branches is calculated separately.

where E_i are ro-vibrational energy levels labelled by the general index i which represents all good quantum numbers: J, p, q and h - the index numbering consecutive solutions; $g_i = (2J+1)g_{ns}$ is the state dependent degeneracy factor discussed below.

Nuclear spin statistical weights. The nuclear spin statistical weight g_{ns} in eq. (3.3) can be calculated from the knowledge of individual nuclear spins of atoms in a given isotopologue and the use of some group-theoretic techniques. In brief g_{ns} is the number of spin states, which when combined in a product with a ro-vibronic state of a given symmetry produces the total internal state of the molecule which has the symmetry allowed by the Bose-Einstein or the Fermi-Dirac statistic [60, 181] [1]. This statement is based on the assumption that the nuclear spin does not interact with spins of electrons in the molecule or the rotational motion of the molecule, so that the total internal wavefunction of the molecule can be factorized into the nuclear spin part and the ro-vibronic part: $\Phi_{int} = \Phi_{nspin}\Phi_{rve}$. This assumes that nuclear spin energy levels are degenerate. The number of these degenerate nuclear spin states, which for a given ro-vibronic symmetry of the wavefunction generate a representation allowed by the Bose-Einstein or Fermi-Dirac statistics, constitutes the spin statistical weight. Hyperfine interactions, which are not considered here, remove this nuclear spin degeneracy, which causes splitting in energies of spin-rovibronic states. The total nuclear spins of carbon and oxygen atoms are: i(^{12}C) = 0, i(^{13}C) = 1/2, i(^{14}C) = 3, i(^{16}O) = 0, i(^{17}O) = 5/2, i(^{18}O) = 0. This means that the nuclei of ^{13}C and ^{17}O atoms are fermions and the remaining nuclei are bosons. Apart from translational, time-reversal and rotational symmetries, which are irrelevant for the present discussion, two fundamental symmetries are related to spin statistical weights: permutation of identical nuclei and parity. The total internal wavefunction of the molecule can transform either symmetrically or anti-symmetrically with respect to the parity transformation: $E^*\Phi_{int} = \pm\Phi_{int}$. Odd permutation of identical nuclei in the molecule changes sign of the total internal wavefunction when the permuted nuclei are fermions and does not change sign for boson nuclei. Even permutation of identical nuclei preserves the sign of Φ_{int}, hence always has character

[1] Repetitions of these references are omitted in the reminder of this section.

+1. In order to find spin statistical weights for isotopologues of CO_2, it is first necessary to choose a symmetry group in which the ro-vibronic, spin and total internal states will be classified. Molecular states of the symmetric isotopologues of CO_2 can be classified in the $D_{\infty h}(M)$ molecular symmetry group, which is isomorphic with the CNPI G_4 group for this molecule. Asymmetric isotopologues, on the other hand, have no permutation symmetry of identical nuclei and will be classified in the $C_{\infty v}(M)$ molecular symmetry group, which is isomorphic with the G_2 CNPI group. Let us choose two example isotopologues, $^{16}O^{12}C^{16}O$ and $^{17}O^{12}C^{17}O$, for which the procedure of finding spin statistical weights will be presented.

Because the nucleus of the ^{17}O is a fermion with spin 5/2, an odd permutation of oxygen atoms in $^{17}O^{12}C^{17}O$ will cause a sign change in the total internal molecular wavefunction. This fact is dictated by the Pauli Principle.

Character table for the $D_{\infty h}(M)$ molecular symmetry group given in table 3.1 shows that only Σ_u^+ and Σ_g^- irreducible representations of this group are allowed for the total internal wavefunction, because in these representations the (12) permutation of oxygen atoms has character -1. Ro-vibronic states of $^{17}O^{12}C^{17}O$ can transform as any of the four irreducible representations of $D_{\infty h}(M)$. Thus, the question is, which irreducible representations of the nuclear spin states can generate representations of the total internal wavefunctions allowed by the Fermi-Dirac statistics? The other question is: what is the degeneracy of these statistically allowed nuclear spin states? To answer both questions, first let us classify the nuclear spin functions Φ_{spin} in the $D_{\infty h}(M)$ group. The total number of product spin functions of atoms in

Table 3.1: Part of the character table for the $D_{\infty h}(M)$ molecular symmetry group used in determination of nuclear spin statistical weights for CO_2.

$D_{\infty h}(M)$	E	(12)	E*	(12)*
Σ_g^+	1	1	1	1
Σ_u^+	1	-1	1	-1
Σ_g^-	1	-1	-1	1
Σ_u^-	1	1	-1	-1

$^{17}O^{12}C^{17}O$ is $(2i_{^{17}O}+1)^2 = 6^2 = 36$. For the nuclei of ^{17}O there are 5 possible val-

ues of the projection of the total nuclear spin i in the Z-axis of the LAB frame, which corresponds to respective degenerate nuclear spin states: $|\frac{5}{2},+\frac{5}{2}\rangle \equiv \delta_{+\frac{5}{2}}$, $|\frac{5}{2},+\frac{3}{2}\rangle \equiv \delta_{+\frac{3}{2}}$, $|\frac{5}{2},+\frac{1}{2}\rangle \equiv \delta_{+\frac{1}{2}}$, $|\frac{5}{2},-\frac{1}{2}\rangle \equiv \delta_{-\frac{1}{2}}$, $|\frac{5}{2},-\frac{3}{2}\rangle \equiv \delta_{-\frac{3}{2}}$, $|\frac{5}{2},-\frac{5}{2}\rangle \equiv \delta_{-\frac{5}{2}}$. For the ^{12}C nucleus there is only one spin state: $|0,0\rangle \equiv \gamma$. The product state of the three states of individual nuclear spins corresponds to states with values of the projection of the total nuclear spin on the Z-axis of the LAB frame in the range $m_I = -|2\cdot i_{^{17}O} + i_{^{13}C}|, ..., +|2\cdot i_{^{17}O} + i_{^{13}C}| = -5,-4,...,+4,+5$. Product functions of the three nuclear states form a reducible representation for each value of m_I separately.

Table 3.2: Product nuclear spin states for ^{17}O^{12}C^{17}O. m_I is the projection of the total nuclear spin on the Z-axis of the LAB frame. Shown are only positive values of m_I. Negative m_I's are generated in analogical way. The spin state γ of the ^{12}C nucleus is omitted. In the right column given are irreducible representations of the $D_{\infty h}(M)$ group generated by appropriate products of the nuclear spin functions.

m_I	nuclear spin states	$\Gamma_{spin}^{m_I}$
+5	$\delta_{+\frac{5}{2}}\delta_{+\frac{5}{2}}$	Σ_g^+
+4	$\delta_{+\frac{5}{2}}\delta_{+\frac{3}{2}}$, $\delta_{+\frac{3}{2}}\delta_{+\frac{5}{2}}$,	$\Sigma_g^+ \oplus \Sigma_u^+$
+3	$\delta_{+\frac{5}{2}}\delta_{+\frac{1}{2}}$, $\delta_{+\frac{1}{2}}\delta_{+\frac{5}{2}}$, $\delta_{+\frac{3}{2}}\delta_{+\frac{3}{2}}$	$2\Sigma_g^+ \oplus \Sigma_u^+$
+2	$\delta_{+\frac{5}{2}}\delta_{-\frac{1}{2}}$, $\delta_{-\frac{1}{2}}\delta_{+\frac{5}{2}}$, $\delta_{+\frac{3}{2}}\delta_{+\frac{1}{2}}$, $\delta_{+\frac{1}{2}}\delta_{+\frac{3}{2}}$	$2\Sigma_g^+ \oplus 2\Sigma_u^+$
+1	$\delta_{+\frac{5}{2}}\delta_{-\frac{3}{2}}$, $\delta_{-\frac{3}{2}}\delta_{+\frac{5}{2}}$, $\delta_{+\frac{1}{2}}\delta_{+\frac{1}{2}}$, $\delta_{+\frac{3}{2}}\delta_{-\frac{1}{2}}$, $\delta_{-\frac{1}{2}}\delta_{+\frac{3}{2}}$	$3\Sigma_g^+ \oplus 2\Sigma_u^+$
0	$\delta_{+\frac{5}{2}}\delta_{-\frac{5}{2}}$, $\delta_{-\frac{5}{2}}\delta_{+\frac{5}{2}}$, $\delta_{+\frac{3}{2}}\delta_{-\frac{3}{2}}$, $\delta_{-\frac{3}{2}}\delta_{+\frac{3}{2}}$, $\delta_{-\frac{1}{2}}\delta_{+\frac{1}{2}}$, $\delta_{+\frac{1}{2}}\delta_{-\frac{1}{2}}$	$3\Sigma_g^+ \oplus 3\Sigma_u^+$
-1	$\delta_{-\frac{5}{2}}\delta_{+\frac{3}{2}}$, $\delta_{+\frac{3}{2}}\delta_{-\frac{5}{2}}$, $\delta_{-\frac{1}{2}}\delta_{-\frac{1}{2}}$, $\delta_{-\frac{3}{2}}\delta_{+\frac{1}{2}}$, $\delta_{+\frac{1}{2}}\delta_{-\frac{3}{2}}$	$3\Sigma_g^+ \oplus 2\Sigma_u^+$
-2	$\delta_{-\frac{5}{2}}\delta_{+\frac{1}{2}}$, $\delta_{+\frac{1}{2}}\delta_{-\frac{5}{2}}$, $\delta_{-\frac{3}{2}}\delta_{-\frac{1}{2}}$, $\delta_{-\frac{1}{2}}\delta_{-\frac{3}{2}}$	$2\Sigma_g^+ \oplus 2\Sigma_u^+$
-3	$\delta_{-\frac{5}{2}}\delta_{-\frac{1}{2}}$, $\delta_{-\frac{1}{2}}\delta_{-\frac{5}{2}}$, $\delta_{-\frac{3}{2}}\delta_{-\frac{3}{2}}$	$2\Sigma_g^+ \oplus 2\Sigma_u^+$
-4	$\delta_{-\frac{5}{2}}\delta_{-\frac{3}{2}}$, $\delta_{-\frac{3}{2}}\delta_{-\frac{5}{2}}$	$\Sigma_g^+ \oplus \Sigma_u^+$
-5	$\delta_{-\frac{5}{2}}\delta_{-\frac{5}{2}}$	Σ_g^+

The right column in Table 3.2 has been calculated with the use of the formula for the number of irreducible representations of a group included in a given reducible representation: $a_i = \frac{1}{h}\sum_R \chi^{\Gamma_{spin}^{m_I}}[R]\cdot\chi^{\Gamma_i}[R]^*$, where h is the order of the molecular symmetry group and R stands for symmetry operations in the group, $\chi^{\Gamma_{spin}^{m_I}}[R]$ is the character of the operation R in the reducible representation $\Gamma_{spin}^{m_I}$ and $\chi^{\Gamma_i}[R]$ is the character of the operation R in the irreducible representation Γ_i. Let

us choose an irreducible representation of the ro-vibronic state, say Σ_u^+, and find all irreducible representations of nuclear spin states, which if combined with Σ_u^+ in a product, will give one of the two representations allowed by the Fermi-Dirac statistics: Σ_u^+ and Σ_g^-. There are only two types of representations available for the nuclear spin states: Σ_g^+ and Σ_u^+. From the character Table 3.1 $\Sigma_u^+ \otimes \Sigma_g^+ = \Sigma_u^+$ and from Table 3.2 we can see that there are 21 in total Σ_g^+'s which satisfy this equation. Thus, the spin statistical weight for the Σ_u^+ ro-vibronic symmetry species is $g_{ns} = 21$. Weights for other ro-vibronic symmetry species can be calculated in a similar way. All spin statistical weights for $^{17}O^{12}C^{17}O$ are listed in Table 3.3.

Table 3.3: Spin statistical weights g_{ns} for the $^{17}O^{12}C^{17}O$ molecule classified in the $D_{\infty h}(M)$ molecular symmetry group. Γ_{rve}, Γ_{spin} and Γ_{int} are the irreducible representations of the ro-vibronic state, nuclear spin state and the total internal molecular state, respectively.

Γ_{rve}	Γ_{spin}	Γ_{int}	g_{ns}
Σ_g^+	$15\Sigma_u^+$	Σ_u^+	15
Σ_u^+	$21\Sigma_g^+$	Σ_u^+	21
Σ_g^-	$21\Sigma_g^+$	Σ_g^-	21
Σ_u^-	$15\Sigma_u^+$	Σ_g^-	15

For the $^{17}O^{13}C^{17}O$ isotopologue, for which there are two available nuclear spin functions for the ^{13}C atom, all weights are simply multiplied by 2, as the single carbon atom does not affects any properties associated with the permutation symmetry of identical nuclei, yet has two independent nuclear spin states, which need to be accounted for. This gives a state independent factor (2), and a state dependent factor: 15:21 (for Σ_g^+, Σ_u^- and Σ_u^+, Σ_g^- representations respectively). In the case of the main $^{16}O^{12}C^{16}O$ isotopologue, for which all nuclei are bosons with spin 0, there exists only one nuclear spin state, which belongs to the Σ_g^+ representation. In such case, the total internal wavefunctions can be generated only from ro-vibronic states of Σ_u^+ and Σ_g^- symmetry. For these ro-vibronic representations, there is a single corresponding spin state, hence the appropriate spin statistical factors are $g_{ns} = 1$. For the other two ro-vibronic symmetry species: Σ_g^+ and Σ_u^-, there are no available spin functions, which would generate representations of the total inter-

nal wavefunction allowed by the Bose-Einstein statistics, hence the spin statistical weights for these representations are $g_{ns} = 0$. Ro-vibrational states, for which no nuclear spin function can be found to generate an allowed representation of the total internal wavefunction do not exist in nature and are called *missing states*. The corresponding hypothetical energy levels are called *missing levels*. In the case of $^{16}O^{12}C^{16}O$ the observable energy levels correspond to ro-vibrational states which consist of sums of products $\Phi_{vib}\Phi_{rot}$, which have the total symmetry either Σ_u^+ or Σ_g^- (in the electronic ground state). With these requirements it can be shown that observable ro-vibrational states with a symmetric vibrational part ($n\nu_1$, the symmetric part of the irreducible representation for $n\nu_2$ vibration, even quanta in the ν_3 mode) have J-even and e-Wang symmetry (Σ_g^- total symmetry). For odd number of quanta in the asymmetric stretching ν_3 mode, the allowed by statistics energy levels have J-odd and e-Wang symmetry. The f-Wang symmetry is allowed only for levels in the degenerate bending manifold and only for J-even when the vibrational state has odd number of ν_2 quanta and for J-odd when the vibrational state has even number of ν_2 quanta. These rules for observable energy levels are straightforwardly derived from the character table for the $D_{\infty h}(M)$ group and from the knowledge of the classification of rotational and vibrational basis wavefunctions in this molecular symmetry group.

Spin statistical weights for all 13 isotopologues are given in Table 3.4.

3.4 Resonance interactions of energy levels

This section is dedicated to introducing the concept of resonance interaction between ro-vibrational states. A general theoretical formulation given below will be further supported by two examples with CO_2 in sections 3.4.3 and 3.4.4. Finally, a simple theory for transition intensity borrowing, which accompanies resonance interactions, is developed. This theory serves in section 3.4.6 to formulate a theoretical descriptor, which aims in quantifying the sensitivity of line intensities to small perturbations in the ro-vibrational wavefunction. Further on, this new descriptor will be used in qualitative discussion of reliability of calculated line intensities in CO_2.

3.4.1 What is a resonance interaction?

A resonance interaction between two energy levels occurs when three conditions are satisfied [181]: a) the levels have similar (identical) energies; b) quantum states associated with the energy levels have identical symmetry; c) an interaction operator exists, which mixes the interacting states.

In the variational formulation of the nuclear motion problem, the task of solving the SE reduces to diagonalisation of the ro-vibrational Hamiltonian, which is represented by a square Hermitian matrix for a chosen basis. The choice of this zero-order basis set determines which matrix elements of the Hamiltonian will be large, which will be small and which will vanish by symmetry conditions. Typically, a product basis set is used, with separate functions for vibrational and rotational degrees of freedom:

$$\Phi^0_{rv} = \Phi_{rot}\Phi_{vib} \tag{3.5}$$

in which Φ_{rot} is a rigid-rotor eigenfunction and Φ_{vib} is an eigenfunction of the harmonic oscillator. For the case of triatomic molecules, the most popular choice for the rotational basis is $\Phi_{rot} = |J,k,M\rangle$, that is symmetric-top eigenfunctions, characterized by the total angular momentum quantum number J, the projection quantum number k of the total angular momentum on the molecule-fixed z-axis and the pro-

jection quantum number M of the total angular momentum on the Z-axis of the LAB frame. Φ_{vib} is chosen to be either an eigenfunction of the 3D harmonic oscillator or the 3D morse oscillator. Φ_{vib} can be typically written in the abstract bra-ket form as: $|v_1, v_2, l, v_3\rangle = |v_1\rangle|v_2, l\rangle|v_3\rangle$, where v_1, v_2, v_3 are quantum numbers characterizing the vibrational zero-order basis state. l is the vibrational angular momentum quantum number, originating from a degenerate bending motion in a linear triatomic molecule. The solution to the fully coupled ro-vibrational SE is then given by an expansion in these chosen basis functions:

$$\Phi_{rv}^{(n)} = \sum_{v_1,v_2,l,v_3,k} C_{v_1,v_2,l,v_3,k}^{(n)} |J,k,M\rangle|v_1, v_2, l, v_3\rangle \tag{3.6}$$

The quantum numbers v_1, v_2, l, v_3 are good symmetry labels only for the Hamiltonian of the harmonic oscillator. Similarly, the k quantum number is a good quantum number for a symmetric-top rigid rotor Hamiltonian, that is also for molecules at linear geometries. Any small deviations from these model systems cause the v_1, v_2, l, v_3 and k quantum numbers to be only *near quantum numbers* [60]. For large deviations from harmonicity the vibrational labelling of the harmonic oscillator starts loosing its sense. Similarly, strong rotation-vibration interactions cause k to be no longer even a near good quantum number. Such situation occurs predominantly when two zero-order energy levels are involved in a resonance interaction. Let us analyse such resonance interaction on a simple example. Consider a generic two-level system with zero-order basis states having energies E_S^0 and E_W^0 perturbed by an interaction C. The Hamiltonian matrix for this two-level system is written as:

$$\begin{pmatrix} E_S^0 & C \\ C & E_W^0 \end{pmatrix} \tag{3.7}$$

The zero-order unperturbed basis will be also called the *diabatic basis* [182]. Diagonalisation of this matrix gives *adiabatic* energy levels, which exhibit an avoided crossing, as depicted in Figure 3.7. Adiabatic energies then read:

$$E_{\pm} = \frac{1}{2}\left(E_S^0 + E_W^0\right) \pm \frac{1}{2}\sqrt{4|C|^2 + \Delta E^0} \tag{3.8}$$

where $\Delta E^0 = E_W^0 - E_S^0$ is the separation of *diabatic* energy levels. The new adiabatic states are mixtures of diabatic states:

$$\begin{pmatrix} |\tilde{W}\rangle \\ |\tilde{S}\rangle \end{pmatrix} = \begin{pmatrix} c_1 & -c_2 \\ c_2 & c_1 \end{pmatrix} \begin{pmatrix} |W\rangle \\ |S\rangle \end{pmatrix} \tag{3.9}$$

where mixing coefficients are given as: $c_1 = \left(\frac{\sqrt{4|C|^2+\Delta E^0}+\Delta E^0}{2\sqrt{4|C|^2+\Delta E^0}}\right)^{\frac{1}{2}}$ and $c_2 = \left(\frac{\sqrt{4|C|^2+\Delta E^0}-\Delta E^0}{2\sqrt{4|C|^2+\Delta E^0}}\right)^{\frac{1}{2}}$. In the limit of no interaction ($C = 0$) the two diabatic states remain unperturbed. In the limit of the exact resonance ($\Delta E^0 = 0$) we get 50% / 50% mixtures (in-phase and anti-phase) of the two diabatic states.

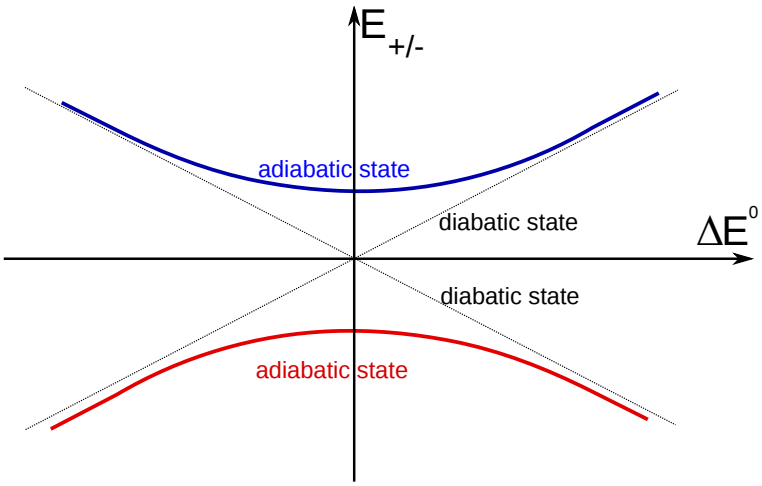

Figure 3.7: Schematic illustration of an avoided crossing of two states with the same symmetry. The dashed black lines represent energies of bare (diabatic) non-interacting states, whereas the blue and red thick curves are adiabatic states. In the x-axis given is the energetic separation of the diabatic states ΔE^0.

Thus adiabatic levels exhibit an avoided crossing at the point where the diabatic levels intersect. According to standard textbooks [60], near the points of resonances, that is near the crossing of diabatic energy levels, most of the standard variational or perturbative formulas fail to accurately reproduce observations. In the following

paragraph, we are going to take a closer look at problems which occur with resonantly interacting energy levels and what consequences such interactions have for observations, such as transition intensity measurements.

Knowing that the interaction operator $\hat{C}$ can mix different ro-vibrational states, which manifests itself in a non-zero off diagonal matrix element C in eq. 3.7, the next question to ask is: what is the necessary condition for a resonance interaction in terms of symmetry of states? The interaction operator must have the symmetry of the ro-vibrational Hamiltonian, which is totally symmetric under operations of the molecular symmetry group. For this reason, the vanishing integral rule [60] allows for rotation-vibration interaction of diabatic states with the same ro-vibrational symmetry only, $\Gamma^1_{rv} = \Gamma^2_{rv}$, where $\Gamma^i_{rv} = \Gamma^i_v \otimes \Gamma^i_r$. This argument can be also derived intuitively: a coupled ro-vibrational wavefunction, which is not a single product of a rotational and a vibrational states must have identical symmetries of its component terms. This is because the whole ro-vibrational wavefunction must transform according to one of the irreducible representations of the molecular symmetry group.

For further discussion, the harmonic oscillator basis is chosen for vibrations and the symmetric-top basis for rotations. We are going to classify resonance interactions, by the type of the perturbing operator $\hat{C}$.

3.4.2 Types of resonance interactions

There are two basic types of perturbations of ro-vibrational energy levels caused by interaction with other ro-vibrational energy levels: *Fermi-type interactions* and *Coriolis-type interactions*. The former type of the resonance interaction occurs when two vibrational levels have the same symmetry, $\Gamma^1_v = \Gamma^2_v$. This is a purely vibrational anharmonic effect and leads to shifting of ro-vibrational energy levels of the whole vibrational band involved in the interaction. The Coriolis-type interaction is J-specific and depends on the symmetry of the vibrational and the rotational part of the wavefunction. As we will show further on, the Coriolis-type resonance is possible between states with $\Delta k = \pm 1, \pm 2$, which for a linear triatomic molecule means also $\Delta l = \pm 1, \pm 2$. The $\Delta l = \pm 2$ interaction is often called *l-type resonance* or *l-doubling resonance*. For future discussion it is useful to introduce the concept of

the *polyad number* [60,183]. For the example of CO_2, the polyad number is defined as $P = 2v_1 + v_2 + 3v_3$, where v_1, v_2, v_3 are the vibrational quantum numbers of symmetric stretching, bending and asymmetric stretching, respectively. The weights standing by the vibrational quantum numbers in the polyad number formula are associated with relative energetics of vibrational fundamentals: $\omega_3 \approx 3\omega_2 \approx 2\omega_1$. The majority of resonance interactions are enclosed within the space of states with the same polyad number. However sometimes an interpolyad anharmonic interaction can occur, which will be distinguished from the intra-polyad Fermi interaction.

3.4.3 Example: Fermi-type resonance in CO_2

Anharmonic terms in the PES cause Fermi-interaction of vibrational levels of the same symmetry, as shown in eq. 3.9. An example of the Fermi-resonance interaction is mixing between the $v_1 v_2 l v_3 n = 10001$ and $v_1 v_2 l v_3 n = 02001$ energy levels in CO_2. Both states have identical Σ_g^+ symmetry and the perturbing operators here are the cubic and quartic terms in the PES. Here n is defined as an index labelling vibrational states which are subject to Fermi-mixing with some other vibrational states. Interactions of energy levels carry consequences for transition intensities. If one of the energy levels involved in a weak transition in the harmonic approximation is in Fermi resonance with an energy level which participates in a strong transition, then intensity borrowing due to mixing of the *dark state* with the *bright state* can significantly increase the transition intensity of the weak (dark) vibrational band, regardless of J value. As a result, intensity of the whole band is shifted by this type of interaction.

3.4.4 Example: Coriolis-type resonance in CO_2

Coriolis-type interactions are usually associated with operators, which are products of vibrational coordinates, vibrational angular momentum and angular momentum operators, e.g. $\zeta Q_i p_i J_j$. Here ζ is the scalar Coriolis-constant [60,68]. Because Q_i and p_i have the same symmetry, the non-vanishing rule for matrix elements generated by this type of perturber states that the product of irreducible representations of two interacting energy levels must contain an irreducible representation of the j-th

component of the total angular momentum operator $\vec{J}$.

As an example of the Coriolis-type resonance let us consider two energy levels in CO_2: 11101 ($v_1 = 1, v_2 = 1, l = 1, v_3 = 0$) and 00011 ($v_1 = 0, v_2 = 0, l = 0, v_3 = 1$). Figure 3.8 displays these energy levels with their vibrational symmetries and energies. It is clear that the 11101 and 00011 energy levels have different vibrational symmetries, thus cannot interact by a pure vibrational-anharmonic mechanism. However, when we list possible symmetries of ro-vibrational states generated from these vibrational states, there are combinations of J and k quantum numbers for which ro-vibrational energy levels in the 11101 and 00011 manifolds have the same symmetry. For example, when the symmetry of the 11101 energy level (Π_u) is combined with the symmetry of k-odd rotational wavefunction Π_g it produces the following sum of irreducible representations: $\Pi_u \times \Pi_g = \Sigma_g^+ \oplus \Sigma_g^- \oplus \Delta_g$. At this point it is convenient to move into the $C_{2v}(M)$ group with the classification. In this group the $D_{\infty h}$'s Π_u state correlates with $A_1 \oplus B_1$ symmetry and the Σ_u^+ correlates with the B_2 symmetry.

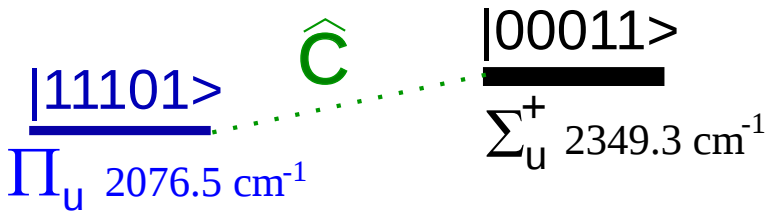

Figure 3.8: Schematic illustration of a resonance interaction between two energy levels in CO_2 through operator the Coriolis operator $\hat{C}$. Π_u is the vibrational symmetry of the $|11101\rangle$ state and Σ_u^+ is the vibrational symmetry of the $|00011\rangle$ state. Energies of respective states are given in wavenumbers.

One may ask a question: why did we move into the $C_{2v}(M)$ group? First of all, it is subjectively more convenient to operate with a familiar group, which contains no degenerate representations. Secondly, selection rules for interaction matrix elements derived in the less general $C_{2v}(M)$ group will also hold in the more general C_s group. The implication in the opposite direction is not always true. The symmetry of rotational wavefunctions in the $C_{2v}(M)$ group is $A_1 \oplus B_1$ for even values of k in the $|J,k\rangle$ state and $A_2 \oplus B_2$ for odd values of k. The selection rule for the J quantum

number is $\Delta J = 0$. By combining the rotational and vibrational symmetries we obtain for the 11101 vibrational state two possible ro-vibrational symmetries: $A_1 \oplus B_1$ for even values of k and $A_2 \oplus B_2$ for odd values of k. The 00011 vibrational state also generates two possible ro-vibrational symmetries: $A_2 \oplus B_2$ for even values of k and $A_1 \oplus B_1$ for odd values of k. We can see therefore, that only states with opposite parity of the k quantum number can be connected via a Coriolis interaction. Indeed, as we will see in section 3.5 in Figure 3.20 the intensity of the R branch of the 11101 – 00001 band is affected by J-localized resonance interaction between the 11101 and the 00011 state. Although the whole 11101 – 00001 band is subject to Coriolis interaction with the 00011 state only near a particular J value, where this interaction grows rapidly to give a very noticeable intensity alternation.

3.4.5 A theory for ro-vibrational intensity borrowing

The goal of this section is to provide a theoretical method for assessing the 'reliability' of the variationally calculated matrix elements of an arbitrary quantum-mechanical operator. The accuracy of variational wavefunctions and energy levels is determined by the accuracy of the underlying potential energy surface (PES). For this reason, the term 'reliability' of results correlates with 'the accuracy of the PES used'. In this sense, we are aiming at finding a measure of how sensitive are the variational matrix elements (e.g. the transition dipole moment) to small changes in the PES. This measure will formally depend on the energetic separation of states involved in the interaction $\Delta E_{ij} = E_i - E_j$ (not the states between which a transition occurs) and on the deviation of the PES from a reference PES: $\Delta V(r_1, r_2, \theta) = V(r_1, r_2, \theta) - V^0(r_1, r_2, \theta)$. With these assumptions, the term 'reliability' refers to the most accurate PES considered, rather then to the exact (experimental) values. In other words, we assume the most accurate PES (reference PES V^0) as the exact model for reality. Of course this does not mean that we are providing a method for estimating an uncertainty for matrix elements of operators, which can be later compared to experimental values. Rather we aim to give a procedure for stating how sensitive these matrix elements are when a different PES is used from the reference PES. The reference PES may generate energy levels with some

systematic shift with respect to experiment, thus the sensitivity measure can not be directly related to the absolute error of the calculated matrix elements. Nevertheless, such multiple-PES-based procedure can deliver information about how strong are the resonance interactions of energy levels, provided that we have control over the deviation between the reference PES and the working PES. By this it can be for example possible to estimate which variationally calculated transition intensities can be trusted and which of them are very sensitive to the quality of the PES (accuracy of the wavefunction).

Matrix elements between interacting states. It has been already shown, that the *energy levels resonance* is possible between states with the same ro-vibrational symmetry. Coriolis operators are proportional to components of the total angular momentum operator $\hat{J}_i$, which in turn can be expressed by ladder operators ($\hat{J}^{\pm}$), which mix states with different k quantum number (the projection of the total angular momentum on the z-axis of the molecule-fixed frame). In general, a Coriolis operator, which has the symmetry of the total ro-vibrational Hamiltonian, contains also linear momentum and position operators, which can mix different vibrational zero-order states, as well as squares of the total angular momentum operators, which allow for mixing of states with $\Delta k = \pm 1, \pm 2$.

The other necessary condition for a resonance is non-symmetry based, but related to the energetics of the two interacting energy levels. The strength of anharmonic and ro-vibrational interactions strongly depend on the energetic separation of the zero-order energy levels. More precisely, the non-vanishing interaction matrix element C from eq. (3.7) can be rewritten in the following form:

$$C_{ij} = \langle \Phi_i^0 | \hat{C} | \Phi_j^0 \rangle = \frac{\langle \Phi_i^0 | [\hat{C}, \hat{H}_{rv}^0] | \Phi_j^0 \rangle}{E_i^0 - E_j^0} \tag{3.10}$$

which reveals a singularity at $E_i = E_j$. Here the zero-order states Φ_i^0 are eigenstates of the Coriolis-decoupled ro-vibrational Hamiltonian: $H_{rv}^0 \Phi_i^0 = E_i^0 \Phi_i^0$. Matrix elements of the commutator $[\hat{C}, \hat{H}_{rv}^0]$ are finite and non-zero, thus the coupling matrix element approaches infinity when the energy levels become degenerate. In reality, ideal accidental degeneracies of two zero-order energy levels are never observed,

hence the interaction matrix elements are always finite, although they can take very large values and be very sensitive to small changes in the accuracy of the wavefunction. Because the denominator in eq. 3.10 is very small, any small perturbation $\delta\Phi_i^0$ to the wavefunction can cause a significant change to the value of the interaction term C_{ij}. As a consequence, variational wavefunctions need to be calculated with a very high accuracy, to properly reproduce the values of the interaction matrix elements near resonances. This is obviously one of the drawbacks of variational methodology.

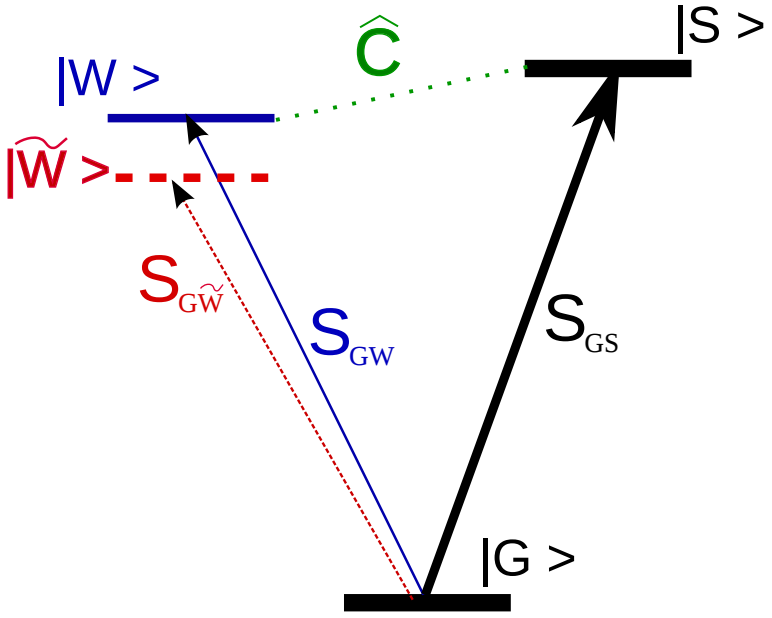

Figure 3.9: Schematic illustration of intensity borrowing caused by a resonance interaction between two energy levels through operator $\hat{C}$. The $S \leftarrow G$ transition is from the ro-vibrational ground state $|G\rangle$ and the associated line strength is S_{GS}. $W \leftarrow G$ transition is from the ro-vibrational ground state $|G\rangle$ and the associated line strength is S_{GW}. The interaction between $|W\rangle$ and $|S\rangle$ energy levels leads to intensity borrowing of the $W \leftarrow G$ transition, which results in an altered transition line strength $S_{G\tilde{W}}$.

Now, the question is: near a resonance, when $E_i^0 - E_j^0$ is small, how does a small change in the wavefunction $\delta\Phi_i^0$ affect the matrix element of the interaction operator C_{ij}? In answering this question, we shall first follow an informal intuitive picture and compare this to a more formal approach of perturbation theory.

Infinitesimal perturbation approach. Assume that the full ro-vibrational Hamiltonian $H^0_{rv} = T + V^0$, with the reference PES V^0, generates a set of eigenfunctions $\{|\psi^0_i\rangle\}_{i=1,2,\ldots}$. In this eigenbasis the Coriolis operator $\hat{C}$ is diagonal, because $H^0_{rv}|\psi^0_i\rangle = E^0_i|\psi^0_i\rangle$. The full ro-vibrational Hamiltonian $H_{rv} = T + V$, with the second test-PES V, generates a set of slightly different eigenfunctions $\{|\psi_i\rangle\}_{i=1,2,\ldots}$, which correspond to slightly different eigenvalues: $\hat{H}_{rv}|\psi_i\rangle = E_i|\psi_i\rangle$. In both cases the kinetic energy operator is the same. Nevertheless, a change in the PES (ΔV) will result in a change to the wavefunction, so that $H^0_{rv}|\psi_i\rangle \neq E^0_i|\psi_i\rangle$. In the standard variational formulation the reference wavefunction is expanded in a well defined basis:

$$|\psi^0_i\rangle = \sum_j d^0_{ij}|\Phi^0_j\rangle \tag{3.11}$$

Basis sets are identical in both cases (reference and test); the only change is in the variational expansion coefficients.

$$|\psi_i\rangle = \sum_j d_{ij}|\Phi^0_j\rangle \tag{3.12}$$

Matrix elements of the Coriolis operator $\hat{C}$ in the reference eigenbasis can be written as:

$$\langle\psi^0_i|\hat{C}|\psi^0_j\rangle = C^0_{ij}\delta_{ij} \tag{3.13}$$

This matrix is diagonal and the expectation values of the Coriolis operator in this basis are considered as known reference values based on the highest quality PES. Now assume analogous matrix elements in the test eigenbasis:

$$\langle\psi_i|\hat{C}|\psi_j\rangle = C_{ij}\delta_{ij} \tag{3.14}$$

This matrix is also diagonal, but the expectation values are different with respect to the reference case. After expanding matrix elements from eq. 3.14 in the variational basis we get:

$$C_{ij} = \sum_{k,l} d^*_{ik} d_{jl} \langle \Phi^0_k | \hat{C} | \Phi^0_l \rangle \tag{3.15}$$

The change in values of the matrix elements of the Coriolis operator in the test eigenbasis with respect to the reference values comes mainly from non-vanishing elements $\langle \Phi^0_k | \hat{C} | \Phi^0_l \rangle$, for which the zero-order basis states are energetically close. Remaining terms in the sum will contribute negligibly if the PES distortion is small. For this reason, let us focus on a particular matrix element which significantly contributes to the change in value of C_{ij}. Because the new wavefunctions $|\psi_i\rangle$ (test eigenfunctions) have slightly different expansion coefficients d_{jl} than in the reference eigenfucntions $|\psi^0_i\rangle$, one can think of it as if the basis for the test set of functions has been slightly changed (we incorporate the part of the value of the new expansion coefficient, $d_{ij} = d^0_{ij} + \delta d_{ij}$, into the new basis function). Thus we may write: $|\Phi_j\rangle := |\Phi^0_j\rangle + |\delta\Phi_j\rangle$. Working with variations in expansion coefficients or variations of the basis function is equivalent, but for more compact notation it was decided to vary the basis function. As a consequence, the chosen significant Coriolis interaction matrix element in the sum in eq. 3.15 is given as

$$\langle \Phi_k | \hat{C} | \Phi_l \rangle = \langle \Phi^0_k | \hat{C} | \Phi^0_l \rangle + \langle \delta\Phi_k | \hat{C} | \Phi^0_l \rangle + \langle \Phi^0_k | \hat{C} | \delta\Phi_l \rangle + \langle \delta\Phi_k | \hat{C} | \delta\Phi_l \rangle \tag{3.16}$$

The last term is of order of $(\delta\Phi^0_k)^2$ and can be neglected. The perturbed interaction matrix elements are represented as a sum of the original interaction matrix elements $\langle \Phi^0_k | \hat{C} | \Phi^0_l \rangle$ plus a correction term of type $\langle \delta\Phi_i | \hat{C} | \Phi^0_j \rangle$. The latter can be further written as follows:

$$\langle \delta\Phi^0_i | \hat{C} | \Phi^0_j \rangle = \frac{\langle \delta\Phi^0_i | [\hat{C}, \hat{H}^0_{rv}] | \Phi^0_j \rangle}{E^{0\prime}_i + (E^0_i - E^0_j)} \tag{3.17}$$

where $E^{0\prime}_i = E^0_i + \delta E_i$ and $E^0_i - E^0_j := \Delta E^0$. This correction term contributes to the change in value of the matrix elements of the Coriolis interaction operators. With a constant, known distortion in the PES ΔV, the change in the value of the energy

level is assumed to be known and small: δE_i. Then one may write

$$\delta E_i \langle \delta\Phi_i^0 | \hat{C} | \Phi_j^0 \rangle = \frac{\langle \delta\Phi_i^0 | [\hat{C}, \hat{H}_{rv}^0] | \Phi_j^0 \rangle}{1 + \frac{\Delta E^0}{\delta E_i}} \tag{3.18}$$

As soon as δE_i is non zero, the magnitude of the correction to the interaction matrix element depends on ΔE^0 as $\frac{const}{1+\frac{\Delta E^0}{\delta E_i}}$, hence for $\Delta E^0 = 0$ takes the maximal value.

To summarize, we have shown above that separation of zero-order non-interacting energy levels ΔE^0 determines the magnitude of the resonance-induced variation of the interaction matrix elements.

The present discussion over resonance interactions is primarily dedicated to application in estimating reliability of calculated transition intensities. Henceforth, the key question to answer is: how do resonance interactions of energy levels influence intensities of ro-vibrational transitions.

We are going to assume a typical (but not common) situation, when the upper energy level involved in a transition accidentally crosses near another energy level and ro-vibrational symmetries of these two levels are identical. Such situation is schematically depicted in Figure 3.9, where a weak transition from state $|G\rangle$ to $|W\rangle$ is accompanied by a strong transition from state $|G\rangle$ to $|S\rangle$. The energy levels associated with states $|W\rangle$ and $|S\rangle$ are nearly degenerate. Also, ro-vibrational symmetries of both states are identical (they have appropriate vibrational symmetries, equal J quantum numbers and the approximate quantum number k differing by 1 or 2). In such case, we are interested in the transition line strength:

$$T_{GW} = |S_{GW}|^2 = |\langle G | \hat{\mu}(Q) | W \rangle|^2 \tag{3.19}$$

where G and W labels ro-vibrational states between which the transition occurs. $\hat{\mu}(Q)$ is the transition dipole moment surface, which depends on nuclear coordinates denoted as Q.

Perturbation theory approach. Until now we have been operating on 'small' distortions of wavefunctions and surfaces in the configuration space. A more formal way to approach the problem of sensitivity of transition intensities is by the use of

perturbation theory. In the same way as the *Herzberg-Teller effect* [60] is responsible for intensity borrowing in vibronic transitions, the present formulation explains the intensity borrowing in terms of resonance interactions of ro-vibrational energy levels. Let us employ the interaction scheme from Figure 3.9. Assume that the $|W\rangle = |\phi^W_{vib}\rangle|\phi^W_{rot}\rangle$ state is perturbed by the $|S\rangle = |\phi^S_{vib}\rangle|\phi^S_{rot}\rangle$ state via an interaction described by operator $\hat{C}$. In the first-order perturbation theory the $|W\rangle$ state reads:

$$|\tilde{W}\rangle = |\tilde{\phi}^W_{vib}\rangle|\tilde{\phi}^W_{rot}\rangle = |\phi^W_{vib}\rangle|\phi^W_{rot}\rangle + \sum_I \frac{\langle\phi^W_{vib}|\langle\phi^W_{rot}|\hat{C}|\phi^I_{rot}\rangle|\phi^I_{vib}\rangle}{E^0_W - E^0_I}|\phi^I_{vib}\rangle|\phi^I_{rot}\rangle \quad (3.20)$$

If the symmetry of the $|S\rangle$ state is appropriate, that is $\Gamma^W_v \otimes \Gamma^W_r = \Gamma^S_v \otimes \Gamma^S_r$, then the matrix element $\langle\phi^W_{vib}|\langle\phi^W_{rot}|\hat{C}|\phi^S_{rot}\rangle|\phi^S_{vib}\rangle$ is non-vanishing. Contributions to the perturbed wavefunction from other energy levels can be small if $|S\rangle$ and $|W\rangle$ states are well isolated from other states (as in the case of 00011 and 11101 states in CO_2). Then the perturbed wavefunction can be inserted in an expression for the transition dipole moment:

$$\langle G|\hat{\mu}(Q)|\tilde{W}\rangle \quad (3.21)$$

where $|G\rangle$ represent the lower energy level (the ground state) in Figure 3.9. Expanding the bra-state in the above equation according to eq. 3.20 gives:

$$\langle G|\hat{\mu}(Q)|\tilde{W}\rangle = \langle G|\hat{\mu}(Q)|W\rangle + \frac{\langle W|\hat{C}|S\rangle}{E^0_W - E^0_S}\langle G|\hat{\mu}(Q)|S\rangle = S_{GW} + \lambda_{SW}S_{GS} \quad (3.22)$$

The magnitude of the admixture of the $|S\rangle$ state to the $|W\rangle$ state resulting in intensity borrowing by the $|W\rangle$ state depends on the value of the λ_{GW} parameter, which in turn depends on the energetic separation of the two energy levels. The intensity of the $S \leftarrow G$ transition is not significantly altered by interaction with the $|W\rangle$ state because the intensity carried by the $W \leftarrow G$ is low.

3.4.6 The concept of a scatter factor

The intensity borrowing effect quantified by eq. 3.22 gives an estimate for the strength of resonance interaction between respective ro-vibrational energy levels. This knowledge, in turn, can be utilized in quantifying how reliable are the calculated transition intensities. Transition intensities insensitive to small changes in the PES are considered reliable, because no resonance interaction affects the energy levels involved in a transition. Below, we introduce a descriptor which will serve as a measure of reliability of calculated transition intensities. Let PES1 be a reference PES for which the line strength for the $W \leftarrow G$ transition is given by S_{GW}. The second PES2 generates the ro-vibrational wavefunction $|\psi\rangle$, which is very similar to the wavefunction $|\psi^0\rangle$ calculated with the PES1 . This variation in the wavefunction causes the change in the line strength according to eq. 3.22. The ratio of intensities calculated with PES1 and PES2 and with identical DMS, which we will be calling *scatter factor*, is given by

$$\rho_{GW} = \frac{|S_{GW} + \lambda_{GW} S_{GS}|^2}{|S_{GW}|^2} \stackrel{\circ}{=} \left| 1 + \lambda_{SW} \frac{S_{GS}}{S_{GW}} \right|^2 \tag{3.23}$$

where the last equality holds only when the expression in the bracket is real (a special case of Schwartz inequality [184]). Eq. 3.23 provides a direct relation between the strength of the interaction of two energy levels λ_{SW} and the sensitivity of the transition intensity to the PES change. It is assumed that the change in the PES is small and controlled, meaning both surfaces are of similar quality, so that $\Delta PES(Q) = PES1(Q) - PES2(Q)$ is small for all Q's. The value of the scatter factor should rapidly grow for transitions involving energy levels affected by resonance interactions. Typically, the energetic condition for a resonance and the $\Delta J = 0$ selection rule lead to J-localized resonances. Such resonances occur when two energy levels, with the same ro-vibrational symmetry and the same J become energetically close. This observation cues into the idea of a method for detection of resonance interactions of energy levels with *ab initio* calculations. If one calculates the ratio of intensities for the same transition, but calculated with slightly different PESs, it

can be possible to elucidate information about the strength of interactions of energy levels involved in the transition with other energy level. This strategy has been applied for the CO_2 line lists, for all 13 isotopologues, in which each line has a scatter factor assigned.

MESM in a local domain? So far we have been considering the matrix elements sensitivity measure (MESM) in terms of global distortion of the PES ($\Delta PES(Q)$). It would be however interesting to explore the possibility of finding some correspondence between local features of the PES, which directly affect the accuracy of the calculated energy levels. Is it possible to relate specific regions of the PES, and quantify how a local disturbance in this PES affects the energy levels? It is rather intuitive that small localized perturbation to the PES in a high energy region, which corresponds to a large amplitude distortion of the molecule, will have little effect on some low lying energy levels. In this sense, it is interesting to find a geometrically defined region in the configuration space, which can significantly contribute to the accuracy of a calculated energy level. Finding such subspaces in the PES could potentially help in indicating which local parts of the PES need to be modelled very accurately in order to accurately reproduce energy levels involved in some type of the resonance interaction. Alternatively, one could try a more straightforward approach, based on fitting the PES to experimental energy levels, with higher weights imposed on energy levels affected by resonances. For this purpose, a MESM could be a good guide for the values of the weighting function. Analysis of this problem is dedicated for future study.

3.4.7 Coriolis interactions in the DVR3D formalism

DVR3D uses geometrically defined internal coordinates, in which the classic normal-mode interaction picture is concealed in the complicated form of the kinetic energy operator, given in eqs. (2.15, 2.16) in chapter 2. Nevertheless, by looking at the effective vibrational Hamiltonian in eq. (2.19) and eq. (2.20), one can find terms in the $\hat{K}_{rv}$ part which couple states with $\Delta k = \pm 1$ and $\Delta k = \pm 2$. These terms are responsible for Coriolis-type interactions in DVR3D. Note that variational approaches such as DVR3D, which use an exact kinetic energy operator, capture automatically

all ro-vibrational resonance interactions. Any problems with the accuracy of computed energy levels and wavefunctions near resonances can be attributed either to convergence issues or inaccuracies in the PES.

3.5 Sensitivity analysis

The dominant source of uncertainty in line intensities in the absence of resonance interactions is given by the *ab initio* DMS. For CO_2, the accuracy of the UCL DMS described in section 3.3.2 was considered in detail by Polyansky *et al.* [28] who suggested that for the vast majority of transitions below 8000 cm^{-1} it should give intensities accurate to better than 0.5 %. A characteristic of an *ab initio* DMS is that entire vibrational bands are reproduced with very similar accuracy. This is because to a significant extent ro-vibrational transitions in a molecule like CO_2 can be thought of as the product of a vibrational band intensity and a Hönl-London factor [60]. Although DVR3D does not explicitly use Hönl-London factors, the use of an effectively exact nuclear motion kinetic energy operator ensures that these rotational motion effects are accounted for exactly.

As shown in section 3.4, the nuclear motion wavefunctions give a secondary but, under certain circumstances, important contribution to the uncertainties. Variational nuclear motion programs yield very highly converged wavefunctions and in situations where the PES is precise the intensities show little sensitivity to the details of how they are calculated. For example, wavefunctions calculated using Radau coordinates give intensities very similar (to within 0.1 %) to those computed in the previous study [28] using Jacobi coordinates and different basis sets. As mentioned earlier, where the wavefunctions do play an important role is in capturing the interaction between different ro-vibrational states. Such resonance interactions can lead to intensity stealing and, particularly for so-called dark states, huge changes in transition intensities.

The idea of using the scatter factor, explained in section 3.4.6, was originally introduced by Lodi and Tennyson [56, 185] for water to capture accidental resonances which were not fully characterized by the underlying PES. Under these cir-

cumstances calculations with different procedures should give markedly different results. The procedure does not yield an uncertainty as such, it simply establishes which transition intensities are correctly characterized by the calculation and hence have an uncertainty reflecting the underlying DMS, and which are not, in which case the predictions were deemed as unreliable and alternative sources of intensity information was recommended.

In other words, trustworthy lines should be stable under minor PES/DMS modifications. One problem with this strategy is that if the alternate PES (or DMS) differs too much from the reference (best) PES then large intensity variations can be found which do not reflect problems with the best calculation, but rather inaccuracy of the lower quality PES. This issue already arose in a study on HDO [186] where the *ab initio* and fitted surfaces showed significant differences. For CO_2 the *ab initio* PES is relatively inaccurate and hence far from the high quality semi-empirical Ames-1 PES; it was for this reason a third PES was constructed, by performing a light-touch fit of the *ab initio* PES to $J = 0 - 2$ energy levels obtained with the Ames-1 PES (see section 3.3.2).

Here therefore the Lodi-Tennyson strategy [56] is followed, but we constructed and evaluated six line lists for the main isotopologue utilizing the three different PESs and two different DMSs introduced in section 3.3.2. For each of the other isotopologues of CO_2, after testing the main isotopologue, four line lists were created using only Ames-1 and Fitted PESs.

Practically, the procedure for finding the scatter factor is as follows: two sets of ro-vibrational wavefunctions are produced, with two different PESs (PES1 and PES2). For each set of ro-vibrational wavefunctions transition intensities are then calculated with two different DMSs (DMS1 and DMS2). This gives four line lists: (PES1,DMS1), (PES1,DMS2), (PES2,DMS1) and (PES2,DMS2). Schematically this is displayed in Figure 3.10. In the next step, transition lines are matched between the four line lists in a two-step algorithm. First, a straightforward match between lines calculated with the same PES is made. This generates two sets of line lists, which contain two transition intensities for each matched transition line. In the

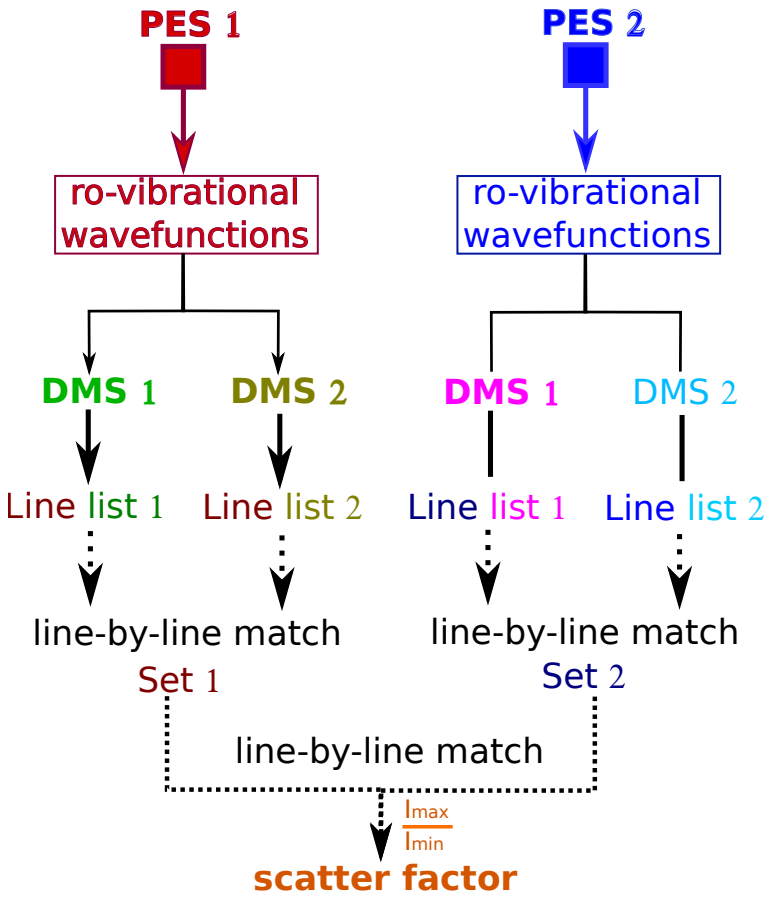

Figure 3.10: A general scheme for calculating the scatter factor ρ.

second stage, a match between the two sets of lines from stage 1 is made. The most efficient way of doing so is by prior matching of energy levels through available quantum numbers J and e/f as well as energetic proximity criteria. Usually not all lines between the two sets from stage one can be unambiguously matched. The percentage of matched lines strongly depends on the difference in quality of the two PESs. Having all 4 line lists matched line-by-line, for each 'matched' line, the ratio of strongest to weakest transition intensity is calculated, yielding a scatter factor ρ, as schematically depicted in Figure 3.11.

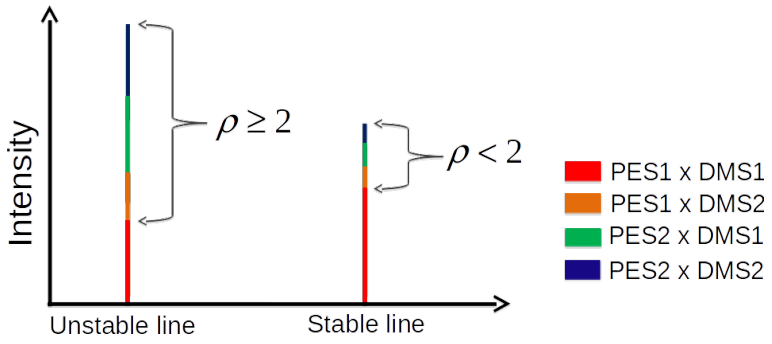

Figure 3.11: Schematic illustration of the concept of the scatter factor ρ. Two situations are given. Left: an unstable line; right: a stable line. Here, the critical value for the scatter factor, dividing stable lines from unstable lines, was chosen to be $\rho_{crit} = 2$.

The magnitude of the scatter factor, determined by the ratio of the strongest to the weakest transition intensity for a given line informs about the sensitivity of the this transition line to minor PES and DMS changes.

3.6 Summary of line lists

With details given in sections 3.3.1 and 3.3.2, a total of 54 room-temperature line lists for CO_2 were calculated using UCL's high-performance computing facility: Legion. For the main isotopologue ($^{16}O^{12}C^{16}O$,'626') six line lists were calculated and for each of the remaining 12 isotopologues four line lists were produced, in order to assign a scatter factor to each line. The reference (highest quality) line list for each isotopologue used Ames-1 PES and UCL DMS. Table 3.4 summarizes line lists [2] computed for all 13 isotopologues of CO_2. The total number of lines in the HITRAN2012 database is usually lower than in remaining line lists, which suggests several spectral gaps in HITRAN2012, especially for less abundant isotopologues. These gaps are all covered by the present calculations, which shows one of the advantages of *ab initio* calculations: complete spectral coverage. Also, there are several bands missing in the CDSD-296 database [187], which are present in the UCL line lists. The reason for missing bands in CDSD-296 is unavailability of experimental data for some spectral regions in the 0–8000 cm^{-1} range, and CDSD-

[2] Calculated line lists are available as supplementary materials to refs. [37–39].

296 heavily relies on empirical data to create its entries.

The procedure for matching lines between HITRAN2012 and present calculations was based on matching of energy levels, with rigorous restrictions on rotational quantum numbers and e/f parities as well as 0.3 cm^{-1} tolerance for energy difference. The next step was to match transition lines between HITRAN2012 and UCL line lists. The procedure relied on a simple algorithm, where corresponding lines were matched using already matched energy levels list. As a result nearly all lines for all isotopologues in the 0–8000 cm^{-1} region were mapped between the UCL line lists and HITRAN2012. The RMSD in line positions was in range 0.08–0.1 cm^{-1} for all isotopologues, which confirmed the claimed $<$0.1 cm^{-1} accuracy of the Ames-1 PES.

Table 3.4: Summary of 13 room temperature (T=296 K) line lists of carbon dioxide.

Isotopologue	626	636	646	727	737	828	838	628	627	637	638	728	738
ZPE[a] [cm^{-1}]	2535.92	2483.08	2436.75	2500.75	2447.50	2469.05	2415.39	2502.61	2518.35	2465.33	2449.38	2484.93	2431.48
J_{MAX}	129	119	130	99	50	101	50	118	112	99	102	99	84
SF(ortho:para)[b]	1:0	2:0	7:0	15:21	30:42	1:0	2:0	1	6	12	2	6	12
Q_{296}(This work)	286.095	576.652	2033.395	10 902.24	21 758.08	323.438	644.754	607.855	3536.724	7129.752	1223.560	3760.428	7583.400
Q_{296}(CDSD-296)[c]	286.098	576.652	N/A	10 971.90	22 129.96	323.418	652.234	607.828	3542.639	7141.561	1225.518	3766.689	7595.295
Q_{296}(Ames-296)[d]	286.094	576.644	2033.353	10 971.91	22 129.96	323.424	652.242	607.713	3542.610	7140.024	1225.270	3766.044	7593.900
Q_{296}(HITRAN)[e]	286.936	578.408	N/A	11 001.67	N/A	324.211	653.756	609.480	3552.678	7162.908	1229.084	3776.352	7615.248
Abundance [f]	0.9842	1.1057(-2)	1.0	1.3685(-7)	1.5375(-9)	3.9556(-6)	4.4440(-8)	3.9470(-3)	7.3399(-4)	8.2462(-6)	4.4345(-5)	1.4718(-6)	1.653(-8)
N(This work) [g]	162 010	68 635	41 610	6530	1501	10 441	2637	117 490	71 580	22 667	39 980	14 349	3573
N(CDSD-296) [g]	160 499	68 640	N/A	6530	1500	10 444	2635	113 122	70 692	23 815	39 979	15 140	3621
N(Ames-296) [g]	162 558	68 739	42 072	6545	1634	10 531	3050	117 744	71 639	22 704	40 034	14 529	3573
N(HITRAN2012)	160 292	68 856	N/A	5187	N/A	7070	121	114 023	71 182	2953	26 737	821	N/A
Matched[h]	160 289	68 856	N/A	5187	N/A	7069	121	110 292	71 016	2736	26 713	816	N/A

[a] Zero point energy computed with DVR3D with the Ames-1 PES; [b] Nuclear spin statistical weights [c] 2015 Edition of CDSD [187]; [d] [157]; [e] TIPS-2011 [188]; [f] HITRAN2012 abundances were taken from Ref. [157]; [g] For 10^{-27} cm/molecule intensity cut-off in 646 and 10^{-30} cm/molecule after scaling by the natural abundance for the other isotopologues; [h] present line lists with 10^{-33} cm/molecule intensity cut-off were used in the comparison.

The values of partition functions calculated with DVR3D and Ames-1 PES were compared to the partition functions supplied by the HITRAN2012, Ames-296 and CDSD-296 line lists. A systematic shift of 0.3 – 0.5% is observed for all isotopologues for partition functions between the present calculation and HITRAN2012. The latter values were calculated using TIPS method [188], which is inherently approximate, as based on the product approximation to the respective degrees of freedom. For this reason, the presently calculated partition functions should be considered as more accurate. As a result, the partition functions for isotopologues of CO_2 calculated with the Ames-1 PES have been included in the recent (2016) release of HITRAN [189].

Support for this decision comes from comparison of values of the partition functions from the CDSD-296 database, Ames-296 line lists and present calculations. All three approaches calculate partition functions explicitly from eq. 3.4. The presently computed partition functions are usually somewhat lower than their Ames-296 counterparts. This is because the former ones are computed using a smaller set of energy levels than in the original Ames-296 line lists. Therefore, for line intensity calculations the Ames-296 partition functions from Huang *et al.* [157] were used (those included in HITRAN2016). Figure 3.12 gives a general overview of the 296 K line list for the main CO_2 isotopologue in the 0 – 8000 cm^{-1} spectral region. The calculated transition intensities are compared to the HITRAN2012 database.

In order to relate results from the present study to data given by experiments and databases, it is necessary to choose a measure for intensity deviation between two data sets. As a primary measure of relative intensity deviation the following standard formula was used:

$$S = \left(\frac{I_{UCL}}{I_{EXP}} - 1 \right) \cdot 100\% \tag{3.24}$$

where I_{UCL} stands for line intensity from UCL line list given in cm/molecule and I_{EXP} is experimental intensity.

This measure is adequate for small deviations but poorly illustrates highly dis-

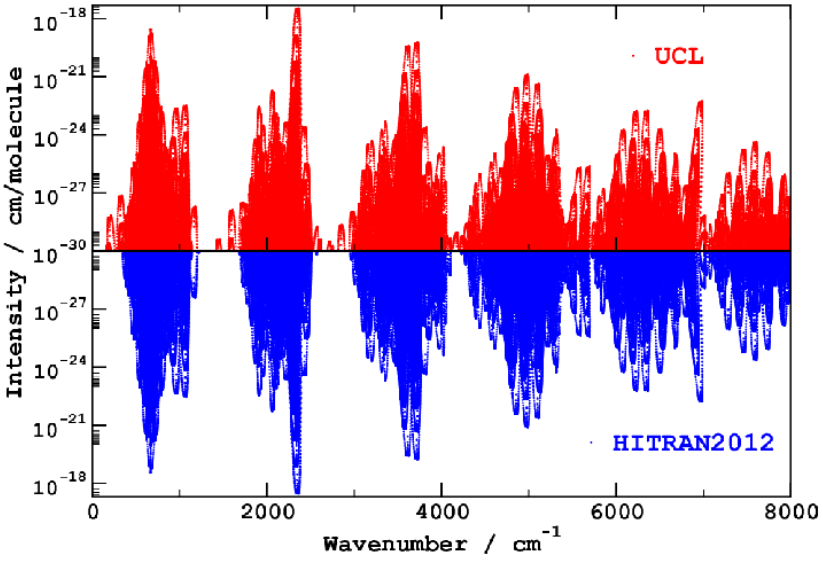

Figure 3.12: General comparison of the HITRAN2012 and UCL CO_2 296 K line lists for the 0 – 8000 cm^{-1} region for the main isotopologue.

crepant intensities, due to its asymmetric functional form. For larger deviation spans, for example to show graphically a general overview, it was decided to use a symmetrized measure:

$$S_{sym} = \frac{1}{2}\left(\frac{I_{UCL}}{I_{EXP}} - \frac{I_{EXP}}{I_{UCL}}\right) \cdot 100\% \tag{3.25}$$

This measure, in turn, yields far from intuitive numbers near 0% deviation. In comparisons, these two measures will be used interchangeably, depending on the span of intensity deviations.

3.7 Error analysis: a method for detecting resonances

This section presents details of the reliability analysis for line intensities for infrared spectra of 13 isotopologues of CO_2. Theoretical background for this analysis was given in sections 3.4 and 3.5.

3.7.1 Scatter factor statistics

For the main isotopologue of CO_2 six line lists were generated, which utilized the three different PESs and two different DMSs introduced in section 3.3.2. For this purpose three sets of nuclear-motion wavefunctions were produced: the first based on the Ames-1 semi-empirical PES, second based on the UCL *ab initio* PES and the third on the fitted PES. Those three sets of wavefunctions were combined with the two *ab initio* DMSs (UCL DMS and Ames DMS), to give line intensities. Having six line lists in hand, the next step was to match line-by-line pairs of respective line lists, as described in section 3.5: (Ames PES & Ames DMS, Ames PES & UCL-DMS)=(AA,AU), (UCL-*ab initio* & Ames DMS, UCL-*ab initio* & UCL-DMS)=(UA,UU), (fitted PES & Ames DMS, fitted PES & UCL-DMS)=(FA,FU). This first stage was straightforward, yielding almost 100% match as the line lists being compared differ only in DMS, which does not affect energy levels. The second stage involved matching the Ames-PES based with UCL-PESs based line lists, i.e. (AA,AU) vs. (UA,UU) and (AA,AU) vs. (FA,FU). In both cases line-by-line matching was preceded by matching of energy levels. In the case of Ames vs. UCL 90% of lines stronger than 10^{-30} cm/molecule were matched, while the Ames vs. Fitted resulted in high 99% matching percentage. This confirms that reducing the RMSD between Ames-1 based energy levels and *ab initio* UCL PES based energy levels from 6.2 cm^{-1} to Fitted PES based energy levels with RMSD = 1.4 cm^{-1} makes a significant difference. Note that since the (AU) line list provides the best estimates of the intensities, there is no benefit in performing a (UA,UU,FA,FU) scatter factor analysis.

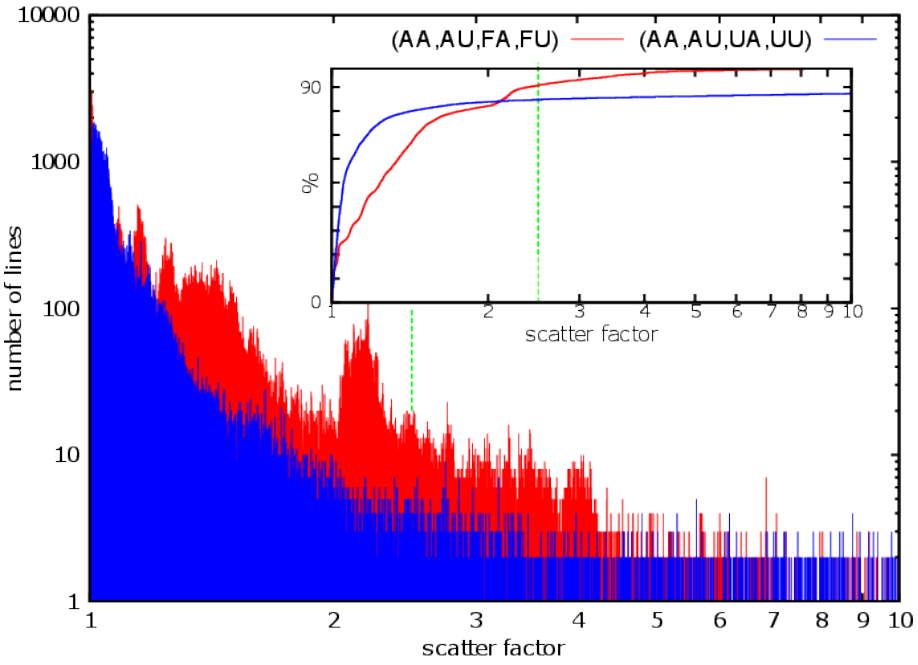

Figure 3.13: Scatter factor, ρ, statistics for two sets of PES-DMS combination ((AA,AU,FA,FU) and (AA,AU,UA,UU)) for the main isotopologue of CO_2. Inset: cumulative distribution function for ρ. See text for further details.

For each 'matched' line, the ratio of strongest to weakest transition intensity was calculated, yielding a scatter factor ρ. Figure 3.13 shows scatter factors statistics for the two sets of interest. Such statistics aims in supporting the choice of a critical value for the scatter factor. After carefully analysing Figure 3.13, there were two reasons for abandoning the *ab initio* UCL PES: a) incomplete match with Ames-1 based energy levels caused difficulties in assigning the scatter factor to transitions. We can clearly see that (AA,AU,UA,UU) set has a more uniform and compact distribution of ρ. However statistics for the *ab initio* UCL PES are based on 90% of total lines, which is visible in the cumulative distribution function for (AA,AU,UA,UU) in the inset of Figure 3.13; b) *ab initio* UCL PES as significantly lower quality than the Ames-1 PES. As a result the *ab initio* PES gave a number of false positive resonances, meaning that there were lines with large values of the scatter factor, and no real perturbation was present in this energetic region. These false positives were solely artifacts of the insufficient quality of the UCL *ab initio* PES.

With the choice of the (AA,AU,FA,FU) as a working set of lines, Figure 3.13 suggests $\rho = 2.5$ is a reasonable value for the critical value of the scatter factor. A more detailed analysis of individual bands, given below, suggests that this is indeed an appropriate value. The plateau of the cumulative distribution function for (AA,AU,FA,FU) is reached at $\rho \approx 4$, at which around 99% of all lines having a smaller value of the scatter factor. This potentially determines another critical value, separating 'intermediate' and 'unstable' lines.

Below, vibrational bands were classified by means of this descriptor, which serves as a measure of line stability. The line list (AU) was divided into three classes of lines: stable, intermediate and unstable; following established arbitrary limits on ρ for a line to be considered stable ($1.0 \leq \rho < 2.5$), intermediate ($2.5 \leq \rho < 4.0$) and unstable ($\rho \geq 4.0$). Similar analysis was repeated for each isotopologue of CO_2. Each transition in the primary line list (AU) received a scatter factor.

In Figure 3.14 the statistics for the scatter factor for all 13 isotopologues is presented.

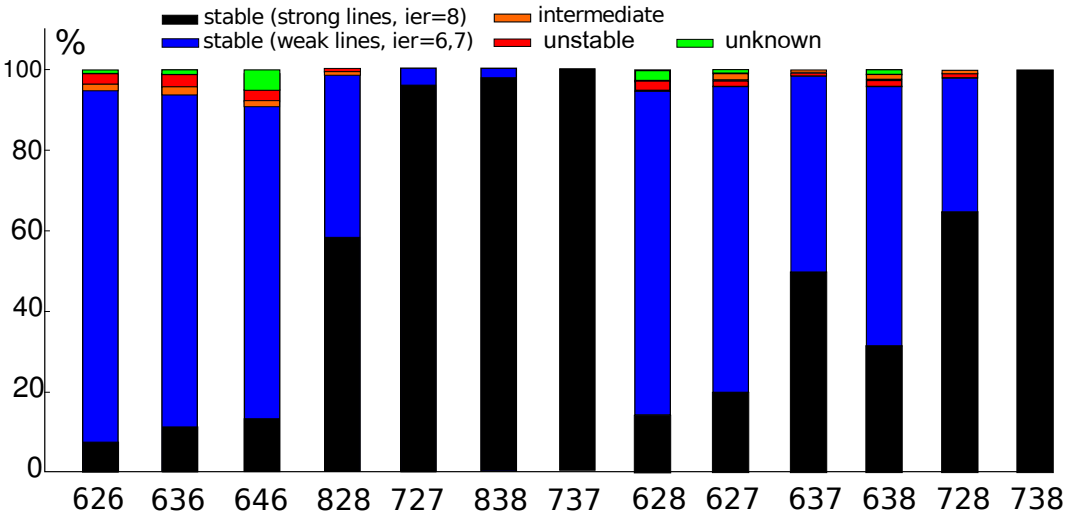

Figure 3.14: Scatter factor statistics for all 13 isotopologues of carbon dioxide. Respective colours denote percentages of lines classified to particular stability domain. The y axis corresponds to percentage of total lines present in UCL line lists. Black regions give percentage of stable and strong lines ($> 10^{-23}$ cm/molecule), for which the highest HITRAN intensity accuracy code was assigned ($ier = 8$, see www.hitran.org) meaning that the line intensity can be considered sub-percent accurate. The assignment of uncertainties in line intensities to AU line lists is discussed further below.

All transition intensities in CO_2 line lists were scaled by the their natural abundance and the 10^{-23} cm/molecule intensity cut-off dividing the 'strong' and 'weak lines was kept constant for all isotopologues. This resulted in much fewer lines included in line lists for the less abundant isotopologues, explaining why for example for the 737 and 738 isotopologues nearly all lines are stable. These lines correspond to the strongest lines in the 626 isotopologue, which are mostly stable.

In order to appreciate the landscape of scatter factor distributions, it is instructive to introduce scatter factor maps as a function of lower and upper energy level. Figure 3.15 shows a map where color codes represent values of the scatter factor for a given transition. The advantage of this particular representation is that one gains a full overview of all energetic regions, where transition intensities appear to be sensitive to minor inaccuracies of the PES. These lines are marked as red dots in Figure 3.15.

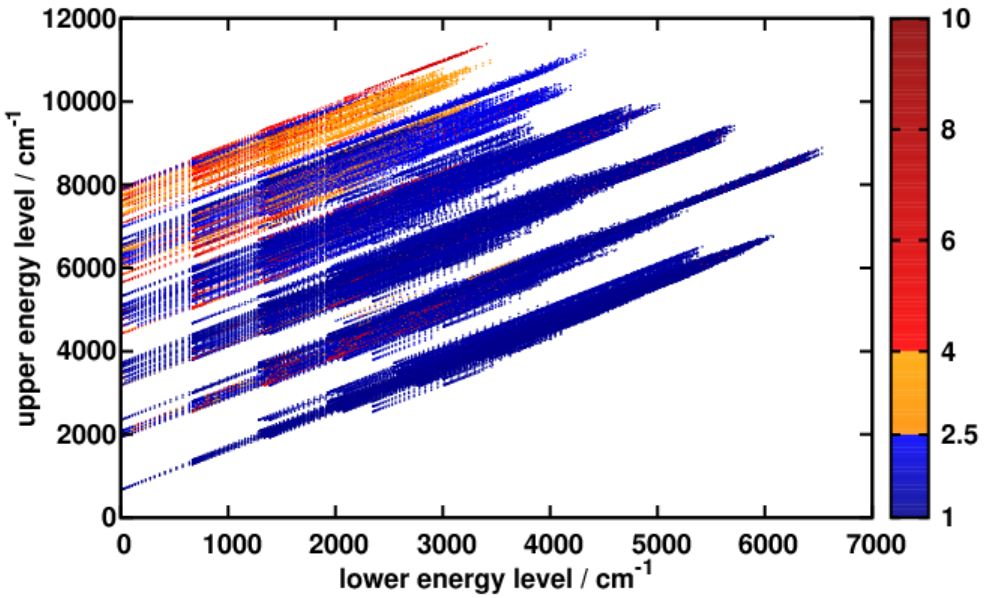

Figure 3.15: Scatter factor map for the main isotopologue (626) as a function of lower and upper energy level for transitions stronger than 10^{-30} cm/molecule. The color code represents the values of scatter factor, ρ. Three regions of line stability were determined: blue-stable, orange-intermediate and red-unstable. See text for further details

The fundamental bands are easily identified as straight lines originating at 0 cm^{-1} lower energy in Figure 3.15. The lowest hot bands originate at around 668 cm^{-1}, complicating the whole picture. A general conclusion from Figure 3.15 is that the higher energy of a level involved in a transition, the higher tendency for the transition to be unstable. The color coding in the figure divides scatter factor space into 3 regions of increasing instability, marked blue, orange and red, respectively. The blue region is considered to be stable and corresponding intensities are reliable. The orange region is intermediate between stable and unstable, hence transitions marked orange need careful consideration. The red region contains highly unstable lines whose computed line intensities should not be trusted. There are a few super-unstable transitions ($\rho > 10$) which are not shown on the plots; these lines are usually associated with a strong resonance interaction with some other energetically-close level. Analysis of scatter factors for individual bands can yield insight. By zooming in an energetic region of interest, as done in Figure 3.16, it is straightforward to pick up entirely unstable bands or single transitions which happen to fall into resonance.

Figure 3.16 illustrates the general trend of decreasing stability of lines with increasing energy of states involved in a transition. This has been already observed for the main 626 isotopologue in Figure 3.15. In general, the scatter factor pattern does not change significantly over different symmetric isotopologues, which means that resonance interactions are mostly common for all symmetric isotopologues. This is because changing nuclear masses in symmetric isotopologues of CO_2 shifts vibrational energy levels by a few wavenumbers, and resonance interactions of vibrational energy levels present for the main isotopologue persist for other isotopologues too. For asymmetric isotopologues, a qualitatively different situation with broken symmetry of identical nuclei leads to appearance of some new resonances and disappearance of others, which is captured by scatter factor maps displayed in Figure 3.17. Sporadic red points localized in small energetic areas are indicative of J-localized resonances, while long chains of unstable points suggest instability of whole bands. The latter effect can be associated with combination of

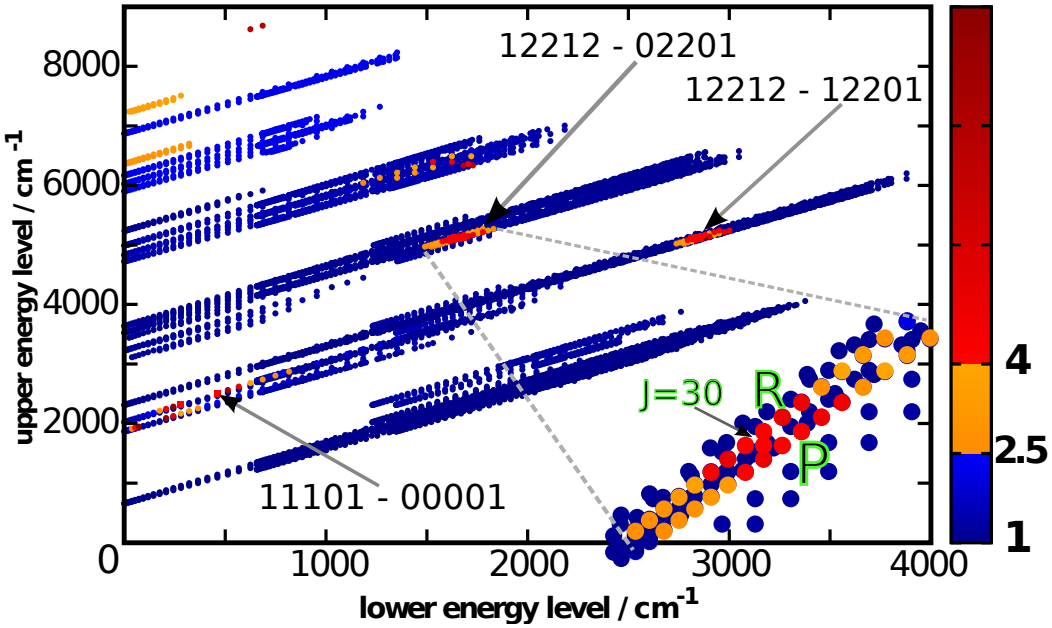

Figure 3.16: Scatter factor map for the 828 isotopologue. Colour coding denotes respective classification of lines: blue stands for stable lines, orange for intermediate lines and red for unstable lines. The arrows indicate selected bands for which a J-localized peak in the scatter factor is observed. The zoomed inset in right bottom corner shows the peak region of the scatter factor for the 12212 – 02201 band. Both P and R branches are affected by the interaction around $J = 30$.

Fermi-type resonance and limited accuracy of the Fitted PES, especially for higher energies.

It is instructive to give a more detailed insight into resonances by plotting scatter factor as a function of m quantum number for each band separately within a given polyad number change (ΔP). m is the rotationally-derived quantum number defined as equal to -J(lower energy level) for the P branch, J(lower energy level) for the Q branch, and J(lower energy level)+1 for the R branch, and J is the rotational quantum number. The polyad number for carbon dioxide is defined as $P = 2v_1 + v_2 + 3v_3$, where v_1, v_2, v_3 are the vibrational quantum numbers of symmetric stretching, bending and asymmetric stretching, respectively. Figure 3.18 displays scatter factor analysis of several bands with $\Delta P = 3$ in the 828 isotopologue.

For $\Delta P = 3$ three unstable bands were found: 23301 – 12202 , 11101 – 00001 and 11102 – 00001, as shown in Figure 3.18. The first of the three bands contain

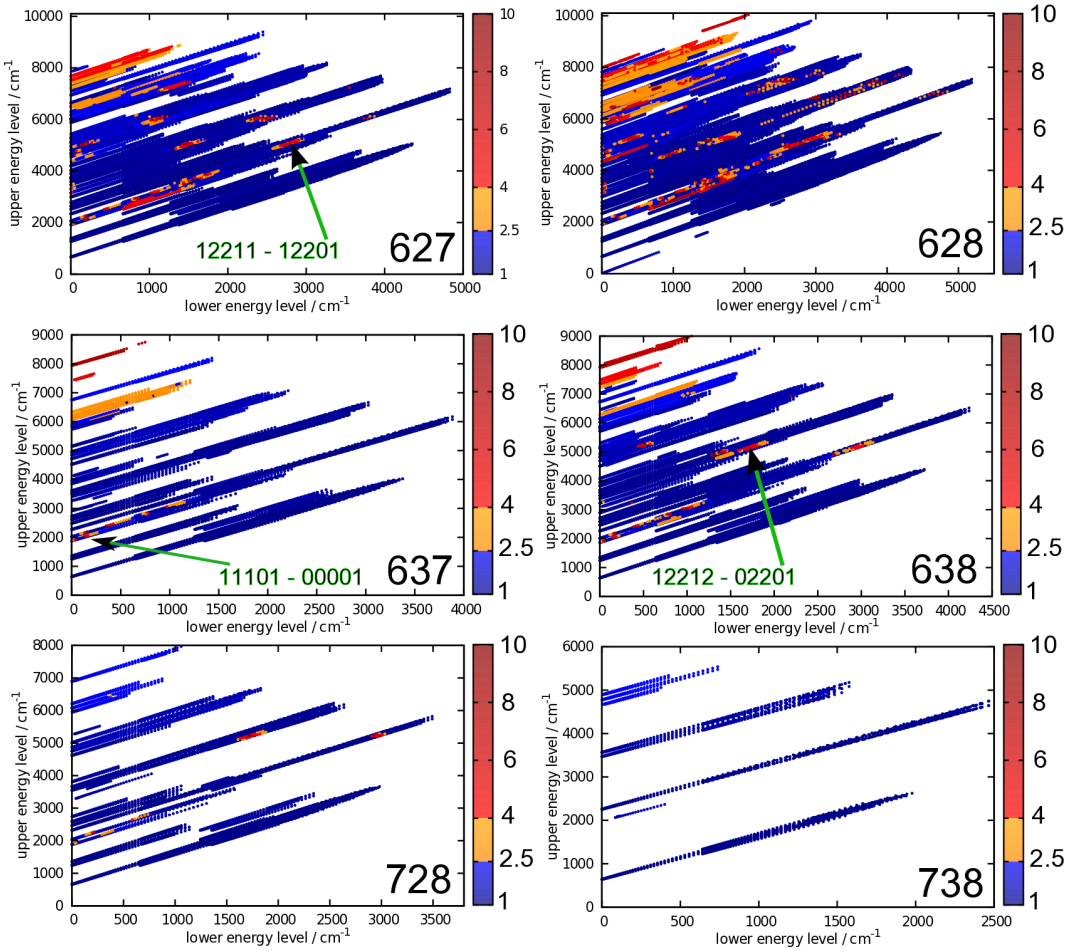

Figure 3.17: Scatter factor maps for all six asymmetric isotopologues of CO_2. Colour coding classifies transitions as: stable(blue), intermediate(orange) and red(unstable). The arrows indicate examples of bands involved in a resonance interactions.

transitions for which upper energy levels (localized around a particular J value) become energetically close to rotational states of some other vibrational state; in this case to levels from the 12212 state. This may lead to a strong resonance interaction between states. In the case of the last two bands, an intensity borrowing mechanism from the strong asymmetric stretching fundamental is responsible for the instability of line intensities around a particular J. For $\Delta P = 5$, both 12212 – 02201 and 23301 – 02201 bands are subject to a J-localized resonance, as also depicted further in Figure 3.22. This is due to mutual interaction of the upper levels of these bands, which are energetically close. For $\Delta P = 7$, the 22213 – 02201 band exhibits a weak J-localised peak in the scatter factor around $J = 34$. The 31101 – 00001 band is

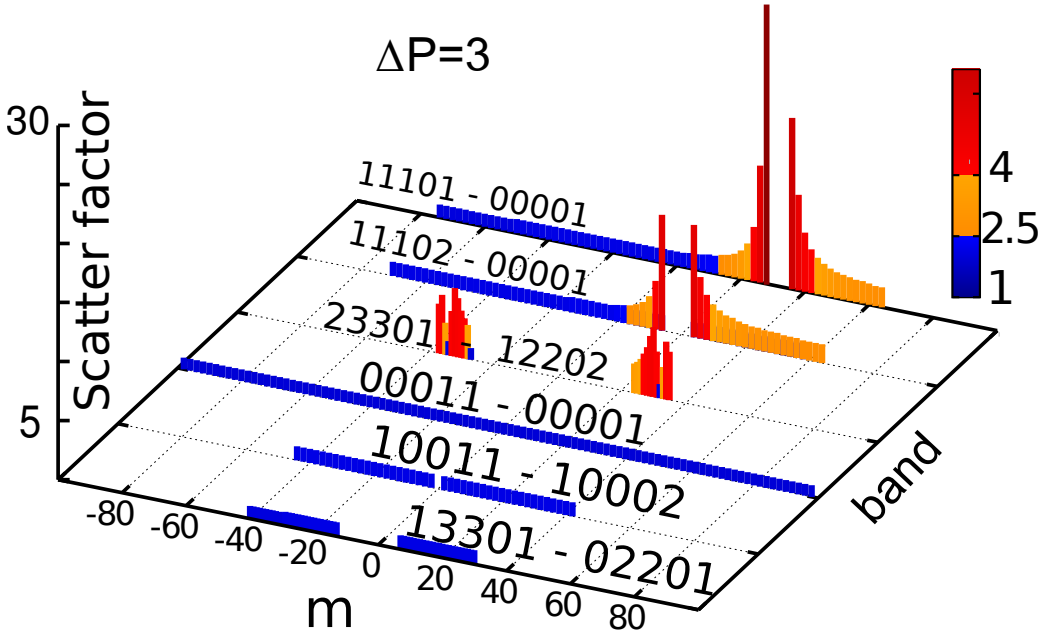

Figure 3.18: Scatter factor distribution for selected bands of 828 with polyad change $\Delta P = 3$. Colour code denotes classification of transition as stable (blue), orange (intermediate) or unstable (red), measured by the scatter factor.

weakly perturbed by interaction between the 31101 and 20012 states in the vicinity of $J = 68$. Bands with higher polyad change number ($\Delta P = 9, 11$) are in general less stable, following uniform distribution of the scatter factor. From the above analysis it follows that a more appropriate spectroscopic label, by means of which the absorption bands affected by resonance intensity borrowing are characterised, is the upper state polyad number P_{upper}.

Resonances occur when ro-vibrational energy levels of two or more states cross or nearly cross in the vicinity of a single J value. A prominent example of near crossing situation is the 11101 – 00001 band, which is perturbed by the 00011 state (intrapolyad interaction). Because the 00011 – 00001 fundamental is very strong and the perturbed band is relatively weak, significant intensity stealing is observed. This case is depicted in Figure 3.19, where relative intensity between HITRAN and UCL are drawn against the m quantum number. In Figure 3.19 colour coding quantifies the stability of the transition intensity. A J-localized resonance is visible around $m = +36$, clearly correlating with both high instability of lines (marked by

red points) and large deviations of UCL line intensities from HITRAN2012 line intensities. For this reason, UCL transition intensities near $m = 36$ are unreliable.

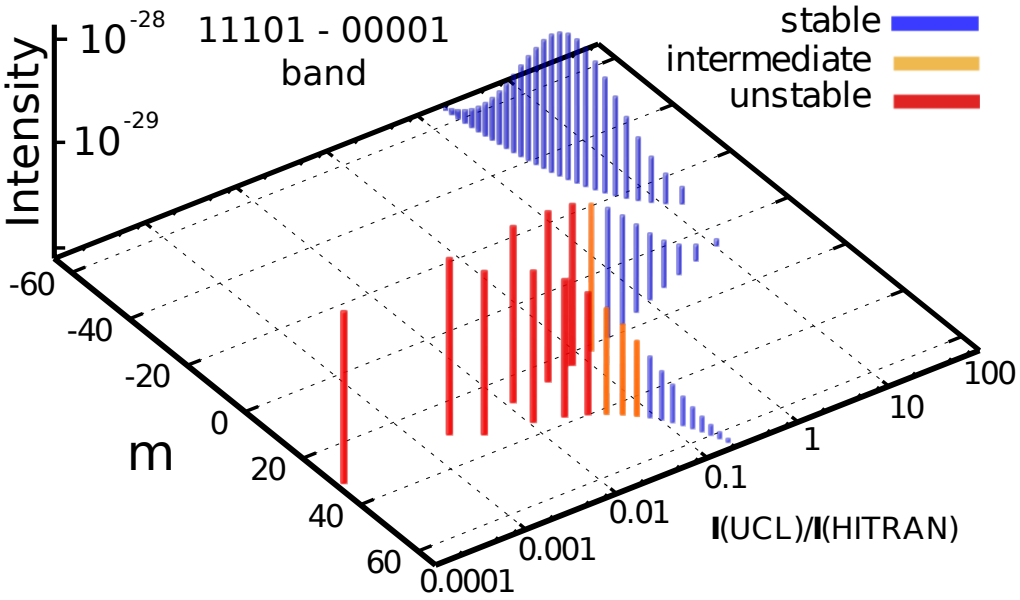

Figure 3.19: Relative intensities plotted against HITRAN2012 line intensities for the 11101–00001 band for the 828 isotopologue. This is an example of a band involved in resonant Coriolis interaction. Blue, orange and red points denote stable, intermediate and unstable lines, respectively.

This quasi-singularity in line intensity occurs due to the Coriolis interaction with the strong 00011–00001 band, which equally perturbs P and R branches of the 11101–00001 band, and manifests itself by intensity borrowing, which in turn leads to the strengthening of the P-branch and to suppression of the R-branch.

A view of the 636 isotopologue in Figure 3.20 supports the thesis that resonance interactions may affect only selected rotational branches. Here the scatter factor for the P,Q and R branches of the 11101 – 00001 band in 636 is plotted as a function of m. Only the R branch is affected by intensity borrowing. Similar picture emerges from Figure 3.21, where the scatter factor for P,Q and R branches of the 11102 – 00001 band in 626 is plotted as a function of the upper energy level; showing energetic localization of the resonance. Analogical behaviour is observed for resonance-affected bands in other CO_2 isotopologues.

Thus, to summarize this part, the scatter factor analysis is capable of detecting

resonance interactions of ro-vibrational energy levels, which are branch-specific and J-specific.

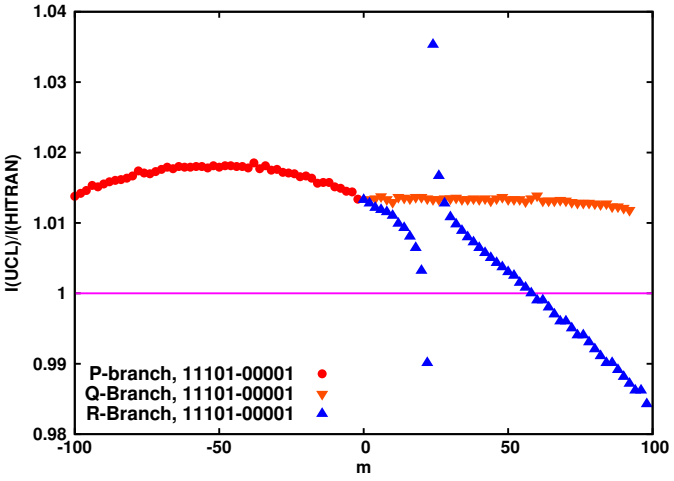

Figure 3.20: Relative intensities plotted against HITRAN2012 line intensities for 11101–00001 band for the 636 isotopologue. This is an example of a band involved in resonant Coriolis interaction.

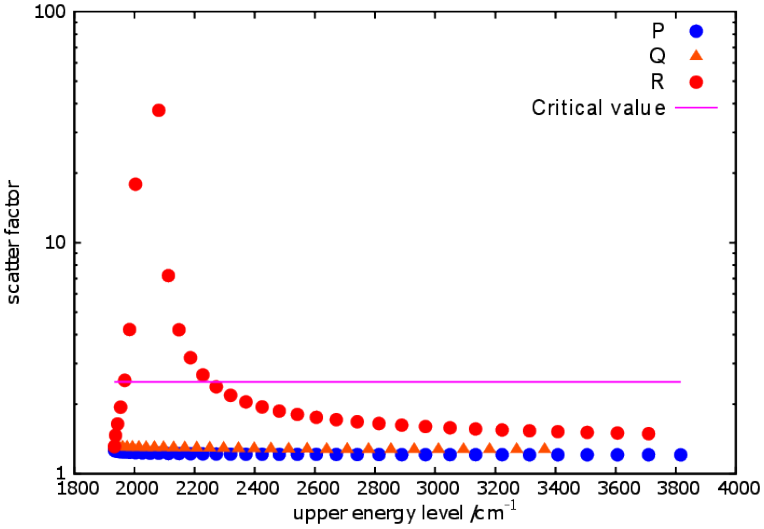

Figure 3.21: Scatter factor as a function of lower energy level for the 11102 – 00001 band in 626. The purple line denotes critical value of the scatter factor ($\rho = 2.5$). Different colouring was used for the P, Q and R branches.

Another interesting example, this time of the intrapolyad interaction, is the

pair: 23301 (perturber) and 12212 – 02201 (perturbed band), for which the intensities scheme is depicted in Figure 3.22.

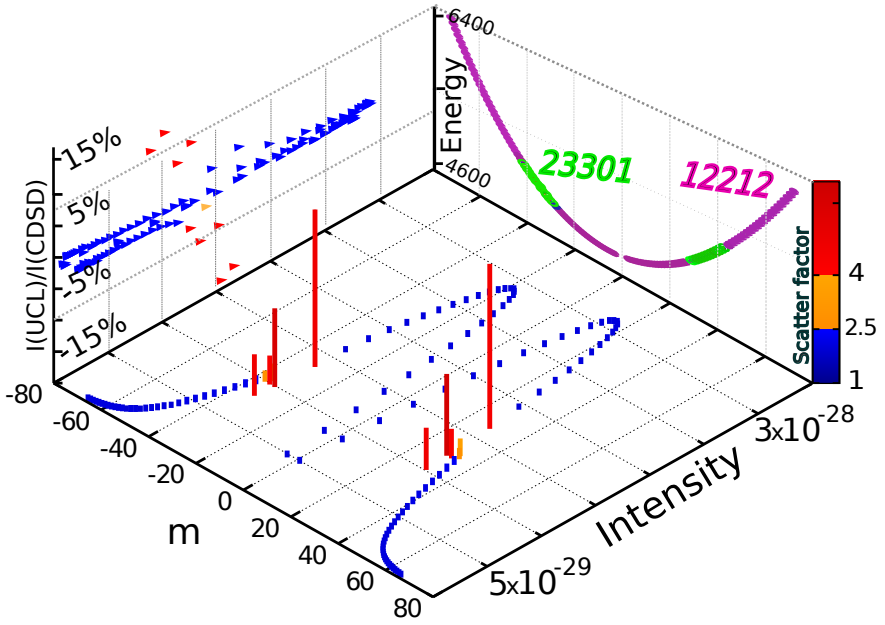

Figure 3.22: Multidimensional graph characterising the 12212 – 02201 band of $^{12}C^{18}O_2$. The base plane depicts m dependence of line intensities with bar height and color code measuring the value of the scatter factor. The far right plane represents m dependence of energy levels of the perturbed state (12212) and perturber (23301), which happen to nearly overlap around $m = \pm 36$. Left plane gives intensity ratios of lines taken from the present line list and CDSD-296 database [187].

Figure 3.22 shows perfect correlation between line stability measured by the scatter factor and agreement with CDSD-296 line intensities, where large discrepancies surround the region of elevated scatter factor (marked with red filled triangles in Figure 3.22). Very similar behaviour for line positions of the 12212 – 02201 band was noted by Borkov *et al.* for 727 [190], whose simple polynomial fit of the line positions resulted in a J-localised quasi-singularity in deviation of line positions.

One would expect that at least some of the large deviations in line intensities (see Figures 3.20 and 3.22) can be assigned to the influence of a resonance. Indeed, the correlation between high deviations in intensity and high scatter factor values is strikingly pronounced. Therefore we may consider the scatter factors used as a legitimate measure of reliability of a theoretical line list. Effective reproduction

of experimental line intensities for 'resonance bands' is a challenge for variational calculations. As the transition dipole moment is very sensitive to small inaccuracies of the ro-vibrational wavefunction, and requires almost perfect reproduction of the PES in this region, which is currently beyond reach of the variational methodology (electronic structure calculations). For the time being, the best that can be done is to identify these sensitive transitions and use other sources of transition intensities, such as the Effective Hamiltonian calculations, which have proven to be very successful for reproduction of resonance affected bands [162, 191]. However, the main drawback of the Effective Hamiltonians is a necessity of a very detailed semi-empirical parametrisation of these resonance affected bands, which requires a lot of experimental data. For this reason a list of bands, which may be perturbed by resonance interactions would be a helpful handout for both experimentalists and theorists working with CO_2. Below are listed selected strongest bands for different isotopologues of CO_2, for which the scatter factor analysis was performed individually. In Table 3.5 classification of bands of 626 is given as stable, stable with J-localized resonance, and as sensitive in the rightmost column.

Table 3.5: Characterization of selected CO_2 bands for the main 626 isotopologue. Given for each band are the band centre in cm^{-1}, the total band strength in cm/molecule, the total number of lines in the band, the number of stable lines with scatter factor $\rho < 2.5$, the number of intermediate lines with $2.5 \geq \rho < 4.0$, the median of the scatter factor distribution $\tilde{\rho}$, and the maximum and minimum value of ρ.

Band	Centre	Strength	Total	Stable	Inter.	$\tilde{\rho}$	ρ_{max}	ρ_{min}	Type
00011-00001	2349.949	9.20×10^{-17}	129	129	0	1.0	1.0	1.0	stable
01101-00001	668.159	7.97×10^{-18}	183	183	0	1.0	1.0	1.0	stable
01111-01101	2335.133	7.09×10^{-18}	341	341	0	1.0	1.0	1.0	stable
10011-00001	3715.622	1.53×10^{-18}	119	119	0	1.1	1.1	1.1	stable
10012-00001	3613.662	1.01×10^{-18}	119	119	0	1.1	1.1	1.1	stable
02201-01101	669.309	6.15×10^{-19}	340	340	0	1.0	1.0	1.0	stable
02211-02201	2321.865	2.71×10^{-19}	317	317	0	1.0	1.0	1.0	stable
10012-10002	2328.264	1.73×10^{-19}	115	115	0	1.0	1.0	1.0	stable
10001-01101	720.044	1.57×10^{-19}	169	169	0	1.0	1.0	1.0	stable
10002-01101	617.239	1.46×10^{-19}	169	169	0	1.0	1.0	1.0	stable
11111-01101	3721.742	1.21×10^{-19}	310	310	0	1.1	1.1	1.0	stable
10011-10001	2327.419	1.04×10^{-19}	113	113	0	1.0	1.0	1.0	stable
11112-01101	3578.816	7.58×10^{-20}	309	309	0	1.1	2.2	1.0	stable
03301-02201	670.458	3.54×10^{-20}	316	316	0	1.0	1.0	1.0	stable
20012-00001	4978.659	3.40×10^{-20}	110	110	0	1.4	1.5	1.3	stable
11102-10002	647.831	2.16×10^{-20}	162	162	0	1.0	1.0	1.0	stable
11112-11102	2313.744	1.47×10^{-20}	294	292	2	1.0	3.2	1.0	stable, J-local
11101-10001	689.438	1.36×10^{-20}	159	159	0	1.0	1.0	1.0	stable
20011-00001	5100.494	1.10×10^{-20}	107	107	0	1.4	1.5	1.3	stable
03311-03301	2308.597	1.03×10^{-20}	291	291	0	1.0	1.0	1.0	stable
11111-11101	2312.260	7.23×10^{-21}	290	290	0	1.0	1.0	1.0	stable
20013-00001	4854.447	7.13×10^{-21}	109	109	0	1.5	1.5	1.5	stable
11101-02201	740.173	6.14×10^{-21}	308	308	0	1.0	1.0	1.0	stable
11102-02201	595.761	5.33×10^{-21}	304	304	0	1.0	1.0	1.0	stable
11101-00001	2077.641	5.17×10^{-21}	107	97	3	1.9	1500	1.4	stable, J-local
12212-02201	3724.349	4.75×10^{-21}	284	284	0	1.1	1.1	1.1	stable
20012-10002	3693.261	3.69×10^{-21}	104	104	0	1.1	1.1	1.0	stable
20013-10002	3569.048	3.12×10^{-21}	104	104	0	1.1	1.1	1.0	stable
20011-10001	3712.291	2.96×10^{-21}	102	102	0	1.1	1.1	1.0	stable
04401-03301	671.607	1.80×10^{-21}	290	290	0	1.0	1.0	1.0	stable
12202-11102	654.112	1.57×10^{-21}	294	294	0	1.0	1.0	1.0	stable
00031-00001	6973.378	1.38×10^{-21}	101	101	0	2.1	2.2	2.0	stable
00011-10001	961.746	9.01×10^{-22}	99	99	0	1.2	1.2	1.2	stable
12201-11101	685.423	8.03×10^{-22}	291	291	0	1.0	1.0	1.0	stable
11102-00001	1933.229	6.19×10^{-22}	156	146	3	1.4	37	1.2	stable, J-local
30011-00001	6503.913	5.17×10^{-23}	24	0	24	2.6	2.6	2.6	sensitive
12201-01101	2094.904	5.01×10^{-22}	300	271	7	1.3	1200	1.1	stable, J-local
30013-00001	6228.740	4.54×10^{-22}	99	99	0	2.3	2.3	2.3	stable
30012-00001	6348.693	4.54×10^{-22}	99	99	0	2.2	2.3	2.1	stable
20001-11101	719.501	3.89×10^{-22}	146	146	0	1.0	1.0	1.0	stable
13311-13302	2490.039	9.13×10^{-24}	75	10	65	2.5	3.5	2.4	sensitive
40012-00001	7735.305	3.19×10^{-24}	24	0	24	2.6	2.6	2.6	sensitive
40011-00001	7921.693	2.10×10^{-25}	24	0	24	2.6	2.6	2.6	sensitive
23302-22201	481.776	9.92×10^{-26}	90	90	0	1.0	1.0	1.0	stable
30004-11102	1859.407	6.77×10^{-26}	24	0	24	2.6	2.6	2.6	stable, J-local

For the 626 isotopologue 108 out of 116 bands stronger than 10^{-25} cm/molecule are stable. Bands involving bending excitations are also very stable. For some bands, such as 32203–03301 and 42201–03301 J-localized instabilities appear only weakly, generating peaks in ρ which do not exceed the critical value. For other isotopologues the situation is qualitatively similar. Table 3.6 gathers information about vibrational bands perturbed by a resonance interaction with other vibrational state for the $^{16}O^{12}C^{18}O$ (628) isotopologue. Data on other isotopologues can be found in Table 3.9 and in UCL *ab initio* line lists published in refs. [37–39] also available as a part of the ExoMol database (www.exomol.com).

Table 3.6: List of selected $^{16}O^{12}C^{18}O$ vibrational bands perturbed by a resonance interaction. The columns give: vibrational quantum numbers of the perturbed band, vibrational assignment of the perturbing state, type of interaction: Inter-polyad or Coriolis, band centre, total band strength, the total number of lines in the band in UCL line list, the number of stable lines, the number of intermediate lines, median of the scatter factor in the band $\tilde{\rho}$, maximum scatter factor in the band ρ_{max}, minimum scatter factor in the band ρ_{min} and instability classification: J-localized(branch) or diffuse.

Vibrational band	Perturber	Type	Centre	Strength	Total	Stable	Inter.	$\tilde{\rho}$	ρ_{max}	ρ_{min}	Stability
11111 – 00001	31104	Inter-pol.	4346.974	3.88E-27	154	153	1	1.2	3.1	1.1	J-local
31112 – 01101	51105	Inter-pol.	6263.825	1.02E-25	332	312	4	2.2	422.5	2.2	J-local
11101 – 00001	00011	Coriolis	2050.068	1.69E-23	277	261	9	1.2	2124.0	1.1	J-local(R)
11102 – 00001	00011	Coriolis	1902.447	2.95E-24	266	251	9	1.2	2599.0	1.2	J-local(R)
12212 – 00001	23301	Coriolis	4838.085	1.52E-26	148	138	0	1.5	15.2	1.4	J-local
23301 – 00001	12212	Coriolis	4825.853	1.46E-27	61	24	15	1.1	8.0	1.1	sensitive
21112 – 01101	41105	Inter-pol.	4894.770	9.37E-24	448	422	2	1.5	7843.0	1.4	J-local
21102 – 00001	10012	Coriolis	3281.717	3.76E-25	239	138	0	1.2	115.2	1.2	sensitive
21111 – 01101	41104	Inter-pol.	5063.241	2.92E-24	410	363	0	1.4	3.1×10^5	1.4	sensitive
40014 – 00001	60007	Inter-pol.	7338.180	2.95E-26	134	0	123	3.6	3480.0	3.6	J-local
31113 – 01101	42202	Coriolis	6098.911	1.56E-25	345	326	0	2.3	7.6×10^5	2.2	sensitive
22212 – 22202	25501	Cor.+l-type	2262.766	3.07E-27	227	207	0	1.0	3444.0	1.0	J-local
30003 – 00001	14402	Anh.+l-type	3855.968	1.43E-24	162	158	0	1.2	1.1×10^7	1.2	J-local
30013 – 00001	50006	Inter-pol.	6127.111	2.24E-24	165	160	0	2.3	4.6×10^5	1.3	J-local
41113 – 01101	61106	Inter-pol.	7459.917	2.45E-27	199	5	8	4.1	114.2	1.7	sensitive
05521 – 00001	33314	Inter-pol.	7851.812	3.98E-29	14	0	0	102.2	1436.0	94.5	sensitive

3.8 The story of the 2 μm band

In this section, we are going to focus on one particular important vibrational absorption band in the main isotopologue of CO_2, which has been used to measure the quantity of this greenhouse gas in the Earth's atmosphere. It will be shown how the accuracy of experiments and theoretical calculations improved over the years and how a subtle interplay between theory and experiment can push the state of the art. Establishing new standards involves mutual validation of the most accurate theoretical calculations and measurements. On the example of a band located in the 2 μm absorption region in CO_2 we are going to show why *ab initio* results are an essential part in the validation of measurements and in re-assessment of true experimental uncertainties.

3.8.1 Why is the 2 μm band so important?

The quantity of carbon dioxide in Earths atmosphere, its role in climate change as well as possible sources, migration mechanisms and reservoirs of this gas have become a vividly discussed topic both in scientific and non-scientific circles over the past decades. A number of space missions have been launched in the past to search for answers to fundamental questions about CO_2, in particular where CO_2 is being produced (sources) and where it is going (sinks). This activity is clearly vital to monitoring and hopefully controlling CO_2 and hence climate change [114].

Orbiting Carbon Observatory-2 (OCO-2) satellite launched on 2 July 2014 and the Japanese Greenhouse Gases Observing Satellite (GOSAT) launched on 23 January 2009 are dedicated to accurately measure the column-averaged dry air molar fraction of CO_2 in the Earth's atmosphere. Specifically, the OCO-2 mission aims to provide maps of CO_2 in a high, few km^2, spatial resolution to pinpoint variations of CO_2 concentration at the 1 part per-million (ppm) level. Such remote sensing measurement must be supported with an appropriate spectroscopic model for successful retrieval of concentrations from measured absorption intensities. The measurements essentially utilize the Lambert-Beer law: $\frac{I}{I_0} = e^{-\sigma(\tilde{\nu})\cdot N\cdot L}$, in which the intensity of the absorbed radiation I and the reference radiation intensity I_0 are directly measure in the on-board instrument. The path length L is accurately estimated from

the distance the light must cross between the Earth's surface and the detector in the satellite. For calculation of N - the concentration of CO_2 the absorption cross section $\sigma(\tilde{\nu})$ is required. Absorption cross section depends on the wavenumber $\tilde{\nu}$ and is related to the integral line intensity by the relation: $\sigma(\tilde{\nu}) = \int I(\tilde{\nu}' - \tilde{\nu}) f(\tilde{\nu}') d\tilde{\nu}'$. Absorption cross sections can be obtained either from laboratory experiments or theoretical calculations. The latter require calculation of integral line intensities and line shapes. The 1 ppm variation of the CO_2 concentration N near the present global atmospheric CO_2 level ($\approx$ 400 ppm), corresponds to 0.3% relative variation in integral transition intensity. Thus ideally, reference transition intensities provided by experiment or theory should be 0.3% accurate [16].

At the start of the present work, the best experimentally derived models for transition intensities and line shapes were capable of providing 1%–3% accuracy, which translates into certainty of CO_2 concentration from the satellite measurements of 1.5 – 3.5 ppm over land and 1.5–2.5 ppm over ocean [17]. In OCO-2 instruments, the determination of CO_2's concentration is based on measurements of the absorption of the sunlight reflected from the Earth's surface in the 1.61 μm and 2.06 μm spectral regions.

These two CO_2 absorption regions are called the 'weak' and the 'strong' CO_2 absorption bands, respectively. The reason for the choice of these particular spectral regions is their relatively high absorption intensity and little spectral congestion from other CO_2 bands and lines from other molecules. For a number of years, there have been attempts to raise the sensitivity of experimental apparatus to achieve the goal of 0.3% accuracy in intensity measurements. The HITRAN database is specifically dedicated for this type of purposes, and since its early days, a particular effort has been put to accurately model the 'weak' and the 'strong' CO_2 bands. Several independent groups, both theoretical and experimental, competed to provide the most accurate line intensities for the 1.61 μm and 2.06 μm CO_2 bands.

Below are listed selected studies from the past years, which were considered the-state-of-the-art at their publication times. The earliest very high precision and accuracy experiments were reported by Castrillo *et al.* in 2003 [192], followed by

Casa *et al.* [193] in 2007 and in 2009 [194] from the same group. NASA's JPL (Toth *et al.* [195]) performed their independent measurements in 2008 dedicated to the OCO mission (which failed at launch in 2009). Soon after, Wuebbeler *et al.* [29] reported a high accuracy measurement of a single line in the 20012 – 00001 band (which is the main band located near 2 μm). In 2014 a highly accurate theoretical line list from NASA Ames research center (Huang *et al.* [149, 157, 161]) was published. In the following year the UCL DMS was constructed by Polyansky *et al.* [28, 37] and measurements by Bielska *et al.* [28] confirmed the quality of UCL DMS, which was later used in calculation of the UCL line list for the main CO_2 isotopologue [37], released in late 2015. A few months later, NASA's collaborative experimental study by Benner *et al.* [128] and Devi *et al.* [31] reported measurements of the 1.61 μm and 2.06 μm CO_2 bands, specifically dedicated for the OCO-2 data retrieval process. Finally, very recently (2016/2017), three independent experiments, with newly developed ultra-high accuracy spectroscopic techniques, were performed by Hodges *et al.* from NIST (USA) [30, 196], Brunzendorf *et al.* [33] from PTB in Berlin (Germany) and Odintsova *et al.* [32] from Napoli (Italy). Given below is a short story, a summary of the debate over the 1% discrepancy between theory and some experiments for the 'weak' and the 'strong' CO_2 bands. In the end, this debate helped to establish new standards in high-resolution molecular spectroscopy, especially in the interplay between computation and measurements of line intensities.

3.8.2 Issues with HITRAN 2012

Figure 3.23 presents a general comparison of the 20012 – 00001 band intensities for the main isotopologue of CO_2 between the present calculation (named ExoMol) and the HITRAN 2012 database [176]. In Figure 3.23 the atmospherically relevant band is the strongest band located in the 4800–4900 cm^{-1} spectral region and consists of P and R branches, as expected from parallel bands. Visually, the agreement between the present calculations and the HITRAN 2012 database is excellent. For this reason, a more accurate representation for intensities is here suitable.

Accordingly, Figure 3.24 gives an intensity comparison between the present

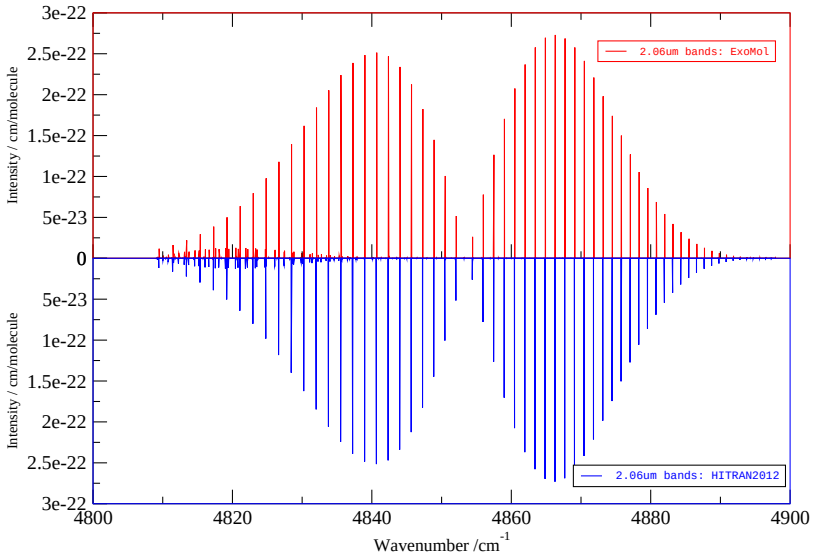

Figure 3.23: General comparison of the 20012 – 00001 band in the main isotopologue of CO_2 between the present calculation (named ExoMol) and the HITRAN 2012 database [176].

line list and the HITRAN 2012 database for the 20012 – 00001 CO_2 band. HITRAN 2012 used two separate data sources for this band: NASA JPL (Toth *et al.* [195]) and an unpublished version of CDSD-296 database [170]. The point of source switch is clearly visible near $J = 64$, where a jump in relative deviation from the present calculations is observed. This is the point where the experimental data ended and the database had to rely on results from semi-empirical effective Hamiltonian calculations included later in the CDSD-296 database. A nearly 4% discontinuity in the intensity pattern indicates serious inconsistency between the two sources used in the HITRAN 2012 database. In addition to that, an arc-like structure is observed in the relative deviation pattern for the Toth's *et al.* measurement. This was an unusual feature, which required explanation, because both Toth *et al.* and the present calculation claimed near 1% accuracy. One of these claims must have been too optimistic. In such form, transition intensities provided by HITRAN 2012 could not be reliably used in atmospheric CO_2 concentration retrieval models. Further insight

into origins of arc-like structures observed in HITRAN2012 intensity patterns are given in the following subsections. It is there shown that such features are a common artifact of a certain type of spectroscopic retrieval procedure, which relies on Herman-Wallis factors.

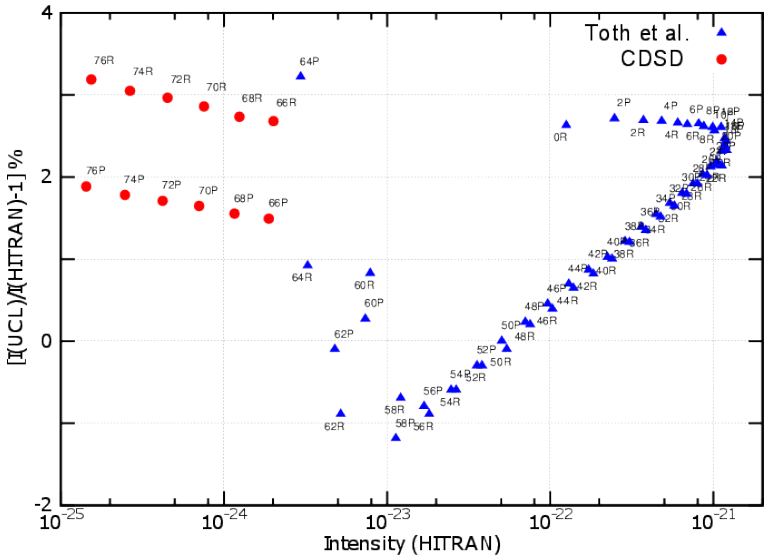

Figure 3.24: HITRAN 2012 vs. UCL line intensities comparison for the 20012 – 00001 band in the main isotopologue of CO_2. Two HITRAN data sources are marked with red (CDSD-296: semi-empirical calculations [170]) and blue (Toth *et al.* - experimental [195]) circles.

3.8.3 2000's, first 'sub-percent' measurements

High accuracy measurements of transition intensities for the 2 μm band began in early 2000's. In Figure 3.25, where several accurate intensity measurements are compared to the present calculations for the 20012 – 00001 band in the main isotopologue of CO_2, there are two panels: the upper panel displays situation before year 2015, and the lower panel gives an update with three independent experiments reported very recently (since 2015). For lines R(2) to R(18), there have been two consecutive measurements performed by the same group (denoted UniNa2), as illustrated with red and black diamonds in the upper panel of Figure 3.25. The uncertainties of both measurements were claimed to be an unprecedented 0.2% level, indicated by the errorbars. However, not only does these data not pass a self-consistency test, showing discrepancies in intensities for two respective mea-

surements of the same lines, but also does not agree with the UCL's theoretical calculations (1% –3% disagreement). The internal discrepancy between the two UniNa2 experiments was more than 1%, which suggested the need for revision of the claimed 0.2% accuracy of Casa *et al.* 's measurements. In 2011 another tentative indication of problems with the UniNa2 data came from Wuebbeler *et al.* [29], who reported very accurate measurement of intensity of a single R(12) line, which agreed with UCL line list within 0.1%. In the meantime the HITRAN 2012 database has been issued and NASA Ames Research Center published a theoretical line list with high quality transition intensities. Both data sets are compared to the present calculations in Figure 3.25. The JPL data (Toth *et al.*) used in HITRAN 2012, as shown in the previous section, exhibits an arc-like structure, which corresponds to $\approx 2.5\%$ deviation from the present calculations. Despite the systematic deviation and the arc structure, these JPL data, which was included in the HITRAN 2012 database, exhibits a very low statistical noise, which suggests high precision of the measurement. The Ames-1 intensities [149, 157, 161] do not have such arc pattern, which is suggested, that the arc-like structures are artifacts of the experimental retrieval procedure. Although Ames-1 transition intensities agree to 0.5% –1% with the present calculations, they feature a non-physical jump in intensity at $J = 0$, that is between P and R branches. This discontinuity is probably caused by problems with the nuclear motion program used by the authors and features in several bands. For sub-percent accuracy, this discontinuity issue must be resolved. Before 2015, the problem of reliable estimation of true accuracy both for theoretical intensity calculations and UniNA2 experiments remained unresolved.

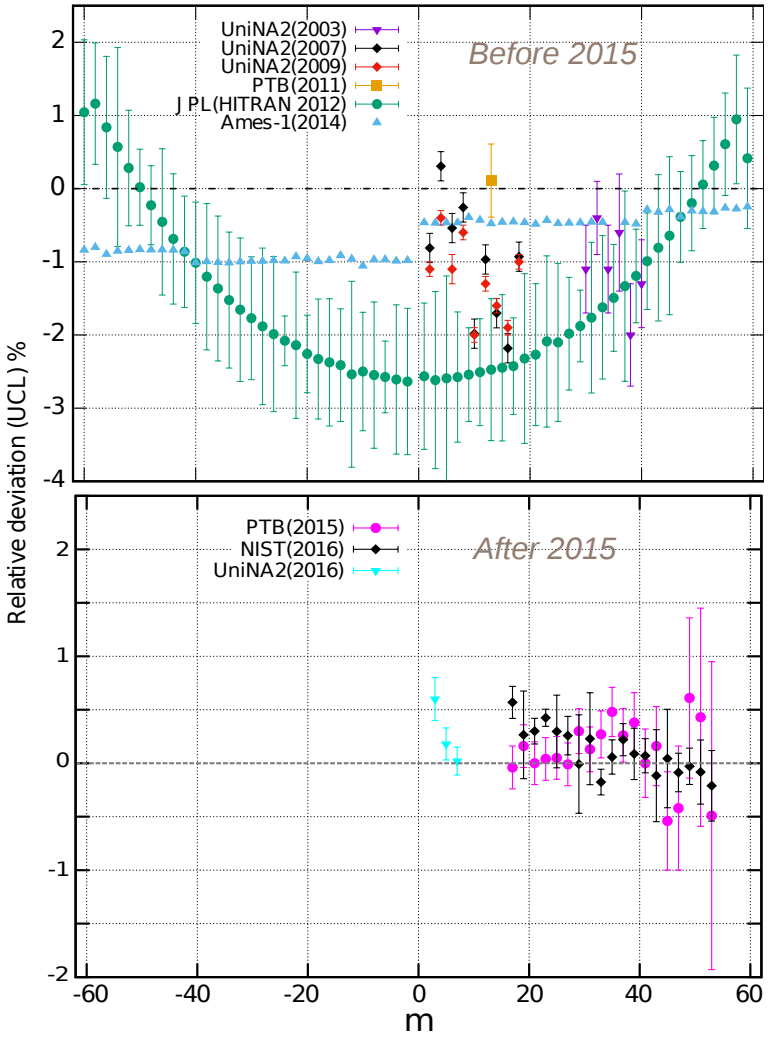

Figure 3.25: Comparison of line intensities between the present study, HITRAN 2012 and other accurate experimental and theoretical sources for the 20012 – 00001 band of $^{12}C^{16}O_2$. Zero relative deviation line corresponds to UCL line intensities. m is defined as equal to -*J*(lower energy level) for the P branch, *J*(lower energy level) for the Q branch, and *J*(lower energy level)+1 for the R branch. Respective data sources were used in the comparison: UniNA2 2003 (Castrillo *et al.* [192]), UniNA2 2007 (Casa *et al.* [193]), UniNA2 2009 (Casa *et al.* [194]), JPL - HITRAN 2012 (Toth *et al.* [195]), PTB 2011 (Wuebbeler *et al.* [29]), Present study 2016 (Zak *et al.* [37]), Ames-1 2014 (Huang *et al.* [149, 157, 161]), PTB 2015 (Brunzendorf *et al.* [33]), UniNA2 2016 (Odintsova *et al.* [32]), NIST 2016 (Hodges *et al.* [30]).

3.8.4 A debate over the 1% - NIST comes to rescue

A definitive conclusion to the debate over whose data is the most accurate has been supplied by recent measurements done independently in the National Institute

of Standards and Technology (NIST) [30], Physikalisch-Technische Bundesanstalt (PTB) in Berlin [33] and Second University of Naples (UniNa2) [32]. The lower panel in Figure 3.25 displays intensity comparison between UCL and very recent high accuracy measurements of the 20012 – 00001 band in CO_2: PTB 2015 (Brunzendorf *et al.* [33]), UniNA2 2016 (Odintsova *et al.* [32]) and NIST 2016 (Hodges *et al.* [30]). Excellent agreement is visible between UCL predictions and PTB and NIST measurements (0.2% – 0.5 %). The 0.1% – 0.2% consistency of measured intensities between NIST and PTB provides also a definitive proof of reliability for the UCL's *ab initio* results. Further support for this statement was delivered with UniNA2's 2016 measurements of three lines in the 20012 – 00001 band (R(2),R(4) and R(6)). The discrepancy between the experiment and UCL calculation was again 0.3%. Further validation for a wider J range would be valuable, but not necessary, because the theoretical procedure used to calculate UCL line lists gives fundamentally uniform accuracy of intensities for the whole vibrational band, i.e. is almost independent of J value. Similar quality of transition intensities was anticipated for several other strong absroption bands in isotopologues of CO_2. Indeed, further confirmations for sub-percent accuracy of UCL *ab initio* computed intensities came from comparisons to new measurements for 20013 – 00001 and 30013 – 00001 bands in the main isotopologue.

Figure 3.26 gives a comparison between UCL intensities for the 30013 – 00001 band, HITRAN 2012 database, Ames-1 line list [149, 157, 161] and measurements by Devi *et al.* [128] and Hodges *et al.* (NIST) [30]. For some time after publication of results by Devi *et al.* there was an ongoing debate about the accuracy of the UCL calculations, due to 1% difference with respect to Devi's measurements (see red filled circles in Figure 3.26). One particular concern about this experiment were the high $|m|$ intensity tails in the 30013 – 00001 band, which appear to be systematically and consistently overestimated in experiment, as can be seen in Figure 3.26. In the Figure, the UCL, Ames-1 and HITRAN 2012 transition intensities deviate from the measurement in the same direction of negative relative deviations. In addition, again, HITRAN 2012 had some problems with discontinuities due to multiple data

sources and Ames-1 showed an intensity jump at the joint of the P and R branches. Nevertheless, the 1% systematic shift between UCL and experimental intensities visible for low $|m|$ values required reconciliation.

Again, a definitive conclusion to the debate over whose data is the most accurate has been supplied by measurements done in the National Institute of Standards and Technology (NIST) [28]. Points marked with black crosses in Figure 3.26 are on average 0.5% stronger than the UCL calculated values, but the systematic shift is in opposite direction from measurements by Devi *et al.* . Because of the low 0.3% uncertainty of the NIST measurements, it was highly probable that Devi's measurements were less accurate than claimed by the authors. Indeed, later re-analysis of raw experimental data and an appropriate refit of the optical path length as well as correction of the model by fitting of the J-dependence to our data eliminated the 1% discrepancy between UCL and Devi's transition intensities [27, 197]. Not surprisingly, the the arc-like intensity patterns in integral intensities from experiment vanished after the refit [27, 197].

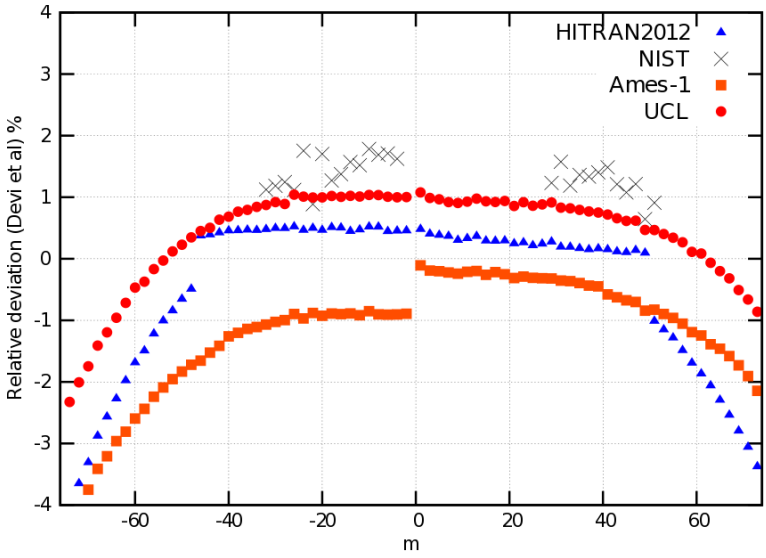

Figure 3.26: Comparison of line intensities of the 30013 – 00001 band of $^{12}C^{16}O_2$ between the present study, HITRAN 2012, Ames-1 line list [149, 157, 161] and measurements by Devi *et al.* [128] and Hodges *et al.* (NIST) [30].

3.8.5 Herman-Wallis factors

In this subsection, a brief explanation of the concept of Herman-Wallis factors is given, with the aim to demystify the arc-like structures appearing in intensity patterns of experiments described in the previous subsection.

In the majority of high accuracy transition intensity measurements the integral ro-vibrational line intensities are fitted to the following expression [31, 128]:

$$I(\tilde{\nu}_{if}) = \frac{S_v \tilde{\nu}_{if} L_i F}{\tilde{\nu}_0 Q(T)} \exp\left(\frac{-E_i}{k_b T}\right)\left[1 - \exp\left(-\frac{\tilde{\nu}_{if}}{k_b T}\right)\right] \tag{3.26}$$

where S_v is the vibrational band strength, $\tilde{\nu}_{if}$ is the transition wavenumber, $\tilde{\nu}_0$ is the band centre, L_i is the Hönl-London factor [60] and F is the Herman-Wallis factor [198], often represented in the following general form:

$$F = \left(1 + a_1 m + a_2 m^2 + a_3 m^3 + a_4 m^4 J(J+1)\right)^2 \tag{3.27}$$

where a_1, a_2, a_3, a_4 are experimentally fitted parameters. Other quantities appear as in eq. 3.3.

The type of expression in eq. 3.26 assumes separation of contributions to transition intensity from rotations (Hönl-London factor L_i) and vibrations (vibrational band strength S_v) corrected with a term called the Herman-Wallis (H-W) factor [198]. This term, originally derived from perturbation theory accounts for contribution to transition intensity from the rotation-vibration interaction. Because eq. 3.26 is a phenomenological one, it is vulnerable to inadequate choices of the functional form of the H-W factor. If this functional form is not flexible enough, it can result in overestimating or underestimating of transition intensities with high J values, making high J extrapolation difficult. This is a consequence of the polynomial form of the H-W factor, which may grow uncontrollably for large $|m|$ values. It is therefore sometimes a difficult task to supply an accurate fit in a wide J range within a single H-W model. An example of inaccuracies in retrieved transition intensities is given in Figure 3.27, where experimental line intensities with large positive m values deviate from UCL *ab initio* results. The *ab initio* expression for

integral line intensity does not require any assumption on the form of the contribution from rotation-vibration interaction. Thus, first principles derived theoretical line intensities can serve as reliability guards capable of capturing defects in experimental retrieval models for high J quantum numbers.

Although H-W factors have been widely used in many data reduction procedures, they are likely to malfunction when sub-percent accuracy is required. Until recently the $\pm 10\%$ margin of error associated with experimental accuracy did not uncover the possible issues with H-W factors. For this reason it is recommended to cross-compare experimentally reduced transition intensities against *ab initio* calculations, which account for the rotation-vibration interaction exactly, such as DVR3D.

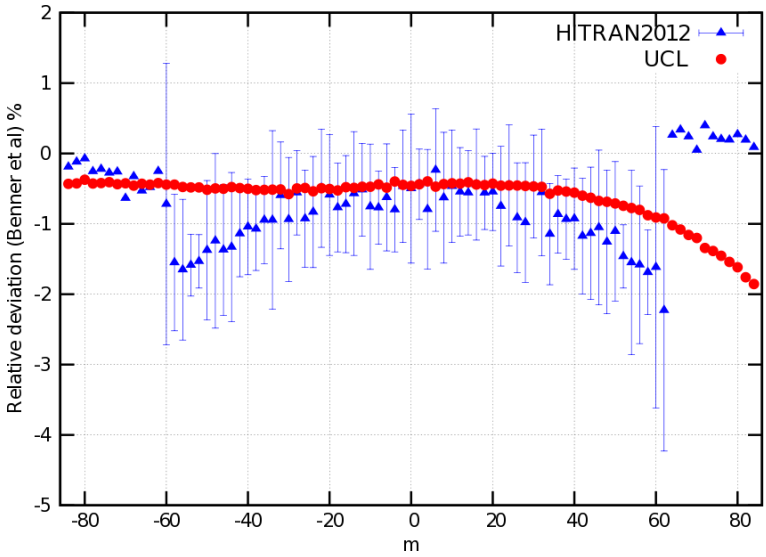

Figure 3.27: Line intensity comparison for the 20013 – 00001 band of $^{12}C^{16}O_2$ between the present study, the HITRAN 2012 database and a measurement by Benner *et al.* [31]. The error-bars in HITRAN data denote 1-σ uncertainty.

Apart from high m divergence between experiment and UCL results due to inadequate form of the H-W factor, the agreement observed for the 20013 – 00001 band (2.00 μm band) is indeed very good. An average systematic shift by about 0.5% from measurements by Benner *et al.* [31] is observed. A bit worse, but still very satisfactory agreement, with less accurate HITRAN 2012 intensities is also visible. At $m \pm 60$ there is a discontinuity in the relative deviations (UCL-HITRAN)

due to source change from NASA JPL intensities from Toth *et al.* to CDSD-296 intensities. It is also plausible that JPL intensities have their high $|m|$ tails inadequately retrieved due to a choice of the H-W model.

To summarize, independent high accuracy measurements of transition intensities for three crucial CO_2 absorption bands in the infrared confirmed sub-percent accuracy of UCL calculated transition intensities for these bands. This was a precedence case, when *ab initio* calculations could compete with state-of-the-art measurements and even in some cases have been proven more accurate than experiment. Moreover, in the course of analysis of experimental data, problems with Herman-Wallis factor models were detected, which triggered corrections to experimental reduction models and eventually lead to tentative reweighing of community's trust for high J transition intensities onto the *ab initio* side.

3.9 Comparison with experiment and databases

This section gives comparisons of the theoretical line lists for carbon dioxide calculated with Ames-1 PES and UCL *ab initio* DMS ('AU' line list) to high-resolution spectral databases (HITRAN 2012, CDSD-296), a theoretical line list from Ames NASA research center and recent accurate measurements. It has been already shown in section 3.8, that three bands in the main CO_2 isotopologue have intensities modelled with sub-percent accuracy. Here, further tests are given in a broader spectral range and for other isotopologues, to provide a critical and comprehensive assessment of UCL line lists. In the next section 3.10, the focus is specifically on the $^{16}O^{12}C^{16}O$ isotopologue ("626"), which is by far the most abundant (98.4%) of all CO_2 isotopologues. Then in section 3.11 five symmetric stable isotopologues of carbon dioxide are analysed: $^{13}C^{16}O_2$ (626) $^{12}C^{17}O_2$ (727), $^{12}C^{18}O_2$ (828), $^{13}C^{17}O_2$ (737) and $^{13}C^{18}O_2$ (838). In section 3.12 asymmetric isotopologues $^{16}O^{12}C^{18}O$ (628), $^{16}O^{12}C^{17}O$ (627), $^{16}O^{13}C^{18}O$ (638),$^{16}O^{13}C^{17}O$ (637), $^{17}O^{12}C^{18}O$ (728) and $^{17}O^{13}C^{18}O$ (738) are compared. The reason for separation of the symmetric and the asymmetric isotopologues is broken permutation symmetry of identical nuclei in the latter group, which results in a non-zero permanent dipole moment. This, in

turn, causes qualitative differences in infrared spectra of symmetric and asymmetric isotopologues (such as existence of purely rotational transitions in asymmetric isotopologues). Finally in section 3.13 the radioactive $^{14}C^{16}O_2$ (646) isotopologue is analysed, with a discussion of potential uses in remote sensing, carbon-dating procedures or even in medical diagnosis.

3.10 The main isotopologue (626)

In this section, the main isotopologue of carbon dioxide $^{16}O^{12}C^{16}O$ ("626") is analysed. In particular, the calculated theoretical line list for this isotopologue is compared with several data sources, such as HITRAN 2012 and CDSD-296 databases. The aim of these comparisons is to verify the accuracy of calculated transition intensities at the level offered by the databases and experiments, which is typically 2-20%. Unlike in section 3.8 on the 2μm band only, this section targets a much broader frequency range, to give a comprehensive global validation of the line list.

3.10.1 Comparison with high-accuracy measurements

First, let us focus on the state-of-the-art intensity measurements for 626. Line positions in the AU line list (UCL line list), as based on the Ames-1 PES, can be considered identical to those computed and analysed in a series of papers by Huang *et al.* [149, 157, 161]. The majority of high accuracy intensity measurements were performed for the 1.6 μm and 2 μm bands. These measurements already served as a proof of sub-percent accuracy of UCL transition intensities presented in section 3.8. Below, in Figure 3.28, yet another confirmation of sub-percent accuracy for the 30014 – 00001 band is given. The UCL and Ames line lists agree almost perfectly for the P branch of this band, and a 0.8% discontinuity in Ames intensities is visible for the R branch. Nevertheless, the agreement is very good. HITRAN 2012 transition intensities also agree to 0.5% with UCL intensities for low m values and systematically drift to $\pm 2\%$ for higher $|m|$'s. This essentially minor discrepancy could be only resolved in favour of either line lists by an additional, ultra-high accuracy measurement. Such measurement was provided by Kiseleva *et al.* [199], where the intensity of the R(52) line of the 30014 – 00001 band was determined

with 1% accuracy. The agreement between UCL and Kiseleva *et al.* is 0.2%, which adds significant confidence to the transition intensities provided in the UCL line list for this band. Such excellent agreement between experiment and the present theoretical calculations also suggest that HITRAN 2012 intensities are not accurate enough, and require updating.

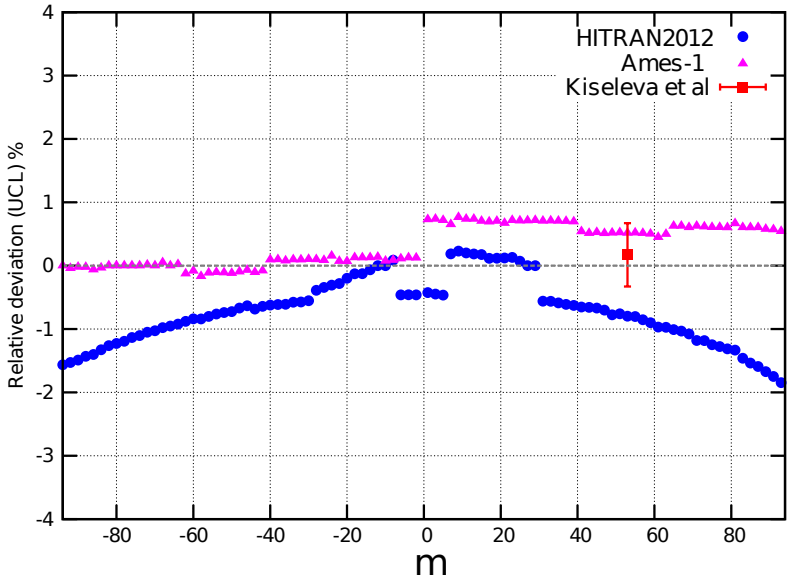

Figure 3.28: Comparison of transition intensities between the present line list for the 626 isotopologue and three accurate data sources: HITRAN 2012 database [200], Ames-1 line list [161] and measurement by Kiseleva *et al.* [199].

Another two lines in $\nu_1 + \nu_3$ band (P(34), P(36)) were measured by Pogany *et al.* [201] with reported 1.1 and 1.3 % uncertainty. The corresponding UCL intensities deviate by 2.0% and 2.5% respectively from line intensities provided by Pogany *et al.* . Nevertheless the UCL intensities are on average 1% closer to the experimental values than the intensities obtained from either Ames-1 or CDSD-296, which suggests that the accuracy of measurements by Pogany *et al.* was plausibly overestimated.

To conclude, the available experimental evidence, which covers a limited number of lines, indicates a very high, probably sub-percent accuracy of transition in-

tensities calculated with the present model for the 626 isotopologue. The accuracy of HITRAN2012 and CDSD-296 database as well as other available experimental data has stated uncertainty in intensities below 1%. Thus, comparison to these data sources allow to establish uncertainty of UCL intensities at best few-percent level. Nonetheless, comprehensive and spectrally broad comparisons to databases need to be made, to provide a possibly complete benchmark.

3.10.2 Comparison with other line lists

In this section a line-by-line comparison to three data sources is given: the theoretical Ames-296 line list [161], HITRAN 2012 [200] and CDSD-296 [187] databases. Such comparison will allow one to draw conclusions about the global accuracy of the UCL line list. Because the stated accuracy of these three data sources is no higher than 2%–20%, the level of validation achieved by comparing to them cannot be lower than this value. Nonetheless, such comparison provides a benchmark, and may allow to select candidate bands which are poorly modelled in the UCL line list. As we will see, there is one series of unreliable bands in the UCL line lists.

Ames-296

Huang *et al.* [161] published infrared line lists for 12 stable and 1 radioactive isotopologues of CO_2. These line lists were calculated with Ames-1 PES [157] and DMS-N2 [149], or (AA) in our notation.

From Ames data a $^{12}C^{16}O_2$ line list was generated for its natural abundance, $T = 296$ K and with an intensity cut-off of 10^{-30} cm/molecule, which we refer to as Ames-296. Ames-296 contains 162 558 lines in the 0 - 8000 cm^{-1} range. To facilitate comparison with other line lists a spectroscopic assignment of this line list was performed. As a first step, for the sake of consistency, it was necessary to compare energy levels from original Ames-296 line list with the DVR3D re-calculation. Accordingly, energy levels up to 6000 cm^{-1} gave a RMSD of 0.05 cm^{-1} and 0.06 cm^{-1} up to 10 000 cm^{-1}. This is slightly more than one would have expected on the basis of previous comparisons [155] and appears to be due a slightly non-optimal choice integration grids in Huang *et al.*'s calculations (Huang and Lee, 2015, private communication).

CDSD-296

The effective operator approach enables one to reproduce all published observed positions and intensities with accuracies compatible with measurement uncertainties. Based on a fitted effective Hamiltonian H_{eff} and effective dipole moment D_{eff} models Tashkun *et al.* [187] created a high resolution spectroscopic databank "CDSD-296" aimed at atmospheric applications. The databank contains the calculated line parameters (positions, intensities, air-and self-broadened half-widths, coefficients of temperature dependence of air-broadened half-widths and air pressure-induced lineshifts) of the twelve stable isotopic species of CO_2. The reference temperature is 296 K and the intensity cut-off is 10^{-30} cm/molecule.

Figure 3.29 compares Ames-296 and UCL line intensities with the semi-empirical CDSD-296 results. For the sake of clarity only strong bands with intensities greater than 10^{-23} cm/molecule are plotted.

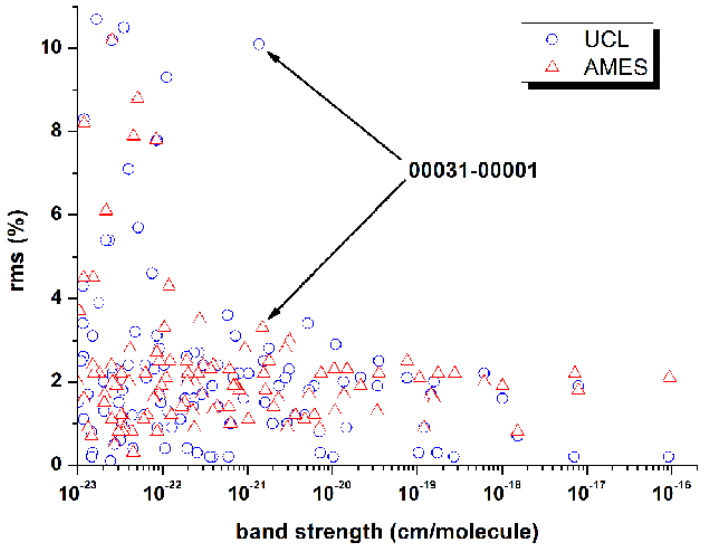

Figure 3.29: Root mean square deviation for band intensities of Ames-296 (red triangles) and the present results (UCL, blue circles) with respect to CDSD-296. This figure was prepared by S. Tashkun [37].

For the strongest bands the UCL line-list agrees much more closely with

CDSD-296 than Ames-296 does. The only real exception to this are the 00031–00001 and 01131–01101 bands. For this family of bands, whose intensity derives from the same dipole moment derivative, the deviations from Ames-296 are three times less than UCL ones. In the final UCL's recommended line lists included in the 2016 edition of the HITRAN database, all absorption intensities of bands including $3\nu_3$ vibrational quanta were replaced with CDSD-296 intensities. 3170 transitions belonging to this family of unreliable bands were identified in the UCL line list.

3.10.3 HITRAN2012

This section gives a comparison of UCL's line list for $^{12}C^{16}O_2$ with the HITRAN 2012 database [200], which contains 160 292 absorption lines in 0 – 8000 cm^{-1} region for the main isotopologue. First of all, a matching procedure was conducted between the UCL calculated energy levels and HITRAN 2012 energy levels. This was done by imposing rigorous restrictions on rotational quantum numbers and Wang e/f parities as well as 0.3 cm^{-1} tolerance to energy difference. This scheme resulted in a match for all 16 777 unique energy levels present in HITRAN 2012 covering J values from 0 to 129 with RMSD of 0.07 cm^{-1}. The largest deviation found between two levels was roughly 0.2 cm^{-1}. This result confirms the high quality of the Ames-1 PES.

The next step was to match transition lines between HITRAN 2012 and UCL line lists. The procedure relied on a simple algorithm, where corresponding lines were matched using already matched energy levels list. As a result all 160 292 lines up to 8000 cm^{-1} were matched with a RMSD of 0.08 cm^{-1} .

There are two main sources of HITRAN2012 data for CO_2 main isotopologue: a small set of 605 lines in 4800-6989 cm^{-1} range originating from experiment (NASA JPL line list) by Toth *et al.* [195] and the majority of transitions from a previous version of the CDSD-296 database. In general, data from the latest version of CDSD-296 [187] are very close to line positions and intensities given in HITRAN 2012.

The estimated uncertainties for all CDSD-296 intensities is given as 20 % or worse in HITRAN (uncertainty code 3, or ier=3). On the other hand, Toth *et al.*'s

intensities are supposed be accurate to better than 2% (uncertainty code 7) or 5% (code 6). For explanation of the HITRAN uncertainty codes see HITRAN website: www.hitran.org.

This reveals two issues with current version of HITRAN:
a) The stated uncertainty estimate of all current entries are insufficiently accurate for remote sensing applications. Comparisons and discussion from section 3.8 already showed that for a number of important bands the actual accuracy of the intensities in HITRAN is much higher than suggested by their estimated uncertainties.
b) line intensity accuracies are not uniform throughout the spectral region, as exemplified in Figures 3.24, 3.27 and 3.26. The ratio of observed to variational line intensities should be roughly constant for a given band, unless there is an isolated resonance. This is because the DVR3D calculations use the complete rotational basis set, exact kinetic energy operator and the exact expression for the line strength. The only major source of inaccuracy in line intensity is the DMS, which affect intensities of the whole bands, rather than individual rotational transitions.

All HITRAN2012 entries taken from a pre-release version of CDSD have been tagged with uncertainty code 3 (20% or worse). However, this number does not reflect actual uncertainties of the intensities. Most of the HITRAN intensities appear to have uncertainties much better than 20%. More detailed information about the actual uncertainties can be found in the official release of CDSD-296 [187].

Intensities of all assigned UCL lines relative to HITRAN 2012 are depicted in Figure 3.30. As expected, discrepancies between the two line lists grow as lines get weaker, which results in a funnel-like shape in the plot which is characteristic of such comparisons (e.g. [202]). The stability of the UCL lines on the scatter factors are also shown; as could be anticipated stable lines predominate at higher intensities.

It is instructive to divide HITRAN 2012 data into subsets of a given intensity accuracy code. Each of those sets can be then compared to the present results separately to provide an estimate for compatibility of two line lists at different levels of accuracy.

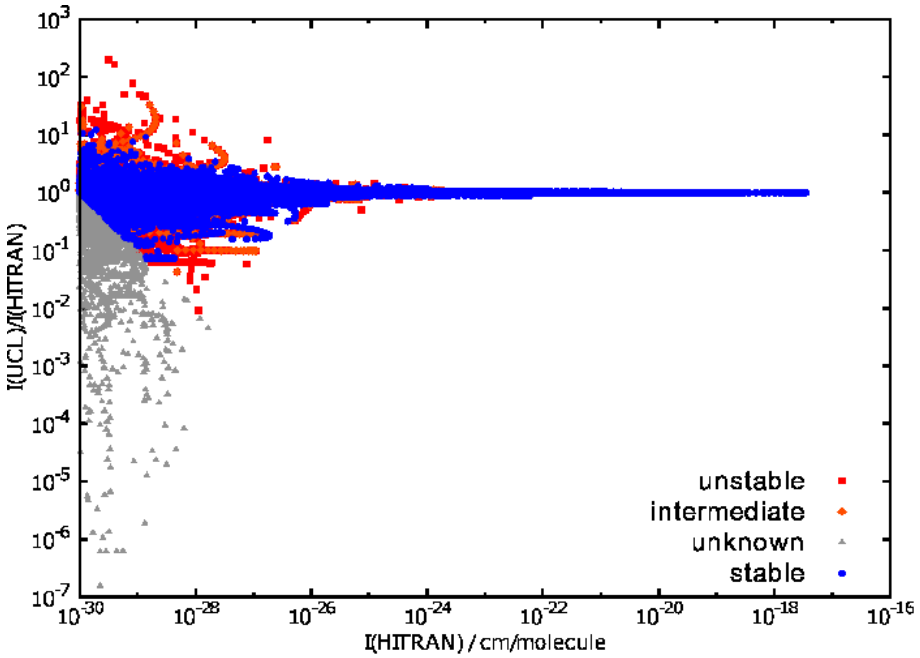

Figure 3.30: Comparison of HITRAN 2012 and UCL line intensities for the main CO_2 isotopologue: UCL to HITRAN intensity ratio as a function of HITRAN line intensity. Blue points stand for unstable lines according to our sensitivity analysis, while red points are considered to be stable. There are 147 000 stable, 7000 intermediate, 4400 unstable and 1 400 unknown lines which are too weak for a scatter factor to be determined reliably.

To achieve that HITRAN intensities with the accuracy code found for CO_2 which is 7 (2 % or better uncertainty) were plotted in Figure 3.31 against the UCL ones. This set of lines encompass the important 20011, 20012, 20013, 30011, 30012, 30013 and 30014 bands (absorption from the vibrational ground state) as well as the asymmetric stretching second overtone 00031. All bands except 'intermediate' 30011 band are stable. Comparisons with high accuracy measurements above have already shown that the present UCL intensities for the 30013 – 00001, 20012 – 00001 and 20013 – 00001 bands are accurate to about 1 % or better.

Again one can see characteristic bow-like structures corresponding to particular rotational transitions within a vibrational band, with the peak of an arc refers to most intense, low J transition. These structures are artifacts which originate from the semi-empirical treatment of the intensities (see section 3.8.4).

A similar situation occurs for bands with HITRAN uncertainty code 6 (accu-

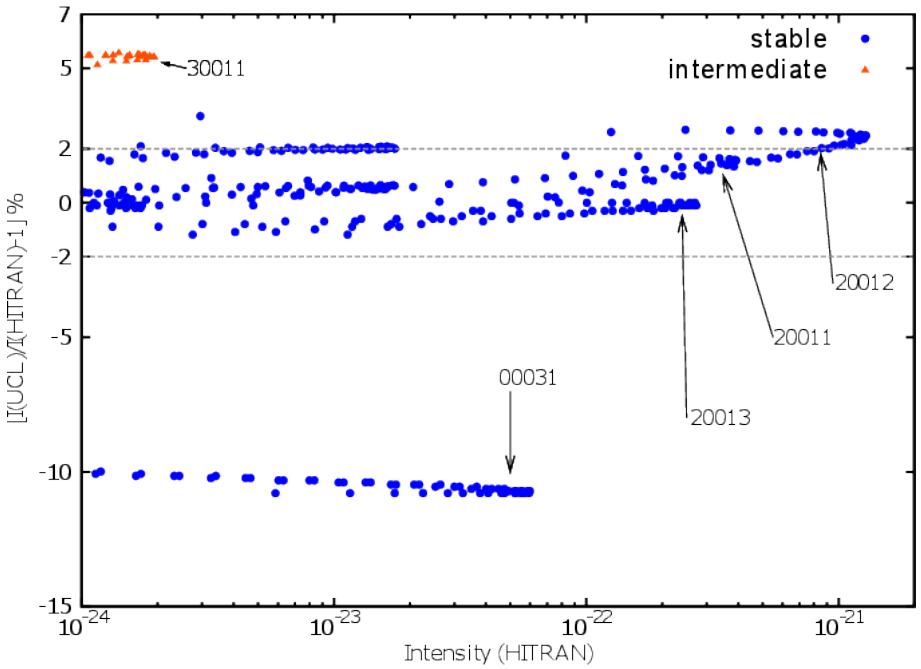

Figure 3.31: Comparison of HITRAN2012 most accurate intensities and UCL line intensities. The dashed line indicates the stated HITRAN uncertainty, i.e. 2% . Arrows label vibrational bands, which all start from the ground 00001 state.

racy of 2% – 5%), see Figure 3.32; here very good agreement is spoiled by 01131 – 01101 band.

Overall, the agreement between HITRAN 2012 and UCL line lists is good. The strongest and the most accurate bands in HITRAN 2012 match UCL bands to within few %, which agrees with the stated accuracy of HITRAN intensities. The only exception is the family of bands involving the ν_3 vibrational quanta, for which the UCL line lists gives markedly less reliable transition intensities. Sporadic large discrepancies between HITRAN and UCL for very weak lines are probably caused by inaccuracy of the effective dipole moment models used to generate HITRAN intensities. These models heavily rely on availability and quality of experimental data, which is often poor for weak bands.

3.11 Other symmetric isotopologues

The key hypothesis which is to be tested in this and following sections is the claim of transferability of accuracy of line intensities from the main CO_2 isotopologue

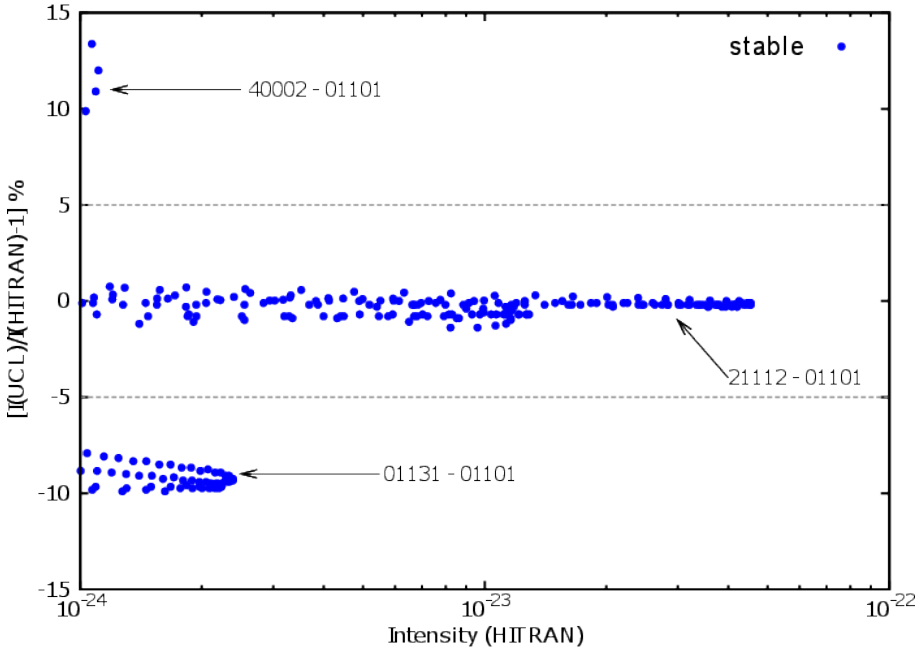

Figure 3.32: Comparison of HITRAN2012 medium-accuracy intensities and UCL line intensities. The dashed line indicates the stated HITRAN uncertainty, i.e. 5%. Arrows label vibrational bands.

onto other symmetric and non-symmetric isotopologues. The Ames-1 PES, which is used throughout this thesis for calculation of line lists was originally generated for the 626 isotopologue and is assumed isotopologue-independent. The magnitude of non-Born-Oppenheimer corrections to the Ames-1 PES is expected to be very small, typically affecting line positions by less than 0.1 cm^{-1} , which was confirmed by comparisons of Ames-1 PES derived energy levels with experimental values [157]. The question about the independence of the UCL DMS on nuclear masses is another, yet even more important concern. A straightforward test to the hypothesis of the independence of the DMS on nuclear masses comes from comparison of transition intensities for isotopologues other than the main 626 with high accuracy experiments. Unfortunately, very few such experiments are available, mainly due to low natural abundance of isotopologues containing ^{17}O,^{18}O or ^{13}C. The next section provides comparisons of calculated UCL intensities to available experimental data for several symmetric CO_2 isotopologues.

3.11.1 Isotopologue 636

Three high accuracy measurements of line intensities are analysed in this section: Devi *et al.* [128], Kiseleva *et al.* [199] and Durry *et al.* [203].

Recently Devi *et al.* [128] performed precise measurements of line intensities of the 626, 636 and 628 isotopologues of carbon dioxide in the 1.6 μm region. Figure 3.33 compares the present calculations and HITRAN 2012 line intensities to these new experimental results. The HITRAN 2012 data comes from the CDSD-296 database. A significant systematic shift of 5% and 10% with respect to Devi's measurement toward higher intensities is observed in Figure 3.33 for both the 30012 – 00001 and 30013 – 00001 band. An almost identical relative deviation pattern is followed by UCL line intensities and the effective Hamiltonian calculations from HITRAN 2012. Possible problems in measured line intensities were also found at $m = +38$ and $m = -40$. These transitions clearly stand out in the comparison pattern for both HITRAN and the present study. High J tails of both bands are bent in a arc-like structure, behaviour which has been already observed for the main isotopologue. Again, such phenomenon can be attributed to limited flexibility of functional form assumed for the Herman-Wallis factors, when reducing the experimental data.

In Figure 3.33, with blue and red filled triangles, compared are also UCL and HITRAN2012 intensities for the 30013 – 00001 band in the main isotopologues with measurements by Benner *et al.* [31]. Comparison shows 0.5% agreement between the experiment and UCL line intensities for the 20013 – 00001 band for the main isotopologue [31], and systematic increase in intensity deviation from $m = 60$ onwards to reach 1.5% deviation at $m = 84$. Both experiments (Devi *et al.* [128] and Benner *et al.* [31]) utilized the same multispectrum nonlinear least squares curve fitting technique to retrieve line profiles and intensities. This similarity in high J behaviour supports the thesis of potential problems with retrieval model used in experimental post processing.

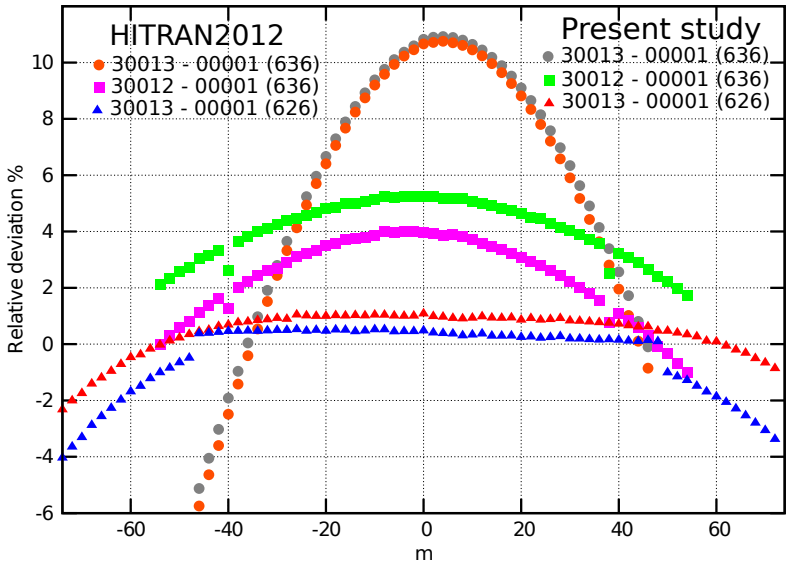

Figure 3.33: Relative deviations (PS/Experiment) of line intensities from measurements by Devi *et al.* [128] plotted against *m* quantum number. Blue and red triangles denote the 30013 – 00001 band of the 626 isotopologue taken from HITRAN 2012 and present study, respectively. Purple and green squares stand for line intensities of the 30012 – 00001 band of the 636 isotopologue taken from HITRAN 2012 and present study, respectively. Orange and grey circles give the line intensities of the 30013 – 00001 band of the 636 isotopologue taken from HITRAN 2012 and present study, respectively. Zero relative deviation means 100% agreement with Devi *et al.* .

The quite worrying 10% discrepancy between the measurement by Devi *et al.* and the UCL line intensities for the 30013 – 00001 band for 636 visible in Figure 3.33 requires a closer investigation. In Figure 3.34 the accuracy of experiments by Devi *et al.* and present calculations has been verified by comparison with very recent Cavity Ring-Down Spectroscopy measurements of CO_2 lines by Kiseleva *et al.* [199]. Their observed intensity of the P(6) line in the 30013 – 00001 band of the 636 isotopologue was found to be within 0.4% of both UCL and HITRAN line intensities. This result is consistent with the comparison between the experiment by Kiseleva *et al.* and the present study for the R(52) line of the 30014 – 00001 band of the main isotopologue (626), for which the discrepancy was only 0.2% from

the UCL theoretically predicted value (see Figure 3.28). Both lines were measured with stated <1% uncertainty budget. This suggests that a similar, presumably sub-percent, accuracy for the line intensities provided here and by HITRAN 2012 for the 30013 – 00001 band of the 636 isotopologue.

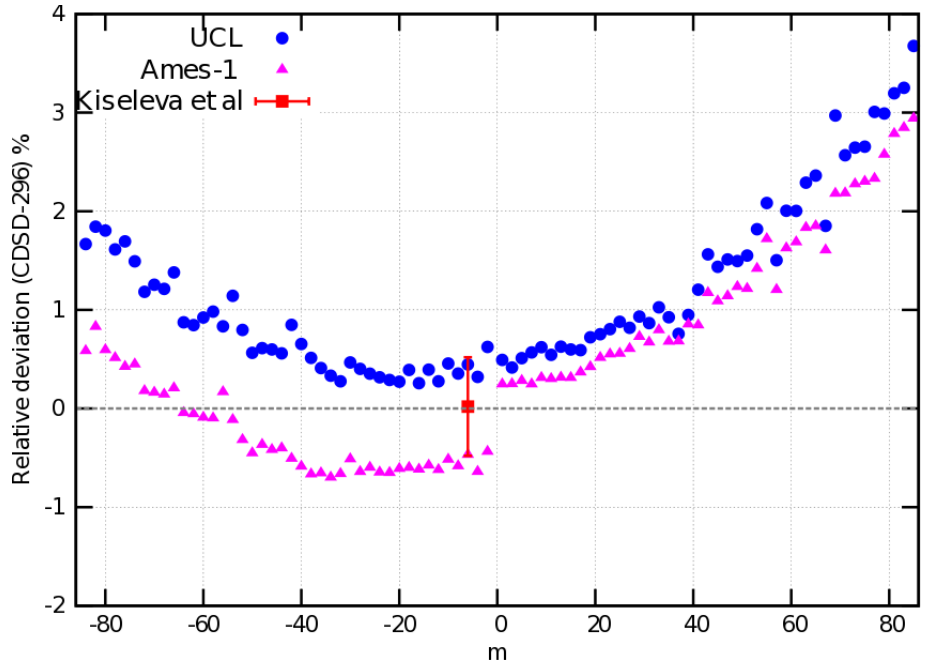

Figure 3.34: Relative deviations (relative to CDSD-296) of line intensities from the UCL line list, Ames-296 line list and a single line measurement by Kiseleva *et al.* [199] plotted against *m* quantum number for the 30013 – 00001 band of the 636 isotopologue.

Measurements from Durry *et al.* [203] deserve special attention, as in their study intensity uncertainties for measured bands of the 636 isotopologue are claimed at the 1% level. Figure 3.35 compares experimental line intensities from Durry *et al.* with HITRAN 2004 [204], HITRAN 2008 [205] and 2008 release of the CDSD database [167, 170], as well as with UCL calculated values. A characteristic wave-like pattern is visible. As all four sources follow this envelope, but with different systematic shifts, the tentative conclusion is that this pattern is an artifact of the Durry *et al.*'s measurements. The results of the present work are shifted toward most negative values of relative deviation, with average systematic shift of 2%. However, intensity comparison for this band for the main 626 isotopologue [31],

given in section 3.8 supports the 1% accuracy UCL theoretical intensities. Therefore it would seem that the stated 1% uncertainty of Durry *et al.*'s measurements may be too optimistic.

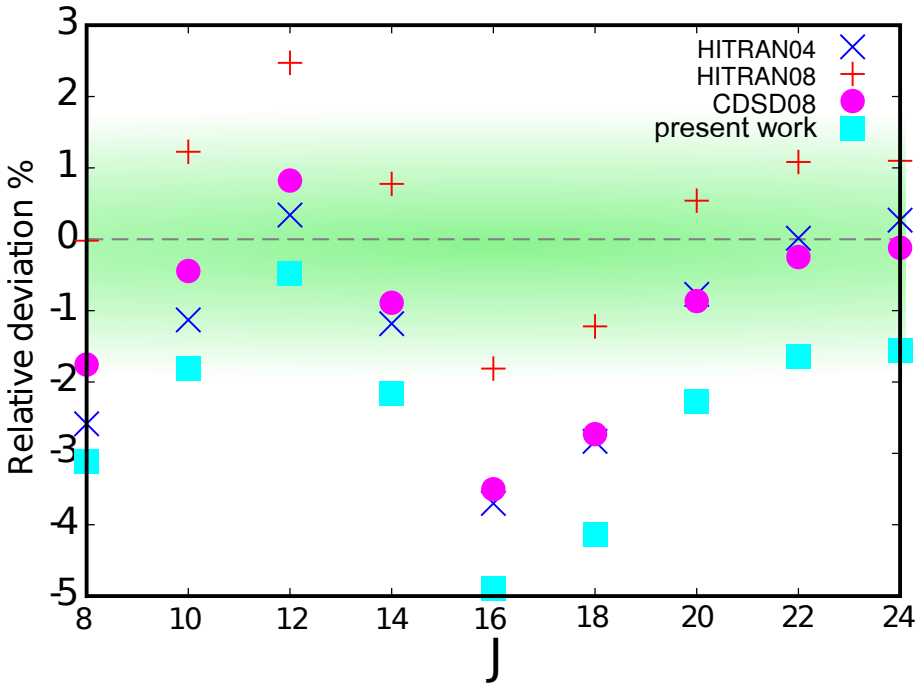

Figure 3.35: Relative deviations of line intensities of the 20012 – 00001 band of the 636 isotopologue from measurements by Durry *et al.* [203] plotted against J quantum number for several databases. Sources considered are HITRAN2004 [204], HITRAN2008 [205], the 2008 release of CDSD [167] and the present work. The 1% deviation region is represented by green edge-blurred strip.

3.11.2 Isotopologue 727

In recent experiments performed on ^{17}O and ^{18}O enriched samples, Jacquemart *et al.* [162] measured several bands for the 727 isotopologue. The authors argue that only lines stronger than 10^{-25} cm/molecule are retrieved with 'good accuracy' and this accuracy is also strongly dependent on the knowledge of isotopic abundances. Figure 3.36 compares intensities of different bands measured by Jacquemart *et al.* with present predictions. It is evident that lines weaker than 1.0×10^{-25} cm/molecule give reduced accuracy, as statistical spread appears an order-of-magnitude larger than for the strong bands measured in this experiment. Hence the experimental results ([162]) for the 30011 – 00001, 31112 – 01101 and

31113 – 01101 band should be considered with caution.

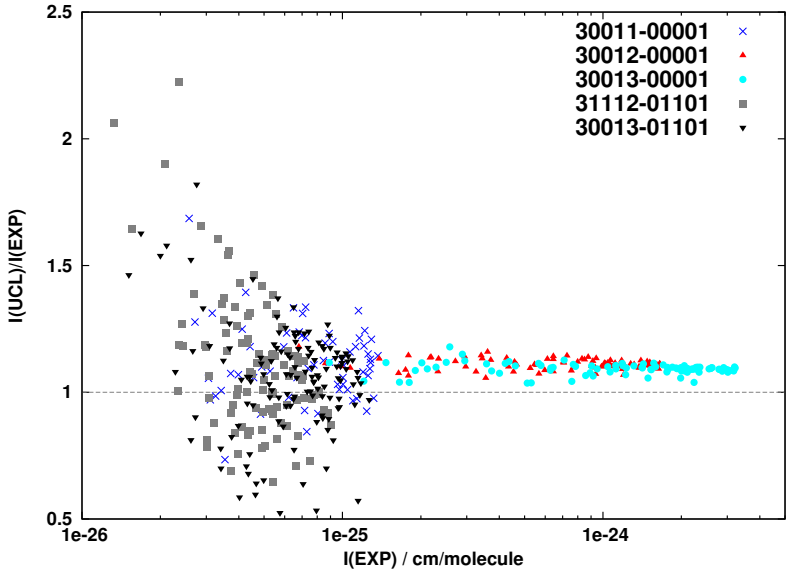

Figure 3.36: Relative intensities (vs. UCL) for several bands of the 727 isotopologue measured by Jacquemart *et al.* [162].

The calculated intensities of the two strongest bands in the 2 μm region, that is 30012 – 00001 and 30013 – 00001, are uniformly shifted by +10% with respect to experiment. As indicated by Jacquemart *et al.* [162], intensities of whole bands are strongly dependent on isotopologue abundance (reported as 22.27%), and this factor is considered to be the main source of possible systematic shifts with respect to other studies. Comparisons with previous measurements by Karlovets *et al.* [191] were made, revealing the new measurements by Jacquemart *et al.* [162] to be on average 3 – 4% stronger. However, samples used by Karlovets *et al.* had very low abundance of 727 (0.04%), which resulted in large statistical error (15%) in the intensities. Therefore with the current level of experimental control over systematic errors it is difficult to reliably refer to measurements better than 10% accuracy. Nonetheless, because theoretical line intensities have constant accuracy for whole bands (except resonances), they can be used to assess the precision of measurements. Small scatter of line intensities throughout these bands (marked red and cyan in Figure 3.36)

confirms the claimed high precision (1%) of the measurement from Ref. [162] above 2.5×10^{-24} cm/molecule, 2% between 5×10^{-25} and 2.5×10^{-24}, 5% between 1×10^{-25} and 5×10^{-25}, and 20% below 1.0×10^{-25}.

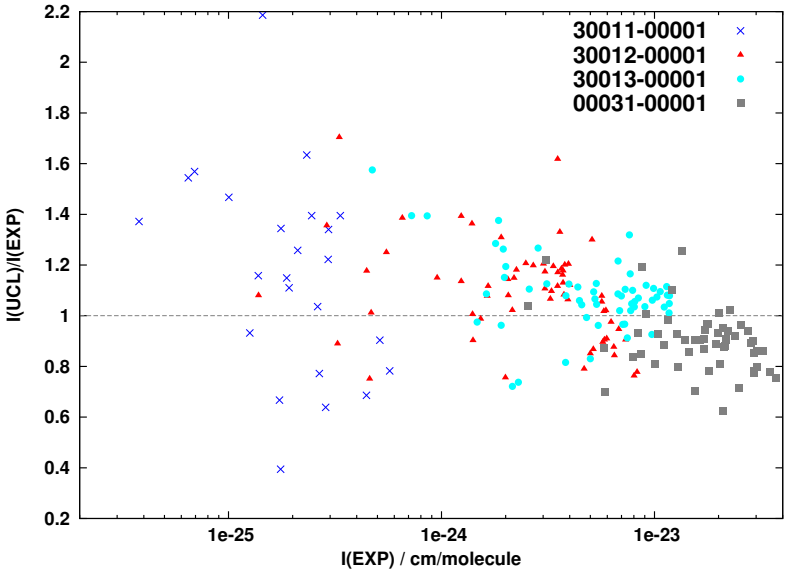

Figure 3.37: Relative intensities (vs. UCL) for several bands of the 727 isotopologue measured by Karlovets *et al.* [191]. Intensities were scaled to unit abundance.

Figure 3.37 compares UCL line intensities to the experimental data from Karlovets *et al.* [191]. The low isotopic abundance of samples used in experiments and large stated uncertainty (15%) means that the comparison despite its large scatter is satisfactory. As for other isotopologues, the 00031 – 00001 band computed by us has an underestimated intensity (grey squares in Figure 3.37). Cyan and red points correspond to 30013 – 00001 and 30012 – 00001 bands, and these experimental points were used to relate the line intensities of these bands in the study by Jacquemert *et al.*.

3.11.3 Isotopologue 828

Recent CW-Cavity Ring Down experiments for enriched sample of the $^{12}C^{18}O_2$ isotopologue by Karlovets *et al.* [206] cover the spectral range of all previous mea-

surements for $\Delta P = 9$ transitions. The study comprises 2870 lines from 59 bands in the 5851 – 6990 cm^{-1} region and was recorded for 25.45 % abundance. Raw experimental data was fitted with an effective operator model to take into account another accurate experimental dataset from Toth *et al.* [207], which has been also included in the 2012 release of the HITRAN database. The estimated 10% uncertainty of the line intensities is the most accurate claim up-to-date. For a detailed review of previous measurements for this isotopologue see Refs. [187, 206] and references therein. Here, highly enriched sample allowed for more precise measurements than in the 727 isotopologue case. Figure 3.38 compares line intensities of the three strongest bands measured by Karlovets *et al.* to present study. The 30012 – 00001 and 30003 – 00001 bands remain within $\pm 2\%$ deviation range, which suggest that the stated experimental uncertainty of 10 % is actually too pessimistic. UCL intensities for the 00031 – 00001 band are shifted down by 14 %, similar to other isotopologues.

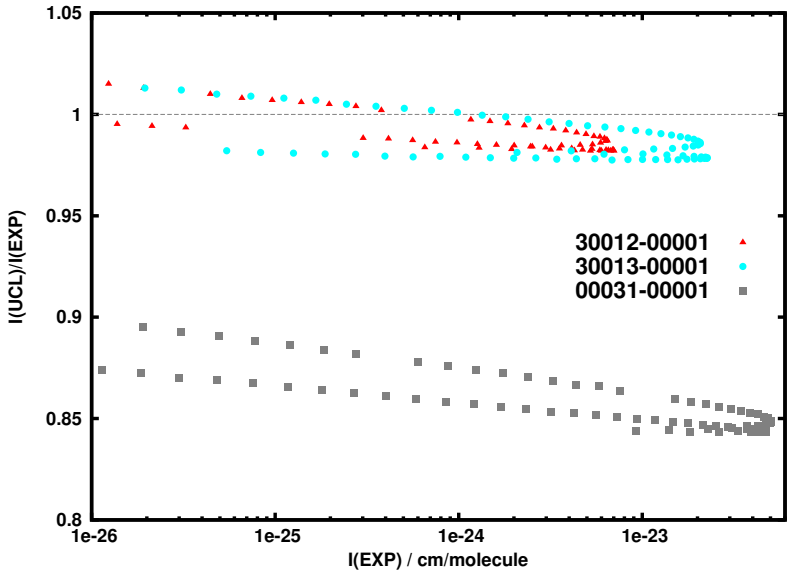

Figure 3.38: Relative intensities (vs. UCL) for several bands of the 828 isotopologue measured by Karlovets *et al.* [206]. Intensities were scaled to unit abundance.

The above results for 636, 727 and 828 isotopologues are summarized in Table 3.7.

Table 3.7: Characterization of selected vibrational bands of three symmetric CO_2 isotopologues. Given for each band and each reference are the number of lines in the band, accuracy declared in the reference, average systematic shift ($\Delta_{sys} = \bar{S}$: average residual with respect to present study), average statistical dispersion ($\Delta_{stat} = \sqrt{\frac{1}{N_{lin}} \sum_{i=1}^{N_{lin}} \left(S_i - \bar{S}\right)^2}$, $S_i = \left| \frac{I_{UCL,(i)}}{I_{exp,(i)}} - 1 \right| \cdot 100\%$) and the total band strength in cm/molecule. The last column (marked UCL-IAO) contains the data from the present study, the total number of lines in the band, suggested accuracy for the band (in %) and the total band strength in cm/molecule.

Iso.	Band	N_{lin}	Strength	acc. (%)	Δ_{sys}(%)	Δ_{stat} (%)	N_{tot}	Strength	acc. (%)
			Karlovets *et al.* (2013) [208]					UCL-IAO	
727	30012–00001	64	2.13×10^{-22}	3-20	+17	13	64	2.22×10^{-22}	1
	30013–00001	58	3.48×10^{-22}	3-20	+13	12	58	3.71×10^{-22}	1
			Jacquemart *et al.* (2015) [162]						
727	30012–00001	85	6.85×10^{-23}	20	+11	2	85	7.59×10^{-23}	1
	30013–00001	93	1.37×10^{-22}	20	+9	2	93	1.50×10^{-22}	1
	31113–01101	130	8.84×10^{-24}	>20	+17	15	130	9.21×10^{-24}	3
			Karlovets *et al.* (2013) [208]						
828	30012–00001	64	1.86×10^{-22}	10	-2	2	64	1.83×10^{-22}	1
	30013–00001	81	6.05×10^{-22}	10	-2	3	81	6.16×10^{-22}	1
	00031–00001	80	1.33×10^{-21}	10	-13	5	80	1.13×10^{-21}	20
			Devi *et al.* (2016) [128]						
636	30012–00001	55	5.41×10^{-24}	10	+4	3	55	5.67×10^{-24}	1
	30013–00001	47	2.03×10^{-24}	10	+8	15	47	2.18×10^{-24}	1

3.11.4 Comparison with HITRAN2012, Ames and CDSD-296

The HITRAN2012 database contains line lists for five symmetric isotopologues: 626, 636, 727, 828 and 838. Uncertainty indices of line positions range from 2 ($\geq$ 0.01 cm^{-1} and $<$ 0.1 cm^{-1}) to 9 ($\geq 10^{-9}$ $cm^{-1}$and $< 10^{-8}$ cm^{-1}) for these line lists. In general, line positions from the latest version of CDSD-296 are very close to the line positions given in HITRAN 2012 and have uncertainties corresponding to indices ranging from 3 to 9 depending on spectral region and quality of underlying experimental entries. Intensities provided by the current release of HITRAN for symmetric isotopologues of carbon dioxide come from two main sources: experiment (NASA JPL line list) by Toth *et al.* [195] and the majority of transitions from a previous version of CDSD. The estimated uncertainties for all CDSD intensities is given as 20 % or worse in HITRAN (uncertainty code 3). However, this number does not reflect the actual uncertainties of the intensities. Most of the HITRAN intensities have the uncertainties much better than 20%. More detailed information

about the actual uncertainties can be found in the official release of CDSD [187], which can be used to get more realistic information about the uncertainties of the line parameters. Intensities from Toth *et al.* are supposed to be accurate to better than 2% (uncertainty code 7) or 5% (code 6). Below are given bulk comparisons between UCL line lists and HITRAN 2012 and CDSD-296 databases, as well as Ames-296 line lists.

3.11.4.1 Isotopologue 636

The HITRAN2012 line list for the second most abundant 636 isotopologue contains 68 856 lines below 8000 cm^{-1}. There are two sources of line intensities: the majority of lines taken from the 2008 version of the CDSD-296 database [167] and two bands (20012–00001 and 20013–00001) from high precision measurements by Toth *et al.* [195]. All lines present in the HITRAN2012 database for this isotopologue were matched to UCL line list with a root mean squared deviation (RMSD) of 0.04 cm^{-1}. Lines that lay far in intensity from theoretical predictions (*vide infra*) were double checked by manual investigation.

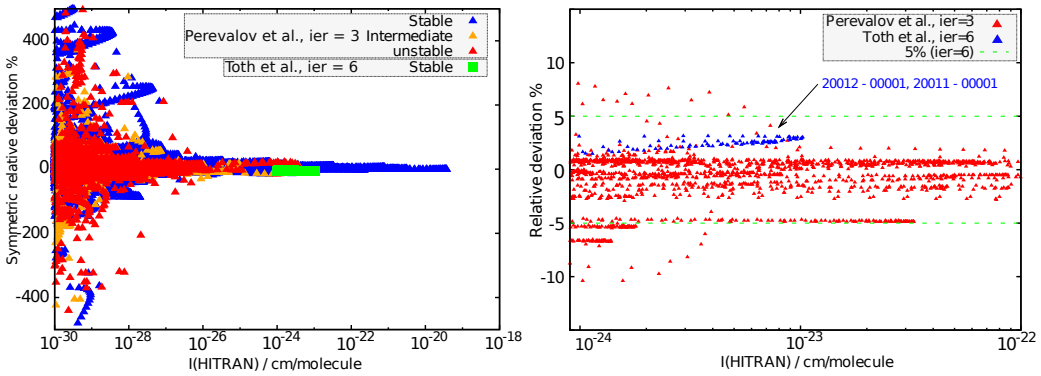

Figure 3.39: Left panel represents symmetric relative deviation for the 636 isotopologue for the two different sources (Perevalov *et al.* [167] and Toth *et al.* [195]) from the HITRAN 2012 database. Right panel is a zoomed image in the region of high accuracy ($ier = 6$) measurement by Toth *et al.* . Dashed green line indicates 5% limit of deviation tolerance associated with $ier = 6$. Two bands measured by Toth *et al.* are marked with arrow.

An overview from Figure 3.39 reveals the rather typical situation of funnel-shaped relative deviation plot. By zooming into the region of high accuracy mea-

surement by Toth *et al.*, one can clearly see that all lines (marked with blue filled triangles in the right panel of Figure 3.39) remain within the claimed 5% uncertainty, additionally exhibiting a very narrow spread.

3.11.4.2 Isotopologue 727

HITRAN 2012 line list for the 727 isotopologue contains 5187 lines below 8000 cm^{-1}, all of which were taken from the effective Hamiltonian calculations by Tashkun and Perevalov [209]. Figure 3.40 compares UCL line intensities (all stable) to HITRAN 2012; we observe the majority of line intensities display a systematic shift of -6% with respect to those recommended by HITRAN. Here again, noticeable arc structures appear. Similar behaviour was observed for the main 626 and the 636 isotopologues. Although most of the arcs are rather flat, there are a few bands which arc structure extends over a wide deviation range. Such occurrences are caused by insufficiently flexible functional form of the Herman-Wallis factors employed to reduce experimental data for those bands, resulting in inaccurately retrieved experimental line intensities, especially for high Js. These serve as an input to the effective Hamiltonian calculations (CDSD, hence HITRAN), thus artifacts of experimental analysis are likely to be propagated within the EH approach.

It has already been shown that inaccuracies of UCL line intensities are largely reflected in systematic shifts of whole bands, rather than statistical scatter, which is assumed to remain almost constant as a function of J. Two bands in Figure 3.40 lie outside the tolerance given by the HITRAN 2012 uncertainty code 3. These are: the 00031 – 00001 band and the 30013 – 00001 band (both indicated with arrows in Figure 3.40). The discrepancy for the former band has been explained in terms of rather poor reproduction of the $3\nu_3$ series of bands by UCL DMS. The behaviour of the latter band however is not clearly understood at this stage and requires further investigation. The working hypothesis is that the -6% systematic shift applies to all bands, hence the 30013 – 00001 band when shifted by +6%, should match the 20% tolerance region, which is also regarded as provisional.

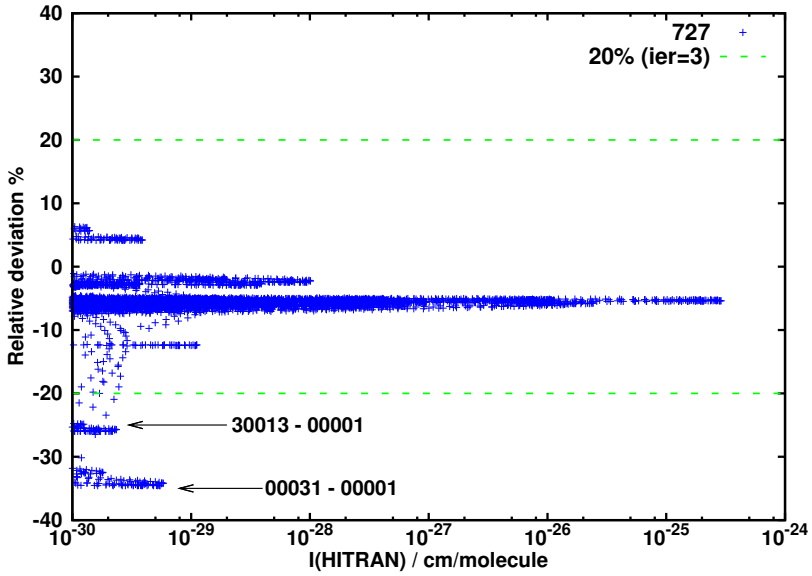

Figure 3.40: Relative intensities (cf. eq. (3.25)) plotted against HITRAN 2012 line intensities for the 727 isotopologue. Green dashed horizontal line represents deviation from HITRAN2012 data equal to $\pm 20\%$.

3.11.4.3 Isotopologue 828

HITRAN 2012 line list for the 828 isotopologue contains 7071 lines below 8000 cm^{-1}. There are three sources of line intensities: 6280 lines taken from CDSD-296 [167] with *ier* (uncertainty index) equal to 3 and 4, 722 lines taken from a 1994 update to older variational calculations [210] with *ier* equal to 2, and finally 69 lines taken from measurements by Toth *et al.* [195] with ier assigned to 3. Figure 3.41 compares intensities from the present study to HITRAN 2012 data. Despite the low uncertainty index, line intensities originating from Rothman *et al.* [210] agree within $\pm 20\%$ with UCL results. Transitions around 2.06 μm measured by Toth *et al.* [195] are enclosed in 10% region reflecting the *ier* value for this set. Data points originating from CDSD-296 are divided into two sets with differing uncertainty index. The more accurate subset (marked with orange rotated crosses) is clearly squeezed along the relative deviation axis and exhibits almost no systematic shift. In contrast, the lower accuracy subset from CDSD spreads over a large region in

relative deviation space. This suggests that both sets were calculated with separate input parameters of different quality. The 30013 – 00001 band ($ier = 4$) deviates around +2% from CDSD predictions, while the relatively strong 00031 – 00001 band ($ier = 4$) lies 11% below the zero deviation line (visible in Figure 3.41). It should be noted that large deviations of the lower accuracy CDSD-296 data ($ier = 3$) occur for very weak lines, for each the respective experimental data to fit the effective dipole moment parameters are absent. In these cases the parameters of the principal isotopologue were used in CDSD-296.

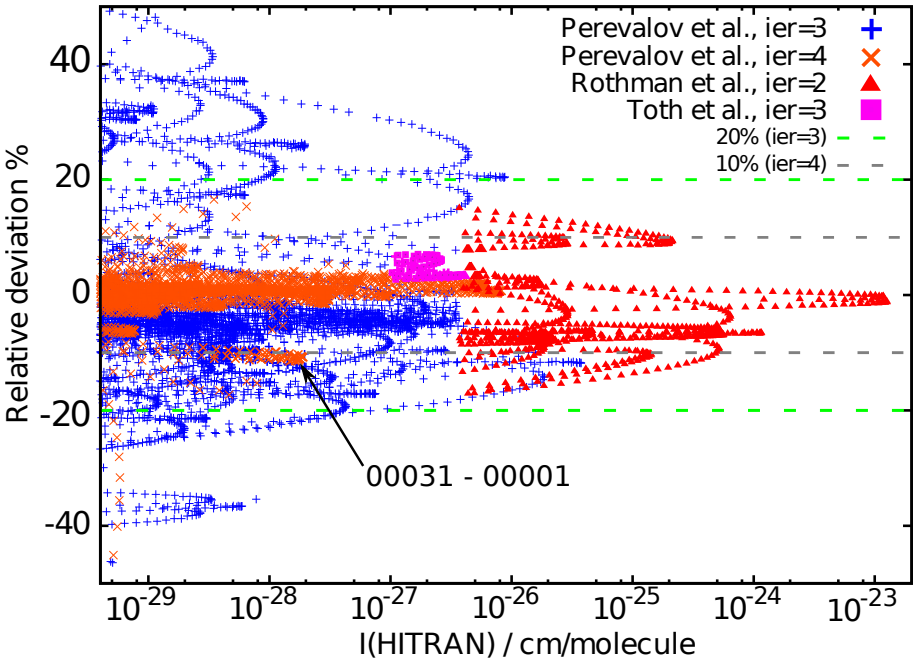

Figure 3.41: Relative intensities from the present study plotted against HITRAN 2012 line intensities for the 828 isotopologue. Only ±50% region is depicted. Dashed grey and green lines correspond to 10% and 20% deviation, respectively. Blue crosses correspond to a subset of lines taken from Perevalov *et al.* [167] which has been assigned to $ier = 4$. Consequently, rotated orange crosses represent $ier = 3$ from the same reference. Red filled triangles refer to Rothman *et al.* [210], while purple filled squares stand for the small set of lines provided by Toth *et al.* [195].

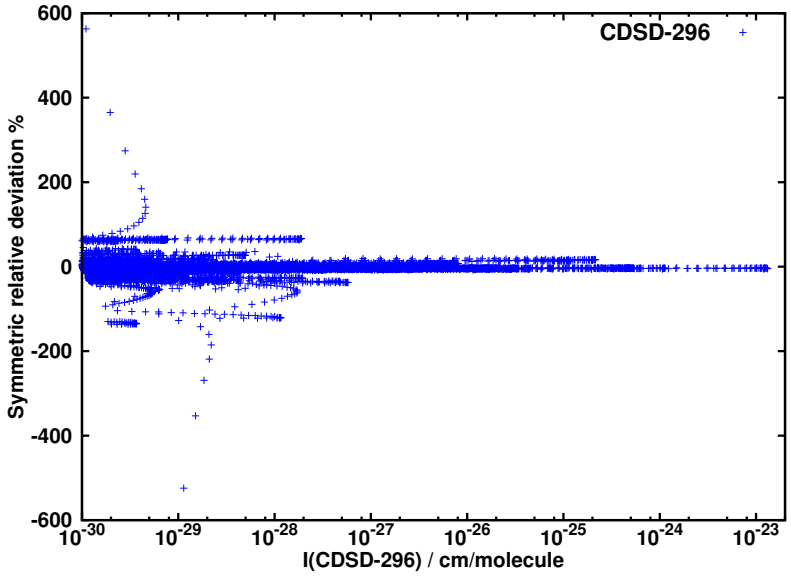

Figure 3.42: Symmetric relative intensities (cf. eq. (3.25)) plotted against HITRAN 2012 line intensities for the 828 isotopologue. Only ±500% region is depicted. Blue crosses correspond to a subset of lines taken from Perevalov *et al.* [167] which has been assigned to $ier = 4$. Consequently, rotated orange crosses represent $ier = 3$ from the same reference. Red filled triangles refer to Rothman *et al.* [210], while purple filled squares stand for the small set of lines provided by Toth *et al.* [195].

Figure 3.42 shows that all strong lines ($> 10^{-28}$ cm/molecule) follow a funnel shape envelope, thereby reflecting the typical relation between intensity and accuracy of lines. However several weaker lines, which constitute whole bands, align in wide arc structures with large systematic shift. This is particularly visible for lowered accuracy lines from HITRAN 2012 (blue crosses in Figure 3.42). These lines were directly incorporated from HITRAN 2008. The current release of the CDSD database improved on accuracy of these weak lines.

3.11.4.4 Isotopologue 838

Only limited data are available for the 838 isotopologue in the 2012 edition of HITRAN. 121 lines measured by Toth *et al.* [195] have uncertainty code 3 and cover three bands in the 2 μm region: 20011 – 00001, 20012 – 00001 and 20013 – 0000. All lines present in this set are matched to UCL line list with a RMSD = 0.04

cm^{-1}. Here, similar to the 727 case, a systematic shift of around 10% is visible. This causes three transitions to breach the stipulated accuracy tolerance. Nevertheless, this should be considered as rather illusory due to the systematic shift of lines coming from all three bands. Figure 3.43 shows calculated intensities relative to HITRAN 2012, where all computed lines are classified as stable.

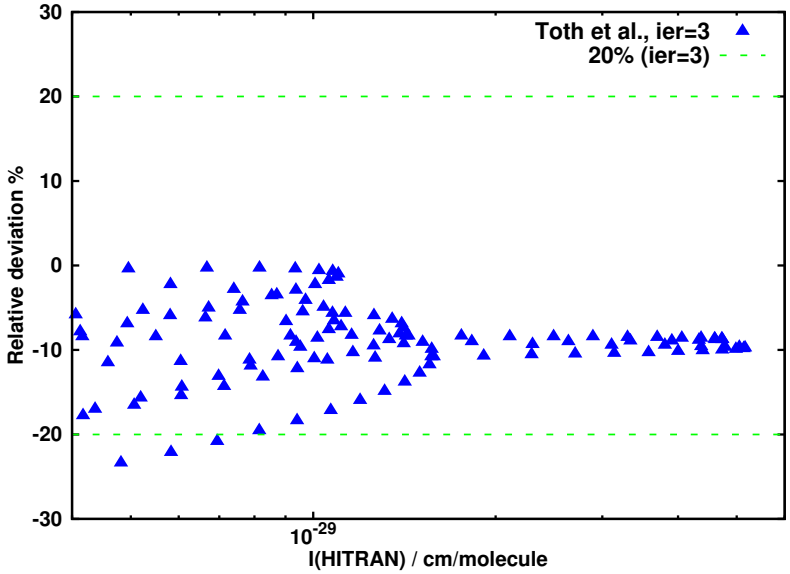

Figure 3.43: Relative intensities plotted against HITRAN 2012 line intensities for the 838 isotopologue. The triangles represent the 121 lines measured by Toth *et al.* [195] and included in the current version of HITRAN.

3.11.4.5 Overview

A rather naive attempt to find the answer to the question if accuracy of the presently employed computational scheme based on *ab initio* DMS holds at the same level for all symmetric isotopologues is presented in Figure 3.44. In the Figure the 20012 – 00001 band for the five symmetric CO_2 isotopologues is compared between HITRAN 2012 and UCL line lists. Clearly, the uncertainty of HITRAN intensities, which ranges here from 2% to over 20% (marked with uncertainty coded in Figure 3.44), is unsatisfactory to give a definitive answer to the posed question. In the meantime let us formulate a weaker query: do UCL theoretical line intensities for a

chosen band (here 20012 – 00001) maintain similar relative deviation from consistent, highly accurate experimental data source for all symmetric isotopologues? By analysing Figure 3.44 the short answer ppears to be no.

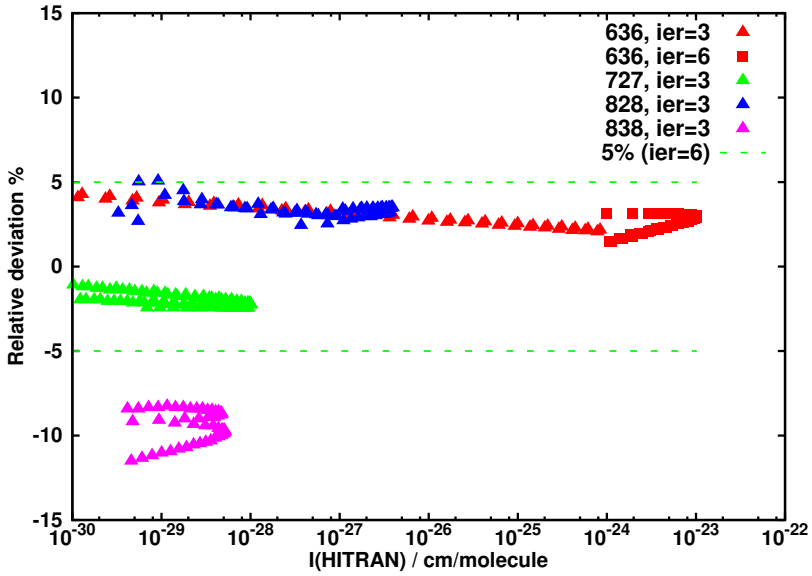

Figure 3.44: Relative intensities plotted against HITRAN 2012 line intensities for the 20012 – 00001 band for four symmetric isotopologues. Red filled squares represent lines (636) measured by Toth *et al.* [195] appearing with $ier = 6$. The remaining lines have code $ier = 3$.

All lines compared above match the stipulated HITRAN uncertainty, that is lines with $ier = 6$ fit the 5% tolerance, and the rest of the lines are 20% or less away from HITRAN 2012 values. Minor discontinuity related to change of source of data is seen for the 636 isotopologue. Relatively good overall agreement between UCL line list and HITRAN 2012, revealing only sporadic deviations that exceed the claimed HITRAN accuracy, but yet justified and facilitated with comparisons with recent and highly accurate measurements, allow to draw a conclusion that replacing current HITRAN line intensities with UCL computed values would significantly increase the accuracy, reliability and consistency of the database.

3.11.4.6 Ames-296

Table 3.8 presents a comparison of RMSD of intensities between Ames-296 line list, UCL line list and CDSD-296 line list for 14 strongest bands of CO_2 for six symmetric isotopologues. By looking at a given isotopologue, a general trend for both UCL and Ames is that the perpendicular bands ($\Delta l = +1, +2, ...$) are in worse agreement with CDSD than the parallel bands. On average, UCL based band intensities are in better agreement with CDSD than Ames for 626 and 636. The 828 isotopologue exhibits a similar level of agreement for UCL and Ames, and larger deviations from CDSD-296 for UCL calculated bands than Ames calculated bands are observed for 727, 838 and 737. It is difficult to indicate a single reason for this particular pattern of deviations. For the time being it is safe to say that CDSD entries, as experimentally tuned, are less accurate for less abundant isotopologues, thus derived uncertainties do not allow us to judge in favour of either DMS.

Table 3.8: DMS statistics for 14 strongest carbon dioxide bands for six symmetric isotopologues. Numbers in columns correspond to root-mean-square-deviations of band intensities from the CDSD-296 database.

Isotopologue		626		636		828		727		838		737	
Band	Stability	UCL	Ames	UCL	Ames	UCL	Ames	UCL	Ames	UCL	Ames	UCL	Ames
00011 – 00001	Stable	0.2	2.1	0.8	2.5	1.9	0.5	4.6	2.3	5.7	3.4	4.9	1.8
01101 – 00001	Stable	1.9	1.7	2.9	2.6	2.3	2.4	5.9	1.4	4.9	4.7	5.0	4.0
01111 – 01101	Stable	0.2	2.2	0.7	2.5	1.8	0.8	4.6	2.2	5.6	3.7	4.9	1.7
02201 – 01101	Stable	2.2	2.1	7.3	7.0	2.7	2.5	6.3	1.6	5.4	5.0	5.3	4.2
02211 – 02201	Stable	0.2	2.2	0.7	2.6	1.8	0.6	4.5	2.3	5.7	3.3	4.9	1.7
03301 – 01101	Stable	2.5	2.2	11.2	10.9	3.1	2.9	6.6	2.0	5.8	5.5	-	-
10001 – 01101	Stable	2.0	1.7	0.5	0.9	2.5	2.2	6.1	1.2	5.0	4.3	4.9	3.4
10002 – 01101	Stable	1.7	1.9	1.9	2.1	2.4	2.5	5.9	1.5	5.3	5.3	5.2	4.3
10011 – 00001	Stable	0.7	0.8	4.3	4.1	6.9	7.1	4.9	9.4	3.1	3.0	4.7	3.7
10011 – 10001	Stable	0.3	2.1	0.7	2.7	1.9	0.5	4.6	2.2	5.7	3.3	4.9	1.7
10012 – 00001	Stable	1.6	1.9	1.6	1.6	8.3	9.1	5.4	10.4	3.5	2.8	6.4	4.8
10012 – 10002	Stable	0.3	2.1	0.7	2.6	1.9	0.5	4.6	2.2	5.7	3.3	4.8	1.7
11111 – 01101	Stable	0.9	0.9	4.4	4.3	3.6	3.6	5.0	9.4	2.3	2.3	3.8	2.9
11112 – 01101	Stable	2.1	2.5	2.4	3.0	3.6	4.5	5.2	10.3	3.2	2.4	6.3	4.6

3.12 Asymmetric isotopologues

3.12.1 Comparison with high accuracy measurements

Experimental knowledge of intensities for the asymmetric isotopologues of CO_2 has been significantly improved recently by measurements on isotopically enriched samples. This is particularly important for atmospherically relevant bands in the 1.6 μm and 2 μm spectral regions. Space missions [7] and ground-based observations dedicated to detection and quantification of the total carbon dioxide content in the Earth's atmosphere are based on simultaneous measurements on these two regions. Thus, due to their practical importance, the 20012 – 00001, 20013 – 00001 and 30013 – 00001 bands should be assessed carefully for all abundant isotopololgues, as lines from different species are likely to interfere. A line-by-line comparison of UCL calculated intensities with recent measurements of these three bands for the 628 isotopolgue is given below.

In Figure 3.45, the four panels represent comparisons between Ames, CDSD, UCL line intensities and high-quality experiments by Toth *et al.* [207], Jacquemart *et al.* [211], Benner *et al.* [31] and Borkov *et al.* [190]. The three studies (Ames, CDSD and UCL) are denoted with black squares, red dots and blue triangles, respectively. All graphs show provisional sub-10% agreement between theory and experiment. Another common observation for all four panels is that for the 20012 – 00001 band line intensities are ordered as UCL $<$ Ames $<$ CDSD, and differences between the studies usually do not exceed 1%. This suggests similar quality of the line lists for this band. Toth *et al.* provides $\pm 2\%$ systematic uncertainty and J-dependent 0.5-7 % statistical uncertainty on line intensities (marked with green error bars in the upper left panel of Figure 3.45). UCL intensities match the stated experimental error bar, showing 2-3% systematic shift for $m \in (-30, 30)$ and characteristic, arc-like behavior for higher absolute values of m. Comparisons to Jacquemart *et al.* and Borkov *et al.* reveal small, 1-4 % systematic shift with respect to all three line lists. A markedly different situation is depicted in the left lower panel, in the study by Benner *et al.* . Here an arc pattern of residual intensity is observed. Similar artifact has been also found (and discussed in previous sections) in measure-

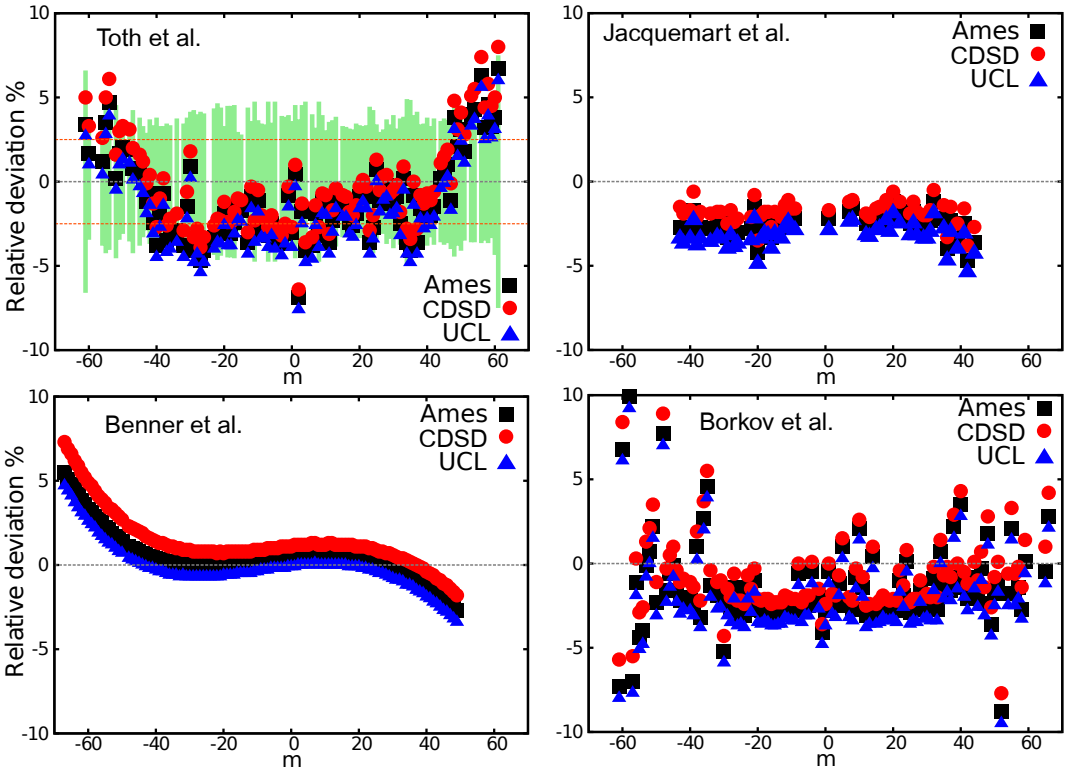

Figure 3.45: Ames, CDSD-296 and UCL line intensities for the 20012 – 00001 band of $^{16}O^{12}C^{18}O$ compared to four recent experimental works by: Toth *et al.* [207] (upper left panel), Jacquemart *et al.* [211] (upper right panel), Benner *et al.* [31] (lower left panel) and Borkov *et al.* [190] (lower right panel). Blue triangles, red dots and black squares denote relative deviations from the measurement (in %) of UCL, CDSD-296 and Ames line intensities respectively. *m* labels rotational transitions and corresponds to *J*(lower)+1 for the R branch and -*J*(lower) for the P branch. For the left uppermost panel experimental error bars were added together with horizontal orange dashed lines indicating experimental uncertainty for the systematic shift in the transition intensity.

ments on the main isotopologue of CO_2, and can be attributed to issue connected to the Herman-Wallis factors used in the retrieval procedure.

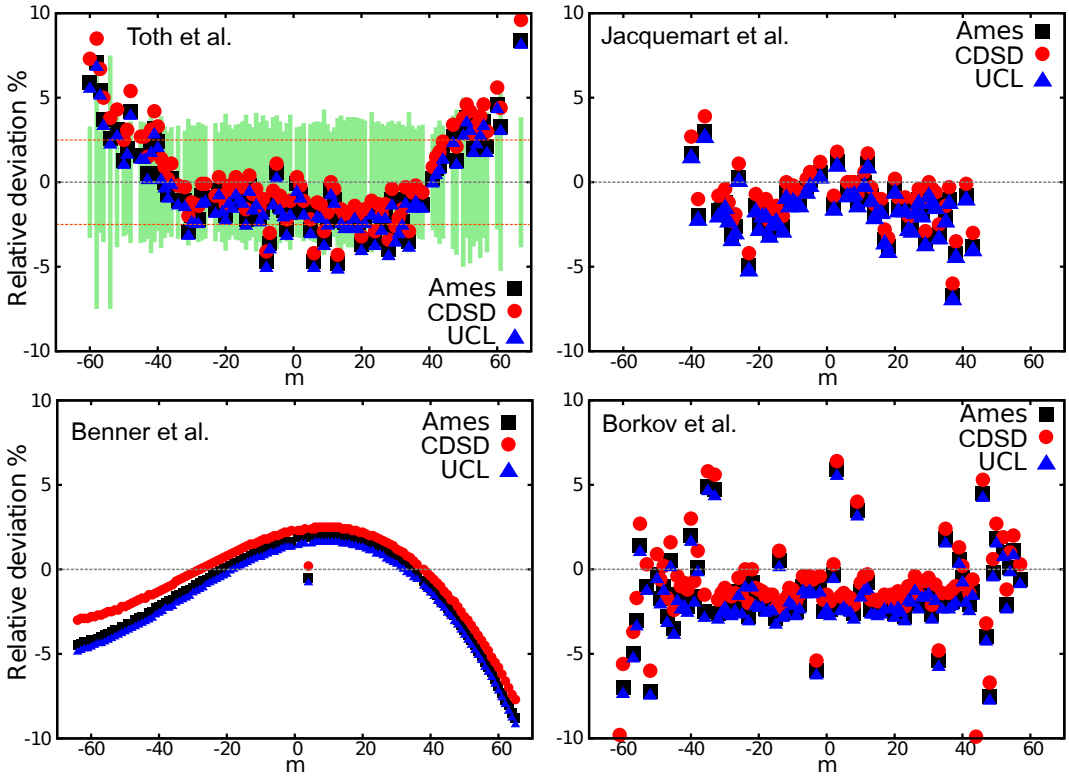

Figure 3.46: Ames, CDSD-296 and UCL line intensities for the 20013 – 00001 band of $^{16}O^{12}C^{18}O$ compared to four recent experimental works by: Toth *et al.* [207] (upper left panel), Jacquemart *et al.* [211] (upper right panel), Benner *et al.* [31] (lower left panel) and Borkov *et al.* [190] (lower right panel). Blue triangles, red dots and black squares denote relative deviations from the measurement (in %) of UCL, CDSD-296 and Ames line intensities respectively. *m* labels rotational transitions and corresponds to *J*(lower)+1 for the R branch and -*J*(lower) for the P branch. For the left uppermost panel experimental error bars were added together with horizontal orange dashed lines indicating experimental uncertainty for the systematic shift in the transition intensity.

Analogous conclusions can be drawn from Figure 3.46, where the UCl, CDSD and Ames line lists are compared to measurements on the 20013 – 00001 band. Note that all three line lists give an average negative systematic shift with respect to the experimental values. Line intensities of the 20012 – 00001 and 20013 – 00001 bands together with the line intensities of other five bands published by Toth *et al.* [207] were used for the determination of the concentration of the $^{16}O^{12}C^{18}O$ isotopologue in the sample used by Jacquemart *et al.* [211] and Borkov *et al.* [190]. This may indicate that the experimental studies underestimate the concentration of the 628 isotopologue, causing the intensities of individual lines to be systematically

overestimated.

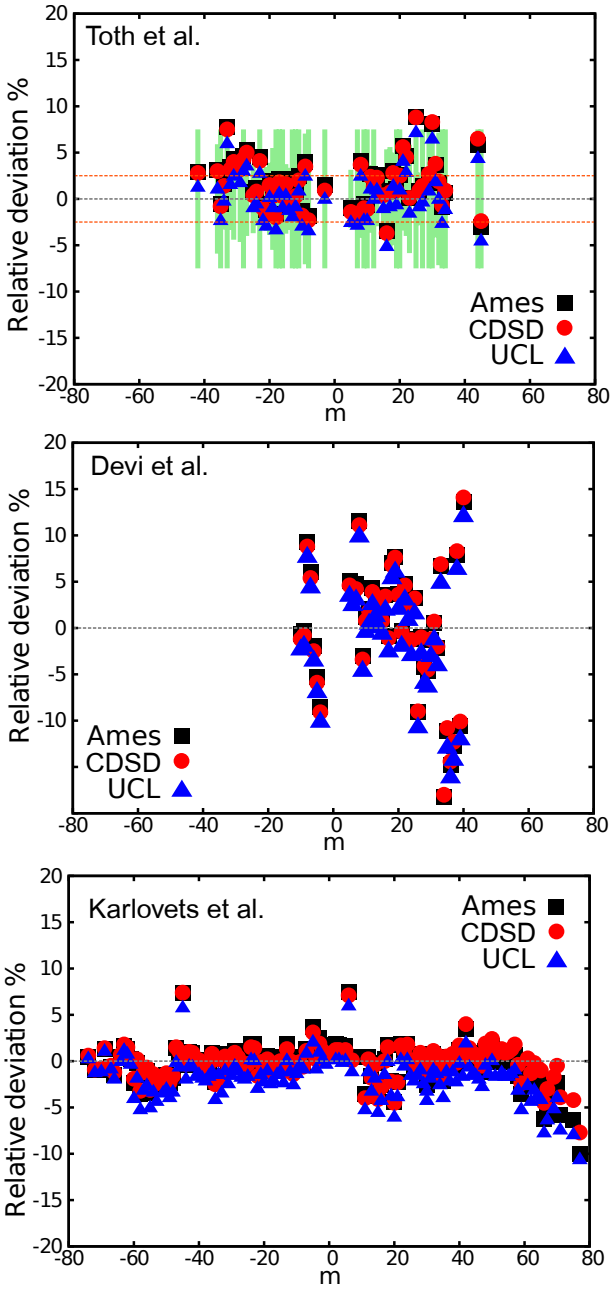

Figure 3.47: Ames, CDSD-296 and UCL line intensities for the 30013 – 00001 band of $^{16}O^{12}C^{18}O$ compared to three recent experimental works by: Toth *et al.* [207] (uppermost panel), Devi *et al.* [128] (middle panel) and Karlovets *et al.* [206] (lowest panel). Blue triangles, red dots and black squares denote relative deviations from the measurement (in %) of UCL, CDSD-296 and Ames line intensities respectively. *m* labels rotational transitions and corresponds to *J*(lower)+1 for the R branch and -*J*(lower) for the P branch. For the uppermost panel experimental error bars were added together with horizontal orange dashed lines indicating experimental uncertainty for the systematic shift in the transition intensity.

Intensities for the 30013 – 00001 band of $^{16}O^{12}C^{18}O$ (called 'the weak CO_2 band') have been accurately determined in three studies. The uppermost panel in the Figure 3.47 compares UCL, CDSD and Ames line intensities for this band to measurements by Toth *et al.* [207]. All three theoretical studies match the experimental error bars. UCL intensities (blue triangles) provide an almost zero systematic shift for this band. The J-dependent scatter of relative deviations between theory and experiment is most likely caused by the statistical fluctuations of the experiment. Very similar picture emerges from the middle graph in Figure 3.47. Here the experimental scatter (Devi *et al.*) reaches 20%, whereas the systematic shift is again close to 0%. One possible explanation for this is a lower signal-to-noise ratio in the experiment of Devi *et al.*, although inconsistent retrievals from crude data could be also the cause. To lowest panel in Figure 3.47 depicts measurements by Karlovets *et al.* on ^{18}O-enriched samples. Except for two points with large discrepancies at $m = -44$ and $m = +8$, the comparison gives an overall very good agreement Ames, CDSD and UCL, with average systematic shift of 1-2%. The 30013 – 00001 band has been previously verified to be reproduced at sub-percent accuracy for the main 626 isotpologue [37], and less abundant symmetric 636 isotopologue [199]. Results shown and discussed above support the thesis, that UCL DMS is capable of reproducing the true line intensities in the 1.6 μm region with accuracy not worse than 1-3% for the asymmetric isotopologues and 1% or better for the symmetric ones. For the 2.06 μm region, containing the 'the strong CO_2 bands' a thorough investigation of line intensities was made in section 3.8, concluding that sub-percent accuracy is given by the UCL calculated intensities for the 20013 – 00001 and 20012 – 00001 bands. The essential question to ask is, whether this high accuracy is transferable to the asymmetric isotopologues.

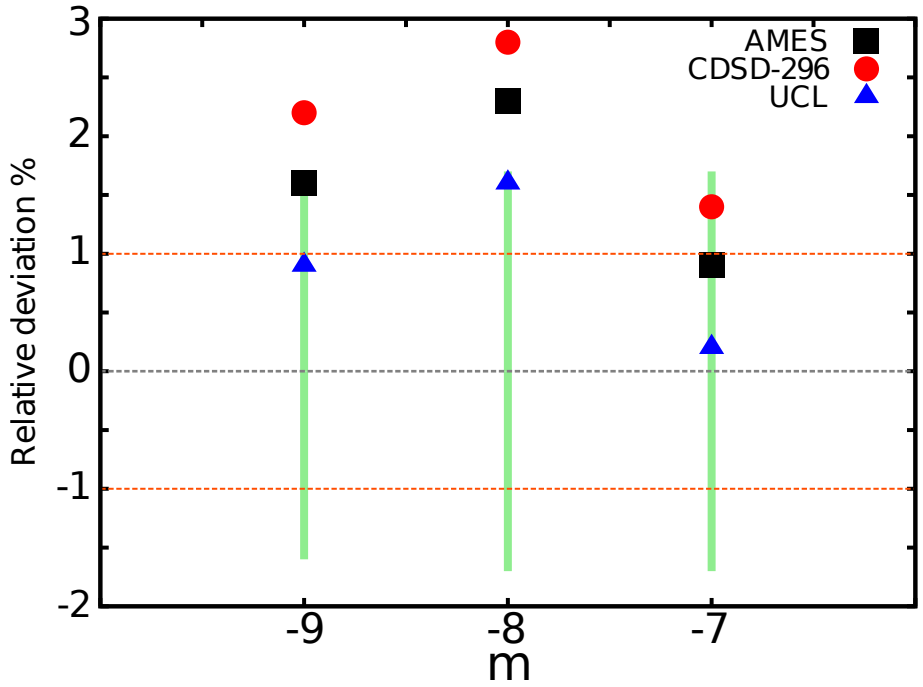

Figure 3.48: Experimental line intensities measured by Durry *et al.* [203] for the P branch of the 20012 – 00001 band of $^{16}O^{12}C^{18}O$ depicted against respective transition intensities taken from Ames, CDSD-296 and UCL line lists. *m* labels rotational transitions and corresponds to *J*(lower)+1 for the R branch and -*J*(lower) for the P branch.

Durry *et al.* [203] performed intensity measurements with a near-infrared tunable diode laser spectrometer providing 1% stated accuracy and sub-percent precision on a sample containing $^{16}O^{12}C^{18}O$ in the 2.06 μm spectral region. Results of this experiment are compared to the Ames, CDSD-296 and UCL line intensities in Figure 3.48. To the best of author's knowledge, this is the most accurate intensity measurement reported on an asymmetric isotopologue of carbon dioxide. From the Figure 3.48 it is readily seen that only the UCL line intensities for P(7), P(8) and P(9) lines match the experimental error bar. An average systematic shift of +1% is observed for the UCL intensities, +1.5% for Ames and +2.0% for CDSD-296. Thus, one can tentatively conclude on plausible sub-percent accuracy of UCL line intensities for this band.

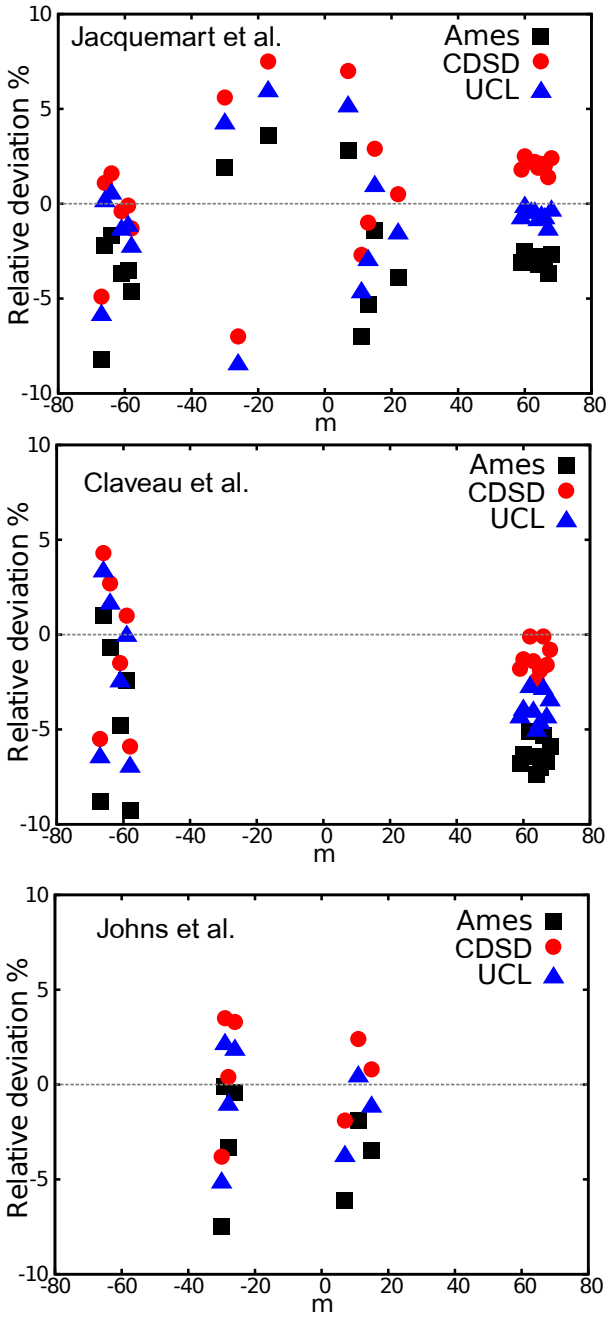

Figure 3.49: Ames, CDSD-296 and UCL line intensities for the 00011 – 00001 band of $^{16}O^{12}C^{17}O$ compared to three experimental works by: Jacquemart *et al.* [211] (uppermost panel), Claveau *et al.* [212] (middle panel) and Johns *et al.* [213](lowest panel). Blue triangles, red dots and black squares denote relative deviations from the measurement (in %) of UCL, CDSD-296 and Ames line intensities respectively. *m* labels rotational transitions and corresponds to *J*(lower)+1 for the R branch and -*J*(lower) for the P branch.

Figure 3.49 compares transition intensities from different measurements for

the asymmetric stretching fundamental (00011 – 00001 band) of the 627 isotopologue. Experiments by Jacquemart *et al.* [211] (uppermost panel in Figure 3.49), Claveau *et al.* [212] (middle panel in Figure 3.49) have stated 5% systematic uncertainty and undetermined statistical uncertainty, while measurements by Johns *et al.* [213] (lowest panel in Figure 3.49) have 2% stated systematic uncertainty and 2-3% statistical uncertainty. Ames, CDSD and UCL line lists give similar deviations from experiments, showing systematic shifts smaller than 5%. For all three panels in Figure 3.49, Ames transition intensities are usually weaker than UCL intensities, whereas CDSD intensities are usually stronger than UCL intensities. At the same time UCL lines give the smallest systematic deviation from experiments.

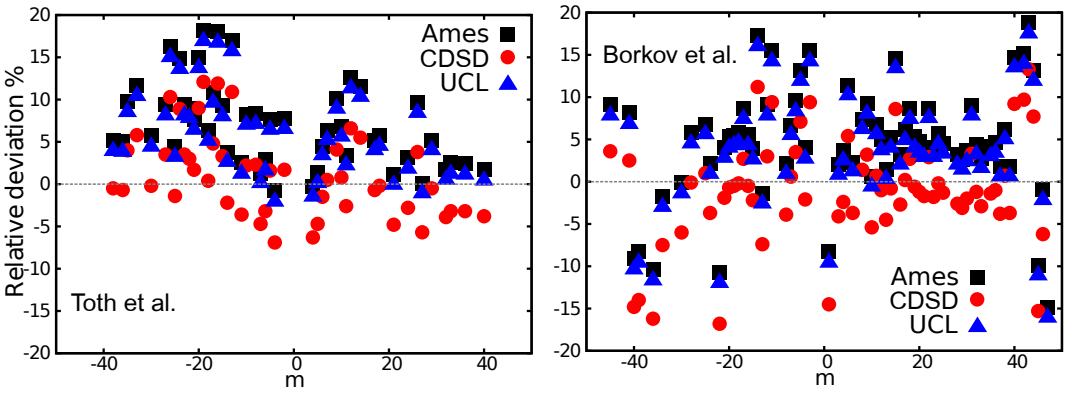

Figure 3.50: Ames, CDSD-296 and UCL line intensities for the 20011 – 00001 band of $^{16}O^{13}C^{17}O$ compared to two experimental works by: Toth *et al.* [214] (left panel) and Borkov *et al.* [190] (right panel). Blue triangles, red dots and black squares denote relative deviations from the measurement (in %) of UCL, CDSD-296 and Ames line intensities respectively. *m* labels rotational transitions and corresponds to *J*(lower)+1 for the R branch and -*J*(lower) for the P branch.

Figure 3.50 displays comparison between two experimental studies by Toth *et al.* [214] (left panel) and Borkov *et al.* [190] (right panel) respectively, and three line lists: Ames, CDSD and UCL. The former experiment has stated 2.5% systematic uncertainty and 10% statistical uncertainty, while the latter experiment has 4% systematic uncertainty and 0.5 - 7% statistical uncertainty. The agreement between measurements and line lists reflects the relatively high uncertainties, showing similar statistical scatter for all three line lists, but essentially smaller systematic deviation for the CDSD line list, which was constructed by fitting to measurements

by Toth *et al.* Systematic deviation from experiment is again very similar (around 1%) for UCL and Ames intensities. Also, CDSD, Ames and UCL follow the same pattern, indicating that the statistical scatter visible in Figure 3.50 is of experimental origin.

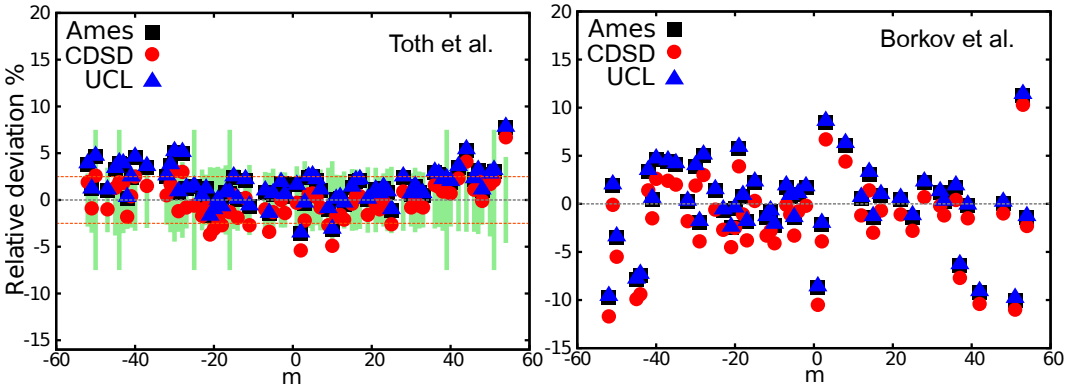

Figure 3.51: Ames, CDSD-296 and UCL line intensities for the 10011 – 00001 band of $^{16}O^{13}C^{18}O$ compared to two experimental works by: Toth *et al.* [214] (left panel) and Borkov *et al.* [215] (right panel). Blue triangles, red dots and black squares denote relative deviations from the measurement (in %) of UCL, CDSD-296 and Ames line intensities respectively. *m* labels rotational transitions and corresponds to *J*(lower)+1 for the R branch and -*J*(lower) for the P branch. In the left panel experimental error bars were added together with horizontal orange dashed lines indicating experimental uncertainty for the systematic shift in the transition intensity.

In Figure 3.51, which compares Ames, CDSD and UCL line lists to experiments by Toth *et al.* [214] (left panel) and Borkov *et al.* [215] (right panel), large deviations of Ames and UCL from measured line intensities are visible for several lines of the P branch of the 10011 – 00001 band in $^{16}O^{13}C^{18}O$. Ames and UCL line list provide similar values of transition intensities for these lines (agree within 2%), whereas CDSD intensities do not exhibit any unusual deviation. This observation can be rationalized by the fact that effective operators used to construct the CDSD database were parametrized by experimental intensities from ref. [214]. The statistical scatter of the measured line intensities indicates insufficient experimental precision. Average systematic shift from measurements is within 1% from experiment for CDSD, Ames and UCL line lists.

Another problem to address is how intensities of lines transfer between iso-

topologues for the Ames and UCL line lists, and how do they relate to CDSD-296. It is eye-catching in Figure 3.52 that Ames and UCL intensities for the 00011 – 00001 and 01101 – 00001 bands are very similar, showing agreement at $< 0.5\%$ level for the majority of lines. In contrast, line intensities from CDSD give significant systematic shifts and noticeable arc structures, characteristic for the empirically determined quantities. Therefore, we may expect Ames and UCL to exhibit similar behavior with isotopic substitution. Here, no discontinuity in intensity pattern around $J = 0$ is observed for the Ames line lists, unlike for the main isotopologue [161].

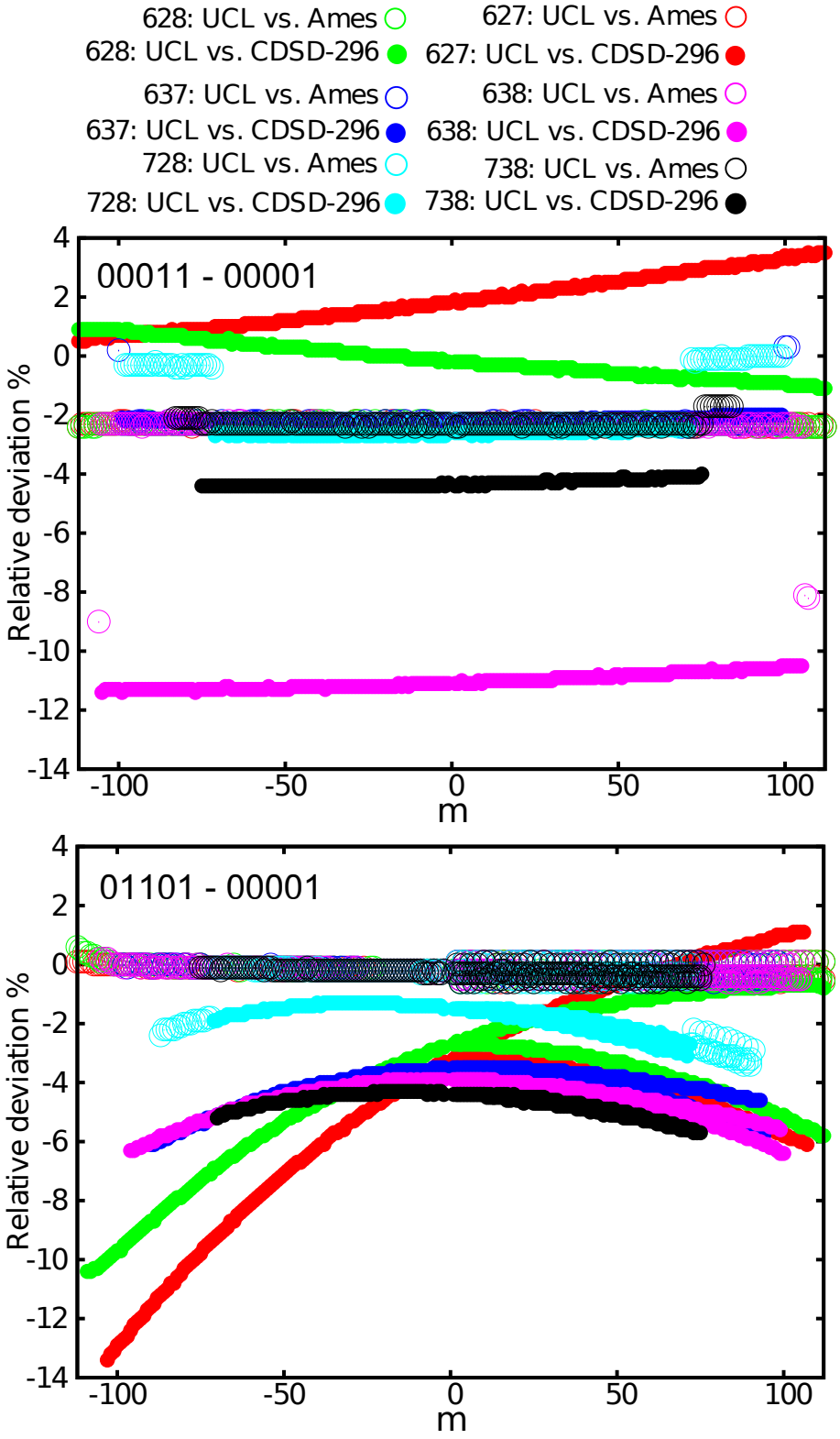

Figure 3.52: Comparison of intensities of two fundamental bands for all six asymmetric isotopologues of CO_2, between UCL, Ames and CDSD line lists. m labels rotational transitions and corresponds to J(lower)+1 for the R branch and -J(lower) for the P branch.

3.12.2 Comparison with other line lists

Table 3.9 compares measured band intensities for six asymmetric isotopologues of CO_2 to the calculated values from the Ames-1, UCL and CDSD-296 line lists.

Table 3.9: Band statistics for the asymmetric isotopologues of CO_2: 628,627,637,638,728,738. Selected are the strongest bands of each isotopologue, that have high quality experimental intensities available. The strongest bands of each isotopologue are compared between Ames-1, CDSD-296 and UCL line lists and most accurate experiments. Given for each band are the band center in cm^{-1}, the total number of measured lines in the band, J(minimum), J(maximum), the total band strength in cm/molecule, symmetric relative deviation S[a] in %, root-mean square deviation (RMSD)[b] of intensity in %, the polyad number[c] change , the stability of the band based on the scatter factor analysis, reference to experimental data.

			J	J			UCL		Ames		CDSD				
Band	Center	Total	min	max	unc.[e]	Strength	S[a]	RMSD[b]	S	RMSD	S	RMSD	ΔP [c]	T.[d]	Source
628															
00011 – 00001	2328.373	19	4	37	3–7	9.26×10^{-20}	0.9	2.3	-1.4	2.6	0.8	2.3	3	s	[213]
01101 – 00001	660.902	45	1	46	4–6	1.07×10^{-20}	1.3	3.3	1.0	3.3	-1.0	3.4	1	s	[216]
01101 – 00001	660.902	37	43	66	5–7	5.74×10^{-22}	3.9	7.0	3.7	6.9	0.9	5.0	1	s	[217]
10011 – 00001	3674.396	81	0	75	4	2.24×10^{-21}	-1.3	3.0	-1.4	3.1	0.5	2.9	5	s	[215]
10011 – 00001	3674.396	68	0	58	3	2.72×10^{-21}	-2.4	2.7	-2.5	2.7	-0.7	1.3	5	s	[211]
10012 – 00001	3569.661	78	1	76	4	2.97×10^{-21}	-2.2	3.7	-2.9	4.1	-0.3	3.1	5	s	[215]
02201 – 01101	665.733	121	3	52	3–7	9.36×10^{-22}	2.9	7.1	2.7	7.0	1.4	6.5	1	s	[217]
11111 – 01101	3685.269	102	2	62	4–5	1.99×10^{-22}	-1.8	4.5	-1.8	4.5	-0.5	4.1	5	s	[215]
11111 – 01101	3685.269	139	1	64	3–10	2.69×10^{-22}	0.8	23.2	-1.1	3.1	-0.0	2.9	5	s	[207]
11111 – 01101	3685.269	265	9	31	3	7.62×10^{-23}	-1.3	1.8	-1.3	1.8	-0.1	1.3	5	s	[211]
11112 – 01101	3540.235	109	1	69	4–5	1.65×10^{-22}	-0.6	4.4	-1.4	4.6	-0.1	4.3	5	s	[215]
11112 – 01101	3540.235	150	1	61	3–10	2.53×10^{-22}	-1.0	2.9	-1.8	3.3	-0.5	2.8	5	s	[207]
11112 – 01101	3540.235	19	9	36	3	5.36×10^{-23}	-1.5	1.8	-2.3	2.5	-0.7	1.4	5	s	[211]
10001 – 01101	701.257	78	2	52	3–7	4.52×10^{-22}	-1.8	3.8	-2.3	4.1	0.1	3.1	1	s	[217]
20012 – 00001	4904.123	106	0	62	3–10	1.13×10^{-22}	-1.7	3.1	-1.0	2.8	-0.2	2.8	7	s	[207]
20012 – 00001	4904.123	3	7	9	1	4.91×10^{-24}	0.9	1.1	1.6	1.7	2.1	2.2	7	s	[203]
20012 – 00001	4904.123	51	1	45	3	7.50×10^{-23}	-3.2	3.3	-2.5	2.6	-1.8	1.9	7	s	[211]
20012 – 00001	4904.123	116	0	67	1–2	1.28×10^{-22}	-0.2	1.4	0.5	1.5	1.4	2.2	7	s	[31]
20012 – 00001	4904.123	117	0	67	4–6	1.23×10^{-22}	-2.2	3.7	-1.5	3.4	-0.6	3.1	7	s	[190]
10002 – 01101	594.837	48	2	41	5–7	2.46×10^{-22}	17.5	19.5	17.6	19.5	1.5	8.1	1	s	[217]
20013 – 00001	4790.523	103	0	67	3–10	4.40×10^{-23}	-0.7	2.7	-0.3	2.6	0.4	2.8	7	s	[207]
20013 – 00001	4790.523	60	0	43	3	3.61×10^{-23}	-1.9	2.4	-1.5	2.2	-0.9	1.8	7	s	[211]
20013 – 00001	4790.523	129	0	65	1–2	4.94×10^{-23}	-1.6	3.1	-1.2	3.0	-0.4	2.5	7	s	[31]
20013 – 00001	4790.523	114	0	63	4–5	4.77×10^{-23}	-1.9	4.2	-1.6	4.0	-0.8	3.8	7	s	[190]
20011 – 00001	5041.845	82	0	48	3–10	2.29×10^{-23}	-0.5	3.4	0.9	3.5	1.3	3.8	7	s	[207]
20011 – 00001	5041.845	40	2	57	3–5	1.18×10^{-23}	-2.6	3.3	-1.2	2.4	-0.8	2.0	7	s	[211]

20011 – 00001	5041.845	110	0	58	4–6	2.39×10^{-23}	-3.7	5.7	2.3	4.9	-1.7	4.6	7	s	[190]
00021 – 00001	4640.227	69	0	47	3–10	1.08×10^{-23}	-2.4	3.1	-1.9	2.8	-1.1	2.3	6	s	[218]
00021 – 00001	4640.227	94	0	62	4–10	1.12×10^{-23}	-2.0	4.6	-1.6	4.4	-0.6	4.2	6	s	[207]
00021 – 00001	4640.227	97	0	56	3–10	1.29×10^{-23}	-0.1	2.4	0.3	2.4	1.2	2.9	6	s	[215]
00021 – 00001	4640.227	119	0	62	4–10	1.43×10^{-23}	-2.5	4.9	-2.1	4.7	-1.1	4.2	6	s	[190]
11102 – 10002	642.338	41	4	33	5–7	4.05×10^{-23}	3.8	6.3	3.6	6.2	-3.5	6.0	1	s	[217]
20002 – 00001	2613.511	102	0	57	3–10	1.98×10^{-23}	-0.9	3.2	-2.6	4.0	0.1	3.3	4	s	[207]
20002 – 00001	2613.511	73	0	47	3	1.80×10^{-23}	-0.6	1.0	-2.3	2.5	0.2	0.8	4	s	[211]
10001 – 00001	1365.107	92	0	64	5	3.05×10^{-23}	1.8	3.1	-0.4	2.5	0.3	2.8	2	s	[219]
10002 – 00001	1260.161	99	0	62	5	2.90×10^{-23}	0.4	3.0	-	-	-0.8	3.0	2	s	[219]
11101 – 10001	683.566	35	8	35	5–7	2.37×10^{-23}	2.0	4.4	1.6	4.2	2.3	4.5	1	s	[217]
20003 – 00001	2500.024	104	0	61	3–11	1.27×10^{-23}	-1.1	3.9	-3.3	5.0	-0.7	3.2	4	s	[207]
20003 – 00001	2500.024	62	3	42	3	1.00×10^{-23}	-0.2	0.8	-2.3	2.4	0.5	1.3	4	s	[211]
01111 – 01101	2318.568	20	18	69	3–7	1.96×10^{-23}	-2.6	4.4	-4.9	6.1	-2.5	4.4	3	s	[220]
21112 – 01101	4898.372	146	2	53	3–10	7.66×10^{-24}	3.6	4.6	4.2	5.1	0.5	3.1	7	u	[207]
21112 – 01101	4898.372	46	2	35	3–23	3.38×10^{-24}	13.0	44.6	13.7	44.9	9.6	43.2	7	u	[190]
21112 – 01101	4898.372	127	2	49	4–11	6.52×10^{-24}	-3.2	9.2	-2.6	9.0	-6.3	10.7	7	u	[31]
20013 – 10002	3531.097	32	0	47	4	6.70×10^{-24}	0.0	5.1	-0.8	5.2	-1.0	5.3	5	s	[207]
20013 – 10002	3531.097	49	0	49	3–8	1.05×10^{-23}	1.6	2.7	0.8	2.4	0.5	2.4	5	s	[215]
11101 – 00001	2047.133	62	2	63	3–33	9.79×10^{-24}	1.8	6.6	11.1	18.6	1.2	4.8	3	u	[221]
11101 – 00001	2047.133	25	11	41	3	5.38×10^{-24}	-2.1	2.8	8.0	9.6	-3.3	3.7	3	u	[211]
20012 – 10002	3648.313	26	4	45	4	4.92×10^{-24}	-0.2	4.2	-0.4	4.2	-1.8	4.6	5	s	[207]
20012 – 10002	3648.313	37	3	46	3–11	7.19×10^{-24}	0.7	2.4	0.5	2.3	-0.9	2.4	5	s	[215]

627

00011 – 00001	2345.147	7	6	30	2–4	6.24×10^{-21}	-1.0	2.7	-3.3	4.1	0.7	2.6	3	s	[213]
00011 – 00001	2345.147	15	58	68	5	9.09×10^{-23}	-3.2	4.2	-5.5	6.1	-1.1	2.7	3	s	[212]
00011 – 00001	2345.147	15	58	68	3	9.09×10^{-23}	-3.1	4.2	-5.5	6.1	-1.1	2.8	3	s	[222]
00011 – 00001	2345.147	23	6	68	5	8.45×10^{-21}	-0.8	3.2	-3.1	4.4	1.2	3.4	3	s	[211]
01101 – 00001	667.005	35	3	39	4–8	1.44×10^{-21}	0.5	3.4	0.3	3.4	-2.9	4.9	1	s	[212]
01101 – 00001	667.005	38	2	56	5	1.24×10^{-21}	4.5	7.5	4.3	7.4	1.4	5.4	1	s	[216]
01111 – 01101	2331.998	60	5	53	3	1.48×10^{-21}	-2.1	3.4	-4.4	5.1	-0.2	2.6	3	s	[212]
01111 – 01101	2331.998	41	9	53	5	9.37×10^{-22}	-3.0	3.8	-5.3	5.8	-1.0	2.8	3	s	[211]
10011 – 00001	3694.108	87	0	59	5	7.70×10^{-22}	-2.2	2.4	-2.3	2.5	-2.1	2.3	5	s	[211]
10011 – 00001	3694.108	95	0	80	4	5.86×10^{-22}	-1.5	3.2	-1.6	3.3	-1.2	3.3	5	s	[215]
10012 – 00001	3590.512	70	0	80	4	4.44×10^{-22}	-1.5	3.5	-	-1.2	3.3	5.0	3	s	[215]
02201 – 01101	661.326	80	4	46	5	1.48×10^{-22}	3.4	5.4	3.1	5.2	-0.2	4.2	1	s	[212]
10001 – 01101	709.023	61	2	37	5	7.78×10^{-23}	-2.7	4.5	-3.2	4.8	-0.2	3.5	1	s	[212]
20012 – 00001	4938.605	71	0	60	5	1.55×10^{-23}	-2.6	2.7	-1.9	2.1	-0.3	0.9	7	s	[211]
20012 – 00001	4938.605	28	12	47	1–11	9.01×10^{-24}	-0.0	23.7	0.7	23.7	2.3	23.6	7	s	[31]
20012 – 00001	4938.605	134	0	73	4–6	2.39×10^{-23}	-1.6	3.4	-0.9	3.2	0.8	3.2	7	s	[190]
20012 – 00001	4938.605	83	0	62	2	1.54×10^{-23}	-0.2	1.9	0.4	1.9	2.1	3.0	7	s	[223]
10002 – 01101	604.522	43	3	35	5	4.73×10^{-23}	11.6	13.5	11.7	13.5	-0.2	6.5	1	s	[212]
11111 – 01101	3704.311	150	2	72	4–10	4.03×10^{-23}	-0.8	3.5	-0.8	3.6	-0.4	3.5	5	s	[215]
11112 – 01101	3560.198	133	1	66	4–10	3.10×10^{-23}	-0.5	3.9	-1.3	4.1	-0.5	4.0	5	s	[215]

20013 – 00001	4820.757	43	0	60 5	3.02×10^{-24}	-2.0	2.4	-1.7	2.2	-0.3	1.3 7	s	[211]
20013 – 00001	4820.757	123	0	68 4–7	7.06×10^{-24}	-0.6	2.6	-0.3	2.5	1.3	2.8 7	s	[190]
20013 – 00001	4820.757	38	4	47 2–13	3.86×10^{-24}	7.9	18.3	8.2	18.5	9.6	19.2 7	s	[31]
20013 – 00001	4820.757	80	0	55 2	5.53×10^{-24}	0.2	1.6	0.5	1.7	1.9	2.5 7	s	[223]
20011 – 00001	5069.677	75	0	62 5	4.01×10^{-24}	-2.9	3.1	-1.6	1.9	-0.3	1.1 7	s	[211]
20011 – 00001	5069.677	131	0	67 4–7	6.07×10^{-24}	-2.0	3.5	-0.7	2.9	0.7	3.0 7	s	[190]
20011 – 00001	5069.677	82	0	61 2	4.21×10^{-24}	3.4	3.7	4.7	4.9	6.0	6.2 7	s	[223]
21112 – 01101	4930.435	296	1	59 4–7	2.67×10^{-24}	0.5	4.1	1.2	5.0	2.4	4.7 7	u	[190]
00021 – 00001	4654.446	280	0	62 4–7	2.11×10^{-24}	-	0.8	4.3	0.1	4.2	6.0 2	s	[190]
20012 – 10002	3665.553	48	1	52 4	1.49×10^{-24}	-0.0	3.1	-0.2	3.1	1.0	3.2 5	s	[215]
10001 – 00001	1377.543	52	1	43 5	1.35×10^{-24}	1.7	4.7	-0.5	4.4	-0.3	4.3 2	s	[219]

637

00011 – 00001	2270.243	18	4	43 5	1.45×10^{-22}	1.9	2.6	-0.4	1.8	-0.3	1.8 3	s	[222]
10011 – 00001	3607.792	55	0	62 4	7.03×10^{-24}	5.6	6.6	5.5	6.5	-0.6	3.6 5	s	[215]
10011 – 00001	3607.792	28	1	48 3–10	4.96×10^{-24}	4.7	7.1	4.6	7.0	-1.6	5.7 5	s	[214]
10012 – 00001	3506.855	56	1	61 4	2.98×10^{-24}	5.3	6.1	4.5	5.4	-0.9	3.2 5	s	[215]
10012 – 00001	3506.855	12	1	38 3–13	9.00×10^{-25}	6.9	10.2	6.1	9.7	0.4	7.6 5	s	[214]
11111 – 01101	3620.197	51	5	53 4–7	3.85×10^{-25}	6.4	8.7	6.3	8.7	0.6	5.9 5	s	[215]
20012 – 00001	4848.635	75	0	50 4–9	1.91×10^{-25}	5.1	7.2	5.8	7.7	-0.8	5.1 7	s	[190]
20012 – 00001	4848.635	65	2	47 4–10	3.63×10^{-25}	5.1	7.1	5.7	7.6	-0.9	5.0 7	s	[214]
11112 – 01101	3482.365	66	4	55 4–27	1.73×10^{-25}	5.0	7.0	5.6	7.4	-1.0	4.9 5	s	[215]
20011 – 00001	4956.342	48	1	40 10	7.97×10^{-26}	5.8	7.6	7.1	8.6	1.1	5.0 7	s	[214]
20011 – 00001	4956.342	69	0	47 4–9	9.89×10^{-26}	3.4	7.5	4.6	8.1	-1.2	6.8 7	s	[190]
20013 – 00001	4722.116	49	3	44 4–9	1.93×10^{-26}	3.9	8.5	4.1	8.6	-0.3	7.5 7	s	[190]
00031 – 00001	6753.152	86	0	55 10	1.01×10^{-26}	5.9	7.6	-2.2	5.3	2.0	5.1 9	s	[191]
00021 – 00001	4528.497	45	4	38 4–12	5.86×10^{-27}	2.5	10.3	2.9	10.4	0.7	10.3 6	s	[215]
30012 – 00001	6185.757	43	2	43 10	1.99×10^{-27}	-6.1	10.7	-3.8	9.6	-0.2	8.9 9	s	[191]
20013 – 10002	3451.176	5	15	34 4	1.42×10^{-27}	3.7	5.4	2.8	4.9	-1.6	4.4 5	s	[215]
20011 – 10001	3609.826	2	12	14 4	1.22×10^{-27}	7.7	7.7	7.6	7.7	2.2	2.5 5	s	[215]
30013 – 00001	6074.545	28	3	33 10	7.97×10^{-28}	-7.2	11.6	-5.8	10.8	-0.3	9.1 9	u	[191]
01131 – 01101	6715.988	80	1	39 10	5.20×10^{-28}	0.7	9.0	-7.5	11.7	-2.8	9.3 9	s	[191]
21112 – 01101	4820.294	2	17	23 5–8	3.20×10^{-28}	11.3	13.5	11.9	13.9	4.6	8.6 7	u	[190]
30011 – 00001	6320.672	31	2	40 10	2.19×10^{-28}	-19.4	21.6	-14.4	17.2	-0.4	9.5 9	s	[191]
10031 – 00001	8040.610	6	6	31 10	4.56×10^{-29}	-	-	-0.4	10.4	-8.2	13.3 11	s	[191]
40013 – 00001	7417.626	25	4	31 10	2.22×10^{-29}	-14.4	29.4	-12.0	28.3	-40.6	48.4 11	s	[224]
10032 – 00001	7917.301	10	27	46 10	1.78×10^{-29}	21.7	31.4	24.5	33.4	23.9	29.0 11	s	[224]

638

10011 – 00001	3588.279	51	0	54 4	3.13×10^{-23}	0.1	4.4	-0.1	4.4	-1.8	4.7 5	s	[215]
10011 – 00001	3588.279	76	0	61 3–10	4.79×10^{-23}	1.7	2.8	1.6	2.7	-0.0	2.2 5	s	[214]
01111 – 01101	2249.097	63	6	68 3–10	7.07×10^{-23}	7.9	9.3	5.5	7.4	-3.3	5.9 3	s	[214]
10012 – 00001	3491.854	40	2	56 4	1.32×10^{-23}	2.2	4.2	1.5	3.8	-0.8	3.9 5	s	[215]
10012 – 00001	3491.854	82	1	60 3–21	2.74×10^{-23}	3.0	4.3	2.2	3.9	0.0	2.9 5	s	[214]

10012 – 10002	2242.514	30	3	51	3–10	2.97×10^{-24}	10.0	10.4	7.7	8.2	-1.1	3.0	3	s	[214]
20012 – 00001	4815.291	94	0	55	3–10	1.44×10^{-24}	19.0	19.1	19.7	19.7	-0.1	1.7	7	s	[214]
20012 – 00001	4815.291	58	2	40	4–10	9.72×10^{-25}	0.6	21.0	1.3	21.1	-19.0	28.6	7	s	[190]
20012 – 00001	4815.291	1	17	18	5	5.78×10^{-26}	114.4	23.8	115.3	24.0	87.0	18.1	7	s	[31]
11112 – 01101	3457.958	46	5	46	4	8.69×10^{-25}	3.1	7.3	2.2	7.0	0.0	6.6	5	s	[215]
11112 – 01101	3457.958	63	2	40	10	1.28×10^{-24}	5.9	7.2	5.0	6.5	3.0	4.9	5	s	[214]
11111 – 01101	3597.621	10	16	27	4–7	4.87×10^{-25}	3.0	10.4	2.9	10.4	2.0	10.3	5	s	[215]
11111 – 01101	3597.621	37	2	37	10	1.60×10^{-24}	8.3	9.2	8.3	9.1	7.3	8.3	5	s	[214]
10011 – 10001	2240.770	19	5	48	3–11	1.30×10^{-24}	12.0	12.8	9.6	10.6	0.8	4.6	3	s	[214]
20011 – 00001	4925.749	121	0	48	3–14	1.09×10^{-24}	31.4	106.3	32.8	107.7	8.3	86.6	2	s	[190]
02211 – 02201	2231.148	8	14	52	3–10	6.02×10^{-25}	16.8	18.3	14.4	16.2	5.6	9.2	3	s	[214]
20013 – 00001	4690.702	69	1	47	3–10	2.09×10^{-25}	19.9	20.1	20.1	20.3	-1.1	2.9	7	s	[214]
20013 – 00001	4690.702	12	7	27	5–17	4.63×10^{-26}	5.4	27.2	5.6	27.2	-16.4	31.7	7	s	[190]
10001 – 00001	1336.378	28	7	37	5	2.36×10^{-25}	-4.1	7.7	-6.4	9.2	-0.3	6.3	2	s	[219]
00021 – 00001	4507.263	74	1	43	11	1.85×10^{-25}	20.8	21.0	21.2	21.3	-0.3	2.7	6	s	[214]
20002 – 00001	2583.005	22	6	33	15	7.86×10^{-26}	9.0	17.2	7.3	16.4	-0.2	14.6	4	s	[225]
00031 – 00001	6727.618	135	0	74	10	6.65×10^{-26}	17.8	18.7	9.4	11.1	0.0	5.0	9	s	[191]
10002 – 00001	1238.299	14	8	26	5	5.78×10^{-26}	-9.5	10.7	-12.0	13.0	-0.3	4.8	2	s	[219]
11101 – 00001	2005.545	20	10	36	20	4.98×10^{-26}	-3.9	25.6	10.6	27.6	-1.7	25.8	3	u	[226]
21112 – 01101	4797.940	50	4	33	11	4.28×10^{-26}	19.3	19.7	19.8	20.2	0.3	4.1	7	u	[214]
30012 – 00001	6139.386	106	0	65	10	1.72×10^{-26}	6.6	11.6	9.0	13.1	-0.8	9.4	9	s	[191]
30013 – 00001	6025.888	108	0	61	10	1.42×10^{-26}	8.7	12.7	10.1	13.8	-0.8	9.3	9	u	[191]
01131 – 01101	6692.165	211	1	64	10	5.57×10^{-27}	17.0	19.4	8.7	12.6	-0.1	8.1	9	s	[191]
30011 – 00001	6278.752	74	0	61	10	1.87×10^{-27}	1.5	11.5	8.2	17.0	1.1	10.9	9	s	[191]
10031 – 00001	8007.762	60	1	42	5–10	1.85×10^{-27}	3.4	12.1	5.4	13.0	-0.4	11.8	11	s	[227]
31113 – 01101	5994.504	112	1	47	10	8.80×10^{-28}	12.5	18.8	18.5	43.8	0.1	12.3	9	u	[191]
10032 – 00001	7910.834	63	0	62	5–10	8.49×10^{-28}	19.4	20.1	21.9	22.5	22.6	23.2	11	s	[224]
31112 – 01101	6145.467	86	1	47	10	8.32×10^{-28}	7.6	15.4	9.8	16.6	-0.5	13.3	9	u	[191]
30014 – 00001	5875.121	42	1	46	10	6.23×10^{-28}	3.9	12.5	5.1	12.9	-0.1	11.8	9	s	[191]
02231 – 02201	6658.965	121	2	42	10	1.93×10^{-28}	18.5	20.9	10.1	13.9	0.9	9.2	9	s	[191]
40013 – 00001	7350.955	42	0	52	5–10	1.72×10^{-28}	-2.7	12.4	-0.3	12.1	-24.5	27.5	11	s	[224]
31111 – 01101	6307.493	76	5	44	10	1.57×10^{-28}	-0.7	13.6	5.0	14.5	-1.1	13.6	9	s	[191]
11132 – 01101	7862.551	119	4	44	5–10	1.25×10^{-28}	24.5	26.9	26.9	29.2	29.4	30.5	11	s	[224]
10032 – 10002	6665.932	51	0	42	10	8.38×10^{-29}	10.2	15.1	1.5	11.2	-1.3	10.9	9	s	[191]
20022 – 00001	7019.329	51	1	47	5–10	8.03×10^{-29}	10.8	20.2	13.6	21.9	17.8	23.3	10	s	[224]
40012 – 00001	7480.795	49	2	49	5–10	7.96×10^{-29}	4.8	12.7	9.6	15.4	-14.4	17.6	11	s	[224]
40014 – 00001	7219.259	35	1	32	5–10	6.50×10^{-29}	10.6	13.7	12.0	14.9	-12.8	15.5	11	u	[224]
11121 – 00001	6446.108	47	3	46	10	6.47×10^{-29}	7.1	16.9	7.9	17.1	-1.0	15.0	9	s	[191]
10031 – 10001	6669.082	39	2	40	10	3.79×10^{-29}	13.2	18.7	4.0	13.8	-8.2	15.4	9	s	[191]
20021 – 00001	7123.107	39	2	46	5–10	2.86×10^{-29}	10.0	24.4	14.8	26.9	23.0	23.0	10	s	[224]
11122 – 00001	6316.706	38	2	44	10	2.78×10^{-29}	7.4	16.6	-4.3	15.3	-3.5	13.6	9	s	[191]
40013 – 10002	6110.334	16	4	33	10	2.39×10^{-29}	9.3	16.5	11.4	17.8	1.3	12.9	9	s	[191]
40011 – 00001	7651.175	13	4	30	10–30	2.36×10^{-30}	17.2	30.3	30.1	39.6	-	-	11	s	[224]
20033 – 10002	7832.367	13	7	28	10–30	1.48×10^{-30}	26.7	35.7	23.5	32.0	-	-	11	s	[224]

10012 – 00001	3546.567	83	0	62	3–10	1.74×10^{-24}	10.2	11.0	9.5	10.4	-1.5	4.6	5	s	[207]
10012 – 00001	3546.567	227	0	62	3	1.35×10^{-24}	8.5	8.7	7.9	8.0	-3.1	3.5	5	s	[211]
10012 – 00001	3546.567	75	0	83	4	1.33×10^{-24}	9.2	9.5	8.5	8.8	-2.4	3.6	5	s	[215]
00011 – 00001	2291.385	17	37	68	3	4.15×10^{-24}	2.3	3.8	-0.0	3.0	-0.3	3.0	3	s	[211]
10011 – 00001	3655.831	67	0	60	3–10	1.14×10^{-24}	7.9	8.3	7.8	8.2	-3.3	4.1	5	s	[207]
10011 – 00001	3655.831	64	0	59	3	9.22×10^{-25}	8.8	8.9	8.8	9.8	-2.3	2.5	5	s	[211]
10011 – 00001	3655.831	65	1	72	4	8.15×10^{-25}	10.0	10.3	9.9	10.3	-1.0	2.9	5	s	[215]
11112 – 01101	3516.783	105	3	51	3–10	1.12×10^{-25}	16.1	16.5	15.3	15.7	4.6	5.8	5	s	[207]
11112 – 01101	3516.783	65	3	51	3	6.95×10^{-26}	10.5	10.7	9.7	9.9	-1.2	2.3	5	s	[211]
11112 – 01101	3516.783	122	1	68	4	8.27×10^{-26}	11.8	12.1	11.0	11.3	0.4	2.6	5	s	[215]
11111 – 01101	3665.648	55	3	43	3–25	5.78×10^{-26}	15.1	16.0	15.1	16.0	4.3	6.9	5	s	[207]
11111 – 01101	3665.648	23	9	33	3	2.70×10^{-26}	10.8	10.9	10.9	10.9	0.1	1.1	5	s	[211]
11111 – 01101	3665.648	96	2	65	4	7.25×10^{-26}	11.3	11.8	11.3	11.8	0.7	3.5	5	s	[215]
20012 – 00001	4867.609	81	2	54	3–11	4.26×10^{-26}	10.6	10.9	11.2	11.5	-0.2	2.3	7	s	[207]
20012 – 00001	4867.609	51	0	60	3	2.36×10^{-26}	10.6	10.7	11.3	11.3	-0.2	1.1	7	s	[211]
20012 – 00001	4867.609	125	0	68	4–6	5.01×10^{-26}	11.1	11.7	11.8	12.4	0.4	3.8	7	s	[190]
20013 – 00001	4754.845	83	0	51	3–10	2.28×10^{-26}	10.7	11.1	11.0	11.4	-1.3	3.1	7	s	[207]
20013 – 00001	4754.845	54	1	57	3	1.50×10^{-26}	12.0	12.0	12.3	12.3	-0.1	0.8	7	s	[211]
20013 – 00001	4754.845	122	0	67	4–6	2.63×10^{-26}	11.7	12.2	12.0	12.5	-0.3	3.6	7	s	[190]
20011 – 00001	5013.232	49	2	42	3–14	5.03×10^{-27}	5.5	7.6	6.9	8.6	-5.7	7.6	7	s	[207]
20011 – 00001	5013.232	56	1	47	3	4.83×10^{-27}	11.8	11.9	13.2	13.2	0.7	1.2	7	s	[211]
20011 – 00001	5013.232	106	0	59	4–6	7.94×10^{-27}	10.0	11.2	11.4	12.5	-1.1	5.2	7	s	[190]
21112 – 01101	4861.905	58	5	31	3–30	1.65×10^{-27}	9.6	11.1	10.2	11.6	-1.5	5.8	7	u	[207]
21112 – 01101	4861.905	157	2	51	4–8	3.10×10^{-27}	11.3	13.1	11.8	13.6	0.3	6.6	7	u	[190]
20013 – 10002	3509.533	35	1	60	4	3.56×10^{-27}	13.3	13.8	12.5	13.0	2.3	4.4	5	s	[215]
20012 – 10002	3623.717	35	1	38	4	2.69×10^{-27}	12.9	13.5	12.7	13.3	1.9	4.4	5	s	[215]
00021 – 00001	4621.032	103	0	60	4–6	1.38×10^{-27}	15.0	21.9	15.5	22.2	2.2	15.5	6	s	[190]
00021 – 00001	4621.032	84	0	52	4–5	1.13×10^{-27}	12.2	12.7	12.7	13.1	-0.5	3.3	6	s	[215]
00031 – 00001	6894.409	118	0	69	10	2.06×10^{-27}	15.1	16.1	6.2	8.2	-0.1	3.9	9	s	[191]
21113 – 01101	4709.841	141	2	53	4–6	1.65×10^{-27}	13.7	15.0	13.9	15.2	1.5	6.1	7	s	[190]
21113 – 01101	4709.841	14	34	49	4–6	6.01×10^{-29}	12.4	13.0	12.7	13.2	0.2	3.7	7	s	[215]
20011 – 10001	3662.486	24	5	50	4–6	1.30×10^{-27}	16.6	17.7	16.7	17.7	6.2	8.7	5	s	[215]
20012 – 10001	3511.956	29	0	50	4–6	1.04×10^{-27}	14.1	14.8	13.5	14.2	2.5	4.9	5	s	[215]
00011 – 10002	1073.481	39	5	41	5	1.02×10^{-27}	-11.1	12.0	-15.1	15.7	-0.2	4.4	1	s	[222]
30013 – 00001	6073.047	121	0	68	10	8.58×10^{-28}	2.8	16.5	3.7	9.5	1.4	5.4	9	u	[191]
21111 – 01101	5037.195	115	2	40	4–6	7.38×10^{-28}	9.8	11.8	11.1	13.0	-2.6	7.1	7	u	[190]
12211 – 02201	3645.173	10	27	42	4–6	2.85×10^{-28}	14.2	15.3	14.3	15.4	4.1	7.0	5	s	[215]
30012 – 00001	6207.046	101	0	68	10	2.85×10^{-28}	-0.6	6.6	2.3	6.9	0.2	4.2	9	s	[191]
12212 – 02201	3463.565	24	30	53	4–6	2.83×10^{-28}	11.6	13.4	12.6	14.7	0.3	4.8	5	s	[215]
30014 – 00001	5946.265	103	0	65	10	1.93×10^{-28}	1.3	5.9	2.5	6.2	2.7	5.2	9	s	[191]
30013 – 10002	4826.273	37	3	37	10	1.46×10^{-28}	15.4	33.7	12.6	18.5	-2.1	10.0	7	s	[190]
00011 – 10001	961.639	15	6	28	5	1.40×10^{-28}	-6.2	7.9	-10.8	11.8	-0.3	5.0	1	s	[222]
01131 – 01101	6855.418	141	1	67	10	1.25×10^{-28}	14.9	16.7	6.0	9.6	1.1	5.9	9	s	[191]
30003 – 00001	3809.903	57	1	41	4–6	1.21×10^{-28}	11.9	13.7	11.4	13.2	0.1	5.4	6	u	[215]

21102 – 00001	3256.129	63	6	54	4–6	1.08×10^{-28}	14.6	17.2	13.8	16.2	-0.7	5.5	5	u	[215]
21113 – 11102	3473.795	16	11	32	4–6	9.87×10^{-29}	11.7	13.6	10.8	12.8	0.9	7.0	5	s	[215]
30014 – 10002	4696.570	26	7	35	5–7	5.64×10^{-29}	11.6	14.5	11.8	14.7	-1.4	8.8	7	s	[190]
30014 – 10002	4696.570	3	28	30	4	4.78×10^{-30}	13.1	15.5	14.3	15.6	1.1	6.4	7	s	[215]
31113 – 01101	6047.520	140	1	60	10	4.78×10^{-29}	2.0	7.6	3.3	8.0	-	-	9	u	[191]
01121 – 00001	5255.181	32	7	35	5–7	3.54×10^{-29}	12.1	15.3	2.1	10.0	24.7	25.9	7	s	[190]
30012 – 10001	4860.218	14	11	24	6–8	2.75×10^{-29}	7.7	16.3	8.4	16.6	-2.6	14.5	7	s	[190]
30002 – 00001	3954.525	31	5	33	5–11	2.45×10^{-29}	17.3	19.8	17.3	19.8	-	-	6	s	[215]
31112 – 01101	6217.194	129	1	53	10	2.42×10^{-29}	-0.4	8.5	2.3	8.8	-	-	9	s	[191]
30011 – 00001	6391.247	86	0	51	10	2.39×10^{-29}	-2.2	6.2	4.6	7.4	-	-	9	s	[191]
738															
10011 – 00001	3566.725	39	2	51	4	8.24×10^{-27}	1.8	4.5	1.7	4.5	-1.7	4.5	5	s	[215]
10012 – 00001	3469.362	62	0	66	4	7.67×10^{-27}	2.5	3.7	1.7	3.2	-0.0	2.8	5	s	[215]
11112 – 01101	3441.685	81	4	49	4	6.00×10^{-28}	1.3	4.1	0.4	3.9	-0.5	3.9	5	s	[215]
20012 – 00001	4773.323	56	2	43	4–11	3.36×10^{-28}	-0.6	6.9	0.0	6.9	-3.2	7.5	7	s	[190]
11111 – 01101	3564.013	15	11	34	4	2.25×10^{-28}	6.0	8.4	6.0	8.4	2.8	6.5	5	s	[215]
20013 – 00001	4663.710	38	4	32	5–9	6.25×10^{-29}	2.4	11.5	2.6	11.5	1.1	11.3	7	s	[190]
20013 – 00001	4663.710	20	7	31	4–5	3.31×10^{-29}	1.1	6.3	1.3	6.3	-0.3	6.2	7	s	[215]
20011 – 00001	4887.298	20	6	29	5–17	4.22×10^{-29}	-4.5	12.7	-3.2	12.3	-8.9	14.9	7	s	[190]
00031 – 00001	6698.146	91	0	63	10	2.15×10^{-29}	23.5	24.5	14.9	16.4	-	-	9	s	[191]
30013 – 00001	5972.284	39	3	41	10	3.59×10^{-30}	10.8	16.5	12.3	17.5	-	-	9	s	[191]
30012 – 00001	6085.038	34	4	39	10	3.08×10^{-30}	13.0	18.3	15.5	20.1	-	-	9	s	[191]
01131 – 01101	6662.913	66	1	45	10	8.80×10^{-31}	15.1	18.6	6.3	12.4	-	-	9	s	[191]
10032 – 00001	7869.363	67	2	47	5–10	5.86×10^{-31}	31.0	33.2	33.5	35.6	-	-	11	s	[224]

[a] see eq. 3.25

[b] rmsr: root-mean square residual

[c] The polyad number for CO_2 is defined as: $P = 2v_1 + v_2 + 3v_3$, where v_1, v_2, v_3 are the vibrational quantum numbers of the symmetric stretching, bending and the asymmetric stretching, respectively.

[d] Type of band: Stable('s'), unstable('u')

[e] Uncertainty interval of the measurement (in %), defined as root-mean square of statistical uncertainty plus systematic uncertainty of the measurement.

In general, by looking at Table 3.9, the dipole moment surfaces of Ames and UCL appear to be of similar quality, generating band intensities that differ by few percent. A more detailed analysis reveals that both line lists follow similar intensity trends within a single band as well as between bands. A more detailed investigation of small discrepancies between Ames-1 and UCL has been alredy done in section 3.12.1. For less abundant isotopologues, such as 638 and 728, deviations of theoretical line intensities from experimental values often exceed stated uncertainty of measurements [190, 191, 211, 215], which suggests inaccuracies in retrieval proce-

dure or in isotopic abundances in measured samples. Band intensities given by the CDSD-296 database match more closely the experimentally determined values than the remaining two line lists. The effective dipole moment calculations, on which the CDSD-296 database relies, are supplied with experimental entries, some of which have been taken from the references listed in Table 3.9. For this reason, CDSD-296 generates smaller overall deviations from experiment. Unfortunately, none of these measurements provide sub-percent uncertainty budget for intensities. This means one can conclude only approximately on the mutual relation between the experiments and theoretical studies (most of the measurements give 5-20% uncertainty for the line intensities). Therefore, a comparison to a preferably sub-percent accurate study is needed. Only one such measurement has been performed by Durry *et al.* [203] on three ro-vibrational lines of 628 (see Figure 3.48).

Figure 3.53 gives an overview of the relative agreement of the Ames and UCL line lists to CDSD-296.

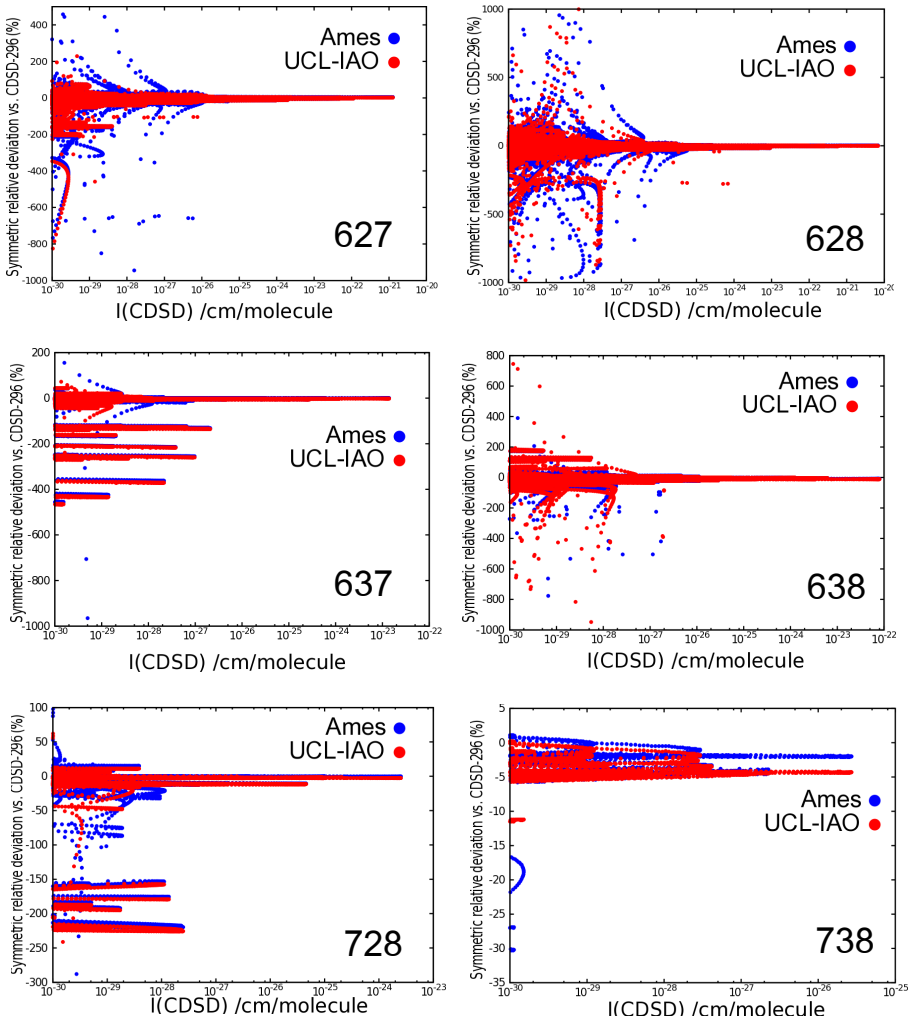

Figure 3.53: Comparison of Ames and UCL line lists with the CDSD-296 database for six isotopologues of CO_2. Red and blue points denote relative percent deviation of UCL and Ames intensities from CDSD intensity, respectively. Symmetric relative deviation (see eq.3.25) is plotted against line intensity (in cm/molecule) from CDSD-296 scaled by the natural abundance.

For strong lines, both Ames and UCL line lists give a good overall match to CDSD-296. For weaker lines, intensity discrepancies between the line lists and CDSD become more visible, reaching several hundreds percent. If Ames and UCL intensities do not nearly coincide, then usually the UCL intensity is much closer to the corresponding CDSD-296 value. A few bands for the 637 and 728 isotopo-

logue are systematically shifted toward large negative deviations in intensity both for Ames and UCL, hence may demand closer attention, and perhaps a re-evaluation in future editions of CDSD.

Figure 3.54 gives an overview comparison between UCL and HITRAN2012 intensities for all six asymmetric isotopologues of CO_2. The characteristic funnel-like shape is followed by the majority of lines. The 728, 637 and 638 isotopologues however, contain few moderately strong bands, exhibiting suspiciously high systematic deviations from the UCL line list. For this reason, is may be believed that intensities of these CDSD-296 bands cannot be trusted, and require refinement by additional experimental data or a theoretical approach. It should be noted that the majority of lines in HITRAN 2012 comes from the effective Hamiltonian calculation also enclosed in the CDSD-296 database.

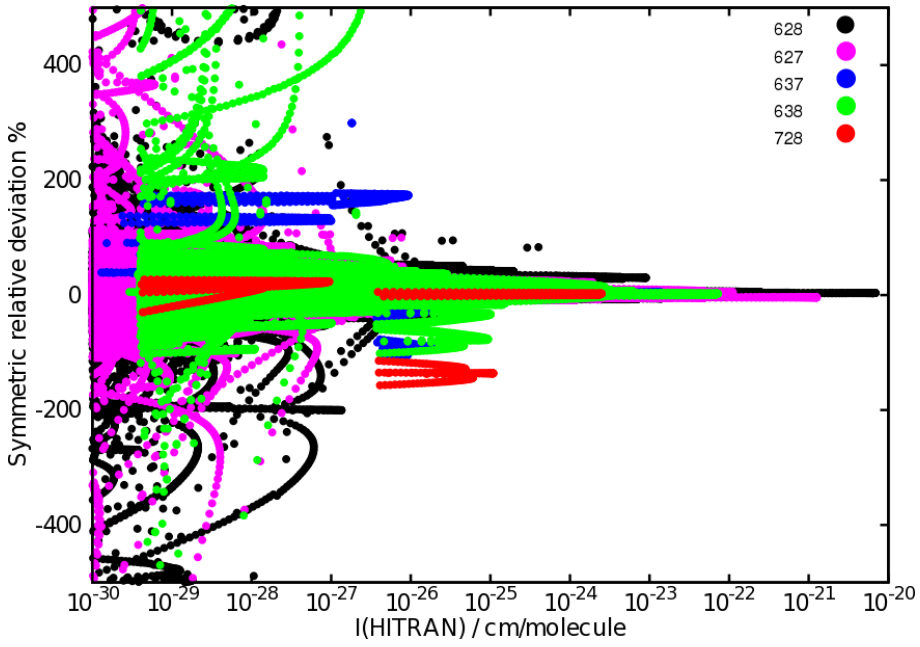

Figure 3.54: General comparison of the UCL and HITRAN 2012 line lists for all six asymmetric isotopologues of CO_2. Symmetric relative deviation is plotted against line intensity (in cm/molecule) from HITRAN 2012 scaled by the natural abundance.

3.13 The radioactive isotopologue (646)

Due to its trace atmospheric abundance, $1.234(14) \times 10^{-12}$ [139], only the strongest ro-vibrational absorption lines of radiocarbon dioxide ($^{14}C^{16}O_2$, 646) are accessible to accurate measurements. There are only 36 lines (all belonging to the 00011–00001 band) which have intensities above 10^{-30} cm/molecule at room temperature. However, a growing number of experiments reaches for ever higher abundances of 646 in measured samples, which creates access to weaker transitions. For this reason, the present line list for 646 was calculated in a wide $J = 0, ..., 130$ range in the 0–8000 cm^{-1} transition wavenumber region, assuming unit abundance.

Out of the strongest lines present in the infrared spectrum of 646, only the $P(20)$ line of the asymmetric stretching fundamental (2209.10 cm^{-1}) is located in a spectral region essentially free of major interferences from other abundant atmospheric species like H_2O or CH_4. For this reason, this line is most commonly chosen as a reference for determination of radioactive carbon concentrations. Therefore, the $P(20)$ line of the asymmetric stretching fundamental plays a distinct role in monitoring of carbon dioxide emission caused by fossil fuel combustion. Although knowledge of the absolute value of the line strength to obtain the ^{14}C concentrations in SCAR measurements performed on fossil samples [147] can be avoided by using a more convoluted experimental procedure, encouraged by a successful retrieval of natural abundance of 646 by utilizing theoretically calculated line intensity (claimed 5% accurate) by Galli *et al.* [26], with the hope that the updated and plausibly sub-percent accurate intensities will be utilized in future experiments as a reference or calibration data. Usually, a sample to be analysed is cooled down to 195 *K* or 170 *K* in order to diminish interference effects from the nearby (separated by 230 MHz) line of the 636 isotopologue ($P(19)$ line of the 05511 – 05501 band). For this reason attention is also paid to line intensities at low temperature for this particular transition. Table 3.10 compares intensities of the $P(20)$ and $P(40)$ lines obtained from several measurements and theoretical calculations together with their respective uncertainties.

Table 3.10: Intensities of the $P(20)$ and $P(40)$ lines of the 00011 – 00001 band for $^{14}CO_2$ taken from different experimental sources.

Reference	Temperature K	Strength(uncertainty) $\times 10^{-18}$ cm/molecule
$P(20)$ Galli *et al.* [26]	195	3.10(15)
$P(20)$ Present study	195	3.07(3)
$P(20)$ Genoud *et al.* [143]	295	2.52(26)
$P(20)$ Present study	295	2.82(3)
$P(20)$ Present study	170	2.97(3)
$P(40)$ McCartt *et al.* [148]	300	0.627(30)
$P(40)$ Present study	300	0.572(6)

Both $P(20)$ and $P(40)$ lines are considered stable according to the transition intensity sensitivity analysis ($\rho = 1.026$). Line intensity given by Galli *et al.* agree to 1% with the UCL value for $T = 195\ K$. Genoud *et al.* gives room temperature line intensity flagged with 10% uncertainty, which lies 11% below the UCL prediction. The $P(20)$ line is 5 times stronger than $P(40)$, however the latter one is located in a less crowded spectral region. From this reason McCartt *et al.* used the $P(40)$ line to produce calibration curve for concentration of radioactive carbon in the SCAR technique, where reference concentrations were determined by accelerator mass spectrometry. In their spectroscopic model, McCartt *et al.* use a line intensity at 300 K taken from measurements by Galli *et al.* [26] (9% above UCL intensity) and line intensities of interfering isotopologues from the HITRAN 2012 database. This leads to negative concentrations resulting from fitted calibration curve. One of the possible reason for that could be inaccurate line strength used in the retrieval model. Of equal importance are however: the accuracy of ^{14}C abundance in samples and the intensities of the satellite lines of other carbon dioxide isotopologues. Line intensities provided by UCL line lists are internally consistent and have been proven to agree within experimental uncertainty to state-of-the-art measurements. Table 3.10 also lists UCL prediction for the line intensity at $T = 170$ K, a temperature which is commonly used for intensity measurements for the $P(20)$ line.

Vibrational assignments of the UCL line list for 646 were based on isotopic shifts of energy levels and respective assignments for the 626 and 636 isotopologues. For this purpose energy levels for the 626 and 636 isotopologues were

extrapolated and matched to 646 calculated energy levels. Next, the DVR3D calculated line positions for 646 were compared to experimental frequencies by Dobos *et al.* [228]. The tunable diode laser measurements supplied accuracy of 0.001 cm^{-1} or better in the 2229 – 2259 cm^{-1} spectral range of the asymmetric stretching fundamental; this yields an RMSD $= 0.004$ cm^{-1}. This result shows that calculated line positions deviate from experiment just above the stated experimental accuracy, hence may be considered as highly reliable for the 00011 – 00001 band. For this band the average deviation from the EH calculations for 5 symmetric isotopologue levels is 0.018 cm^{-1}, which could probably be reduced by treatment of mass-dependent non-Born-Oppenheimer effects. A more recent study performed by Galli *et al.* [144], where high-resolution optical-frequency-comb-assisted cavity ring-down technique was used to measure ro-vibrational line positions in 2190 – 2250 cm^{-1} region with accuracy of few MHz. Comparison with this study resulted in 0.005 cm^{-1} RMSD, thereby establishing the provisional uncertainty of the DVR3D line positions to 0.005 cm^{-1} for the asymmetric stretching fundamental. The study by Galli *et al.* awaits accurate intensity evaluation. This creates an opportunity for further utilization of present results and comparison with experiments, when done.

3.14 HITRAN 2016 recommended UCL line lists

For each of 13 isotopologues of CO_2 two types of line lists were prepared. The first type named 'UCL' contains line positions calculated using Ames-1 PES with DVR3D program and line intensities using UCL DMS ('AU' line list). Each line is supplemented with the appropriate scatter factor ρ, given in the last column. The second type named 'recommended UCL-IAO line list' contains line positions from the effective Hamiltonian calculations by Tashkun and Pervalov [37–39]. In both types of line lists the vibrational assignments are taken from the newest version of the CDSD-296 database, although for a few lines manual reassignments of the CDSD-296 vibrational quantum numbers were necessary. For the radiocarbon isotopologue (646), which is not included in the CDSD-296 database, an isotope

extrapolation procedure (as described in section 3.13) was applied to obtain vibrational assignments.

The recommended UCL-IAO line lists were incorporated as a part of the HITRAN2016 database [196] (www.hitran.org), after minor modifications summarized below.

First of all, a small number of line positions was taken directly from experiment. This was the case whenever lines were affected by the interpolyad anharmonic resonance interactions, for which the effective Hamiltonian model is not accurate enough. Appropriate source codes for experimental data used in the UCL-IAO recommended line lists are:

- **627:** "3" source code stands for data taken from [229]

- **628:** "4" source code stands for data taken from [208];"5" source code stands for line positions corrected with differences between EH calculated and observed line positions for 31112-01101 or 41113-01101 bands taken from Karlovets *et al.* [208]

- **638:** "3" source code stands for data taken from [206];"5" source code stands for line positions corrected with differences between EH calculated and observed line positions for the 31113-01101 band taken from Karlovets *et al.* [206]

- **728:** "3" source code stands for data taken from [208]

The majority of lines in the recommended line lists have their source code "1" for transition intensities, which stands for UCL-calculated data. On the other hand, the majority of line positions come from the effective operator calculations by Tashkun and Perevalov [37–39], with "2" source code assigned.

The uncertainty-code assignment was based on the following criteria. Intensities of stable lines ($\rho < 2.5$) belonging to bands stronger than 10^{-23} cm/molecule (for unit abundance) were taken from UCL DMS calculations and assigned HITRAN uncertainty code 8 (i.e. accuracy of 1% or better). Stable lines belonging

to parallel bands weaker than 10^{-23} cm/molecule also come from UCL DMS computation and were given uncertainty code 7 (i.e. accuracy 1 – 2 %). Intermediate lines ($4.0 > \rho \geq 2.5$) and stable lines belonging to perpendicular bands weaker than 10^{-23} cm/molecule feature HITRAN uncertainty code 6 (i.e. accuracy 2 – 5%). Line intensities of bands containing the $3\nu_3$ vibrational excitation as well as unstable lines ($\rho \geq 4.0$) were taken from the effective Hamiltonian calculations [37–39]. Before publishing as a part of the HITRAN2016 database, all line lists were carefully evaluated band-by-band, which resulted in a number of vibrational reassignments.

All line positions and line intensities for which a scatter factor was not assigned were taken from the effective Hamiltonian computation. This was the case for only for a very small fraction of lines (see Figure 3.14). Abundances for each isotopologue were taken from the HITRAN2012 database and the final line lists used an abundance-scaled intensity cut-off 10^{-30} cm/molecule. For the radiocarbon isotopologue (646) unit abundance was assumed and 10^{-27} cm/molecule intensity cut-off cm/molecule.

3.15 Concluding remarks on CO_2

Results of comparisons discussed in this chapter suggest that the present UCL line lists for all 13 isotopologues of CO_2 represent the theoretical and experimental state-of-the-art accuracy in transition intensities. Spectral completeness, uniformity of errors within a single band and sub-percent accuracy of the most important bands resulted in inclusion of present line lists in the 2016 edition of the HITRAN database. Below, Figure 3.55 presents a chart showing how the HITRAN uncertainty index for line intensities has changed with the update from UCL line lists. With the UCL entries, the uncertainty in line intensities in the HITRAN database lowered significantly, with the most atmospherically and astrophysically relevant transitions modelled with sub-percent accuracy, which fulfilled the working goal of the CO_2 project.

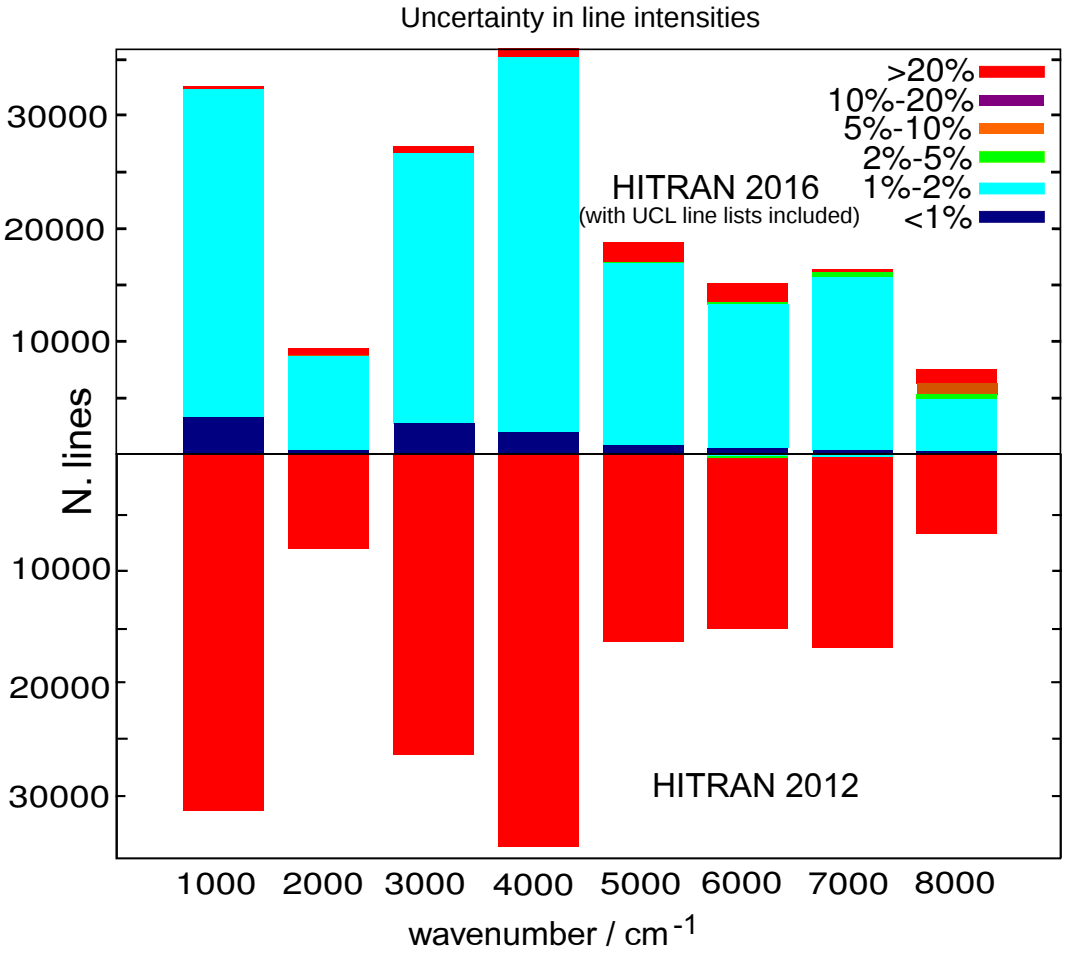

Figure 3.55: Bar chart comparing uncertainties in line intensities for the 626 isotopologue in the 2012 and 2016 editions of the HITRAN database.

Chapter 4

Room temperature Born-Oppenheimer ro-vibronic UV line lists for SO_2 and CaOCa molecules

4.1 Introduction

A considerable number of triatomic species are of great importance in studies of Earth's and exoplanetary atmospheres: H_2O, CO_2, SO_2, O_3, H_2S, NO_2, HCN, etc. [230, 231]. All these molecules absorb ultraviolet (UV) light, which is associated with an electronic transition. This fact can be utilized in qualitative and quantitative characterisation of atmospheres, by comparing measured spectra to theoretical predictions. Qualitative molecular fingerprint studies with low-resolution remote-sensing instruments need only approximate band shapes and intensities which can be provided by theory. On the other hand, quantitative analysis of concentrations of molecules from the UV absorption spectroscopy require high quality modelling of ro-vibronic line positions, line intensities as well as line shapes.

Line-by-line data, which is the most useful for remote sensing is currently mainly supplied from spectroscopic databases such as HITRAN [196], HITEMP [34] and GEISA [35]. In the UV spectral region however, due to limited availabil-

ity and quality of experimental studies, these databases often contain only cross-sections. This is the case also for the SO_2 molecule, even though SO_2 retrievals are generally based on absorption measurements in the UV. For successful retrieval of molar fractions of molecules in the atmospheric measurements, all absorption lines in a given spectral region have to be characterized, requiring high-resolution supporting data and this currently represents a major challenge. In addition to that, reference spectra taken directly from experiment show issues with completeness of the data as well as insufficient quality of line intensities. This creates a demand for a systematic scheme for producing low-uncertainty spectroscopic parameters for ro-vibronic transitions. When proven accurate enough, results of such calculations could be potentially included in the above mentioned spectroscopic databases. This was already the case in the infrared absorption region, where theoretical calculations with the DVR3D suite by Tennyson *et al.* [59] were shown to provide high accuracy line intensities for molecules such as CO_2 [32, 37–39] (discussed in chapter 3) and H_2O [75, 232–235].

In this chapter we implement and test a theoretical procedure, outlined in chapter 2, which can be used to generate UV absorption line positions and transition intensities for triatomic molecules. This is achieved by extending the existing DVR3D code for ro-vibrational infrared calculations to electronic transitions. The resulting calculated parameters of ro-vibronic transitions are supposed to serve as a theoretical reference model for measured line positions and transition intensities, for further utilization in the atmospheric science.

There are a number of theoretical methods and their computer implementations for calculation of UV absorption spectra of triatomic molecules. Transition frequencies are often directly determined from measurements or indirectly from effective Hamiltonian models [236–238], which give much higher accuracy than variational calculations. On the other hand, transition intensity calculations often require support from *ab initio* models [239]. These models, in order to meet the high accuracy requirement, need to be derived from appropriately high level electronic structure calculations and nuclear motion theory. Resolution of rotational lines is thus neces-

sary which means that couplings between the rotational, vibrational and sometimes electronic motion must be considered.

Electronic transitions triggered by UV photons can be modelled quantum-mechanically from a range of perspectives. The most common approach uses empirically-tuned effective Hamiltonians supported by Franck-Condon transition intensities [240]. Effective Hamiltonians rely heavily on experimental data which is often of limited availability and quality. Thus, although accurate, the effective Hamiltonian approach has a drawback of limited robustness, as for example typically a separate quantum mechanical model is needed for every molecule and every isotopologue [241–243]. For this reason, *ab initio* methodologies for calculating ro-vibronic transition frequencies and intensities are usually employed, serving as the first stage in the modelling process [37–39, 244]. Furthermore, the *ab initio* method can be extended to consider highly excited states which are important for high temperature studies such as those needed for exoplanets. Exotic or poisonous chemical species, such as TiO, VO, HCN, PH_3 or H_2F^+, some of which exist in the interstellar medium [245], whereas some are believed to be present in cool stars [246], are prominent examples of systems for which *ab initio* theory is the only viable approach to prediction of infrared (IR) or UV spectra [247–249]. Experimental characterization of this type of molecules is largely inhibited by problems with synthesis and stability of compounds, as well as temperature limitations in laboratory measurements.

A number of programs for solving the ro-vibronic Schrödinger equation are available, such as RENNER [250–252] by Odaka *et al.* which is dedicated to linear Renner-type triatomic molecules, or more general variational codes for solving the triatomic spin-ro-vibronic problem based on MORBID by Jensen *et al.*, [253–256] which uses an approximate kinetic energy operator for nuclei, RVIB3 [257–259] by Carter, Handy *et al.* is designed only for semi-rigid triatomic molecules with three or less interacting electronic states. A bottleneck in the variational methodology is diagonalising the large matrices required for calculations of highly excited rotational states; thus its applicability is limited by computing power. This limita-

tion can be partially overcome with the use of the discrete variable representation (DVR) [89,90,260], which is presently well known for its computational efficiency. The DVR3D suite by Tennyson *et al.* [59, 261] used in chapter 3 to generate ro-vibrational line lists for isotopologues of CO_2 uses exact kinetic energy (EKE) operator in the Born-Oppenheimer approximation. The computationally efficient two-step procedure [86] for solving ro-vibrational Schrödinger equation (DVR3D code) allowed for generation of 54 room temperature line lists for CO_2 in a relatively short time. The DVR3D computer code has been used to generate a considerable number of ro-vibrational line lists [37–39,56,76,262], with wavefunctions and energy levels calculated in several cases up to values of the rotational quantum number $J > 100$. The accuracy of these wavefunctions and energy levels is largely determined by the quality of the potential energy surface (PES) and the dipole moment surface (DMS). The accuracy of transition intensities of ro-vibrational line lists generated for isotopologues of CO_2 with *ab initio* DMS has reached and arguably exceeded experimental accuracy [28, 32, 37–39]. As a result, for 12 isotopologues of carbon dioxide in the 0 – 8000 cm^{-1} wavenumber range, the theoretical transition intensities calculated with DVR3D have been included in the HITRAN2016 spectroscopic database [196]. In this chapter, we extend the thoroughly tested DVR3D computer code to electronic excitations.

Time-dependent methods have also been used to simulate IR and UV molecular spectra. Although primarily designed for larger systems, time-dependent methods, such as Multiconfiguration time-dependent Hartree (MCTDH) [263–266] or molecular dynamics, are applicable to triatomics too [267]. The main issue with current application MCTDH and molecular dynamics approaches is the absence of detailed modelling of $J > 0$ transitions, and that no rotation-vibration couplings are reflected in wavefunctions. The effect of Coriolis couplings is, for instance, visible in the UV spectrum of SO_2 ($\tilde{C}\ ^1B_2 \leftarrow \tilde{X}\ ^1A_1$ electronic transition) [240, 268]. Another serious disadvantage of MCTDH methods in high accuracy spectra modelling are the approximate Hamiltonians used, which limits the accuracy of calculations for highly anharmonic systems. For this reason the EKE operator, with complete

description of rotational motion as well as rotation-vibration couplings remains the best option for high accuracy calculations. For example, some remote-sensing experiments rely on measurements of a single rotational line, hence after the identification stage, based on the recognition of a fingerprint for a given molecule, a quantitative study based on absolute and accurate ro-vibronic intensities is needed. Many models based on Franck-Condon calculations often provide only relative intensities of bands, calculated from overlaps of the vibrational wavefunctions, which is of limited use in quantitative spectroscopy [269, 270].

The primary objective of the present chapter is to test the procedure (described in chapter 2) for solving the Schrödinger equation for any triatomic molecule, for two un-coupled electronic states in the Born-Oppenheimer approximation, and subsequent computation of transition intensities between the stationary states obtained. This theoretical scheme is tested on the SO_2 molecule. Here, we explore the possibility of extending DVR3D to calculation of ro-vibronic spectra of triatomic molecules within the Born-Oppenheimer approximation and with transition dipole moment surface (TDMS) between two electronic states. DVR3D has already been successfully applied in ro-vibrational calculations of energy levels and wavefunctions in electronically excited states of FeCO [271]. The next procedural step is to enable computation of transition intensities between two Born-Oppenheimer electronic states. Here, this is done at two levels of approximation: the Franck-Condon (FC) approximation [272] with ro-vibrationally coupled wavefunctions, and the transition dipole moment surface approach, which fully accounts for the dependence of the electronic transition dipole moment on internal coordinates of the molecule.

As a case study for the new procedure, the UV absorption spectrum for the $\tilde{C}\ ^1B_2 \leftarrow \tilde{X}\ ^1A_1$ electronic transition in SO_2 is calculated. Sulphur dioxide plays a substantial role in atmospheric chemistry. Detailed understanding of vibronic absorption properties of all major isotopologues of sulphur dioxide is essential for explaining the mass-independent isotope fractionation effect observed for SO_2 in the Earth's atmosphere [273]. SO_2 is a major component of Venus' atmosphere,

it also accompanies Earth's volcanic activity and industrial activities. Sources and migrations can be monitored by detecting hazes of SO_2 [44].

The infrared absorption spectra of atmospheric sulphur dioxide are often congested with absorption bands from other molecules, especially water. For this reason measurements of SO_2 in the UV region have gained a growing attention over the years, and a few satellite instruments are currently operating in the UV, for example GOME-2 [42] and OMI [43], reviewed in ref. [41]. These measurements require high accuracy spectroscopic models to support assignment of lines and to provide reference line strengths for concentration retrieval. In addition to that, cross sections at different temperatures and pressures for several molecules need to be provided prior to the measurement, in order to retrieve accurate concentrations of the molecule of interest in the atmosphere; here SO_2. Currently, such parameters can be obtained consistently only from theoretical calculations. Thus, along with the development of experimental instrumentation and methodology, a parallel progress is needed in the accurate description and understanding of the nuclear dynamics in excited electronic states of SO_2 and other atmosphere-present compounds.

The most popular choice for the UV absorbing bands are the A and B bands of SO_2 located in the 270–400 nm wavelength region [274, 275], for which a theoretical description has been given by Xie *et al.* [276]. The strongest absorption in the UV is however attributed to the dipole allowed $\tilde{C}\ ^1B_2$ state. This electronic state, chosen here as a case study, has a highly anharmonic potential energy surface with a double-well structure [51]. Although the strongest absorption for the $\tilde{C}\ ^1B_2 \leftarrow \tilde{X}\ ^1A_1$ transition is located near 200 nm [277], for the present purposes, the longer wavelength 220–235 nm absorption region is selected. This spectral region involves transitions to the lowest vibrational states of the $\tilde{C}\ ^1B_2$ electronic state, and has been chosen due to limitations of the *ab initio* potential energy surface used here.

High resolution spectra for the $\tilde{C}\ ^1B_2 \leftarrow \tilde{X}\ ^1A_1$ electronic transition in the 220–235 nm region were recorded by Yamanouchi *et al.* [270], Rufus *et al.* [278] and more recently by Blackie *et al.* [279], where a review on past measurements is pre-

sented. Other lower resolution measurements were published by several authors, see for example Danielache *et al.* [280] and Sako *et al.* [281]. There are a number of theoretical studies on spectroscopy of the $\tilde{C}\ ^1B_2$ state. Early papers by Xie *et al.* [282] and Bludský *et al.* [283] paved the way for more accurate descriptions, recently provided by Kłos *et al.* [284] and Kumar *et al.* [285]. High quality *ab initio* spectra for the transition to the $\tilde{C}\ ^1B_2$ state, do not so far however include rotational structure. Results from Kłos *et al.* [284] will serve as a benchmark for $J = 0$ calculations with the present procedure. Particularly for non-symmetric triatomic molecules, the present approach can provide information on the so called *axis-switching effect* [286–290], which is inherently accounted for in the model.

Section 4.2 discusses the electronic structure calculations for the $\tilde{C}\ ^1B_2$ and the $\tilde{X}\ ^1A_1$ state in SO_2. Section 4.3 gives details of the nuclear motion calculations. Results of line position and transition intensity calculations are given in section 4.4, where transition intensities are compared against other theoretical calculations as well as experimental data, and the significance of the TDMS is discussed. Finally in section 4.5, the CaOCa molecule is investigated. In the same way as for SO_2 a Born-Oppenheimer ro-vibronic low-J ($J <10$) line list is generated for this molecule.

4.2 The potential energy surface and the transition dipole moment surface

The potential energy surface for the $\tilde{C}\ ^1B_2$ electronic state was generated from 3000 geometries in bond length – bond angle coordinates. Stretching coordinates were chosen in the range: $r_1, r_2 \in [1.2; 1.9]$ Å, with 0.05 Å increments. Angles between the $S-O$ bonds were sampled from 60° to 180° with 5° increments.

Electronic structure calculations were performed with the explicitly correlated multi-reference internally contracted configuration interaction method with Davidson correction (ic-MRCI-F12+Q) in the *aug*-cc-pVTZ basis set, as implemented in the MOLPRO2015 package [177]. The reference wavefunctions were calculated with the state-averaged CASSCF method, with equal weight averaging over two singlet states. For 18 electrons occupying 19 orbitals, 12 orbitals were used (9a',

3a') for the active space and 7 as core orbitals (6a', 1a"). The PES was fitted with the least-squares method to the functional form:

$$V(y_1,y_2,y_3) = \sum_{j,k,l} C_{jkl} y_1^j y_2^k y_3^l \tag{4.1}$$

where $y_1 = \frac{1}{2}(x_1 + x_2)$, $y_2 = \frac{1}{2}(x_1 - x_2)$ and $y_3 = \theta - \theta_{eq}$. Here x_1, x_2 are Morse coordinates $x_1 = 1 - e^{-a_1(r_1 - r_1^{eq})}$, $x_2 = 1 - e^{-a_2(r_2 - r_2^{eq})}$. The functional form and coefficients were chosen to secure the correct shape of the PES at C_{2v} geometries. For a fixed angle $\theta = \theta_0$, the PES $V(r_1, r_2, \theta_0)$ has a saddle point when $r_1 = r_2$, and two non-C_{2v} minima in the r_1–r_2 plane, which are symmetry connected, as shown in Figure 4.1. A non-uniformly weighted fit to 623 *ab initio* points with energies below 5000 cm^{-1} in $\theta \in [90°; 130°]$, gave σ =12 cm^{-1} root-mean square residual (RMSR) between the fitted surface and *ab initio* points.

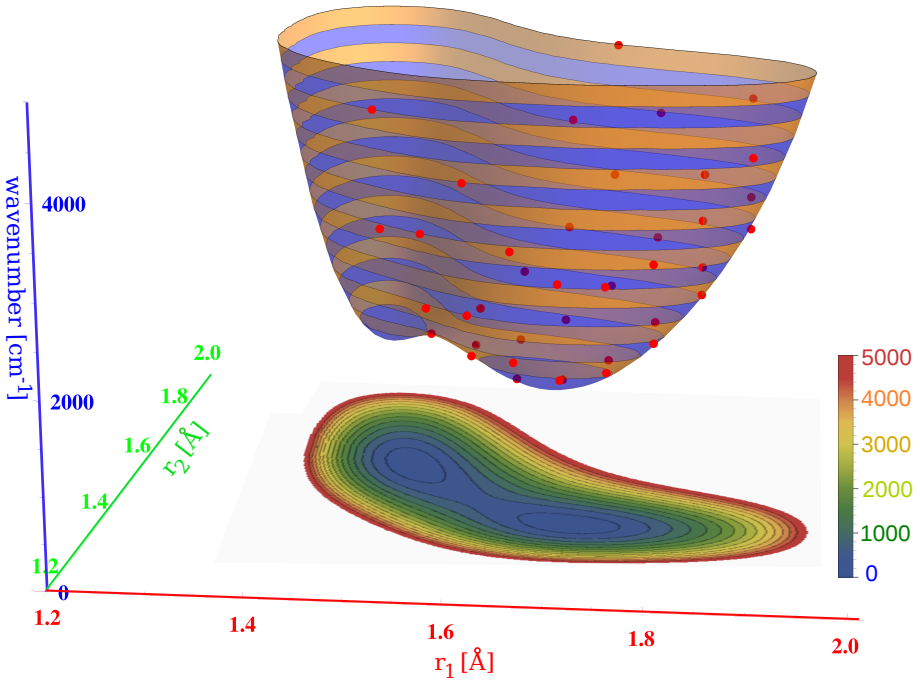

Figure 4.1: Potential energy surface for the $\tilde{C}\ ^1B_2$ electronic state calculated at $\theta = 120.0°$. *Ab initio* points are marked in red.

The global C_s equilibrium geometry for the $\tilde{C}\ ^1B_2$ is located at $r_1^{eq} = 1.640$ Å,

$r_2^{eq} = 1.496$ Å, $\theta^{eq} = 104.3°$. There are two other local minima near $\theta = 80°$ and $\theta = 165°$. The latter is a C_{2v} symmetric minimum with energy 400 cm^{-1} above the global minimum. This well, displayed in Figure 4.9, generates additional low lying energy levels, which have not been yet characterized by spectroscopy. A separate fit for the second well near linearity gave RMSR= 17 cm^{-1}.

For the electronic $\tilde{X}\ ^1A_1$ state we used a highly accurate potential energy surface of Huang *et al.* [291,292]. This is a semi-empirical PES based on CCSD(T)/cc-pVQZ-DK calculations and refinement to experimental energy levels in the J=0–80 range. The RMSR of the fit to *ab initio* points was 0.21 cm^{-1} below 30 000 cm^{-1} and the root-mean square deviation from experimental levels was 0.013 cm^{-1}. The equilibrium geometry of the electronic ground state $r_1^{eq} = 1.431$Å, $r_2^{eq} = 1.431$Å, $\theta^{eq} = 119.32°$ corresponds to C_{2v} symmetry.

The transition dipole moment surface between $\tilde{X}\ ^1A_1$ and $\tilde{C}\ ^1B_2$ electronic states was calculated as the expectation value of the electric dipole moment operator, at the same level of theory as the $\tilde{C}\ ^1B_2$ PES. A fit to the functional form from eq. (4.1) was performed with 1852 *ab initio* points in the [85°:140°] angle range. The RMSR for the x-component of the surface (x-axis chosen to bisect the angle between S–O bonds) was 0.03 a.u., and the RMSR for the z-component of the surface was 0.02 a.u. High accuracy is not the aim of the present study, thus these values for residuals were acceptable. At equilibrium geometry the z-component of the transition dipole moment vanishes, as shown in Figure 4.2. The transition dipole moment depends on the nuclear coordinates relatively weakly, nevertheless the non-constant TDMS may significantly influence transition intensities; this is discussed in section 4.4.

The PES and TDMS are available for use in the form of FORTRAN95 routines as supplementary materials to ref. [293].

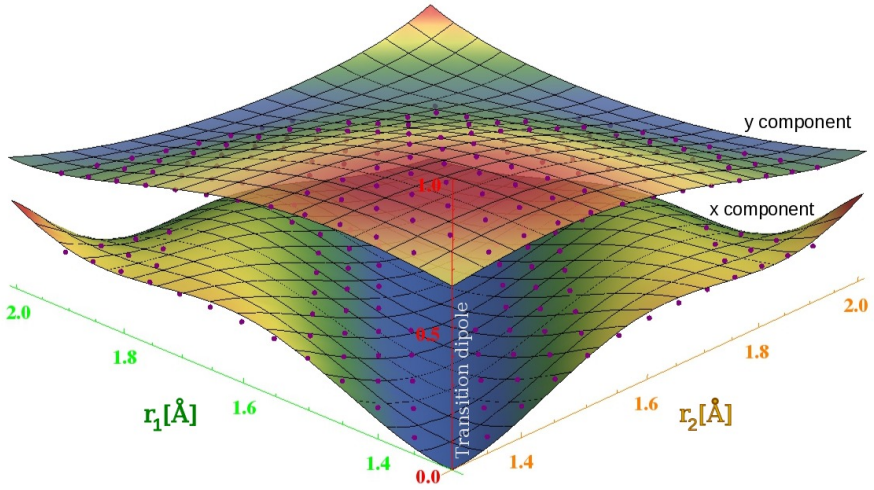

Figure 4.2: Two components of the transition dipole moment function between $\tilde{X}\ ^1A_1$ and $\tilde{C}\ ^1B_2$ electronic states for $\theta = 120.0°$. The upper surface is the y-component and the lower surface is the x-component, which vanishes for C_{2v} geometries. *Ab initio* points are marked with red.

4.3 Nuclear motion calculations

4.3.1 Wavefunctions and energy levels

Born-Oppenheimer ro-vibrational wavefunctions and energy levels were obtained separately for the $\tilde{X}\ ^1A_1$ and the $\tilde{C}\ ^1B_2$ electronic states. For each electronic state, a two step procedure described in chapter 2 for solving the nuclear Schrödinger equation was applied. The DVR representation of matrix elements of the Hamiltonian, as implemented in DVR3D, carries the advantage of diagonal potential energy matrix in any chosen basis. A Morse-like oscillator basis set [59, 85] was used for the S–O stretching coordinates and associated Legendre functions for the bending motion. The parameters of the stretching basis set were optimized to ensure the fastest convergence of $J = 0$ energy levels in the $\tilde{C}\ ^1B_2$ electronic state. The final set of optimized parameters, basis set size and other parameters for nuclear motion calculations are listed in Table 4.1. The vibrational energy levels are insensitive to the value of the dissociation energy D_e in the Morse-like oscillator basis functions, hence D_e was set to $0.3E_h$ in all cases. The equilibrium bond length r_e and width α of the Morse-like basis was scanned in the $r_e \in [2.8; 3.5]a_0$, $\alpha \in [0.008; 0.030]E_h$

region for different sizes of the stretching basis (the NPNT parameter in DVR3D in the 30 – 90 range). The number of angular basis functions was independently optimized, and the corresponding NALF parameter was set to 60. As a result, the optimal set of basis set parameters was: $r_e = 2.9\ a_0$, $D_e = 0.30\ E_h$, $\alpha = 0.012\ E_h$ and NPNT= 90. With this basis optimal basis set the accuracy of vibrational energy levels in the electronic ground state was controlled by comparison with the ExoAmes line list [76]. In the light of the main idea of the present work, we do not require spectroscopic accuracy for present calculations. For this reason, we established convergence criteria at 2 cm^{-1} and tolerance for deviation from experiment at 20 cm^{-1} for the lowest $J = 0$ energy level of the $\tilde{C}\ ^1B_2$ electronic state .

The final size of the DVR3DRJZ Hamiltonian was truncated at 1000, which was sufficient to provide good convergence for the lowest 100 energy levels. Diagonalisation of this matrix leads to ro-vibrational energy levels and wavefunctions labelled by the J-rotational quantum number and the e/f Wang symmetries. Nuclear masses in Dalton units (Da) for sulphur and oxygen were used: 31.963294 Da (^{32}S), 15.990525 Da (^{16}O) [178]. For evaluation of integrals a DVR scheme based on 90-point Gauss-Laguerre and a 60-point Gauss-Legendre quadratures was used, for stretching and bending coordinates respectively. With this choice the range of quadrature points for stretching coordinates is $r_i \in [1.13; 1.86]$Å, thus this range is contained in the domain of applicability of the present fit. With this basis set the zero-point energies for the $\tilde{X}\ ^1A_1$ and $\tilde{C}\ ^1B_2$ electronic states are ZPE$_g$ = 1538.19 cm^{-1} and ZPE$_e$ = 776.45 cm^{-1} respectively. In the second variational step (program ROTLEV3), for each J value separately 200 ro-vibrational basis functions were used to solve the full Coriolis-coupled nuclear motion problem.

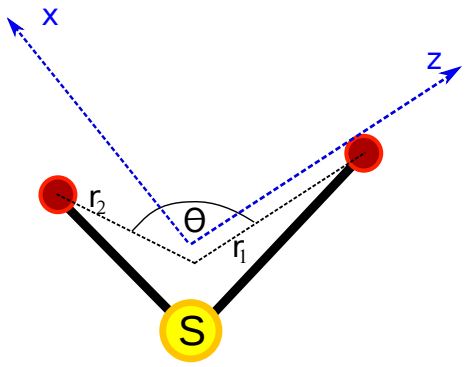

Figure 4.3: Schematic picture of the molecule-fixed frame embedding used in nuclear motion calculations for SO_2. r_1 and r_2 are Radau stretching coordinates.

Coordinates:	Radau (r_1,r_2,θ)
BF frame embedding:	z-axis along r_1
Basis set	identical for both el. states
'Stretching' r_1,r_2:	90 Morse-like oscillator functions
Morse-like oscillator basis parameters:	$r_e = 2.9\ a_0$, $D_e = 0.30\ E_h$, $\alpha = 0.012\ E_h$
Number of DVR points for stretching:	90 (Gauss-Laguerre quadrature)
Bending θ:	60 (Associated Legendre Polynomials)
Number of DVR points for bending:	60 (Gauss-Legendre quadrature)
Rotations	Complete basis set of symmetric-top wavefunc.
Truncated Hamiltonian size in the first step:	1000
Truncated Hamiltonian size in the second step:	500
Computation time[a] ($J = 0$)	10 min.
Scaling with J (computation time)	$\sim J$ (first step), $\sim J^2$ (second step)
Intensity calculations	
Common DVR grid for both electronic states	
Computation time ($J'' = 0 \rightarrow J' = 1$)	15 min.
Scaling with J'' (computation time)	$\sim J^2$

Table 4.1: Summary of the parameters of the nuclear motion calculations for the $\tilde{X}\ ^1A_1$ and the $\tilde{C}\ ^1B_2$ electronic states of SO_2. In the table given are: the type of coordinates used, the type of molecule-fixed frame embedding, basis set parameters and some technical details of the computation. [a] Test computations were performed on a stationary PC with Intel(R) Core(TM) i5-2500@3.30 GHz processor and 8 GB of RAM.

Identical embeddings (see Figure 4.3), coordinates and DVR grids were chosen for both electronic states. The criterion for this choice was to optimize the accuracy of the electronic excited state. The simple shape of the ground state PES gives weaker dependence on the choice of embedding and basis set parameters, when

an appropriately large basis set is used. Radau internal coordinates were chosen for description of vibrational degrees of freedom. The z-axis of the molecule-fixed frame was chosen along one of the Radau coordinates (r_1), which nearly overlaps with one of the the S–O bonds ('bond embedding'). The bond embedding was observed to give significantly better convergence than the bisector embedding for the $\tilde{C}\,^1B_2$ electronic state, which has its equilibrium geometry at two non-equivalent S–O bond lengths, that is at C_s symmetry. The fit of the PES for the $\tilde{C}\,^1B_2$ state necessitated adding walls at large internuclear distances, to avoid potential dropping to non-physical values. The positions of these walls were adjusted so as not to influence the values of energy levels for the present basis size. For larger basis sizes, the range of quadrature points for stretching coordinates can sample regions of the PES, which are beyond the range of applicability of the present fit. These regions have high energy, thus adding walls with energy $0.1E_h$ to the present fit assures the correct asymptotics for all r_1 and r_2 values. The potential walls were added at $r = 1.3$ Å, $r = 2.0$ Å and $\theta = 85°$, $\theta = 130°$.

4.3.2 Axis-switching effect

Not only does the equilibrium geometry of the molecule change upon the electronic transition, but also an additional rotation of the molecule-fixed coordinate system is required [286]. The former effect can be directly attributed to the difference in shapes of the potential energy surfaces for the two electronic states that causes the vibrational basis set optimized for the electronic excited state to be no longer optimal for the electronic ground state. In the terminology of normal modes it means that normal coordinates in the electronic excited states are rotated (leading to the so-called Duschinsky effect [288, 289, 294]) with respect to normal coordinates in the electronic ground state. The effect of rotation of the molecule-fixed coordinate system affects the Euler angles, causing rotation of the rotational basis set. Although in many systems these artifacts of the electronic transition are marginal, they sometimes significantly soften rotational selection rules, allowing for appearance of whole vibrational "forbidden" bands, as observed in HCN [287] and SiHD [290]. For example, in the HCN molecule, for the ($\pi^* \leftarrow \pi$) electronic transition only

$\Delta K = \pm 1$ sub-bands are allowed by rotational selection rules. However stimulated-emission-pumping (SEP) experiments [295] observed weak $\Delta K = 0$ transitions to levels with non-zero vibrational angular momentum ($l = 1$). This type of transition is forbidden by rotational selection rules and has been convincingly attributed to non-rigidity of the molecule during the transition between linear $\tilde{X}$ electronic ground state and bent $\tilde{A}$ electronic state [286, 287]. In calculations, the magnitude of the axis-switching effect depends on the choice of the molecule-fixed frame, the choice of coordinates and the basis set. Axis-switching is strongly pronounced in the *Eckart frame*, the molecule-fixed coordinate system which needs to be rotated when changing the electronic state, in order to satisfy the conditions of the minimal rotational-vibrational coupling in both states separately.

The axis-switching effect suggests that the rotational basis functions should be labelled with the quantum numbers for electronic states too. However, the completeness of the rotational basis used in the present model guarantees that the rotational part is accounted for exactly regardless of the electronic states. Therefore, rotational states in the electronic excited state, which are nominally functions of rotated Euler angles can be modelled with the un-rotated rotational basis of the electronic ground state (or vice-versa). An appropriately large vibrational basis set can also eliminate any inaccuracies resulting from the *Duschinsky effect*, meaning that the vibrational basis is nearly complete hence does not depend on the electronic state. For the reasons discussed above we can drop the electronic index i for the rotational and vibrational basis states and use them as given in eq. (2.36) and (2.37). As a result, at the cost of extra computational time, the geometric effects associated with the electronic transition are fully modelled. Thus, ro-vibronic transitions forbidden by rotational selection rules, which appear in line lists calculated with the present model, may be attributed to the axis-switching effect.

The present approach utilizes an identical basis set to calculate ro-vibrational energies and wavefunctions in the ground and the excited state of the molecule (we assume a system with two electronic states). In DVR, this means that the ro-vibrational wavefunctions for both electronic states are defined on the same grid,

which provides the advantage of straightforward integration over internal coordinates of the molecule. For this reason, matrix elements between ro-vibrational states of the electronic ground and excited state can be evaluated as a sum of products of respective functions at given grid points.

4.4 Results and discussion

$J = 0$ energy levels calculated with the present *ab initio PES* for the $\tilde{C}\,^1B_2$ electronic state are listed in Table 4.2, where a comparison with literature calculations based on two different *ab initio* surfaces is made. The *ab initio* MRCI+Q/aug-cc-pVTZ PES by Tokue *et al.* [296] was based on 6300 geometries and was interpolated by the moving least-squares method combined with the Shepard method [297]. The *ab initio* ic-MRCI-F12+Q/aug-cc-pVTZ PES of Kłos *et al.* [284] was interpolated with spline functions. Table 4.2 also gives the semi-empirical energy levels from Jiang *et al.* [240] and measured energies of Yamanouchi *et al.* [270]. The present calculated values for vibrational energy levels are in a good agreement with experiment and semi-empirical calculations by Jiang *et al.* [240]. Clearly the present PES is more accurate than the one given by Tokue *et al.* [296]. The root-mean square deviation (RMSD) between the experimentally tuned energy levels from Jiang *et al.* [240] and the present calculation for $J = 0$ energy levels is 13 cm^{-1} below 1500 cm^{-1} which practically equals the RMSD for the *ab initio* calculations by Kłos *et al.*. The level of the present PES is comparable to the PES of Kłos *et al.* [284], as both surfaces were calculated with the same *ab initio* method. The advantage of the present approach, which is based on a fit to a functional form, manifests in savings in the number of *ab initio* points necessary. This way of producing a PES would be thus recommended, when a higher level of theory is used for the electronic structure calculations.

Table 4.2: Comparison of the $J = 0$ energy levels (cm^{-1}) calculated with the present *ab initio* PES for the $\tilde{C}\ ^1B_2$ electronic state to theoretical values from Kłos *et al.* [284], Tokue *et al.* [296], semi-empirical calculations by Jiang *et al.* [240] and measured energies [270]. In the first column a vibrational assignment is given; the second column gives the symmetry of the state in the C_{2v} group. The b_2 levels are dipole forbidden from the vibrational ground state of the $\tilde{X}\ ^1A_1$ electronic state. Energy levels from the second potential well localized around $\theta = 165^\circ$ were excluded from the table.

(ν_1 ν_2 ν_3)	Sym.	Present	Kłos *et al.* [284]	Tokue *et al.* [296]	Jiang *et al.* [240]	Exp. [270]
(001)	b_2	195	223		212	
(010)	a_1	368	375	394	377	377
(002)	a_1	544	575	598	561	561
(011)	b_2	560	590		582	
(020)	a_1	734	748	772	751	752
(003)	b_2	880	912		890	
(012)	a_1	916	943	979	929	
(021)	b_2	924	956		949	
(100)	a_1	960	960	935	960	960
(030)	a_1	1101	1118		1122	1122
(004)	a_1	1246	1264		1245	1245
(013)	b_2	1258	1271		1252	
(101)	b_2	1258	1275		1261	
(022)	a_1	1289	1309		1299	1300
(031)	b_2	1291			1313	
(110)	a_1	1330			1337	1337
(005)	b_2	1465			1595	
(014)	a_1	1609			1604	1604
(023)	b_2	1631			1611	
(102)	a_1	1641			1653	1654
(032)	a_1	1647			1662	

Analysis of Table 4.2 suggests that the present *ab initio* PES for the $\tilde{C}\ ^1B_2$ state is applicable in the 0–1700 cm^{-1} range above the zero-point vibrational energy. This range covers vibrational energy levels involved in strong vibronic progressions, thus is sufficient for comparisons to experimental room temperature electronic spectra below the dissociation threshold (≈ 3000 cm^{-1}) of the $\tilde{C}\ ^1B_2$ state. To conclude, the present PES is the most accurate *ab initio* potential energy surface for the $\tilde{C}\ ^1B_2$ state in SO_2, which has been fitted to a predefined functional form. A previous fit to *ab initio* points performed below 5000 cm^{-1} by Bludský *et al.* [283] gave 55 cm^{-1} rmsd with respect to measurement.

Note that at room temperature (296 K) only the lowest vibrational state of the electronic ground states is significantly populated. Population of the asymmet-

ric stretching fundamental $\tilde{X}\ ^1A_1(0,0,\nu_3)$ (≈ 1362 cm^{-1}) is barely 0.1% at that temperature. Therefore in practical calculations, the number of vibrational states needed for the $\tilde{X}\ ^1A_1$ electronic state is limited to the lowest few. The variational methodology means that these lowest energy levels are calculated more accurately than higher lying states. For this reason, if the PES is accurate, as the Ames-1 PES is, satisfactory convergence can be easily achieved, even with a non-optimized basis set.

With the common basis set used in nuclear motion calculations for both electronic states, the DVR3D calculated vibrational zero-point energies for the $\tilde{X}\ ^1A_1$ and $\tilde{C}\ ^1B_2$ states are $\mathrm{ZPE}_g = 1538.19$ cm^{-1} and $\mathrm{ZPE}_e = 776.45$ cm^{-1} , respectively. The former value is consistent with the 1535.63 cm^{-1} ZPE reported by Huang *et al.* and the latter value is somewhat lower than 785.75 cm^{-1} calculated by Kłos *et al.* . The vertical excitation energy for the $\tilde{C}\ ^1B_2 \leftarrow \tilde{X}\ ^1A_1$ transition was taken from the experiment [240]: $T_e = 42573$ cm^{-1} . The partition function at 296 K, used for intensity calculations was taken from Huang *et al.* [291] ($Q(296) = 6336.789$). The temperature range for which calculated vibronic spectra are reliable is determined by the accuracy of the ground state PES. Here, the Ames-1 PES, as very accurate, provides an opportunity for accurate modelling of vibronic hot bands. Room temperature spectra are certainly within the applicability range of the Ames-1 PES.

4.4.1 Vibronic spectra

Ab initio vibronic spectra were calculated using eq. (2.95) for two cases: the Franck-Condon approximation (eq. (2.105)), and with the use of the transition dipole moment surface (eq. (2.101)). The resulting transition intensities are compared in Figure 4.4.

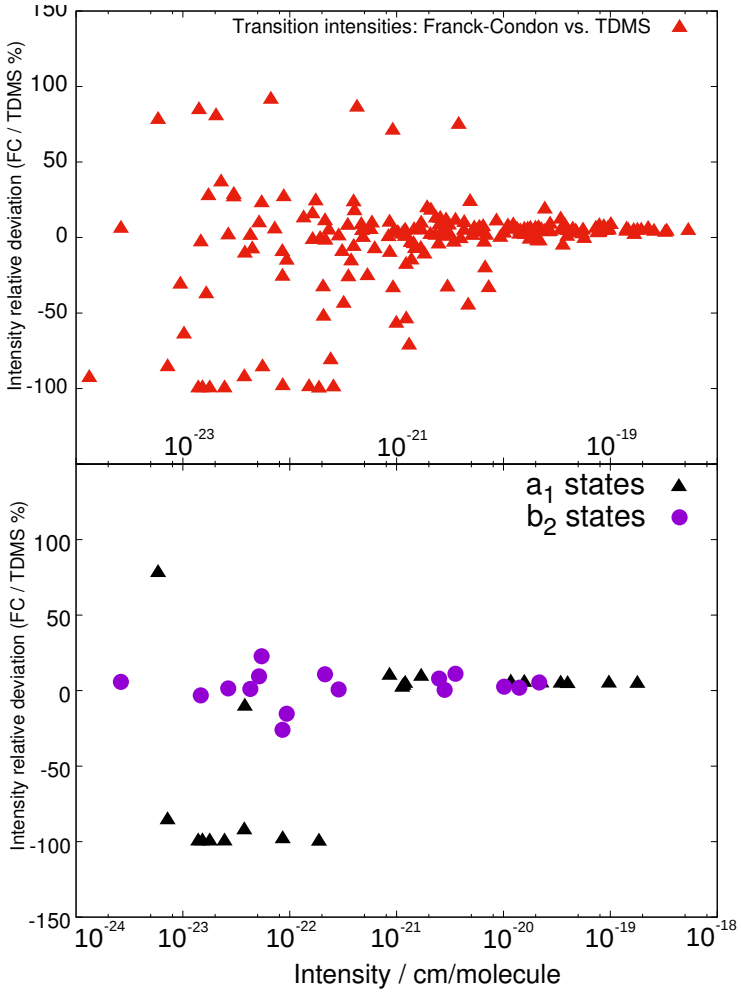

Figure 4.4: Comparison of *ab initio* calculated transition intensities for the $\tilde{C}\ ^1B_2 \leftarrow \tilde{X}\ ^1A_1(v=0)$ electronic transition $(J'=1 \leftarrow J''=0)$ between the Franck-Condon and the transition dipole moment surface levels of theory. The upper panel represents the relative deviation in intensities in the 10^{-18} – 10^{-24} cm/molecule intensity range. The lower panel displays transitions to 40 lowest $J'=1$ energy levels of the $\tilde{C}\ ^1B_2$ state. Transitions to states with a_1 and b_2 symmetries are distinguished.

Figure 4.4 shows no significant difference in strong transition intensities when the FC spectrum is compared to the TDMS spectrum. In general, for strong transitions, which contribute to the overall shape of the absorption band, the difference in transition intensity between the FC and TDMS approach is usually less than 10%, typically 4–6 %. However, as displayed in the lower panel in Figure 4.4, allowing for the dependence of the electronic transition dipole moment on nuclear coordinates can noticeably increase certain transition intensities, which are nominally

very weak in the FC approximation.

Transitions from the a_1 symmetry states in the electronic ground state to the b_2 states in the electronic excited state are forbidden by vibrational dipole selection rules. However rotation-vibration interactions, especially c-axis Coriolis-type interactions can mix states of different vibrational symmetries. The ro-vibrational selection rules require only that the irreducible representations of ro-vibrational states are identical: $\Gamma_{rv} = \Gamma'_{rv}$, where $\Gamma_{rv} = \Gamma_{vib} \otimes \Gamma_{rot}$. In the C_{2v} group, vibrational and rotational selection rules for the $\tilde{X}\ ^1A_1 \rightarrow \tilde{C}\ ^1B_2$ electronic transition allow for transitions $(a_1, eo)_{B_2} \leftarrow (a_1, ee)_{A_1}$ or $(a_1, oe)_{B_2} \leftarrow (a_1, oo)_{A_1}$ in the notation where k_a, k_b - even is denoted as ee and k_a, k_b - odd is denoted as oo. Ro-vibrational selection rules, which apply when states are vibrationally forbidden, but are mixed by Coriolis interactions give the following ro-vibrationally allowed transitions from a_1 states: $(b_2, oo)_{B_2} \leftarrow (a_1, ee)_{A_1}$ or $(b_2, ee)_{B_2} \leftarrow (a_1, oo)_{A_1}$.

Indeed, such transitions forbidden by vibrational selection rules but allowed by ro-vibrational selection rules have been observed in the $\tilde{C}\ ^1B_2 \leftarrow \tilde{X}\ ^1A_1$ ro-vibronic spectrum [268, 298, 299]. The lower panel in Figure 4.4 shows several transitions to "b_2" states. The rotation-vibration interaction feeds such transitions with intensity, which is nonetheless usually of 1–3 orders of magnitude weaker than typical vibrationally allowed transitions. A large number of ro-vibrationally allowed and vibrationally forbidden transitions were found in the present line list, for example transitions in the $\tilde{X}\ ^1A_1(0,0,0) \rightarrow \tilde{C}\ ^1B_2(0,1,1)$ and $\tilde{X}\ ^1A_1(0,0,0) \rightarrow \tilde{C}\ ^1B_2(0,0,3)$ manifold. Intensity calculations with Coriolis-decoupled wavefunctions do not reveal any vibrationally forbidden transitions, thereby proving that the rotational-vibrational coupling is responsible for softening of the selection rules for transitions to b_2 states in the $\tilde{C}\ ^1B_2$ electronic state. The strongest transition to a b_2 state $\tilde{X}\ ^1A_1(0,0,0) \rightarrow \tilde{C}\ ^1B_2(0,1,3)$, has comparable intensity to many moderately weak vibrationally allowed transitions. In this particular case, the large intensity borrowing can be rationalized by strong Coriolis interaction between the $(0,1,3)$ states of b_2 symmetry and the $(0,0,4)$ states of a_1 symmetry, which are only separated by 12 cm^{-1} and this leads to strong mixing. A comprehensive discussion of Coriolis

interaction between ro-vibrational energy levels of the $\tilde{C}\ ^1B_2$ electronic state was given by Park *et al.* [268].

Comparison of the FC and TDMS spectrum with semi-empirical FC calculations of Yamanouchi *et al.* [270] is given in Figure 4.5. The assumption of marginal difference between the FC and TDMS spectra is further confirmed in the upper panel in Figure 4.5. Line positions in the lower panel correspond to measured values. The agreement between the present study and semi-empirical calculations is satisfying. As previously asserted, the contribution from the TDMS to the spectrum is negligible in this spectral region. Thus for qualitative UV spectrum modelling purposes, the Franck-Condon approximation is sufficient. For higher accuracy, which is required for example by remote sensing experiments, the full transition dipole moment surface may be necessary.

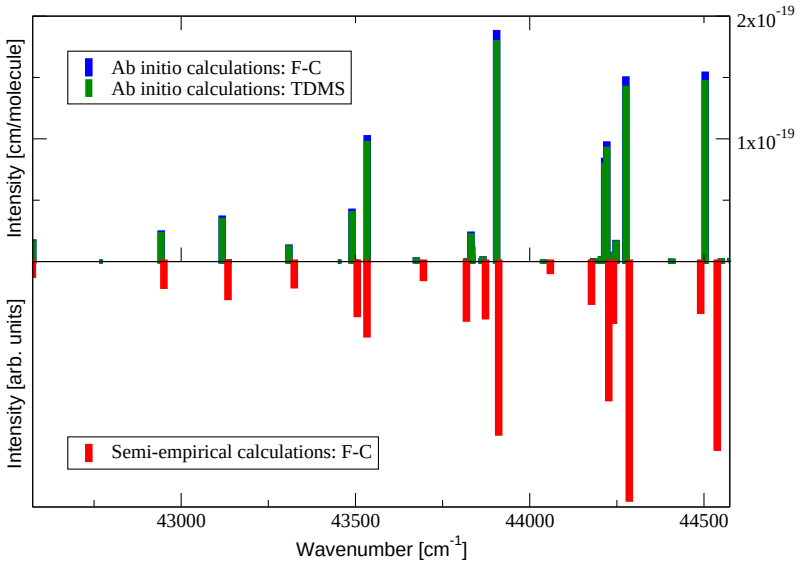

Figure 4.5: Comparison of three calculated vibronic spectra: semi-empirical calculations from Yamanouchi *et al.* [270] in the lower panel; FC and TDMS *ab initio* calculations from the present study in the upper panel. Line positions are given in the 42500 – 44500 cm^{-1} range.

Figure 4.6 gives a comparison between experimental laser-induced fluores-

cence spectrum by Yamanouchi *et al.* [270] (upper panel), semi-empirical Franck-Condon vibronic spectra calculated by Xie *et al.* [282] (middle panel), and present Franck-Condon and TDMS calculations (lowest panel). The overall agreement between the two theoretical studies in the middle and lowest panels is good, with relative intensities following a similar pattern. Changes in intensity caused by the breakdown of the Condon approximation are small in this spectral region. In contrast to emission, the initial wavefunction for room-temperature absorption is well localized around the equilibrium geometry of the vibronic ground state, which suppresses transitions to states with largely distorted geometries (cf. Figure 4.2). In the 225 nm – 235 nm range line positions and intensities agree well between the present theory and experiment. This agreement however becomes worse for shorter wavelengths. Therefore, below 225 nm the present $\tilde{C}\ ^1B_2$ state PES is not accurate enough even for qualitative studies.

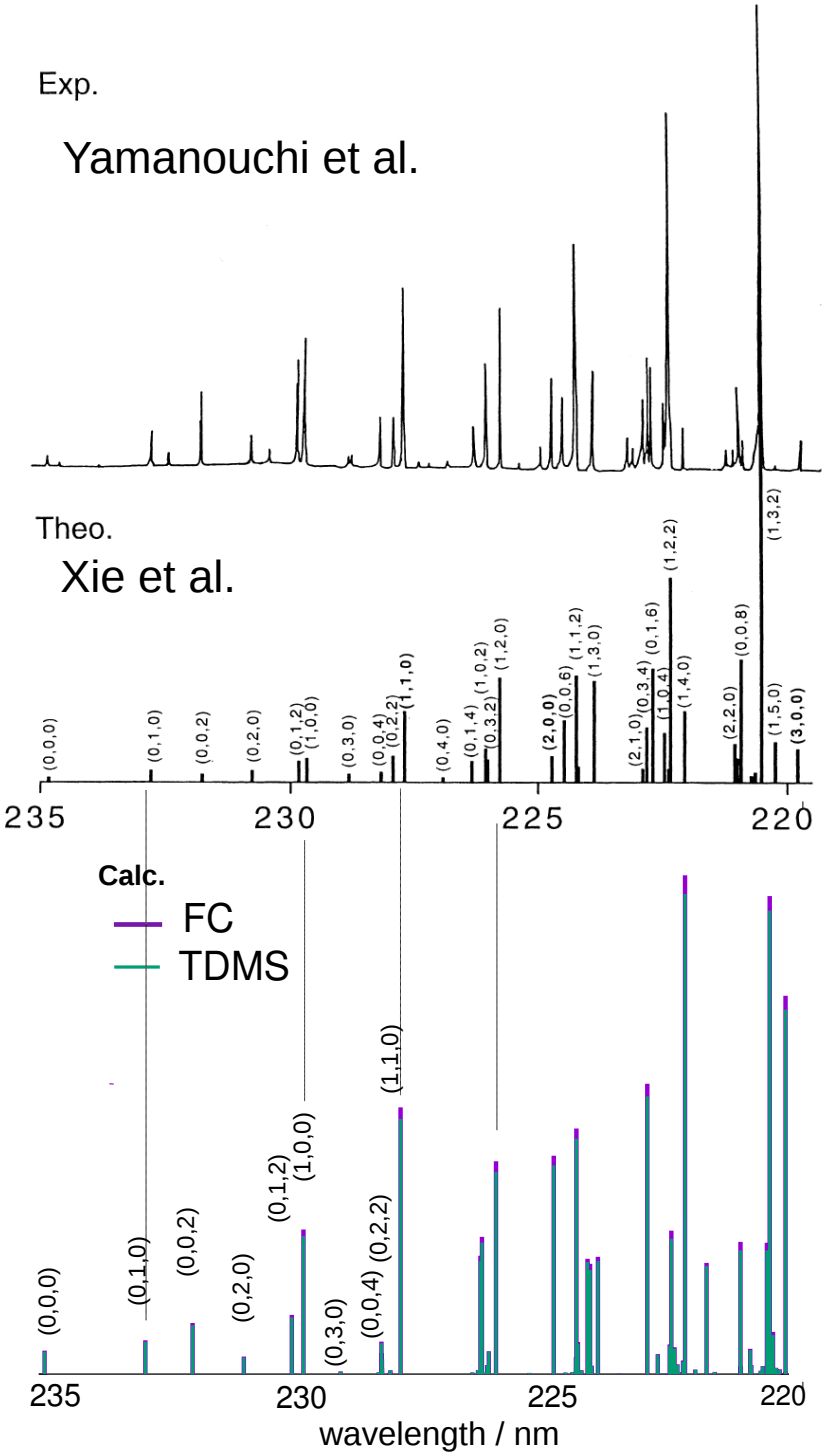

Figure 4.6: Comparison of calculated vibronic spectra with measurement by Yamanouchi *et al.* [270] and semi-empirical calculations of Xie *et al.* [282]. Vibrational assignments were given for 10 lowest calculated transitions. These transitions can be considered as modelled reliably with the present PES and TDMS. The experimental and theoretical spectra were reprinted from Xie *et al.* , Chem. Phys. Lett. 329, 503-510 Copyright (2000), with permission from Elsevier.

Based on the new PES and TDMS a room temperature (295 K) UV line list for the $\tilde{X}\ ^1A_1 \rightarrow \tilde{C}\ ^1B_2$ electronic transition was calculated in the $J = 0-40$ range. The partition function for the electronic ground state was taken from Huang *et al.* [291]. This line list is designed for the 225 nm – 235 nm wavelength range, where it can be considered reliable. A qualitative comparison of the present line list with low-resolution measurements by Wu *et al.* [300] is given in Figure 4.7. Dashed lines correspond to experimental cross section (in cm^2) measured at 295 K with 0.5 Å resolution. *Ab initio* absorption cross sections are marked in red and green in Figure 4.7 and were obtained from integral line intensities by convolution with the Gaussian profile function with full-width at half-maximum (FWHM) of 0.3 cm^{-1} and 8 cm^{-1} respectively; no scaling of line intensities or line positions was made.

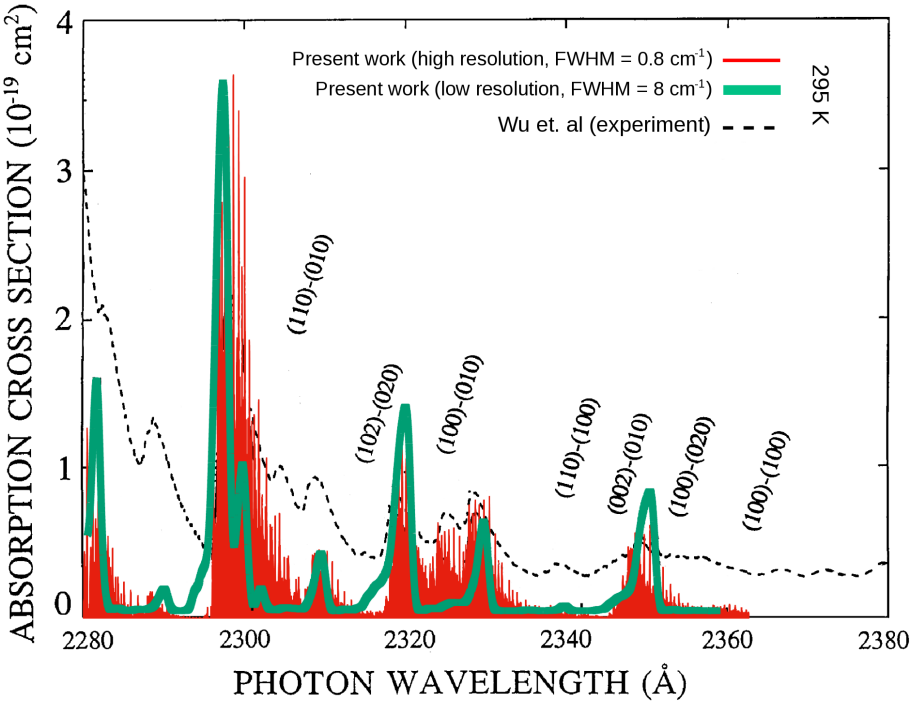

Figure 4.7: Comparison of the *ab initio* and measured absorption cross sections. The *ab initio* cross sections were calculated from the room temperature (295 K) ro-vibronic line list for the $\tilde{X}\ ^1A_1 \rightarrow \tilde{C}\ ^1B_2$ electronic transition in SO_2 in the $J = 0-40$ range. Gaussian line shapes were used with FWHM of 0.3 cm^{-1} (red thin stick spectrum) and 8 cm^{-1} (green thick line spectrum). Measurements were made by Wu *et al.* [300] at 295 K. The experimental spectrum was reprinted from C.Y.R. Wu *et al.* , Icarus 145, 289–296 Copyright (2001), with permission from Elsevier.

The low-resolution theoretical cross section depicted by a thick green line in Figure 4.7 qualitatively reproduces the band centers measured by Wu *et al.* . Comparison of line intensities is however less straightforward due to the non-uniform baseline in the measurements. Hot bands, assigned by Wu *et al.* [300] are also visible in the *ab initio* spectrum, as expected. Qualitatively, the calculated spectrum reproduces the features of the measured spectrum, however for a more detailed insight, the accuracy of the present model should be tested on a higher resolution experimental data.

High-resolution measurements of the $\tilde{X}\ ^1A_1 \rightarrow \tilde{C}\ ^1B_2$ electronic band were reported by Rufus *et al.* [278] (at 295 K) and Blackie *et al.* [279] (at 198 K). Cross-sections from Blackie *et al.* [279] are compared with cross-sections calculated at 198 K from the present *ab initio* line list in Figure 4.8. The FWHM of the experimental rotationally-resolved cross-sections was 0.3 cm^{-1}. In calculations, the Gaussian line shape profile with FWHM = 0.3 cm^{-1} was used and the partition function at 198 K (3246.3) was calculated from ro-vibrational energy levels available from Underwood *et al.* [262]. The shape of the cross-section spectrum is nearly insensitive to addition of transitions with $J > 40$, thus no higher J energy levels need to be calculated for the present comparison. Nonetheless, it is technically possible to obtain a line list with $J > 100$, with the present implementation of the DVR3DUV code.

The uncertainty in the cross-sections measured by Blackie *et al.* was estimated 9–15% for the strongest bands $\sigma \in (10^{-17}\ cm^2, 10^{-18}\ cm^2)$ and more than 20% for bands weaker than $10^{-18}\ cm^2$. Overall agreement between the unassigned measured cross-sections in Figure 4.8 and theoretical cross-sections is very good though. Vibronic assignments are also given in Figure 4.8. These assignments agree with experimental assignments of Danielache *et al.* [280]. Unfortunately, no ro-vibronic assignments for the experimental spectrum are available, which makes a line by line comparison difficult. A major reason for which the spectrum measured by Blackie *et al.* cannot be presently assigned in the rotational resolution is the 10–20 cm^{-1} uncertainty in *ab initio* line positions. Future studies should focus on obtaining

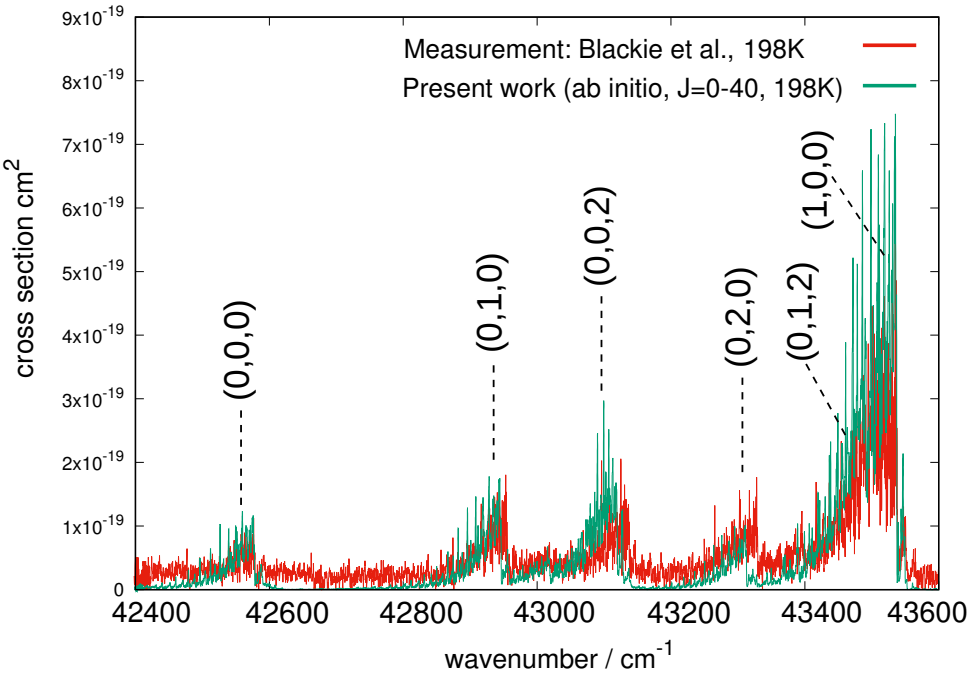

Figure 4.8: Comparison of the *ab initio* and measured absorption cross-sections. The *ab initio* cross-sections were calculated at 198 K from ro-vibronic line list for the $\tilde{X}\ ^1A_1 \rightarrow \tilde{C}\ ^1B_2$ electronic transition of SO_2 in the $J = 0-40$ range. Measurements were made by Blackie *et al.* [279] at 198 K. Vibrational assignments found manually are indicated with dashed lines. All marked transitions are from the vibronic ground state to vibrational states of $\tilde{C}\ ^1B_2$.

a higher quality, more global PES for the $\tilde{C}\ ^1B_2$ state. Then, with the use of the present procedure, a purely *ab initio* based ro-vibronic assignment of experimental spectra could be become possible.

4.4.2 Franck-Condon intensities for a large geometry displacement

The wavefunction for the vibrational ground state in the electronic ground state $\tilde{X}\ ^1A_1$ of SO_2 is very compact, and most of its amplitude is localized near the C_{2v} equilibrium geometry $r_1^{eq} = 1.431$ Å, $r_2^{eq} = 1.431$ Å, $\theta^{eq} = 119.32°$, as displayed in Figure 4.9. For this reason, the vibrational wavefunction overlap between the vibrational ground state of $\tilde{X}\ ^1A_1$ and vibrational states localized in the second well of the $\tilde{C}\ ^1B_2$ state, located near $\theta = 165°$, is likely to be very small. Indeed, Table 4.3 shows that calculated overlap integrals for transitions to the second well are 5–8 orders of magnitude smaller than the respective factors to the main well, where the global minimum for the $\tilde{C}\ ^1B_2$ state is located.

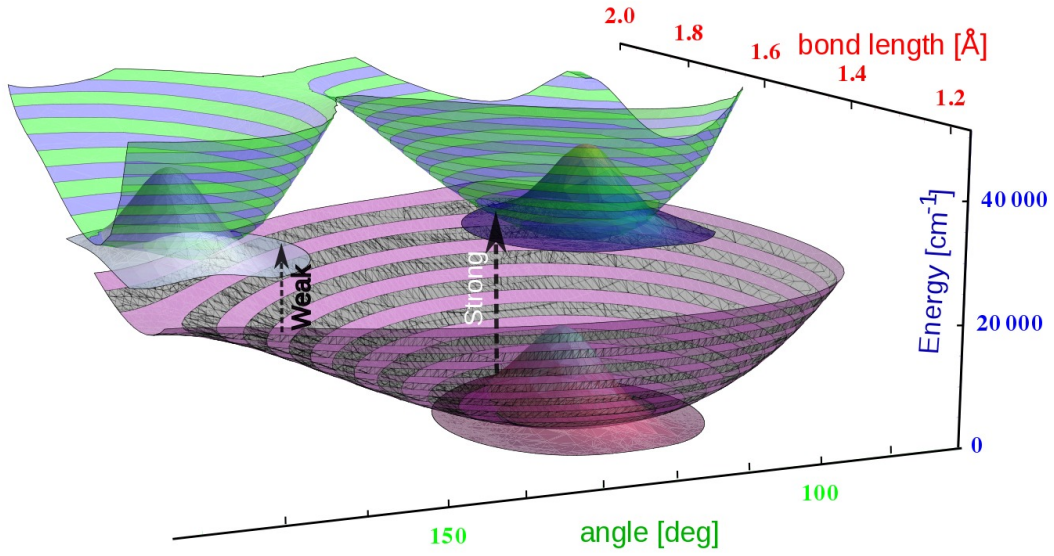

Figure 4.9: Potential energy surfaces for $\tilde{X}\ ^1A_1$ electronic state (purple/grey) and $\tilde{C}\ ^1B_2$ electronic state (green/blue) of SO_2. The other bond length is fixed at $r_2 = 1.7$Å . Wavefunctions for the vibrational ground state of each well are added, with arrows marking Franck-Condon vertical transitions from the electronic ground state.

Table 4.3: Comparison of vibrational overlap integrals calculated between $J = 0$ wavefunctions of the vibronic ground state and vibrational states of the $\tilde{C}\ ^1B_2$ state. Given in columns are respectively: ID of the vibrational state belonging to the electronic excited state, overlap integral calculated for the 1^{st} well located at $\theta = 104^\circ$, overlap integral calculated for the 2^{nd} well located at $\theta = 165^\circ$.

State ID	overlap integral (1^{st} well)	overlap integral (2^{nd} well)
1	8.48×10^{-3}	2.92×10^{-10}
2	1.41×10^{-2}	1.12×10^{-10}
3	1.73×10^{-2}	-1.41×10^{-11}
4	-2.28×10^{-2}	-2.14×10^{-9}
5	1.67×10^{-4}	-1.84×10^{-9}
6	1.71×10^{-2}	1.12×10^{-9}

It is thus justified to neglect the second well completely in the theoretical intensity calculations. This conclusion is expected to be general, applicable to other molecules and other electronic states.

4.5 Ro-vibronic line list for CaOCa

Another molecule studied in this thesis as a test system in the procedure for calculating Born-Oppenheimer ro-vibronic spectra of triatomic molecules is di-Calcium oxide Ca_2O (CaOCa), or Calcium suboxide. This molecule is very challenging to produce in the gas phase in the laboratory and so far there has been no published high-resolution UV or visible spectrum for this system. A single theoretical study was reported on infrared absorption spectra of calcium suboxide by Ostojic *et al.* [301]. These authors also analysed the IR spectrum of the Sr_2O molecule [256]. The hyper-metallic Ca_2O molecule is an example of a class of exotic molecular species, which suffer from lack of experimental characterisation, either due to their toxicity or due to technical difficulties in synthesising and maintaining them. In such instances *ab initio* calculations are a very good predecessor to experiment, providing high-resolution ro-vibronic absorption line positions, giving ro-vibronic assignments of absorption lines and transition intensities. This study on CaOCa was initiated with a request from an experimental group [302] to provide pilot ro-vibronic spectra for this molecule.

In this section we follow analogical procedure to the scheme outlined in the

sections regarding SO_2. We focus here on the electronic ground state $1^1A'$ of Ca_2O and the first excited singlet electronic state $1^1A''$ (classification in the C_s molecular symmetry group). To produce ro-vibronic spectra for the transition between the electronic ground state $1^1A'$ of Ca_2O and the first singlet electronic excited state $1^1A''$, potential energy surfaces for these electronic states were generated. For this purpose *ab initio* electronic energy points were taken from calculations by Fawzy and Heaven [302]. They used multireference configuration interaction (MRCISD) method with state-averaged, full-valence complete active space self-consistent field (SA-FV-CASSCF) wavefunctions. The active space consisted 12 orbitals occupied with 10 valence electrons, where all the valence electrons were correlated. Contributions of higher excitations and relativistic effects were taken into account using the Davidson correction and the Douglas-Kroll (DK) Hamiltonian, respectively. The correlation-consistent polarized weighed core-valence quadruple-zeta basis set (cc-pwCVQZ-DK) was used for all three atoms.

The PES for the $1^1A'$ state was least-squares fitted with 30 parameters to 1253 *ab initio* electronic energy points with the following functional form:

$$V_{1^1A'}(y_1,y_2,y_3) = \sum_{j,k,l} C_{jkl} y_1^j y_2^k y_3^l \tag{4.2}$$

where $y_1 = \frac{1}{2}(x_1 + x_2)$, $y_2 = \frac{1}{2}(x_1 - x_2)$ and $y_3 = \theta_{eq} - \theta$. Here x_1,x_2 are Morse coordinates $x_1 = 1 - e^{-a_1(r_1 - r_1^{eq})}$, $x_2 = 1 - e^{-a_2(r_2 - r_2^{eq})}$. The electronic energies for the $\tilde{X}\ ^1A_1$ electronic state of Ca_2O were generated for 1253 geometries in bond–length, bond–angle coordinates (r_1, r_2, θ). Stretching coordinates were chosen in the range: $r_1, r_2 \in [1.85; 2.21]$ Å. Angles between the $Ca-O$ bonds were sampled from 95° to 180° with 2.5° increment. The uniformly weighted fit gave RMSR = 1.8 cm^{-1} with respect to all used *ab initio* points, and is applicable in the 0 – 5000 cm^{-1} energy range. The equilibrium geometry of the Ca_2O molecule in the electronic ground state corresponds to C_{2v} symmetry with $r_1^{eq} = r_2^{eq} = 2.03$ Å and $\theta^{eq} = 180°$. The PES for the electronic ground state of Ca_2O has a relatively simple, nearly harmonic shape.

The PES fit for the electronic excited $1^1A''$ state turned out to be more challeng-

ing, because of a complicated shape of the PES. The fitted function was divided into two regions: a low angle region (85 – 120°) and a high angle region (120 – 180 °). At low angles the functional form of the PES is identical with that from eq. 4.2. In this angle range the least-squares fit to 420 *ab initio* electronic energy points with 40 parameters was straightforward and resulted in 5 cm^{-1} RMSR. At higher angles, the PES for the $1^1A''$ state morphs into a non-C_{2v} double-minimum form, and reaches a deep double-well structure when the bending angle goes towards molecule's linearity. This situation is depicted in Figured 4.10–4.5. For this reason the functional form for the fit had to be modified:

$$V_{1^1A''}(y_1,y_2,y_3) = \sum_{j,k,l} C_{jkl} y_1^j y_2^k y_3^l + f_{cusp}(r_1,r_2,\theta) \tag{4.3}$$

where $y_1 = \frac{1}{2}(r_1+r_2)$, $y_2 = \frac{1}{2}(r_1-r_2)$ and $y_3 = \cos\theta_{eq} - \cos\theta$. Here r_1, r_2 are Ca–O bond lengths. The extra correction function $f_{cusp}(r_1,r_2,\theta) = \frac{a\cos^2\theta}{(r_1-r_2)^2+b^2} e^{-a(d-\theta)}$ is used to properly shape the region near the C_{2v} geometry ($r_1 \approx r_2$), where a saddle point connecting two the local minima is located. This saddle point has a very sharp ridge, behaving nearly as a cusp. The standard functional form from eq. 4.2 was incapable of reproducing the *ab initio* energies in this region. The final form of the correcting function f_{cusp} was a result of intuition and try-and-error, but eventually resulted in 29 cm^{-1} RMSR of the fit in the 120 – 180 degrees angles region. The a,b,c,d parameters in the cusp-correction function were optimized using the least-square method together with other parameters of the fit (89 total). The fit was non-uniformly weighted with weights of near-cusp points set to two-times the values for other points. All points above 3000 cm^{-1} were weighted half the weight of points below this energy. The functional form and fit coefficients were chosen to secure the correct shape of the PES at C_{2v} geometries. For a fixed angle $\theta = \theta_0$, the PES $V(r_1,r_2,\theta_0)$ has a saddle point when $r_1 = r_2$, and two non-C_{2v} minima in the r_1–r_2 plane, which are symmetry connected, as shown in Figure 4.10. The global minimum for the first singlet electronic excited state is located at linear geometry, with non-equal Ca–O bond lengths. This broken-symmetry can be probably attributed to a vibronic interaction with a higher lying singlet electronic

state.

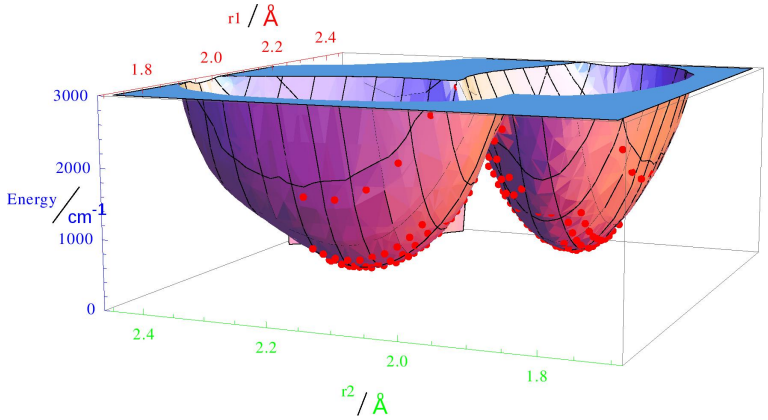

Figure 4.10: 2D-slice at fixed $\theta = 180°$ of the PES for the electronic excited $1^1A''$ state of Ca_2O. *ab initio* points (in red) are overlaid on top of the fitted continuous funcitonal form. A deep double-minimum structure is visible, which suggests non-equal Ca–O bond lengths at linearity.

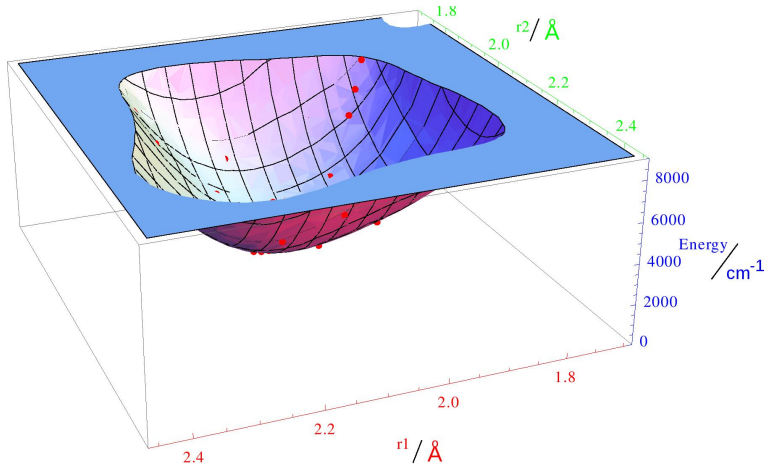

Figure 4.11: 2D-slice at fixed $\theta = 95°$ of the PES for the electronic excited $1^1A''$ state of Ca_2O. *ab initio* points (in red) are overlaid on top of the fitted continuous funcitonal form.

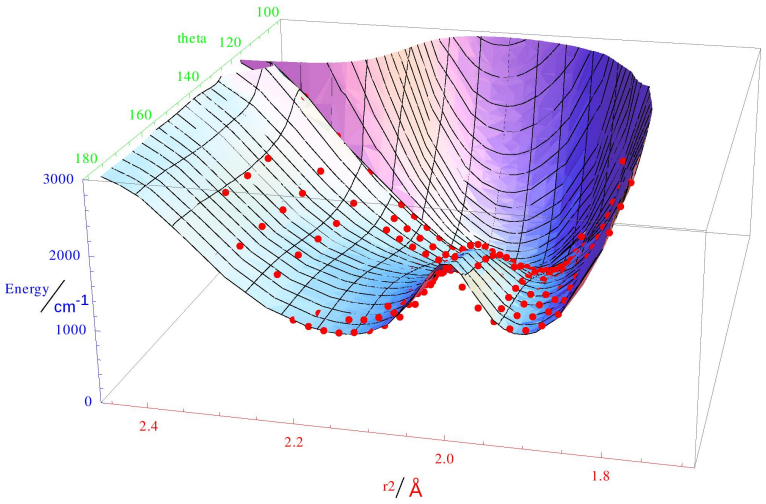

Figure 4.12: 2D-slice at fixed $r_1 = 2.0$ Å of the PES for the electronic excited $1^1A''$ state of Ca_2O. *ab initio* points (in red) are overlaid on top of the fitted continuous funcitonal form. A switching point between the low angle PES and the high ange PES is visible at 120°.

DVR calculations were performed for both electronic states separately with the PESs described above. For this purpose the Morse-like oscillator basis was chosen and optimized using the method described in section 3.2 in chapter 3. The DVR calculations used Radau coordinates in r_1-bond embedding of the molecule-fixed coordinate frame. The optimized parameters of the Morse-like basis read: $r_0 = 4.2a_0$, $D_e = 0.3E_h$, $\omega = 0.012E_h$. With these parameters a satisfactory level ($<$2 cm^{-1} at the energy of 3000 cm^{-1}) of convergence of $J = 0$ energy levels for the electronic excited state was achieved with 80 basis functions for the stretching motion (NPNT=80) and 80 basis functions for the bending motion (NALF=80). The 3D DVR Hamiltonian was truncated at 1000 (MAX3D = 1000). The nuclear masses for Calcium and oxygen were $m_{Ca} = 40.078$ Da and $m_O = 15.990$ Da, respectively. The fitted potential energy functions were given extra potential walls, to prevent from non-physical (negative) values of the potential function for large values of r_1, r_2 or small angles θ. The walls were placed at $r_{min} = 1.75$ Å $r_{max} = 2.45$ Å and $\theta_{min} = 90°$. The height of the wall was $0.1E_h$ and the energy levels were tested for independence of the height of these walls. The calculated zero-point vibrational energies (ZPE) for the electronic ground state was 392.4 cm^{-1} and for the

electronic excited state was 1256.6 cm^{-1} . Rotlev calculations were performed with the IBASS parameter equal to 100. Ro-vibrational energy levels and wavefuncitons were calculated in the 0–10 J range for both electronic states using identical basis set parameters. Transition intensity calculations were performed with the use of the DIPOLE program in the Franck-Condon approximation. The vertical excitation energy used for this purpose was taken from experiment [302]: $T_e = 14535.0$ cm^{-1} . The transition intensities were calculated at 295 K and the partition function for the electronic ground state was calculated set to a dummy value Q(295)=1, due to lack of reliable source of data for this quantity. The spin-statistical factor was set to 1 for even and odd states. As a result, a generic room temperature line list in the 0–10 J range was produced.

Table 4.4 summarizes on $J = 0$ DVR3D-calculated energy levels of the electronic ground state and the first singlet electronic excited state of the Ca_2O molecule.

Table 4.4: Comparison of vibrational energy levels calculated with DVR3D for the $1^1A'$ and $1^1A''$ states of Ca_2O. In the rightmost column vibrational assignments of the energy levels are given.

vib. energy: $1^1A'$	vib. energy: $1^1A'$	assignment
132.81	11.54	ν_2 (bending)
251.29	333.93	$2\nu_2$ / ν_1 (symmetric stretch)
362.20	652.72	$3\nu_2$ / $2\nu_1$
467.06	766.54	
527.85	863.06	
567.52	939.58	
635.29	1114.96	
672.18	1228.09	
682.96	1295.30	
763.12	1448.24	
785.06	1504.14	
816.14	1557.88	
877.94	1562.10	
901.11	1715.48	
938.22	1734.71	
993.92	1766.01	
1014.00	1894.65	
1055.86	1912.34	

In Figure 4.5 a cross-section spectrum is displayed, calculated from the present line list at room temperature. The cross-sections were calculated via convolution of

transition intensities with the Gaussian profile function with FWHM = 0.1 cm^{-1} .

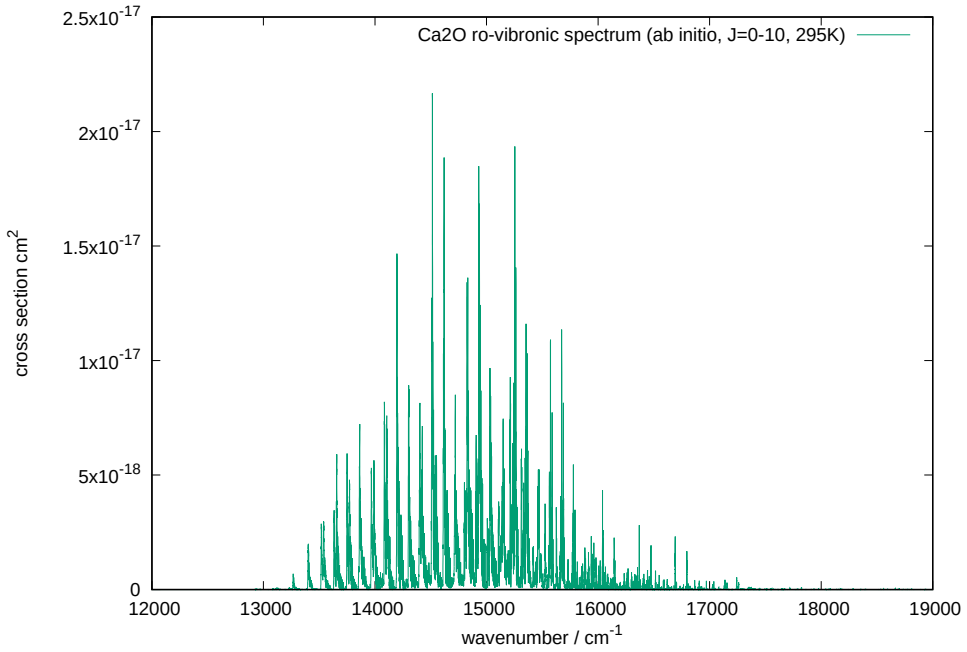

Figure 4.13: Ro-vibronic cross-sections for the $1^1A'' \leftarrow 1^1A'$ electronic transition in Ca_2O. The cross-sections were obtained from room-temperature line list in the 0–10 J range calculated with the DVR3D program. The line shape function used in production of the cross-section spectrum was Gaussian profile with FWHM = 0.1 cm^{-1} .

Future measurements of the electronic spectrum of Ca_2O can benefit from comparisons with the present line list. The accuracy of line positions in the present line list is dictated by the accuracy of the PESs and can be estimated in the 10-40 cm^{-1} range, which suggests that further improvements to the PES fits are necessary. However due to unusual geometry of the upper electronic state PES, this task is currently difficult to complete and may require construction of a diabatic model with two vibronically interacting electronic states included.

4.6 Summary

The theoretical scheme presented in this chapter is based on accurate calculations of ro-vibrational energy levels and wavefunctions for isolated electronic states of SO_2 and Ca_2O in the Born-Oppenheimer approximation, followed by ro-vibronic transition intensity calculations between two electronic states. The scheme presented here give absolute integral intensities, thus is advantageous to traditional approaches based on the Franck-Condon approximation, for which only relative intensities are theoretically available. Utilization of rotation-vibration coupled wavefunctions renders calculated intensities as inherently more accurate than the standard vibrational Franck-Condon calculations. Inclusion of the transition dipole moment surface alternates intensities of the strongest bands by less than 10%, hence may be considered only in quantitative studies. The accuracy of calculated transition intensities depends strongly on the quality of potential energy surfaces, especially for the electronic excited state, for which many vibrational states are required, and which is normally more challenging to generate. This aspect is particularly important for atmospheric science. For example, in the case of SO_2 the high resolution modelling of the strongest absorption region associated with the $\tilde{C}\ ^1B_2 \leftarrow \tilde{X}\ ^1A_1$ electronic transition is still troublesome with the model presented here. However, this is solely because the location of the strongest absorption in this band near 50 000 cm^{-1} requires calculation of highly excited ro-vibrational states of the $\tilde{C}\ ^1B_2$ electronic state, and for this reason an accurate and global PES for this state is needed. With high quality potential energy surfaces provided, the theoretical framework presented in this work can be readily applied to other ro-vibronic bands of SO_2 and other molecules, such as ozone.

An aspect of the ro-vibronic problem which is not addressed here is extending beyond the single state approximation. As shown by Yurchenko and co-workers for diatomic molecules [248, 303, 304], often a significant number of electronic states contribute to the vibronic spectrum; this number is typically larger than three. The computer program DUO due to Yurchenko *et al.* [305] treats full ro-vibronic calculations, allowing for interaction of an arbitrary number of electronic states

in diatomic molecules. A triatomic analogue of DUO is the ultimate aim of this project. For this reason in the next chapter, we are going to discuss the possibility of extending the DVR3D methodology onto a fully coupled non-Born-Oppenheimer ro-vibronic grounds.

Chapter 5

Ro-vibronic transitions beyond the Born-Oppenheimer approximation

5.1 A spin-rotational-vibrational-electronic theory for triatomic molecules. A perspective for extension of DVR3D.

With the DVR3D program [59, 261], which is based on the theory presented in the previous chapters it is possible to produce ro-vibrational line lists (line positions and line intensities) within a single electronic state, or ro-vibronic line lists in the Born-Oppenheimer approximation between different electronic states (no spin-orbit or other vibronic couplings). In this section, we attempt to develop a theory, within the framework of the Sutcliffe's and Tennyson approach to nuclear motion [58, 59, 61, 86], which aims at creating a solution scheme to the fully-coupled (spin-rotational-vibrational-electronic coupling) Schrödinger equation. This equation, when solved, generate non-adiabatic spin-ro-vibronic energy levels and wavefunctions, which can be further used in transition intensities calculations.

As already mentioned in the previous chapter, a number of programs for solving the ro-vibronic Schrödinger equation are available, such as RENNER [250–252] by Odaka *et al.* , which is designed for linear Renner-type triatomic molecules, or more general variational codes for solving the triatomic spin-ro-vibronic problem

based on MORBID by Jensen *et al.* [253–256] which uses an approximate kinetic energy operator for nuclei, RVIB3 [257–259] by Carter, Handy *et al.* is designed only for semi-rigid triatomic molecules with three or less interacting electronic states. In the light of limitations of each of these computer codes, it seems natural to search for a general robust code, which does not carry any significant inherent approximation. No such program has been yet developed, to the best of author's knowledge. Thus, it is reasonable to attempt to extend the existing DVR3D program to satisfy this so far elusive goal. Computationally, a solution to a strongly coupled system with many highly excited states is difficult to marry. Usually either a computer code is based on essentially very accurate quantum-mechanical model (e.g. RVIB3 or a code by Schwenke [49] or Alijah *et al.* [306]), but due to the bottleneck in the variational methodology, which is diagonalising the large matrices required for calculations of highly excited rotational states, has limited use, or an approximate model provides highly excited energy levels and wavefunctions [265–267].

The issue with the computing power needed in purely variational calculations can be partially overcome with the use of the discrete variable representation (DVR) [89,90,260], which is presently well known for its computational efficiency. In addition to that, the DVR3D suite by Tennyson *et al.* [59, 261] uses an exact kinetic energy (EKE) operator, and hence operates at a very high level of theory. The DVR3D computer code has been used to generate a considerable number of ro-vibrational line lists [37–39, 56, 76, 262], with wavefunctions and energy levels calculated in several cases up to values of the rotational quantum number $J > 100$. The accuracy of these wavefunctions and energy levels is largely determined by the quality of the potential energy surface (PES) and the dipole moment surface (DMS). The accuracy of transition intensities in our recent ro-vibrational line lists generated with *ab initio* DMS has reached and arguably exceeded experimental accuracy [28, 37–39], and as a result has been used to replace experimental entries in compilations of spectroscopic databases, such as the HITRAN2016 database [196].

For diatomics, the DUO computer code of Yurchenko and co-workers [248, 303–305] solves the fully coupled ro-vibronic SE using an EKE operator. A propo-

sition for a triatomic analogue of DUO is the goal this chapter. This is done below by extending the theory used by the current version of DVR3D to take into account rotational-vibrational-electronic couplings in the form of an exact quantum-mechanical operator. Next, a tentative proposal is outlined for utilization of the existing DVR3D architecture to implement the newly developed theory.

5.1.1 The Hamiltonian

The general space-fixed nuclear Hamiltonian given in eq. 2.3 can be extended to take into account simultaneously electronic and nuclear degrees of freedom. With such extension, following Sutcliffe [61] the body-fixed molecular Hamiltonian can be written as:

$$\hat{H}(\phi,q,\xi) = \hat{K}(\phi,q,\xi) + \hat{H}_{el.}(\xi;q) \tag{5.1}$$

where the KEO is explicitly given as

$$\begin{aligned}\hat{K}(\phi,q,\xi) = \frac{1}{2}\left[\sum_{\alpha,\beta} M_{\alpha,\beta}\hat{N}_\alpha\hat{N}_\beta + \sum_\alpha \left(\lambda_\alpha + 2\left(M\hat{L}\right)_\alpha\right)\hat{N}_\alpha\right] + \\ -\frac{1}{2}\left[\sum_{\mu,\nu=1}^{3N_{nuc}-6} G_{\mu\nu}\frac{\partial^2}{\partial q_\mu \partial q_\nu} + \sum_{\mu=1}^{3N_{nuc}-6}\tau_\mu\frac{\partial}{\partial q_\mu}\right] + \\ +\frac{1}{2}\left[\sum_{\alpha,\beta} M_{\alpha,\beta}\hat{L}_\alpha\hat{L}_\beta + \sum_\alpha \lambda_\alpha\hat{L}_\alpha\right]\end{aligned} \tag{5.2}$$

The quantities appearing in the above equation are defined as in eq. 2.7, 2.8, 2.9 and 2.10. $\phi := (\alpha,\beta,\gamma)$ denotes the three Euler angles describing the rotational motion, q stands for a general vector (q_1,q_2,q_3) of vibrational coordinates, denoted in previous chapters as (r_1,r_2,θ). ξ is a vector of $3N_e$ electronic position coordinates.

The electronic Hamiltonian is a sum of the following terms:

$$\hat{H}_{el.}(\xi;q) = \hat{T}_e(\xi) + V_{ne}(\xi;q) + V_{ee}(\xi) + V_{nn}(q) \tag{5.3}$$

where $\hat{T}_e(\xi)$ denotes the kinetic energy operator for electrons, $V_{ne}(\xi;q)$ is the electron-nuclei attraction potential energy, $V_{ee}(\xi)$ is the electron-electron repulsion energy and $V_{nn}(q)$ is the nucleus-nucleus repulsion potential energy. Here, it was

decided to operate in the Hund's case (b) [307] (DUO uses Hund's case (a) [305]), with the rotational energy operator proportional to $\hat{N}-\hat{L}$, that is the difference between the ro-vibronic angular momentum and the electronic angular momentum. In such non-relativistic scheme it is a custom to include extra terms, which account for the 'spin-orbit' and 'spin-rotation' interactions. These operators are usually parametrized empirically. Here all nuclear spin related interactions are neglected. With these spin-relativistic add-ons the total Hamiltonian can be written as:

$$\hat{H}(\phi,q,\xi)=\hat{K}_V(q)+\hat{K}_{SRV}(\phi,q)+\hat{K}_{SRVE}(\phi,q,\xi)+\hat{H}_{el.}(\xi;q)+\hat{H}_{SO}(q,\xi)+\hat{H}_{SR}(\phi,q) \tag{5.4}$$

where the KEO was divided into the vibrational part:

$$\hat{K}_V(q)=-\frac{1}{2}\left[\sum_{\mu,\nu=1}^{3N_{nuc}-6}G_{\mu\nu}\frac{\partial^2}{\partial q_\mu\partial q_\nu}+\sum_{\mu=1}^{3N_{nuc}-6}\tau_\mu\frac{\partial}{\partial q_\mu}\right] \tag{5.5}$$

the spin-ro-vibrational part:

$$\hat{K}_{SRV}(\phi,q)=\frac{1}{2}\left[\sum_{\alpha,\beta}M_{\alpha,\beta}\hat{N}_\alpha\hat{N}_\beta+\sum_\alpha\lambda_\alpha\hat{N}_\alpha\right] \tag{5.6}$$

and the spin-ro-vibronic part:

$$\hat{K}_{SRV}(\phi,q)=\frac{1}{2}\left[\sum_{\alpha,\beta}M_{\alpha,\beta}\hat{L}_\alpha\hat{L}_\beta+\sum_\alpha\left(\lambda_\alpha\hat{L}_\alpha+2\left(M\hat{L}\right)_\alpha\right)\hat{N}_\alpha\right] \tag{5.7}$$

The spin-orbit Hamiltonian can be written in a general form as:

$$\hat{H}_{SO}(q,\xi)=\sum_{\mu\nu}A^{SO}_{\mu\nu}(q)\hat{L}_\mu(\xi)\hat{S}_\nu \tag{5.8}$$

and the spin-rotation Hamiltonian is given by:

$$\hat{H}_{SR}(q) = \sum_{\mu\nu} \gamma^{SR}_{\mu\nu}(q)\hat{N}_\mu \hat{S}_\nu \tag{5.9}$$

The spin-orbit coupling and spin-rotation coupling operators are often approximated by effective operators [307]: $\hat{H}_{SR}(q) \approx \gamma^{SR}(q)\sum_\mu \hat{N}_\mu \hat{S}_\mu$, $\hat{H}_{SO}(q) \approx A^{SO}(q)\sum_\mu \hat{L}_\mu \hat{S}_\mu$.

In the above equations $M_{\alpha\beta}$ denotes the generalised inverse moment of inertia introduced and explained by Sutcliffe in [61]. $\lambda_\alpha = -i\left(v_\alpha + 2\sum_{\mu=1}^{3N_{nuc}-6} W_{\mu\alpha}\frac{\partial}{\partial q_\mu}\right)$ and quantities v_α and $W_{\mu\alpha}$ depend on vibrational coordinates only and are defined in ref. [61]. λ_α is related to Coriolis-couplings and cannot be eliminated by a choice of embedding. The molecule-fixed embedding of the coordinate frame is not specified at this point, but the form of λ_α depends on the choice of the embedding. In the vibrational part of the kinetic energy operator $K_V(q)$ the tensor $G_{\mu\nu}$ and vector τ_μ are functions of coordinates, independent of embedding, and are defined in ref. [61]. All internal-coordinate dependent quantities presented above can be calculated with a little use of algebra when a choice of particular internal coordinates in made. Here we only specify that the internal coordinates are orthogonal ($\mu_{ij} = 0$, see eq. 2.7).

With the total Hamiltonian defined, the next step is to choose a spin-ro-vibronic basis set.

5.1.2 Basis set

We shall follow the standard approach to the vibronic-coupling problem, where a Born-Huang (BH) [182] type expansion is assumed for the ro-vibronic wavefunction. This approach however is not the only one [182, 308], and perhaps is not the best one. Unfortunately, no better representation of the ro-vibronic wavefunction has been given so far, to the best of author's knowledge. The problem with the BH representation is that whenever the space of electronic states is narrowed to few states, non-removable singularities appear in the ro-vibronic Hamiltonian, in regions of the configuration space where two adiabatic electronic states intersect. These singularities are stacked on top of singularities related to space-fixed →

molecule-fixed transformation. The latter case can be efficiently dealt with an appropriate choice of the basis set and embedding of the molecule-fixed coordinates frame [58]. The former problem however is non-resolvable in the present framework, where the electronic wavefunctions are eigenfunctions of a clamped-nuclei electronic Hamiltonian [182, 308]. Approximate diabatisation schemes are possible, which eliminate singularities in the non-adiabatic coupling terms (NACT) and diagonal Born-Oppenheimer correction (DBOC). Yet, an open challenge is to find an alternative procedure for defining ro-vibronic matrix elements in terms of some new, neither adiabatic nor diabatic representation.

The general anzatz for the spin-rovibronic wavefunction is assumed similar to the Born-Huang expansion. By this we mean an expansion of the wavefunction as a sum of products of an 'electronic wavefunction' and a 'spin-ro-vibrational wavefunction':

$$|\Psi(\phi,q,\xi)\rangle = \sum_i |\psi_{el.,i}(\xi;q)\rangle |\Phi_{srv,i}(\phi,q)\rangle \tag{5.10}$$

Effectively the expansion in eq. 5.10 is truncated at few electronic states, which couple substantially. The electronic part of the wavefunction is obtained from electronic structure calculations, in a solution to the eigenproblem for the electronic Hamiltonian $\hat{H}_{el.}(\xi;q)|\psi_{el.,i}(\xi;q)\rangle = V_i(q)|\psi_{el.,i}(\xi;q)\rangle$. The electronic basis forms a complete orthonormal set of functions with the standard scalar product: $\langle\psi_{el.,i'}(\xi;q)|\psi_{el.,i}(\xi;q)\rangle = \int \psi^*_{el.,i'}(\xi;q)\psi_{el.,i}(\xi;q)d\xi = \delta_{i'i}$. Although it should be noted, that this is not the only possibility for the representation of the electronic wavefunction, as we will discuss further on. For the primitive rotational basis a complete set of symmetric-top Hamiltonian eigenvectors $|N,k,M\rangle$ is used. Here N stands for the ro-vibronic angular momentum quantum number, k is the projection of the total angular momentum J on the molecule-fixed z-axis and M is the projection of the total angular momentum J on the space-fixed z-axis. A set of commuting observables for this eigenbasis is $\hat{N}^2,\hat{N}_z,\hat{J}^2,\hat{J}_z,\hat{S}^2$. These operators correspond to the following eigenvalue problems[1]

[1] written in atomic units

$$\begin{aligned}
\hat{N}^2|N,k,M\rangle &= N(N+1)|N,k,M\rangle \\
\hat{N}_z|N,k,M\rangle &= k|N,k,M\rangle \\
\hat{J}^2|N,k,M\rangle &= J(J+1)|N,k,M\rangle \\
\hat{J}_z|N,k,M\rangle &= M_J|N,k,M\rangle \\
\hat{S}^2|N,k,M\rangle &= S(S+1)|N,k,M\rangle
\end{aligned} \tag{5.11}$$

This basis can be further symmetry-adapted with the use of the parity transformation $\hat{E}^*$:

$$\begin{aligned}
|N,K,M,p\rangle = \frac{1}{\sqrt{2}}\left[|N,k,M\rangle + (-1)^{N+k+p}|N,-k,M\rangle\right], \qquad K = |k| > 0 \\
|N,K,M,p\rangle = |N,0,M\rangle, \qquad K = 0
\end{aligned} \tag{5.12}$$

This rotational basis is then coupled and symmetry adapted with a spin basis [60]:

$$\begin{aligned}
|\Psi^{J,K,S,p}_{spinrot}\rangle = \sum_{N=|J-S|}^{J+S} \sum_{M=-N}^{N} \sum_{M_s=-S}^{S} (-1)^{N-S+M_J}\sqrt{2J+1} \begin{pmatrix} N & S & J \\ M & M_s & -M_J \end{pmatrix} \times \\
\times |S,M_s\rangle|N,K,M,p\rangle
\end{aligned} \tag{5.13}$$

where $|S,M_s\rangle$ is the spin standard basis: $\hat{S}^2|S,M_s\rangle = S(S+1)|S,M_s\rangle, \hat{S}_z|S,M_s\rangle = M_s|S,M_s\rangle$ and $\langle S',M'_s|S,M_s\rangle = \delta_{S'S}\delta_{M'_s,M_s}$. The total spin quantum number S is associated with a given isolated electronic state. The energy of the molecule in free space is independent of any space-fixed defined quantum number, that is: M, M_J, M_s. Finally, having defined the electronic and spin-rotational basis, we are ready to write the full basis set adopted to represent the molecular Hamiltonian in eq. 5.4:

$$|\Psi^{J,p,h}\rangle = \sum_{S} \sum_{N=|J-S|}^{J+S} \sum_{M=-N}^{N} \sum_{M_s=-S}^{S} \sum_{K=p}^{N} \sum_{m,n,j}^{vib.states} \sum_{i}^{el.states} (-1)^{N-S+M_J} \sqrt{2J+1} \begin{pmatrix} N & S & J \\ M & M_s & -M_J \end{pmatrix} \times$$
$$\times C^{J,p,h}_{i,N,K,m,n,j} |i\rangle |S,M_s\rangle |N,K,M,p\rangle |m^{(i)}\rangle |n^{(i)}\rangle |jK^{(i)}\rangle \tag{5.14}$$

where $|i\rangle$ is a shorthand notation for an i-th eigenfunction of the electronic Hamiltonian $H_{el.}(\xi;q)$, $|S,M_s\rangle$ is the standard spin basis function defined above, $|N,K,M,p\rangle$ is the parity-adapted symmetric-top Hamiltonian eigenvector, $|m^{(i)}\rangle$, $|n^{(i)}\rangle$ are vibrational basis functions for the r_1 and r_2 stretching, respectively and $|jK^{(i)}\rangle$ is a basis function for the bending motion (θ coordinate). Note that the vibrational basis in general depends on the electronic state i as indicated with the superscript (i). Summation over the S quantum number accounts for mixing of electronic states with different spin multiplicity through spin-orbit coupling or spin-rotation coupling. Additionally the bending vibrational basis state is assumed to depend on K, which as discussed in chapter 2, brings the benefit of eliminating spurious singularities in the Hamiltonian, which result from the vanishing Jacobian of the space-fixed to molecule-fixed transformation. Such regularisation of the Hamiltonian is possible when an associated Legendre polynomial basis is used $|jK\rangle = P_j^{(K)}(\cos\theta)$. The superscript in the basis set notation is reserved for good quantum numbers which in the present case are J and p, while h enumerates the final spin-rovibronic energy states.

Because in this work we are using the complete rotational basis set spanned by eigenvectors of the symmetric-top Hamiltonian: $\{|N,k,M\rangle\}_{k=-N,-N+1,\ldots,N-1,N}$, the total Hamiltonian given in eq. 5.4, can be represented in the spectral representation of the symmetric-top Hamiltonian. Such a trick allows to integrate out rotational degrees of freedom of the molecule in an exact, formal way. The matrix of the total Hamiltonian in this basis can be evaluated analytically. Similarly, it is feasible to formally integrate out over all electronic and spin degrees of freedom to yield an effective vibrational Hamiltonian in the following form:

$$\hat{H}(q) = \hat{K}_V(q) + \hat{K}_{SRV}(q) + \hat{K}_{SRVE}(q) + \hat{H}_{el.}(q) + \hat{H}_{SO}(q) + \hat{H}_{SR}(q) \tag{5.15}$$

where

$$2\hat{K}_V(q) = \delta_{K'K}\delta_{s's}\left[\delta_{i'i}\hat{K}_V(q) + \tilde{G}^{i'i} + \tilde{\tau}^{i'i}\right] \tag{5.16}$$

$$\begin{aligned} 2\hat{K}_{SRV}(q) = \delta_{K'K}\delta_{s's}\Big[\delta_{i'i}\left(2b\left(N(N+1)-K^2\right) - K^2 b_0 + k\lambda_0\right) + \hat{\Lambda}_0^{i'i}\Big] + \\ \delta_{K'K+1}\delta_{s's}\frac{1}{2}C_{NK}^{+}\Big[\delta_{i'i}\left(b_{+1}(2K+1) + \lambda_{+}\right) + \hat{\Lambda}_{+}^{i'i}\Big] + \\ +\delta_{K'K-1}\delta_{s's}\frac{1}{2}C_{NK}^{-}\Big[\delta_{i'i}\left(b_{-1}(2K-1) + \lambda_{-}\right) + \hat{\Lambda}_{-}^{i'i}\Big] + \\ +\frac{1}{2}\delta_{K'K+2}\delta_{s's}\delta_{i'i}b_{+2}C_{NK}^{+}C_{NK+1}^{+} + \\ +\frac{1}{2}\delta_{K'K-2}\delta_{s's}\delta_{i'i}b_{-2}C_{NK}^{-}C_{NK-1}^{-} \end{aligned} \tag{5.17}$$

$$\begin{aligned} 2\hat{K}_{SRVE}(q) = \delta_{K'K}\delta_{s's}\left[\sum_{\alpha\beta}M_{\alpha\beta}L_{\alpha\beta}^{i'i} + \sum_{\alpha}\lambda_{\alpha}L_{\alpha}^{i'i} - K\langle i'|(M\hat{L})_z|i\rangle + \hat{\mathcal{O}}^{i'i}\right] + \\ +\delta_{K'K+1}C_{NK}^{+}\langle i'|(M\hat{L})_{+}|i\rangle + \delta_{K'K-1}C_{NK}^{+}\langle i'|(M\hat{L})_{-}|i\rangle \end{aligned} \tag{5.18}$$

$$\hat{H}_{el.}(q) = \delta_{s's}\delta_{K'K}\delta_{i'i}V_{i'i}(q) \tag{5.19}$$

$$\hat{H}_{SO}(q) = A^{SO}(q)\left[\frac{1}{2}\left[\delta_{s's+1}\delta_{K'K}C_{SM_S}^{+}L_{+}^{i'i} + \delta_{s's-1}\delta_{K'K}C_{SM_S}^{-}L_{-}^{i'i}\right] + \delta_{s's}\delta_{K'K}L_z^{i'i}\right] \tag{5.20}$$

$$\hat{H}_{SR}(q) = \gamma^{SR}(q)\left[\frac{1}{2}\left[\delta_{s's+1}\delta_{K'K+1}C^{+}_{SM_S}C^{+}_{NK} + \delta_{s's-1}\delta_{K'K-1}C^{-}_{SM_S}C^{-}_{NK}\right] + \delta_{s's}\delta_{K'K}K\right] \tag{5.21}$$

where $C^{\pm}_{NK} = (N(N+1) \mp K(K+1))^{\frac{1}{2}}$. Here, for clarity of presentation the integration was performed with the use of the primitive spin-rotational-electronic basis: $|i\rangle|s,M_s\rangle|N,K,M\rangle$. Symmetry adaptation, as a linear unitary operation is rather straightforward and can be applied at the implementation stage.

All operators are labelled by the quantum numbers, which define the spin-electronic-rotational basis: J,K,i,S,p. We omit the space-fixed defined quantum numbers as irrelevant to the dynamics in free space. Each operator written above is defined for a given set of good quantum numbers J and p, which are assumed implicit and not denoted for the clarity of presentation. Thus, there are three sets of indices, which define the Hamiltonian hyper-matrix: $K'K$, $i'i$ and $S'S$. The quantities appearing in the above equations for the effective operators are as follows:

$$\begin{aligned}
\tilde{G}^{i'i} &= -\frac{1}{2}\sum_{\mu,\nu=1}^{3N_{nuc.}-6}\left[G_{\mu\nu}\beta^{i'i}_{\mu\nu} + \tau_\mu\alpha^{i'i}_{\mu}\right] \\
\beta^{i'i}_{\mu\nu} &= \langle i'|\frac{\partial^2}{\partial q_\mu \partial q_\nu}|i\rangle, \qquad \alpha^{i'i}_{\mu} = \langle i'|\frac{\partial}{\partial q_\mu}|i\rangle \\
\tilde{\tau}^{i'i} &= -\frac{1}{2}\sum_{\mu,\nu=1}^{3N_{nuc.}-6} G_{\mu\nu}\left(\alpha^{i'i}_{\mu}\frac{\partial}{\partial q_\mu} + \alpha^{i'i}_{\nu}\frac{\partial}{\partial q_\nu}\right) \\
\hat{\Lambda}^{i'i}_{\gamma} &= -2i\sum_{\mu=1}^{3N_{nuc}-6} W_{\mu\gamma}\alpha^{i'i}_{\mu} \quad \gamma = x,y,z \\
\hat{\Lambda}^{i'i}_{0} &= \hat{\Lambda}^{i'i}_{z}, \quad \hat{\Lambda}^{i'i}_{\pm} = \hat{\Lambda}^{i'i}_{x} \mp i\hat{\Lambda}^{i'i}_{y} \\
L^{i'i}_{\alpha\beta} &= \langle i'|\hat{L}_\alpha\hat{L}_\beta|i\rangle \\
L^{i'i}_{\alpha} &= \langle i'|\hat{L}_\alpha|i\rangle \\
\mathscr{O}^{i'i} &= -2i\sum_{\mu=1}^{3N_{nuc}-6}\langle i'|(W\hat{L})_\mu\frac{\partial}{\partial q_\mu}|i\rangle \\
V_{i'i}(q) &= \langle i'|\hat{H}_{el.}(\xi;q)|i\rangle
\end{aligned} \tag{5.22}$$

and all $\pm$ sub-scripted operators appearing in eqs. 5.16 – 5.21 are defined as $A_{\pm} = A_x \mp iA_y$. There are essentially two types of operators, which act on the vibrational basis: functions of vibrational coordinates and differential operators. In the above Hamiltonian there are two types of differential operators enclosed in $\tilde{\tau}^{i'i}$ and λ_α. The former one is associated with derivative couplings of different electronic states (NACT) and the latter is associated with the Coriolis-coupling of ro-vibrational states.

5.1.3 Input functions

To summarize, the fully coupled spin-ro-vibronic procedure (working name: DVR3D-UV) requires the following input functions for solving the stationary Schrödinger equation:

1. $V_i(q)$ - potential energy surfaces (PES) for each adiabatic electronic state of interest.

2. $\alpha_\mu^{i'i}(q)$ - non-adiabatic coupling matrix elements (NACT) between electronic states i and i' and for vibrational coordinate μ.

3. $\beta_{\mu\nu}^{i'i}(q)$ - diagonal Born-Oppenheimer correction (DBOC) terms and pseudo-potential off-diagonal non-adiabatic terms.

4. $A^{SO}(q)$ - spin-orbit coupling surface(s). Note that in general the spin-orbit coupling operator is proportional to a tensor quantity $A_{i'i}^{SO}(q)$ which mixes different spin states.

5. $L_\alpha^{i'i}(q), L_{\alpha\beta}^{i'i}(q)$ - L-coupling and L^2-coupling surfaces, respectively.

6. $\mathscr{O}^{i'i}(q)$ - L-vibronic coupling surfaces.

7. $\gamma^{SR}(q)$ -spin-rotation coupling surface(s). Note that in general the spin-rotation coupling operator is proportional to a tensor quantity $\gamma_{i'i}^{SR}(q)$ which mixes different spin states.

5.1.4 Solution strategy

The solution strategy for the spin-ro-vibronic Schrödinger equation with the effective Hamiltonian from eq. 5.15 consists of a multi-step diagonalisation-truncation procedure. The idea of two-step diagonalisation-truncation originates from Tennyson and Sutcliffe [67, 86, 87] has been proven very efficient, especially in computation of high-J states. In order to maintain this high efficiency and feasibility for highly excited rotational states we shall follow here a similar procedure.

Figure 5.1 depicts a suggestion for the implementation scheme, which can be followed in the future computer implementation of DVR3D-UV. In the first step, we focus on the electronic index of the Hamiltonian, more specifically on its diagonal blocks (marked in purple in the uppermost matrix in Figure 5.1). Each of these blocks is indexed by the K, K' approximate quantum numbers. For clarity of presentation, the uppermost matrix in Figure 5.1 corresponds to a two-dimensional electronic states space. For each electronic diagonal block an appropriate ro-vibrational problem needs to be solved. This ro-vibrational problem is however different from the problem solved in the original ro-vibrational version of DVR3D. Now, some new operators are included into the Hamiltonian, which requires calculation of some additional matrix elements. These matrix elements arise due to vibronic coupling, which is diagonal in the electronic index: the DBOC terms and any diagonal contributions from the operators listed in the previous paragraph. Fortunately, these modified ro-vibrational problems can be separated into the old ro-vibratinal problem solved by the original DVR3D plus additional matrix elements, which can be calculated using quadrature schemes already implemented in DVR3D.

There are more than one possibilities for order in which the total Hamiltonian is diagonalised. Below given are propositions for sequential diagonalisation of the total Hamiltonian and comparison of their approximate computational cost, so the best option can be chosen.

Scenario 1: a) for each diagonal block of the total Hamiltonian (in the electronic index) diagonalise the Coriolis-decoupled problem, as in DVR3DRJZ, but with additional matrix elements, which result from vibronic couplings. Form a com-

posite basis from combined eigenbases of the just diagonalised electronic blocks; b) diagonalise the full Coriolis-coupled problem in this composite basis.

Scenario 2: a) diagonalise separately Coriolis-decoupled problems for each block of the full Hamiltonian indexed by electronic quantum numbers; b) for each of these blocks diagonalise the full Coriolis-coupled problem using a contracted basis from step a); c) diagonalise the full Hamiltonian, which consists of already pre-diagonalised blocks.

We are going to assume the computational complexity for diagonalisation as approximately proportional to the cube of the size of the diagonalised matrix ($\mathscr{O}(N^3)$, denoted for simplicity as N^3) [309]. The vibrational basis for each scenario is assumed of the same size N_v, so that for a given J and p the size of a single electronic block matrix is $N_i = N_v \times (J - p + 1)$. Index i labels electronic states. Solutions the the Coriolis-decoupled problem form a basis, which can be truncated before utilizing in the next stage. Let the truncation parameter be $0 \leq \gamma \leq 1$, so that the Coriolis-coupled matrix for the i-th electronic block to be diagonalised is of size $\gamma \times N_i$. The computational time for scenarios 1–3 can be estimated as follows:

Scenario 1). In step a) we diagonalise separately the Coriolis-decoupled problem inside each of N_{el} independent diagonal electronic blocks of the full Hamiltonian, which gives the cost of $N_{el} \times N_i^3$. Step b), which involves diagonalisation in the full electronic-ro-vibrational Hilbert space generates cost: $\left(\sum_{i=1}^{N_{el}} \gamma N_i\right)^3$ where N_i denotes ro-vibrational basis which in general could be different size for different electronic states. In this fashion the total computational cost in scenario 1 is $T^{(1)} = N_{el} \times N_i^3 + \left(\sum_{i=1}^{N_{el}} \gamma N_i\right)^3 = N_{el}\left(1 + N_{el}^2 \gamma^3\right) N^3$, where in the last equality identical basis size for all electronic states was assumed ($N_i = N$).

Scenario 2). In step a) we diagonalise separately the Coriolis-decoupled problem inside each of $N_{el}(N_{el}+1)/2$ independent diagonal electronic blocks of the full Hamiltonian, which gives the cost of $N_{el}(N_{el}+1)/2 \times N_i^3$. In step b) we solve the Coriolis-coupled problem for each electronic block separately which gives the cost: $N_{el}(N_{el}+1)/2 \times \gamma^3 N_i^3$; assuming that identical ro-vibrational basis size is chosen for each block. Finally in step c) the full electronic-ro-vibrational Hamiltonian ma-

trix is diagonalised. This matrix consists of electronic blocks which are diagonal in K. Diagonalisation of the final Hamiltonian costs $N_{el}^3\gamma^3N^3$. The overall cost then reads: $T^{(2)} = N_{el}\left(\frac{1}{2}(N_{el}+1)(1+\gamma^3)+N_{el}^2\gamma^3\right)\times N^3$.

Comparison of the computational costs for both scenarios considered indicates that scenario 1 has the lowest computational requirements: $T^{(2)} > T^{(1)}$. For this reason the scheme from scenario 1 is recommended for implementation.

With the choice of scenario 1, the (vibronically modified) ro-vibrational problem for each adiabatic electronic state is solved in a two-step scheme. In the first step, K is considered a good quantum number and for each K value a separate vibrational problem is solved, by diagonalising an appropriate Hamiltonian. This situation corresponds to neglecting the off-diagonal terms in K in the big middle matrix in Figure 5.1 and diagonalising each orange Hamiltonian block independently. The resulting Coriolis-decoupled eigenfunctions contain already much information about the nuclear dynamics, thus serve as an excellent basis for the second step, in which terms off-diagonal in K are included. The situation corresponds to diagonalising the full big middle matrix in Figure 5.1, that is including the green and purple blocks of the Hamiltonian.

The variational coefficients of the wavefunction calculated in the first stage are given as

$$|v_1,i,S,K,J,p\rangle = \sum_{j,m,n} {}^{(1)}C_{m,n,j}^{J,p,K,i,v_1,S}|m^{(i)}\rangle|n^{(i)}\rangle|jKp^{(i)}\rangle \tag{5.23}$$

where v_1 is an index enumerating solutions to the Coriolis-decoupled problem. S indexes the total spin of a given electronic state i. The number of solutions $v_{max} = \gamma\times N$ passed to the next stage is essential for the total computational cost. In step 2, for each diagonal electronic block separately, the Coriolis-coupled problem is solved, meaning that the wavefunction after the second stage can be written as:

$$|v_2,i,S,J,p\rangle = \sum_{K=p}^{J}\sum_{v_1=1}^{\gamma\times N} {}^{(2)}C_{v_1,K}^{J,p,i,S,v_2}|v_1,i,S,K,J,p\rangle \tag{5.24}$$

From the eigenbases generated by diagonalisation of each electronic diagonal block

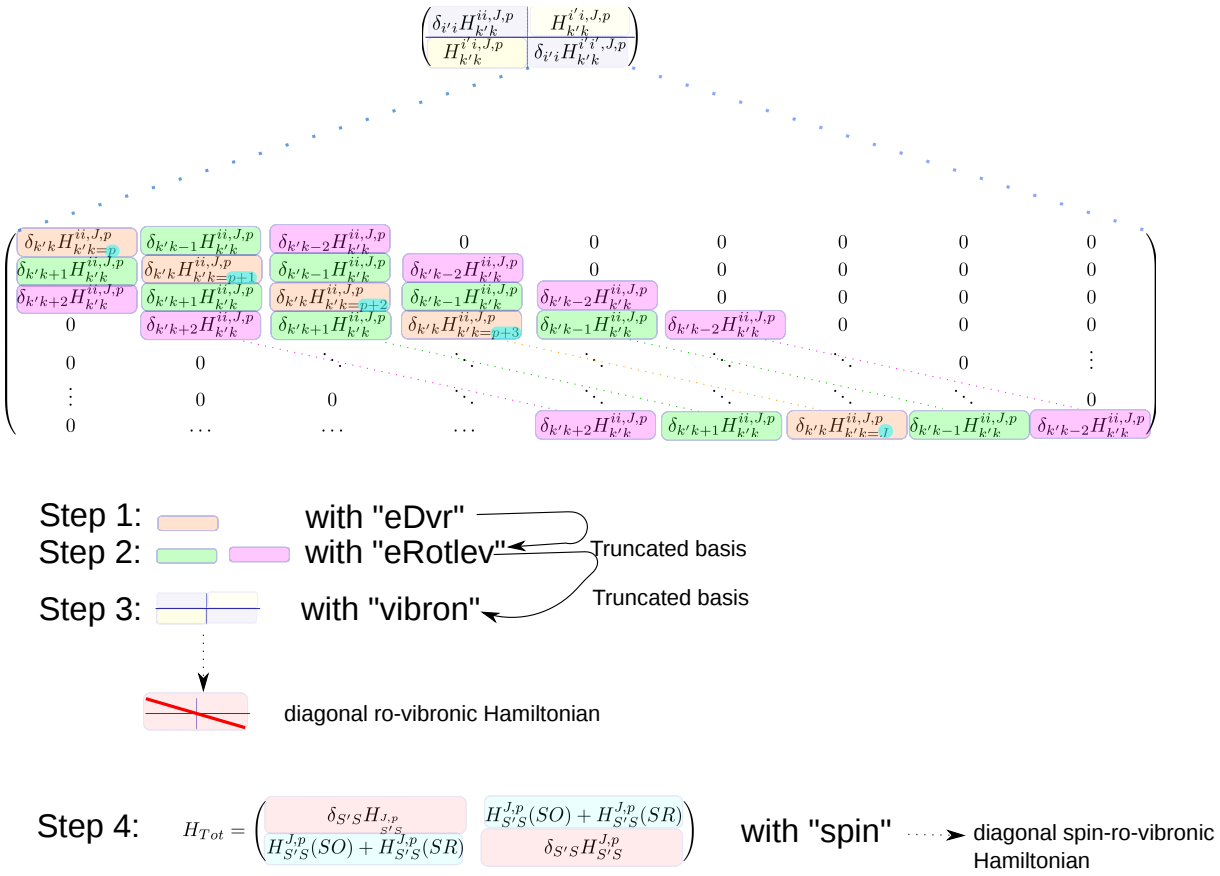

Figure 5.1: A scheme for the representation of the total Hamiltonian on the electronic-rotational manifold. See text for further details.

separately a composite basis is formed:

$$|v_3, S, J, p\rangle_{v_3=1,\ldots,\gamma\times N\times N_{el}} = |v_2, i, S, J, p\rangle_{v_2=1,\ldots\gamma\times N; i=1,..,N_{el}} \tag{5.25}$$

meaning that $v_3 = (v_2, i)$ is now a combined index enumerating elements of the Hamiltonian.

In step 3, a routine called 'vibron' receives the composite basis from step 2. Step two has to be performed for every diagonal block in the electronic coordinate. Depending on the system, the off-diagonal blocks in the electronic Hamiltonian could be treated as some kind of not-too-large perturbation. For this reason, efficient diagonalisation schemes for sparse matrices with small off-diagonal elements could be utilized here.

$$|S,J,p,\tilde{h}\rangle = \sum_{v_3=1}^{\gamma\times N\times N_{el}} {}^{(3)}C_{v_3}^{J,p,S,\tilde{h}}|v_3,S,J,p\rangle \tag{5.26}$$

In the last step, if needed, mixing between different spin states is considered. Such mixing can originate from the spin-rotation coupling terms or off-diagonal terms in the spin-orbit coupling operator. The structure of matrices at this stage should be simple, due to the $\Delta S = \pm 1$ selection rule dictated by the spin-rotation and spin-orbit interactions. Direct diagonalisation of this matrix leads to the final spin-ro-vibronic energy levels and wavefunctions

$$|J,p,h\rangle = \sum_{S=1}^{N_{spin}} \sum_{\tilde{h}} {}^{(4)}C_{s,\tilde{h}}^{S,J,p,h}|J,p,\tilde{h}\rangle. \tag{5.27}$$

The approach to solution of the nuclear motion problem based on the Born-Huang-type expansion of the wavefunction with electronic basis functions chosen as the eigenbasis of the electronic Hamiltonian inherently fails in the vicinity of conical intersections between different adiabatic electronic states. When two electronic states become degenerate, it is straightforward to show, that non-adiabatic coupling matrix elements diverge, producing infinite quantities [310]. Even though in the standard Born-Oppenheimer picture the nuclear wavfunction must have a node at the point of the CI, and in this manner if one assumes that the molecule is not allowed in some way to occupy this particular point in the configuration space (which is by the way a rather ridiculous artifact) then the values of NACTs are very sensitive to small inaccuracies in the electronic wavefunction. This situation can be viewed as some kind of a resonance interaction between two adiabatic electronic states.

From numerical point of view, solving the nuclear motion problem in the adiabatic representation near the CI is a suicidal task. For this reason a number of techniques have been developed, in which the KEO is diagonalised in the electronic coordinate, all under a common label of 'diabatisation' schemes. In the simple space of two interacting electronic states such diabatisation can be performed exactly. However, as shown by Mead and Truhlar [311], solutions to differential equa-

tions defining the diabatic representation for more than two interacting electronic states is ambiguous and cannot be found in the exact way. Several approximate diabatisation schemes have been therefore developed over the years. In the diabatic representation singularities related to NACTs vanish making the requirement of strongly vanishing nuclear wavefunciton at the CI no longer necessary. This clearly indicates that the singularities in the Hamiltonian at the point of CI in the adiabatic representation are artifacts of the method and have little to do with physical reality, especially because the adiabatic and diabatic representation are formally connected by an unitary transformation, which preserves the scalar product. This cognitive dissonance has been a subject to numerous papers [312–314].

Another problem with the existence of CIs is the phase of the electronic wavefunction. Electronic structure programs generally provide the electronic wavefucntion with an arbitrary phase, which depends on the instantaneous configuration of nuclei. Whenever a CI is present and the ro-vibrational wavepacket can encircle this CI, the adiabatic electronic wavefunction becomes double valued, i.e. gains a geometric phase when encircling the CI [315–318]. In order to account for this double-valueless of the electronic wavefunciton, the nuclear wavefunction also needs to be double valued. Alternatively one may think of transforming the electronic and nuclear wavefunctions so that they are single valued. In such case the nuclear motion Hamiltonian needs to be also transformed with a similarity transformation, and this in general affect the nuclear dynamics [319, 320]. In order to find this transformation, again a diabatisation scheme needs to be employed.

Clearly, from this perspective the geometric phase (or Berry phase) is an artifact of the Born-Oppenheimer approximation; but without inclusion of this phase, under some circumstances the dynamics can be simply wrongly modelled [321]. The geometric phase effect then can be regarded at a similar level as the *Jahn-Teller effect* or the *Renner-Teller effect* [60], all of which are a consequence of the Born-Huang expansion, the parametric dependence of the electronic wavefunction on the nuclear coordinates and the spectral representation of the electronic Hamiltonian for the electronic wavefunctions. The 'effect' of distortion of the high-symmetry geom-

etry of the molecule due to 'vibronic interaction' between PESs in the Jahn-Teller effect occurs only because we divide the solution scheme into the 'clamped-nuclei' stage (Born-Oppenheimer) and 'correction' (vibronic interactions). The problems mentioned above in the context of the DVR3D-UV methodology should be a subject of future studies.

Chapter 6

Conclusions

This thesis addresses a number of problems in modern molecular spectroscopy. From the nuclear motion theory point of view, the main focus was on quantum-mechanical description of the rotational-vibrational and rotational-vibrational-electronic motion of triatomic molecules. In chapter 3, rotational-vibrational line lists for 13 isotopologues of carbon dioxide were calculated, together with a theoretical analysis of reliability of computed transition intensities. Completeness and accuracy of these line lists were evaluated against a range of experimental and theoretical studies, providing a comprehensive benchmark, which indicated that the accuracy of calculated transition intensities constitutes a new state-of-the-art for CO_2. For this reason 12 line lists for stable isotopologues of carbon dioxide were included as a part of the HITRAN 2016 spectroscopic database. This fulfilled the working goal of the CO_2 project. The line lists are available for use on the website of the ExoMol project (www.exomol.com), as well as in the newest edition of HITRAN [196]. Transition intensities calculated for two important absorption bands (near 1.6 μm and 2.06 μm) of the main isotopologue of CO_2 have been shown to meet the sub-percent accuracy requirements for remote sensing and can be used in retrieval models for concentration measurements of this greenhouse gas in the Earth's atmosphere, e.g. in NASA's OCO-2 mission.

A theory of Coriolis-type and Fermi-type interactions between ro-vibrational energy levels was presented and later utilized as a background for a method for estimating sensitivity of transition intensities to minor inaccuracies in the wavefunction

(hence in the PES). Application of this method to 13 isotopologues of CO_2 required computation of 54 room-temperature infrared line lists. As a result, each transition intensity was assigned a reliability factor, which has also been found to be a simple descriptor for detecting resonance interactions between energy levels, and a good measure quantifying the strength of such interactions. Information about the strength of interactions between ro-vibrational energy levels was elucidated only by analysing the sensitivity of transition intensities to imperfections in the PES. This technique is believed to be applicable to other molecules as well.

Rotational-vibrational-electronic line lists in the Born-Oppenheimer approximation were calculated for the SO_2 molecule in the UV absorption region and for the CaOCa molecule in the visible region. For this purpose appropriate *ab initio* PESs and a TDMS were generated. These were the first reported *ab initio* ro-vibronic line lists for triatomic molecules, generated with an exact kinetic energy operator. The influence of the nuclear coordinate dependence of the electronic transition dipole moment was discussed with the conclusion, that for low energy excitations intensity difference due to this dependence is rather weak, usually below 10%. By this observation, the Franck-Condon approximation for transition intensities gained a rigorously founded justification. The DVR3D code for electronic transitions thus awaits further applications to other triatomic molecules. The only essential requirement for this purpose is availability of PESs for electronic states of interest.

It appears essential to derive a theoretical procedure implemented in a computer code, which is capable of accurately solving the rotational-vibrational-electronic Schrödinger equation beyond the Born-Oppenheimer approximation. Such scheme would be a natural continuation to the Born-Oppenheimer DVR3D code used for calculation of ro-vibronic line lists for SO_2 and CaOCa. Chapter 5 discussed one possible approach to this problem by derivation of the exact non-relativistic rotational-vibrational-electronic Hamiltonian for a triatomic molecule. Matrix elements of this Hamiltonian in a chosen variational basis were evaluated and a prospective implementation scheme was outlined.

Going beyond the present 0–8000 cm^{-1} spectral applicability region for the UCL line lists is a future challenge. An update to the Ames-1 PES (named Ames-2) published [322] just before submission of this thesis is believed to be applicable at least up to 25 000 cm^{-1}(upper energy level), but the present *ab initio* UCL DMS must be improved. Such improvement would require calculation of additional dipole moment points, which correspond to geometries located at higher electronic energies. Future studies concerning CO_2 should be thus aimed at construction of a global DMS for the electronic ground state of the CO_2 molecule. This would allow for computation of high accuracy high-temperature CO_2 line lists reaching visible and possibly UV absorption region.

Implementation of non-adiabatic effects into DVR3D is another important objective for future research. Almost all triatomic molecules have their electronic excited states significantly affected by vibronic interactions, thus for genuine modelling of rotational-vibrational-electronic spectra of triatomic molecules, a high-quality ro-vibronic model is an absolute necessity. A first step to circumvent this problem was presented in Chapter 5, but further work is obviously needed. Finally, the large amount of data generated for CO_2, SO_2 and Ca_2O is expected to be further utilized, beside remote sensing procedures, in modelling of radiative cooling of molecules in atmospheres, ro-vibrational relaxation models, or monitoring of industrial emissions ($^{14}CO_2$) and volcanic hazes (SO_2).

Bibliography

[1] D. R. Lide, CRC Handbook of Chemistry and Physics, 82nd Edition, CRC Press, 2001.

[2] A. Butz, S. Guerlet, O. Hasekamp, D. Schepers, A. Galli, I. Aben, C. Frankenberg, J. M. Hartmann, H. Tran, A. Kuze, G. Keppel-Aleks, G. Toon, D. Wunch, P. Wennberg, N. Deutscher, D. Griffith, R. Macatangay, J. Messerschmidt, J. Notholt, T. Warneke, Toward accurate CO_2 and CH_4 observations from GOSAT, Geophys. Res. Lett. 38 (2011) L14812. doi:{10.1029/2011GL047888}.

[3] J. B. Abshire, H. Riris, G. R. Allan, C. J. Weaver, J. Mao, X. Sun, W. E. Hasselbrack, A. Yu, A. Amediek, Y. Choi, E. V. Browell, A Lidar Approach to Measure CO_2 Concentrations from Space for the ASCENDS Mission, SPIE 7832 (2010) 78320D. doi:{10.1117/12.868567}.

[4] K. R. Kumar, V. Valsala, Y. K. Tiwari, J. Revadekar, P. Pillai, S. Chakraborty, R. Murtugudde, Intra-seasonal variability of atmospheric CO_2 concentrations over india during summer monsoons, Atmospheric Environment 142 (2016) 229–237. doi:10.1016/j.atmosenv.2016.07.023.

[5] V. A. Velazco, M. Buchwitz, H. Bovensmann, M. Reuter, O. Schneising, J. Heymann, T. Krings, K. Gerilowski, J. P. Burrows, Towards space based verification of CO_2 emissions from strong localized sources: fossil fuel power plant emissions as seen by a CarbonSat constellation, Atmos. Meas. Tech. 4 (2011) 2809–2822. doi:{10.5194/amt-4-2809-2011}.

[6] D. Crisp, H. R. Pollock, R. Rosenberg, L. Chapsky, R. A. M. Lee, F. A. Oyafuso, C. Frankenberg, C. W. O'Dell, C. J. Bruegge, G. B. Doran, A. Eldering, B. M. Fisher, D. Fu, M. R. Gunson, L. Mandrake, G. B. Osterman, F. M. Schwandner, K. Sun, T. E. Taylor, P. O. Wennberg, D. Wunch, The on-orbit performance of the orbiting carbon observatory-2 (OCO-2) instrument and its radiometrically calibrated products, Atmospheric Measurement Techniques Discussions (2016) 1–45doi:10.5194/amt-2016-281.

[7] D. Wunch, P. O. Wennberg, G. C. Toon, B. J. Connor, B. Fisher, G. B. Osterman, C. Frankenberg, L. Mandrake, C. O'Dell, P. Ahonen, S. C. Biraud, R. Castano, N. Cressie, D. Crisp,

N. M. Deutscher, A. Eldering, M. L. Fisher, D. W. T. Griffith, M. Gunson, P. Heikkinen, G. Keppel-Aleks, E. Kyrö, R. Lindenmaier, R. Macatangay, J. Mendonca, J. Messerschmidt, C. E. Miller, I. Morino, J. Notholt, F. A. Oyafuso, M. Rettinger, J. Robinson, C. M. Roehl, R. J. Salawitch, V. Sherlock, K. Strong, R. Sussmann, T. Tanaka, D. R. Thompson, O. Uchino, T. Warneke, S. C. Wofsy, A method for evaluating bias in global measurements of CO_2 total columns from space, Atmos. Chem. Phys. 11 (2011) 12317–12337. doi:10.5194/acp-11-12317-2011.

[8] T. E. Taylor, C. W. O'Dell, C. Frankenberg, P. T. Partain, H. Q. Cronk, A. Savtchenko, R. R. Nelson, E. J. Rosenthal, A. Y. Chang, B. Fisher, G. B. Osterman, R. H. Pollock, D. Crisp, A. Eldering, M. R. Gunson, Orbiting carbon observatory-2 (OCO-2) cloud screening algorithms: validation against collocated MODIS and CALIOP data, Atmospheric Measurement Techniques 9 (3) (2016) 973–989. doi:10.5194/amt-9-973-2016.

[9] D. Wunch, P. O. Wennberg, G. Osterman, B. Fisher, B. Naylor, C. M. Roehl, C. O'Dell, L. Mandrake, C. Viatte, D. W. Griffith, N. M. Deutscher, V. A. Velazco, J. Notholt, T. Warneke, C. Petri, M. D. Maziere, M. K. Sha, R. Sussmann, M. Rettinger, D. Pollard, J. Robinson, I. Morino, O. Uchino, F. Hase, T. Blumenstock, M. Kiel, D. G. Feist, S. G. Arnold, K. Strong, J. Mendonca, R. Kivi, P. Heikkinen, L. Iraci, J. Podolske, P. W. Hillyard, S. Kawakami, M. K. Dubey, H. A. Parker, E. Sepulveda, O. E. G. Rodriguez, Y. Te, P. Jeseck, M. R. Gunson, D. Crisp, A. Eldering, Comparisons of the orbiting carbon observatory-2 (OCO-2) measurements with TCCON, Atmospheric Measurement Techniques Discussions (2016) 1–45doi:10.5194/amt-2016-227.

[10] D. Wunch, G. C. Toon, J.-F. L. Blavier, R. A. Washenfelder, J. Notholt, B. J. Connor, D. W. T. Griffith, V. Sherlock, P. O. Wennberg, The Total Carbon Column Observing Network, Phil. Trans. Royal Soc. London A 369 (2011) 2087–2112. doi:{10.1098/rsta.2010.0240}.

[11] F. Hase, Improved instrumental line shape monitoring for the ground-based, high-resolution FTIR spectrometers of the Network for the Detection of Atmospheric Composition Change, Atmos. Meas. Tech. 5 (2012) 603–610.

[12] P. F. Bernath, C. T. McElroy, M. C. Abrams, C. D. Boone, M. Butler, C. Camy-Peyret, M. Carleer, C. Clerbaux, P. F. Coheur, R. Colin, P. DeCola, M. DeMaziere, J. R. Drummond, D. Dufour, W. F. J. Evans, H. Fast, D. Fussen, K. Gilbert, D. E. Jennings, E. J. Llewellyn, R. P. Lowe, E. Mahieu, J. C. McConnell, M. McHugh, S. D. McLeod, R. Michaud, C. Midwinter, R. Nassar, F. Nichitiu, C. Nowlan, C. P. Rinsland, Y. J. Rochon, N. Rowlands, K. Semeniuk, P. Simon, R. Skelton, J. J. Sloan, M. A. Soucy, K. Strong, P. Tremblay, D. Turnbull, K. A. Walker, I. Walkty, D. A. Wardle, V. Wehrle, R. Zander, J. Zou, Atmospheric

Chemistry Experiment (ACE): Mission overview, Geophys. Res. Lett. 32 (2005) L15S01. doi:{10.1029/2005GL022386}.

[13] P. F. Bernath, The Atmospheric Chemistry Experiment (ACE), J. Quant. Spectrosc. Radiat. Transf. 186 (2017) 3–16. doi:{10.1016/j.jqsrt.2016.04.006}.

[14] H. Fischer, M. Birk, C. Blom, B. Carli, M. Carlotti, T. von Clarmann, L. Delbouille, A. Dudhia, D. Ehhalt, M. Endemann, J. M. Flaud, R. Gessner, A. Kleinert, R. Koopman, J. Langen, M. Lopez-Puertas, P. Mosner, H. Nett, H. Oelhaf, G. Perron, J. Remedios, M. Ridolfi, G. Stiller, R. Zander, MIPAS: an instrument for atmospheric and climate research, Atmos. Chem. Phys. 8 (2008) 2151–2188.

[15] J. Jouzel, Calibrating the isotopic paleothermometer, Science 286 (1999) 910–911.

[16] C. E. Miller, D. Crisp, P. L. DeCola, S. C. Olsen, J. T. Randerson, A. M. Michalak, A. Alkhaled, P. Rayner, D. J. Jacob, P. Suntharalingam, D. B. A. Jones, A. S. Denning, M. E. Nicholls, S. C. Doney, S. Pawson, H. Boesch, B. J. Connor, I. Y. Fung, D. O'Brien, R. J. Salawitch, S. P. Sander, B. Sen, P. Tans, G. C. Toon, P. O. Wennberg, S. C. Wofsy, Y. L. Yung, R. M. Law, Precision requirements for space-based X-CO2 data, J. Geophys. Res. 112 (2007) D10314. doi:{10.1029/2006JD007659}.

[17] B. Connor, H. Bösch, J. McDuffie, T. Taylor, D. Fu, C. Frankenberg, C. O'Dell, V. H. Payne, M. Gunson, R. Pollock, J. Hobbs, F. Oyafuso, Y. Jiang, Quantification of uncertainties in OCO-2 measurements of XCO2: simulations and linear error analysis, Atmospheric Measurement Techniques 9 (10) (2016) 5227–5238. doi:10.5194/amt-9-5227-2016.

[18] C. D. Keeling, H. Brix, N. Gruber, Seasonal and long-term dynamics of the upper ocean carbon cycle at station ALOHA near hawaii, Global Biogeochemical Cycles 18 (4) (2004). doi:10.1029/2004gb002227.

[19] E. E. J. R., C. Thure, D. M. Denise, A History of Atmospheric CO_2 and Its Effects on Plants, Animals, and Ecosystems (Ecological Studies), Springer, 2006.

[20] C. H. Reick, T. Raddatz, J. Pongratz, M. Claussen, Contribution of anthropogenic land cover change emissions to pre-industrial atmospheric CO_2, Tellus B 62 (2010) 329–336. doi:10.1111/j.1600-0889.2010.00479.x.

[21] H. D. Graven, Impact of fossil fuel emissions on atmospheric radiocarbon and various applications of radiocarbon over this century, Proceedings of the National Academy of Sciences 112 (31) (2015) 9542–9545. doi:10.1073/pnas.1504467112.

[22] P. N. Pearson, M. R. Palmer, Atmospheric carbon dioxide concentrations over the past 60 million years, Nature 406 (2000) 695–699. doi:10.1038/35021000.

[23] G. M. Shved, On the abundances of carbon dioxide isotopologues in the atmospheres of mars and earth, Solar System Res. 50 (2016) 161–164. doi:10.1134/S0038094616020064.

[24] S. J. Lehman, J. B. Miller, C. Wolak, J. Southon, P. P. Tans, S. A. Montzka, C. Sweeney, A. Andrews, B. LaFranchi, T. P. Guilderson, J. C. Turnbull, Allocation of terrestrial carbon sources using $^{14}CO_2$: Methods, measurement, and modeling, Radiocarbon 55 (2013) 1484–1495.

[25] H. Tomita, K. Watanabe, Y. Takiguchi, J. Kawarabayashi, T. Iguchi, Radioactive carbon isotope monitoring system based on cavity ring-down laser spectroscopy for decommissioning process of nuclear facilities, J. Power Energy Systems 2 (2008) 221–228. doi:10.1299/jpes.2.221.

[26] I. Galli, S. Bartalini, S. Borri, P. Cancio, D. Mazzotti, P. De Natale, G. Giusfredi, Molecular gas sensing below parts per trillion: Radiocarbon-dioxide optical detection, Phys. Rev. Lett. 107 (2011) 270802. doi:10.1103/physrevlett.107.270802.

[27] F. Oyafuso, V. H. Payne, B. J. Drouin, V. M. Devi, D. C. Benner, K. Sung, S. Yu, I. E. Gordon, R. Kochanov, Y. Tan, D. Crisp, E. J. Mlawer, A. Guillaume, High accuracy absorption coefficients for the orbiting carbon observatory-2 (OCO-2) mission: Validation of updated carbon dioxide cross-sections using atmospheric spectra, J. Quant. Spectrosc. Radiat. Transf. (In press, 2017) doi:10.1016/j.jqsrt.2017.06.012.

[28] O. L. Polyansky, K. Bielska, M. Ghysels, L. Lodi, N. F. Zobov, J. T. Hodges, J. Tennyson, High accuracy CO_2 line intensities determined from theory and experiment, Phys. Rev. Lett. 114 (2015) 243001. doi:10.1103/PhysRevLett.114.243001.

[29] G. Wuebbeler, G. J. P. Viquez, K. Jousten, O. Werhahn, C. Elster, Comparison and assessment of procedures for calculating the R(12) line strength of the $\nu_1 + 2\nu_2 + \nu_3$ band of CO_2, J. Chem. Phys. 135 (2011) 204304. doi:{10.1063/1.3662134}.

[30] J. T. Hodges, National Institute of Standards and Technology, private communication (2017).

[31] D. C. Benner, V. M. Devi, K. Sung, L. R. Brown, C. E. Miller, V. H. Payne, B. J. Drouin, S. Yu, T. J. Crawford, A. W. Mantz, M. A. H. Smith, R. R. Gamache, Line parameters including temperature dependences of air- and self-broadened line shapes of $^{12}C^{16}O_2$: 2.06-μm region, J. Mol. Spectrosc. 326 (2016) 21–47. doi:10.1016/j.jms.2016.02.012.

[32] T. A. Odintsova, E. Fasci, L. Moretti, E. J. Zak, O. L. Polyansky, J. Tennyson, L. Gianfrani, A. Castrillo, Highly accurate intensity factors of pure CO2 lines near 2 μm, The Journal of Chemical Physics 146 (24) (2017) 244309. doi:10.1063/1.4989925.

[33] J. Brunzendorf, V. Werwein, A. Serduykov, O. Werhahn, V. Ebert, CO_2 line strength measurements in the 20012–00001 band near 2 μm, in: The 24th Colloquium on High Resolution Molecular Spectroscopy, 2015, p. O17.

[34] L. S. Rothman, I. E. Gordon, R. J. Barber, H. Dothe, R. R. Gamache, A. Goldman, V. I. Perevalov, S. A. Tashkun, J. Tennyson, HITEMP, the High-Temperature Molecular Spectroscopic Database, J. Quant. Spectrosc. Radiat. Transf. 111 (2010) 2139–2150.

[35] N. Jacquinet-Husson, R. Armante, N. A. Scott, A. Chédin, L. Crépeau, C. Boutammine, A. Bouhdaoui, C. Crevoisier, V. Capelle, C. Boonne, N. Poulet-Crovisier, A. Barbe, D. C. Benner, V. Boudon, L. R. Brown, J. Buldyreva, A. Campargue, L. H. Coudert, V. M. Devi, M. J. Down, B. J. Drouin, A. Fayt, C. Fittschen, J.-M. Flaud, R. R. Gamache, J. J. Harrison, C. Hill, Ø. Hodnebrog, S. M. Hu, D. Jacquemart, A. Jolly, E. Jiménez, N. N. Lavrentieva, A. W. Liu, L. Lodi, O. M. Lyulin, S. T. Massie, S. Mikhailenko, H. S. P. Müller, O. V. Naumenko, A. Nikitin, C. J. Nielsen, J. Orphal, V. I. Perevalov, A. Perrin, E. Polovtseva, A. Predoi-Cross, M. Rotger, A. A. Ruth, S. S. Yu, K. Sung, S. A. Tashkun, J. Tennyson, V. G. Tyuterev, J. Vander Auwera, B. A. Voronin, A. Makie, The 2015 edition of the GEISA spectroscopic database, J. Mol. Spectrosc. 327 (2016) 31–72. doi:10.1016/j.jms.2016.06.007.

[36] J. Tennyson, S. N. Yurchenko, A. F. Al-Refaie, E. J. Barton, K. L. Chubb, P. A. Coles, S. Diamantopoulou, M. N. Gorman, C. Hill, A. Z. Lam, L. Lodi, L. K. McKemmish, Y. Na, A. Owens, O. L. Polyansky, T. Rivlin, C. Sousa-Silva, D. S. Underwood, A. Yachmenev, E. Zak, The ExoMol database: molecular line lists for exoplanet and other hot atmospheres, J. Mol. Spectrosc. 327 (2016) 73–94. doi:10.1016/j.jms.2016.05.002.

[37] E. Zak, J. Tennyson, O. L. Polyansky, L. Lodi, S. A. Tashkun, V. I. Perevalov, A room temperature CO_2 line list with *ab initio* computed intensities, J. Quant. Spectrosc. Radiat. Transf. 177 (2016) 31–42. doi:10.1016/j.jqsrt.2015.12.022.

[38] E. J. Zak, J. Tennyson, O. L. Polyansky, L. Lodi, N. F. Zobov, S. A. Tashkun, V. I. Perevalov, Room temperature line lists for CO_2 symmetric isotopologues with ab initio computed intensities, J. Quant. Spectrosc. Radiat. Transf. 189 (2017) 267–280. doi:10.1016/j.jqsrt.2016.11.022.

[39] E. J. Zak, J. Tennyson, O. L. Polyansky, L. Lodi, N. F. Zobov, S. A. Tashkun, V. I. Perevalov, Room temperature linelists for CO_2 asymmetric isotopologues with ab initio computed intensities, J. Quant. Spectrosc. Radiat. Transf. (In press, 2017) doi:10.1016/j.jqsrt.2017.01.037.

[40] K. Chance, J. Burrows, D. Perner, W. Schneider, Satellite measurements of atmospheric ozone profiles, including tropospheric ozone, from ultraviolet/visible measurements in the

nadir geometry: a potential method to retrieve tropospheric ozone, Journal of Quantitative Spectroscopy and Radiative Transfer 57 (4) (1997) 467–476. doi:10.1016/s0022-4073(96)00157-4.

[41] N. Theys, R. Campion, L. Clarisse, H. Brenot, J. van Gent, B. Dils, S. Corradini, L. Merucci, P.-F. Coheur, M. V. Roozendael, D. Hurtmans, C. Clerbaux, S. Tait, F. Ferrucci, Volcanic SO_2 fluxes derived from satellite data: a survey using OMI, GOME-2, IASI and MODIS, Atmos. Chem. Phys. 13 (12) (2013) 5945–5968. doi:10.5194/acp-13-5945-2013.

[42] C. R. Nowlan, X. Liu, K. Chance, Z. Cai, T. P. Kurosu, C. Lee, R. V. Martin, Retrievals of sulfur dioxide from the global ozone monitoring experiment 2 (GOME-2) using an optimal estimation approach: Algorithm and initial validation, J. Geophys. Res. 116 (D18). doi:10.1029/2011jd015808.

[43] N. Krotkov, S. Carn, A. Krueger, P. Bhartia, K. Yang, Band residual difference algorithm for retrieval of SO_2 from the aura ozone monitoring instrument (OMI), Trans. Geo. Rem. Sens. 44 (5) (2006) 1259–1266. doi:10.1109/tgrs.2005.861932.

[44] S. A. Carn, V. E. Fioletov, C. A. McLinden, C. Li, N. A. Krotkov, A decade of global volcanic SO_2 emissions measured from space, Scientific Reports 7 (2017) 44095. doi:10.1038/srep44095.

[45] E. Carboni, R. G. Grainger, T. A. Mather, D. M. Pyle, G. E. Thomas, R. Siddans, A. J. A. Smith, A. Dudhia, M. E. Koukouli, D. Balis, The vertical distribution of volcanic SO_2 plumes measured by IASI, Atmospheric Chemistry and Physics 16 (7) (2016) 4343–4367. doi:10.5194/acp-16-4343-2016.

[46] M. Baer, Beyond Born-Oppenheimer: Electronic Nonadiabatic Coupling Terms and Conical Intersections, Wiley-Interscience, 2008.

[47] M. Mayer, L. S. Cederbaum, Molecular rotations in vibronically coupled systems, The Journal of Chemical Physics 105 (12) (1996) 4938–4963. doi:10.1063/1.472345.

[48] R. Tarroni, S. Carter, Theoretical calculation of vibronic levels of C_2H and C_2D to 10000 cm^{-1}, The Journal of Chemical Physics 119 (24) (2003) 12878–12889. doi:10.1063/1.1627755.

[49] D. W. Schwenke, Beyond the potential energy surface: ab initio corrections to the Born-Oppenheimer approximation for H_2O, The Journal of Physical Chemistry A 105 (11) (2001) 2352–2360. doi:10.1021/jp0032513.

[50] C. Woywod, M. Stengle, W. Domcke, H. Flöthmann, R. Schinke, Photodissociation of ozone in the chappuis band. i. electronic structure calculations, The Journal of Chemical Physics 107 (18) (1997) 7282–7295. doi:10.1063/1.474969.

[51] G. B. Park, J. Jiang, R. W. Field, The origin of unequal bond lengths in the $\tilde{C}\ ^1B_2$ state of SO_2: Signatures of high-lying potential energy surface crossings in the low-lying vibrational structure, J. Chem. Phys. 144 (14) (2016) 144313. doi:10.1063/1.4945622.

[52] J. Tennyson, M. A. Kostin, H. Y. Mussa, O. L. Polyansky, R. Prosmiti, H_3^+ near dissociation: theoretical progress, Philosophical Transactions of the Royal Society A: Mathematical, Physical and Engineering Sciences 358 (1774) (2000) 2419–2432. doi:10.1098/rsta.2000.0657.

[53] S. Mishra, V. Vallet, L. V. Poluyanov, W. Domcke, Calculation of the vibronic structure of the photodetachment spectra of CCCl- and CCBr-, The Journal of Chemical Physics 125 (16) (2006) 164327. doi:10.1063/1.2363193.

[54] N. Vinci, J. Tennyson, Continuum states of CO^+, J. Phys. B: At. Mol. Opt. Phys. 37 (2004) 2011–2031.

[55] L. Lodi, J. Tennyson, Theoretical methods for small-molecule ro-vibrational spectroscopy, J. Phys. B: At. Mol. Opt. Phys. 43 (2010) 133001.

[56] L. Lodi, J. Tennyson, Line lists for $H_2{}^{18}O$ and $H_2{}^{17}O$ based on empirically-adjusted line positions and ab initio intensities, J. Quant. Spectrosc. Radiat. Transf. 113 (2012) 850–858. doi:10.1016/j.jqsrt.2012.02.023.

[57] B. T. Sutcliffe, J. Tennyson, A generalised approach to the calculation of ro-vibrational spectra of triatomic molecules, Mol. Phys. 58 (1986) 1053–1066.

[58] B. T. Sutcliffe, J. Tennyson, A general treatment of vibration-rotation coordinates for triatomic molecules, Intern. J. Quantum Chem. 39 (1991) 183–196.

[59] J. Tennyson, M. A. Kostin, P. Barletta, G. J. Harris, O. L. Polyansky, J. Ramanlal, N. F. Zobov, DVR3D: a program suite for the calculation of rotation-vibration spectra of triatomic molecules, Comput. Phys. Commun. 163 (2004) 85–116.

[60] P. R. Bunker, P. Jensen, Molecular Symmetry and Spectroscopy, Second Edition, NRC Research Press, Ottawa, Canada, 2006.

[61] B. Sutcliffe, The decoupling of electronic and nuclear motions in the isolated molecule Schrödinger Hamiltonian, in: Advances in Chemical Physics, John Wiley & Sons, Inc., 2004, pp. 1–121. doi:10.1002/9780470141731.ch1.

[62] B. R. Johnson, W. P. Reinhardt, Adiabatic separations of stretching and bending vibrations: Application to h2o, The Journal of Chemical Physics 85 (8) (1986) 4538–4556. doi:10.1063/1.451775.

[63] L. G. Diniz, J. R. Mohallem, A. Alijah, M. Pavanello, L. Adamowicz, O. L. Polyansky, J. Tennyson, Vibrationally and rotationally nonadiabatic calculations on H_3^+ using coordinate-dependent vibrational and rotational masses, Phys. Rev. A 88 (2013) 032506. doi:10.1103/PhysRevA.88.032506.

[64] J. R. Henderson, S. Miller, J. Tennyson, Discrete variable representations of large amplitude ro-vibrational states in a generalised coordinate system, J. Chem. Soc., Faraday Trans. 86 (1990) 1963–1968.

[65] P. Barletta, S. V. Shirin, N. F. Zobov, O. L. Polyansky, J. Tennyson, E. F. Valeev, A. G. Császár, CVRQD adiabatic *ab initio* ground-state potential surfaces for the water molecule, J. Chem. Phys. 125 (2006) 204307.

[66] I. N. Kozin, M. M. Law, J. M. Hutson, J. Tennyson, The rovibrational bound states of Ar_2HF, J. Chem. Phys. 118 (2003) 4896–4904.

[67] J. Tennyson, B. T. Sutcliffe, Discretisation to avoid singularities in vibration-rotation hamiltonians: a bisector embedding for AB_2 triatomics, Intern. J. Quantum Chem. 42 (1992) 941–952.

[68] E. Zak, Normal modes. The true story. (arXiv:1601.04735 [quant-ph], 2015). doi:10.13140/rg.2.1.3916.4248.

[69] E. B. Wilson, J. C. Decius, P. C. Cross, B. R. Sundheim, Molecular vibrations: The theory of infrared and raman vibrational spectra, Journal of The Electrochemical Society 102 (9) (1955) 235C. doi:10.1149/1.2430134.

[70] A. Garcia Ayllon, J. Santamaria, S. Miller, J. Tennyson, Calculated spectra for the N_2–Ar Van der Waals complex, Mol. Phys. 71 (1990) 1043–1054.

[71] E. B. Wilson, J. C. Decius, P. C. Cross, Molecular Vibrations: The Theory of Infrared and Raman vibrational spectra, Dover, New York, USA, 1980.

[72] D. M. Brink, G. R. Satchler, Angular momentum, 3rd Edition, Oxford University Press, 1994.

[73] E. U. Condon, G. H. Shortley, The theory of atomic spectra, Cambridge University Press.

[74] J. H. Schryber, S. Miller, J. Tennyson, Computed infra red absorption properties of hot water vapour, J. Quant. Spectrosc. Radiat. Transf. 53 (1995) 373–380.

[75] O. L. Polyansky, N. F. Zobov, I. I. Mizus, L. Lodi, S. N. Yurchenko, J. Tennyson, A. G. Császár, O. V. Boyarkin, Global spectroscopy of the water monomer, Phil. Trans. Royal Soc. London A 370 (2012) 2728–2748.

[76] D. S. Underwood, J. Tennyson, S. N. Yurchenko, X. Huang, D. W. Schwenke, T. J. Lee, S. Clausen, A. Fateev, ExoMol line lists XIV: A line list for hot SO_2, Mon. Not. R. Astron. Soc. 459 (2016) 3890–3899. doi:10.1093/mnras/stw849.

[77] A. A. A. Azzam, S. N. Yurchenko, J. Tennyson, O. V. Naumenko, ExoMol line lists XVI: A Hot Line List for H_2S, Mon. Not. R. Astron. Soc. 460 (2016) 4063–4074. doi:10.1093/mnras/stw1133.

[78] H. Wei, T. C. Jr., An exact eckart-embedded kinetic energy operator in radau coordinates for triatomic molecules, Chemical Physics Letters 287 (3-4) (1998) 289–300. doi:10.1016/s0009-2614(98)00186-9.

[79] X.-G. Wang, T. Carrington, Computing rovibrational levels of methane with curvilinear internal vibrational coordinates and an eckart frame, The Journal of Chemical Physics 138 (10) (2013) 104106. doi:10.1063/1.4793474.

[80] V. Szalay, Aspects of the eckart frame ro-vibrational kinetic energy operator, The Journal of Chemical Physics 143 (6) (2015) 064104. doi:10.1063/1.4928433.

[81] V. Szalay, Eckart ro-vibrational hamiltonians via the gateway hamilton operator: Theory and practice, The Journal of Chemical Physics 146 (12) (2017) 124107. doi:10.1063/1.4978686.

[82] E. Mátyus, G. Czakó, B. T. Sutcliffe, A. G. Császár, Vibrational energy levels with arbitrary potentials using the eckart-watson hamiltonians and the discrete variable representation, The Journal of Chemical Physics 127 (8) (2007) 084102. doi:10.1063/1.2756518.

[83] A. G. Császár, C. Fábri, T. Szidarovszky, E. Mátyus, T. Furtenbacher, G. Czakó, The fourth age of quantum chemistry: molecules in motion, Phys. Chem. Chem. Phys. 14 (3) (2012) 1085–1106. doi:10.1039/c1cp21830a.

[84] J. Tennyson, B. T. Sutcliffe, Variationally exact ro-vibrational levels of the floppy CH_2^+ molecule, Journal of Molecular Spectroscopy 101 (1) (1983) 71–82. doi:10.1016/0022-2852(83)90007-3.

[85] J. Tennyson, B. T. Sutcliffe, The ab initio calculation of the vibrational-rotational spectrum of triatomic systems in the close-coupling approach, with KCN and H_2Ne as examples, J. Chem. Phys. 77 (1982) 4061–4072. doi:10.1063/1.444316.

[86] J. Tennyson, B. T. Sutcliffe, Highly rotationally excited states of floppy molecules: H_2D^+ with $J \leq 20$, Mol. Phys. 58 (1986) 1067–1085.

[87] B. T. Sutcliffe, S. Miller, J. Tennyson, An effective computational approach to the calculation of vibration-rotation spectra of triatomic molecules, Comput. Phys. Commun. 51 (1988) 73–82.

[88] G. G. E. D. O. Harris, W. D. Gwinn, Calculations of matrix elements for one-dimensional quantum-mechanical problems and the application to anharmonic oscillators, J. Chem. Phys. 43 (1965) 1515–1517.

[89] Z. Bacic, J. C. Light, Theoretical methods for rovibrational states of floppy molecules, Annu. Rev. Phys. Chem 40 (1989) 469–498.

[90] J. C. Light, T. Carrington, Discrete-variable representations and their utilization, Adv. Chem. Phys. 114 (2000) 263–310. doi:{10.1002/9780470141731.ch4}.

[91] H.-S. Lee, H. Chen, J. C. Light, Symmetry-adapted direct product discrete variable representation for the coupled angular momentum operator: Application to the vibrations of (CO2)2, The Journal of Chemical Physics 119 (8) (2003) 4187–4196. doi:10.1063/1.1592511.

[92] M. J. Bramley, T. Carrington, A general discrete variable method to calculate vibrational energy levels of three- and four-atom molecules, The Journal of Chemical Physics 99 (11) (1993) 8519–8541. doi:10.1063/1.465576.

[93] E. Zak, Quantum harmonic oscillator revisited (unpublished,2015). doi:10.13140/rg.2.1.2645.4565.

[94] H. Taseli, Exact solutions for vibrational levels of the morse potential, Journal of Physics A: Mathematical and General 31 (2) (1998) 779–788. doi:10.1088/0305-4470/31/2/032.

[95] E. M. Heatwole, O. V. Prezhdo, Analytic dynamics of the morse oscillator derived by semiclassical closures, The Journal of Chemical Physics 130 (24) (2009) 244111. doi:10.1063/1.3154143.

[96] V. Szalay, T. Szidarovszky, G. Czakó, A. G. Császár, A paradox of grid-based representation techniques: accurate eigenvalues from inaccurate matrix elements, Journal of Mathematical Chemistry 50 (3) (2011) 636–651. doi:10.1007/s10910-011-9843-2.

[97] A. S. Dickinson, P. R. Certain, Calculation of matrix elements for one-dimensional quantum-mechanical problems, J. Chem. Phys. 49 (1968) 4209–4211. doi:10.1063/1.1670738.

[98] J. C. Light, I. P. Hamilton, J. V. Lill, Generalized discrete variable approximation in quantum mechanics, J. Chem. Phys. 82 (1985) 1400–1409. doi:10.1063/1.448462.

[99] L. Lodi, PhD thesis. Theoretical rotational-vibrational spectroscopy of water, University College London, London, UK (2008).

[100] I. N. Levine, Quantum Chemistry (5th Edition), Prentice Hall, 1999.

[101] V. Szalay, Discrete variable representations of differential operators, J. Chem. Phys. 99 (1993) 1978. doi:10.1063/1.465258.

[102] B. T. Sutcliffe, J. Tennyson, S. Miller, The use of supercomputers for the variational calculation of ro-vibrationally excited states of floppy molecules, Theor. Chim. Acta 72 (1987) 265–276.

[103] J. R. Henderson, C. R. Le Sueur, S. G. Pavett, J. Tennyson, Coordinate ordering in the discrete variable representation, Comput. Phys. Commun. 74 (1993) 193–198.

[104] J. Tennyson, S. Miller, C. R. Le Sueur, TRIATOM: a suite for basis set calculations of ro-vibrational spectra of triatomic molecules, Comput. Phys. Commun. 75 (1993) 339–364.

[105] R. N. Zare, Angular Momentum: Understanding Spatial Aspects in Chemistry and Physics, Wiley-Interscience, 1991.

[106] S. Carter, P. Rosmus, N. C. Handy, S. Miller, J. Tennyson, B. T. Sutcliffe, Benchmark calculations of first principles rotational and ro-vibrational line strengths, Comput. Phys. Commun. 55 (1989) 71–75.

[107] J. R. Henderson, J. Tennyson, S. Miller, The calculation of ro-vibrational molecular spectra from first principles, in: J. M. Greenberg, V. Pirronello (Eds.), Chemistry in space, Vol. 323 of NATO ASI series C, Kluwer, Dordrecht, 1991, pp. 423–424.

[108] C. R. Le Sueur, S. Miller, J. Tennyson, B. T. Sutcliffe, On the use of variational wavefunctions in calculating vibrational band intensities, Mol. Phys. 76 (1992) 1147–1156.

[109] P. Atkins, J. de Paula, Physical Chemistry for the Life Sciences, Oxford University Press, 2015.

[110] S. N. Yurchenko, J. Tennyson, E. J. Barton, Molecular line shape parameters for exoplanetary atmospheric applications, J. Phys. Conf. Ser. 810 (2017) 012010. doi:10.1088/1742-6596/810/1/012010.

[111] R. Hashemi, H. Rozario, A. Ibrahim, A. Predoi-Cross, Line shape study of the carbon dioxide laser band I^1, Can. J. Phys. 91 (2013) 924–936. doi:10.1139/cjp-2013-0051.

[112] C. L. Sabine, The oceanic sink for anthropogenic CO_2, Science 305 (5682) (2004) 367–371. doi:10.1126/science.1097403.

[113] A. P. Ballantyne, C. B. Alden, J. B. Miller, P. P. Tans, J. W. C. White, Increase in observed net carbon dioxide uptake by land and oceans during the past 50 years, Nature 488 (7409) (2012) 70–72. doi:10.1038/nature11299.

[114] J. T. Emmert, M. H. Stevens, P. F. Bernath, D. P. Drob, C. D. Boone, Observations of increasing carbon dioxide concentration in earth's thermosphere, Nature Geoscience 5 (2012) 868–871. doi:10.1038/ngeo1626.

[115] K. A. Masarie, P. P. Tans, Extension and integration of atmospheric carbon dioxide data into a globally consistent measurement record, Journal of Geophysical Research 100 (D6) (1995) 11593. doi:10.1029/95jd00859.

[116] F. Chevallier, N. M. Deutscher, T. J. Conway, P. Ciais, L. Ciattaglia, S. Dohe, M. Fröhlich, A. J. Gomez-Pelaez, D. Griffith, F. Hase, L. Haszpra, P. Krummel, E. Kyrö, C. Labuschagne, R. Langenfelds, T. Machida, F. Maignan, H. Matsueda, I. Morino, J. Notholt, M. Ramonet, Y. Sawa, M. Schmidt, V. Sherlock, P. Steele, K. Strong, R. Sussmann, P. Wennberg, S. Wofsy, D. Worthy, D. Wunch, M. Zimnoch, Global CO_2 fluxes inferred from surface air-sample measurements and from TCCON retrievals of the $_2$ total column, Geophysical Research Letters 38 (24) (2011) n/a–n/a. doi:10.1029/2011gl049899.

[117] M. Tessenyi, G. Tinetti, J. Tennyson, G. Savini, E. Pascale, S. Jason, D. Liddle, J. Williams, A. Vora, C. Saunders, Twinkle – a british space mission to explore faraway worlds, in: Proceedings of the International Astronautical Congress, IAC, Vol. 6, International Astronautical Federation, 2015, pp. 4311–4313.

[118] The science of ARIEL (Atmospheric Remote-sensing Infrared Exoplanet Large-survey), Vol. 9904. doi:10.1117/12.2232370.

[119] C. V. Morley, J. J. Fortney, M. S. Marley, K. Zahnle, M. Line, E. Kempton, N. Lewis, K. Cahoy, Thermal emission and reflected light spectra of super earths with flat transmission spectra, The Astrophysical Journal 815 (2) (2015) 110. doi:10.1088/0004-637x/815/2/110.

[120] G. Tinetti, C. A. Griffith, M. R. Swain, J. P. B. P. Deroo, G. Vasisht, D. Kipping, I. Waldmann, J. Tennyson, R. J. Barber, J. Bouwman, N. Allard, L. Brown, Exploring extrasolar worlds: from gas giants to terrestrial habitable planets, Faraday Discuss. 147 (2010) 369–377.

[121] G. Tinetti, J. Beaulieu, T. Henning, M. Meyer, G. Micela, I. Ribas, D. Stam, M. Swain, O. Krause, M. Ollivier, E. Pace, B. Swinyard, A. Aylward, R. van Boekel, A. Coradini, T. Encrenaz, I. Snellen, M. R. Zapatero-Osorio, J. Bouwman, J. Y.-K. Cho, V. Coudé du Foresto, T. Guillot, M. Lopez-Morales, I. Mueller-Wodarg, E. Palle, F. Selsis, A. Sozzetti, P. A. R. Ade, N. Achilleos, A. Adriani, C. B. Agnor, C. Afonso, C. Allende Prieto, G. Bakos, R. J. Barber, M. Barlow, V. Batista, P. Bernath, B. Bézard, P. Bordé, L. R. Brown, A. Cassan, C. Cavarroc, A. Ciaravella, C. Cockell, A. Coustenis, C. Danielski, L. Decin, R. De Kok, O. Demangeon, P. Deroo, P. Doel, P. Drossart, L. N. Fletcher, M. Focardi, F. Forget, S. Fossey, P. Fouqué, J. Frith, M. Galand, P. Gaulme, J. L. González Hernàndez, O. Grasset, D. Grassi, J. l. Grenfell, M. Griffin, C. A. Griffith, U. Grözinger, M. Guedel, P. Guio, O. Hainaut, R. Hargreaves, P. H. Hauschildt, K. Heng, D. Heyrovsky, R. Hueso, P. Irwin,

L. Kaltenegger, P. Kervella, D. Kipping, T. T. Koskinen, G. Kovács, A. La Barbera, H. Lammer, E. Lellouch, G. Leto, M. Lopez Morales, M. A. Lopez Valverde, M. Lopez-Puertas, C. Lovis, A. Maggio, J. P. Maillard, J. Maldonado Prado, J. B. Marquette, F. Martin-Torres, P. Maxted, S. Miller, S. Molinari, D. Montes, A. Moro-Martin, J. L. Moses, O. Mousis, N. Nguyen Tuong, R. Nelson, G. S. Orton, E. Pantin, E. Pascale, S. Pezzuto, D. Pinfield, E. Poretti, R. Prinja, L. Prisinzano, J. M. Rees, A. Reiners, B. Samuel, A. Sánchez-Lavega, J. Sanz Forcada, D. Sasselov, G. Savini, B. Sicardy, A. Smith, L. Stixrude, G. Strazzulla, J. Tennyson, M. Tessenyi, G. Vasisht, S. Vinatier, S. Viti, I. Waldmann, G. J. White, T. Widemann, R. Wordsworth, R. Yelle, Y. Yung, S. N. Yurchenko, EChO, Exp. Astron. 34 (2012) 311–353.

[122] T. Encrenaz, The atmospheres of extrasolar planets, Europhysics News 45 (2014) 23–27. doi:10.1051/epn/2014103.

[123] R. Beer, Remote Sensing by Fourier Transform Spectrometry (Chemical Analysis: A Series of Monographs on Analytical Chemistry and Its Applications), Wiley-Interscience, 1992.

[124] R. Harig, Passive remote sensing of pollutant clouds by fourier-transform infrared spectrometry: signal-to-noise ratio as a function of spectral resolution, Applied Optics 43 (23) (2004) 4603. doi:10.1364/ao.43.004603.

[125] J. M. Hartmann, H. Tran, G. C. Toon, Influence of line mixing on the retrievals of atmospheric CO_2 from spectra in the 1.6 and 2.1 μm regions, Atmos. Chem. Phys. 9 (2009) 7303–7312.

[126] R. R. Gamache, J. Lamouroux, Predicting accurate line shape parameters for CO_2 transitions, J. Quant. Spectrosc. Radiat. Transf. 130,158–171 (2013) doi:10.1016/j.jqsrt.2013.05.021.

[127] R. Toth, L. Brown, C. Miller, V. M. Devi, D. C. Benner, Line strengths of $^{12}C^{16}O_2$: 4550-7000 cm^{-1} , Journal of Molecular Spectroscopy 239 (2) (2006) 221–242. doi:10.1016/j.jms.2006.08.001.

[128] V. M. Devi, D. C. Benner, K. Sung, L. R. Brown, T. J. Crawford, C. E. Miller, B. J. Drouin, V. H. Payne, S. Yu, M. A. H. Smith, A. W. Mantz, R. R. Gamache, Line parameters including temperature dependences of self- and air-broadened line shapes of $^{12}C^{16}O_2$: 1.6-μm region, J. Quant. Spectrosc. Radiat. Transf. 177 (2016) 117–144. doi:10.1016/j.jqsrt.2015.12.020.

[129] J. Hovorka, P. Čermák, P. Veis, Optimization of data retrieval process for spectroscopic CO_2 isotopologue ratio measurements, Laser Physics 27 (5) (2017) 055701. doi:10.1088/1555-6611/aa64b8.

[130] M. Stuiver, R. L. Burk, P. D. Quay, 13C/12C ratios in tree rings and the transfer of biospheric carbon to the atmosphere, Journal of Geophysical Research 89 (D7) (1984) 11731. doi:10.1029/jd089id07p11731.

[131] E. C. February, W. D. Stock, Declining trend in the 13c/12c ratio of atmospheric carbon dioxide from tree rings of south african widdringtonia cedarbergensis, Quaternary Research 52 (02) (1999) 229–236. doi:10.1006/qres.1999.2057.

[132] B. J. Tipple, S. R. Meyers, M. Pagani, Carbon isotope ratio of cenozoic CO_2: A comparative evaluation of available geochemical proxies, Paleoceanography 25 (3). doi:10.1029/2009pa001851.

[133] N. Bouttes, D. Paillard, D. M. Roche, V. Brovkin, L. Bopp, Last glacial maximum CO_2 and 13C successfully reconciled, Geophysical Research Letters 38 (2) (2011). doi:10.1029/2010gl044499.

[134] J. Hovorka, P. Cermak, P. Veis, Optimization of data retrieval process for spectroscopic CO_2 isotopologue ratio measurements, Laser Physics 27 (2017) 055701.

[135] S. V. Kireev, S. L. Shnyrev, I. V. Sobolevsky, A. A. Kondrashov, Development of an on-line CO_2 isotopologues' detection method based on a diode laser in gaseous media, Laser Physics Letters 11 (12) (2014) 125703. doi:10.1088/1612-2011/11/12/125703.

[136] S. V. Kireev, A. A. Kondrashov, S. L. Shnyrev, Applying the diode laser spectroscopy method for high sensitivity on-line control of 13C contained in the gaseous mixture with 12C, Laser Physics Letters 13 (6) (2016) 065702. doi:10.1088/1612-2011/13/6/065702.

[137] C. Guimbaud, C. Noel, M. Chartier, V. Catoire, M. Blessing, J. C. Gourry, C. Robert, A quantum cascade laser infrared spectrometer for CO_2 stable isotope analysis: Field implementation at a hydrocarbon contaminated site under bio-remediation, J. Environ. Sci. 40 (2016) 60–74. doi:10.1016/j.jes.2015.11.015.

[138] S. V. Kireev, S. L. Shnyrev, A. A. Kondrashov, Development of laser noninvasive on-line diagnostics of oncological diseases based on the absorption method in the 4860-4880 cm^{-1} spectral range, Laser Phys. 26 (2016) 075601. doi:{10.1088/1054-660X/26/7/075601}.

[139] I. Levin, T. Naegler, B. Kromer, M. Diehl, R. J. Francey, A. J. Gomez-Pelaez, L. P. Steele, D. Wagenbach, R. Weller, D. E. Worthy, Observations and modelling of the global distribution and long-term trend of atmospheric $^{14}CO_2$, Tellus B 62 (2010) 26–46. doi:10.1111/j.1600-0889.2009.00446.x.

[140] K. A. Rose, E. L. Sikes, T. P. Guilderson, P. Shane, T. M. Hill, R. Zahn, H. J. Spero, Upper-ocean-to-atmosphere radiocarbon offsets imply fast deglacial carbon dioxide release, Nature 466 (2010) 1093–1097. doi:10.1038/nature09288.

[141] R. Taylor, O. Bar-Yosef, Radiocarbon Dating, Second Edition: An Archaeological Perspective, Routledge, 2014.

[142] R. G. Fairbanks, R. A. Mortlock, T.-C. Chiu, L. Cao, A. Kaplan, T. P. Guilderson, T. W. Fairbanks, A. L. Bloom, P. M. Grootes, M.-J. Nadeau, Radiocarbon calibration curve spanning 0 to 50, 000 years BP based on paired 230Th/234U/238U and 14C dates on pristine corals, Quaternary Science Reviews 24 (16-17) (2005) 1781–1796. doi:10.1016/j.quascirev.2005.04.007.

[143] G. Genoud, M. Vainio, H. Phillips, J. Dean, M. Merimaa, Radiocarbon dioxide detection based on cavity ring-down spectroscopy and a quantum cascade laser, Opt. Lett. 40 (2015) 1342. doi:10.1364/ol.40.001342.

[144] I. Galli, P. C. Pastor, G. Di Lonardo, L. Fusina, G. Giusfredi, D. Mazzotti, F. Tamassia, P. D. Natale, The ν_3 band of $^{14}C^{16}O_2$ molecule measured by optical-frequency-comb-assisted cavity ring-down spectroscopy, Mol. Phys. 109 (2011) 2267–2272. doi:10.1080/00268976.2011.614284.

[145] G. Giusfredi, I. Galli, D. Mazzotti, P. Cancio, P. De Natale, Theory of saturated-absorption cavity ring-down: radiocarbon dioxide detection, a case study, J. Opt. Soc. Am. B 32 (2015) 2223. doi:10.1364/josab.32.002223.

[146] G. Giusfredi, S. Bartalini, S. Borri, P. Cancio, I. Galli, D. Mazzotti, P. D. Natale, Saturated-absorption cavity ring-down spectroscopy, Phys. Rev. Lett. 104 (2010) 110801. doi:10.1103/physrevlett.104.110801.

[147] I. Galli, S. Bartalini, P. Cancio, P. De Natale, D. Mazzotti, G. Giusfredi, M. E. Fedi, P. A. Mando, Optical detection of radiocarbon dioxide: First results and AMS intercomparison, Radiocarbon 55 (2013) 213–223.

[148] A. McCartt, T. Ognibene, G. Bench, K. Turteltaub, Measurements of carbon-14 with cavity ring-down spectroscopy, Nuclear Instruments and Methods in Physics Research Section B: Beam Interactions with Materials and Atoms 361 (2015) 277 – 280. doi:http://dx.doi.org/10.1016/j.nimb.2015.05.036.

[149] X. Huang, R. S. Freedman, S. A. Tashkun, D. W. Schwenke, T. J. Lee, Semi-empirical $^{12}C^{16}O_2$ IR line lists for simulations up to 1500 K and 20,000 cm^{-1}, J. Quant. Spectrosc. Radiat. Transf. 130 (2013) 134–146. doi:10.1016/j.jqsrt.2013.05.018.

[150] J. Tennyson, B. T. Sutcliffe, Variationally exact ro-vibrational spectra of non-rigid triatomics: the HeHF Van der Waals molecule, J. Chem. Phys. 79 (1983) 43–51.

[151] J. Tennyson, B. T. Sutcliffe, Variationally exact ro-vibrational levels of the floppy CH_2^+ molecule, J. Mol. Spectrosc. 101 (1983) 71–82.

[152] B. T. Sutcliffe, J. Tennyson, Variational methods for the calculation of ro-vibrational energy levels of small molecules, J. Chem. Soc. 83 (1987) 1663–1674.

[153] J. Tennyson, High Accuracy Rotation-vibration Calculations on Small Molecules, John Wiley & Sons, Chichester, UK, 2011, pp. 551–572.

[154] J. Tennyson, Perspective: Accurate ro-vibrational calculations on small molecules, J. Chem. Phys. 145 (2016) 120901. doi:10.1063/1.4962907.

[155] O. L. Polyansky, A. G. Császár, S. V. Shirin, N. F. Zobov, P. Barletta, J. Tennyson, D. W. Schwenke, P. J. Knowles, High accuracy ab initio rotation-vibration transitions of water, Science 299 (2003) 539–542.

[156] O. L. Polyansky, R. I. Ovsyannikov, A. A. Kyuberis, L. Lodi, J. Tennyson, N. F. Zobov, Calculation of rotation-vibration energy levels of the water molecule with near-experimental accuracy based on an ab initio potential energy surface, J. Phys. Chem. A 117 (2013) 96339643. doi:10.1021/jp312343z.

[157] X. Huang, D. W. Schwenke, S. A. Tashkun, T. J. Lee, An isotopic-independent highly accurate potential energy surface for CO_2 isotopologues and an initial $^{12}C^{16}O_2$ infrared line list, J. Chem. Phys. 136 (2012) 124311. doi:10.1063/1.3697540.

[158] S. V. Shirin, O. L. Polyansky, N. F. Zobov, R. I. Ovsyannikov, A. G. Császár, J. Tennyson, Spectroscopically determined potential energy surfaces of the $H_2{}^{16}O$, $H_2{}^{17}O$ and $H_2{}^{18}O$ isotopologues of water, J. Mol. Spectrosc. 236 (2006) 216–223.

[159] R. B. Wattson, L. S. Rothman, Direct numerical diagonalization - wave of the future, J. Quant. Spectrosc. Radiat. Transf. 48 (1992) 763–780. doi:10.1016/0022-4073(92)90140-Y.

[160] V. Dana, J. Y. Mandin, A. Barbe, J. J. Plateaux, L. S. Rothman, R. B. Wattson, $^{12}C^{16}O_2$ line-intensities in the 4.8 μm spectral region, J. Quant. Spectrosc. Radiat. Transf. 52 (1994) 333–340. doi:10.1016/0022-4073(94)90163-5.

[161] X. Huang, R. R. Gamache, R. S. Freedman, D. W. Schwenke, T. J. Lee, Reliable infrared line lists for 13 CO_2 isotopologues up to E =18,000 cm^{-1} and 1500 K, with line shape parameters, J. Quant. Spectrosc. Radiat. Transf. 147 (2014) 134–144. doi:{10.1016/j.jqsrt.2014.05.015}.

[162] D. Jacquemart, Y. Borkov, O. M. Lyulin, S. A. Tashkun, V. I. Perevalov, Fourier transform spectroscopy of CO_2 isotopologues at 1.6μm: Line positions and intensities, J. Quant. Spectrosc. Radiat. Transf. 160 (2015) 1–9. doi:10.1016/j.jqsrt.2015.03.016.

[163] Y. Tan, X.-Q. Zhao, A.-W. Liu, S.-M. Hu, O. M. Lyulin, S. A. Tashkun, V. I. Perevalov, Cavity ring-down spectroscopy of CO_2 overtone bands near 830nm, J. Quant. Spectrosc. Radiat. Transf. 165 (2015) 22–27. doi:10.1016/j.jqsrt.2015.06.010.

[164] S. Vasilchenko, M. Konefal, D. Mondelain, S. Kassi, P. Čermák, S. A. Tashkun, V. I. Perevalov, A. Campargue, The CO_2 absorption spectrum in the 2.3μm transparency window by high sensitivity CRDS: (i) rovibrational lines, J. Quant. Spectrosc. Radiat. Transf. 184 (2016) 233–240. doi:10.1016/j.jqsrt.2016.07.002.

[165] O. Sulakshina, V. Perevalov, V. Tyuterev, Influence of effective hamiltonian transformations on effective dipole moment parameters of c3v molecules, Journal of Molecular Spectroscopy 135 (2) (1989) 234–249. doi:10.1016/0022-2852(89)90153-7.

[166] J. L. Teffo, O. N. Sulakshina, V. I. Perevalov, Effective Hamiltonian for rovibrational energies and line-intensities of carbon-dioxide, J. Mol. Spectrosc. 156 (1992) 48–64. doi:10.1016/0022-2852(92)90092-3.

[167] V. I. Perevalov, S. A. Tashkun, CDSD-296 (Carbon Dioxide Spectroscopic Databank): updated and enlarged version for atmospheric applications, Cambridge MA, USA, 2008.

[168] S. A. Tashkun, V. I. Perevalov, R. R. Gamache, J. Lamouroux, CDSD-296, high resolution carbon dioxide spectroscopic databank: Version for atmospheric applications, J. Quant. Spectrosc. Radiat. Transf. 152 (2015) 45–73. doi:10.1016/j.jqsrt.2014.10.017.

[169] S. A. Tashkun, V. I. Perevalov, J. L. Teffo, A. D. Bykov, N. N. Lavrentieva, CDSD-1000, the high-temperature carbon dioxide spectroscopic databank, J. Quant. Spectrosc. Radiat. Transf. 82 (2003) 165–196. doi:{10.1016/S0022-4073(03)00152-3}.

[170] S. A. Tashkun, V. I. Perevalov, CDSD-4000: High-resolution, high-temperature carbon dioxide spectroscopic databank, J. Quant. Spectrosc. Radiat. Transf. 112 (2011) 1403–1410. doi:10.1016/j.jqsrt.2011.03.005.

[171] J. R. Henderson, H. A. Lam, J. Tennyson, Highly excited vibrational states of the KCN molecule, J. Chem. Soc. 88 (1992) 3287–3293.

[172] J. R. Henderson, C. R. Le Sueur, J. Tennyson, DVR3D: programs for fully pointwise calculation of vibrational spectra, Comput. Phys. Commun. 75 (1993) 379–395.

[173] J. Tennyson, J. R. Henderson, N. G. Fulton, DVR3D: programs for fully pointwise calculation of ro-vibrational spectra of triatomic molecules, Comput. Phys. Commun. 86 (1995) 175–198.

[174] A. E. Lynas-Gray, S. Miller, J. Tennyson, Infra red transition intensities for water: a comparison of *ab initio* and fitted dipole moment surfaces, J. Mol. Spectrosc. 169 (1995) 458–467.

[175] L. Rothman, I. Gordon, A. Barbe, D. Benner, P. Bernath, M. Birk, V. Boudon, L. Brown, A. Campargue, J.-P. Champion, K. Chance, L. Coudert, V. Dana, V. Devi, S. Fally, J.-M. Flaud, R. Gamache, A. Goldman, D. Jacquemart, I. Kleiner, N. Lacome, W. Lafferty, J.-Y. Mandin, S. Massie, S. Mikhailenko, C. Miller, N. Moazzen-Ahmadi, O. Naumenko, A. Nikitin, J. Orphal, V. Perevalov, A. Perrin, A. Predoi-Cross, C. Rinsland, M. Rotger, M. Šimečková, M. Smith, K. Sung, S. Tashkun, J. Tennyson, R. Toth, A. Vandaele, J. V. Auwera, The HITRAN 2008 molecular spectroscopic database, J. Quant. Spectrosc. Radiat. Transf. 110 (9-10) (2009) 533–572. doi:10.1016/j.jqsrt.2009.02.013.

[176] L. Rothman, I. Gordon, Y. Babikov, A. Barbe, D. C. Benner, P. Bernath, M. Birk, L. Bizzocchi, V. Boudon, L. Brown, A. Campargue, K. Chance, E. Cohen, L. Coudert, V. Devi, B. Drouin, A. Fayt, J.-M. Flaud, R. Gamache, J. Harrison, J.-M. Hartmann, C. Hill, J. Hodges, D. Jacquemart, A. Jolly, J. Lamouroux, R. L. Roy, G. Li, D. Long, O. Lyulin, C. Mackie, S. Massie, S. Mikhailenko, H. Müller, O. Naumenko, A. Nikitin, J. Orphal, V. Perevalov, A. Perrin, E. Polovtseva, C. Richard, M. Smith, E. Starikova, K. Sung, S. Tashkun, J. Tennyson, G. Toon, V. Tyuterev, G. Wagner, The HITRAN2012 molecular spectroscopic database, J. Quant. Spectrosc. Radiat. Transf. 130 (2013) 4–50. doi:10.1016/j.jqsrt.2013.07.002.

[177] H.-J. Werner, P. J. Knowles, G. Knizia, F. R. Manby, M. Schütz, Molpro: a general-purpose quantum chemistry program package, WIREs Comput. Mol. Sci. 2 (2012) 242–253. doi:10.1002/wcms.82.

[178] G. Audi, A. H. Wapstra, The 1995 update to the atomic mass evaluation, Nucl. Phys. A 595 (1995) 409–480. doi:10.1016/0375-9474(95)00445-9.

[179] O. L. Polyansky, J. Tennyson, Ab initio calculation of the rotation-vibration energy levels of H_3^+ and its isotopomers to spectroscopic accuracy, J. Chem. Phys. 110 (1999) 5056–5064.

[180] J. Tennyson, P. Barletta, M. A. Kostin, O. L. Polyansky, N. F. Zobov, *Ab initio* rotation-vibration energy levels of triatomics to spectroscopic accuracy, Spectrochimica Acta A 58 (2002) 663–672.

[181] G. Herzberg, Molecular Spectra and Molecular Structure (3 Volume Set), Krieger Pub Co, 1992.

[182] M. Baer, Introduction to the theory of electronic non-adiabatic coupling terms in molecular systems, Physics Reports 358 (2) (2002) 75–142. doi:10.1016/s0370-1573(01)00052-7.

[183] S. V. Krasnoshchekov, N. F. Stepanov, Polyad quantum numbers and multiple resonances in anharmonic vibrational studies of polyatomic molecules, The Journal of Chemical Physics 139 (18) (2013) 184101. doi:10.1063/1.4829143.

[184] G. H. Hardy, J. E. Littlewood, G. Plya, Inequalities (Cambridge Mathematical Library), Cambridge University Press, 1988.

[185] L. Lodi, J. Tennyson, O. L. Polyansky, A global, high accuracy ab initio dipole moment surface for the electronic ground state of the water molecule, J. Chem. Phys. 135 (2011) 034113. doi:10.1063/1.3604934.

[186] M. J. Down, L. Lodi, J. Tennyson, Line lists for $HD^{16}O$, $HD^{18}O$ and $HD^{17}O$ based on empirical line positions and *ab initio* intensities, J. Quant. Spectrosc. Radiat. Transf.

[187] S. A. Tashkun, V. I. Perevalov, R. R. Gamache, J. Lamouroux, CDSD-296, high resolution carbon dioxide spectroscopic databank: Version for atmospheric applications, J. Quant. Spectrosc. Radiat. Transf. 152 (2015) 45–73. doi:10.1016/j.jqsrt.2014.10.017.

[188] A. L. Laraia, R. R. Gamache, J. Lamouroux, I. E. Gordon, L. S. Rothman, Total internal partition sums to support planetary remote sensing, Icarus 215 (2011) 391–400. doi:10.1016/j.icarus.2011.06.004.

[189] R. R. Gamache, C. Roller, E. Lopes, I. E. Gordon, L. S. Rothman, O. L. Polyansky, N. F. Zobov, A. A. Kyuberis, J. Tennyson, S. N. Yurchenko, A. G. Császár, T. Furtenbacher, X. Huang, D. W. Schwenke, T. J. Lee, B. J. Drouin, S. A. Tashkun, V. I. Perevalov, R. V. Kochanov, Total internal partition sums for 166 isotopologues of 51 molecules important in planetary atmospheres: Application to HITRAN2016 and beyond, J. Quant. Spectrosc. Radiat. Transf. (In press, 2017) doi:10.1016/j.jqsrt.2017.03.045.

[190] Y. G. Borkov, D. Jacquemart, O. M. Lyulin, S. A. Tashkun, V. I. Perevalov, Infrared spectroscopy of ^{17}O- and ^{18}O-enriched carbon dioxide: Line positions and intensities in the 4681–5337 cm^{-1} region, J. Quant. Spectrosc. Radiat. Transf. 159 (2015) 1–10. doi:10.1016/j.jqsrt.2015.02.019.

[191] E. V. Karlovets, A. Campargue, D. Mondelain, S. Kassi, S. A. Tashkun, V. I. Perevalov, High sensitivity Cavity Ring Down spectroscopy of ^{18}O enriched carbon dioxide between 5850 and 7000cm^{-1}: Part III Analysis and theoretical modeling of the $^{12}C^{17}O_2$, $^{16}O^{12}C^{17}O$, $^{17}O^{12}C^{18}O$, $^{16}O^{13}C^{17}O$ and $^{17}O^{13}C^{18}O$ spectra, J. Quant. Spectrosc. Radiat. Transf. 136 (2014) 89–107. doi:10.1016/j.jqsrt.2013.11.006.

[192] A. Castrillo, G. Gagliardi, G. Casa, L. Gianfrani, Combined interferometric and absorption-spectroscopic technique for determining molecular line strengths: Applications to CO_2, Phys. Rev. A 67. doi:10.1103/physreva.67.062503.

[193] G. Casa, D. A. Parretta, A. Castrillo, R. Wehr, L. Gianfrani, Highly accurate determinations of CO_2 line strengths using intensity-stabilized diode laser absorption spectrometry, J. Chem. Phys. 127 (2007) 084311. doi:http://dx.doi.org/10.1063/1.2759930.

[194] G. Casa, R. Wehr, A. Castrillo, E. Fasci, L. Gianfrani, The line shape problem in the near-infrared spectrum of self-colliding CO_2 molecules: Experimental investigation and test of semiclassical models, J. Chem. Phys. 130 (2009) 184306. doi:http://dx.doi.org/10.1063/1.3125965.

[195] R. A. Toth, L. R. Brown, C. E. Miller, V. M. Devi, D. C. Benner, Spectroscopic database of CO_2 line parameters: 4300–7000cm^{-1}, J. Quant. Spectrosc. Radiat. Transf. 109 (2008) 906–921. doi:10.1016/j.jqsrt.2007.12.004.

[196] I. Gordon, L. Rothman, C. Hill, R. Kochanov, Y. Tan, P. Bernath, M. Birk, V. Boudon, A. Campargue, K. Chance, B. Drouin, J.-M. Flaud, R. Gamache, J. Hodges, D. Jacquemart, V. Perevalov, A. Perrin, K. Shine, M.-A. Smith, J. Tennyson, G. Toon, H. Tran, V. Tyuterev, A. Barbe, A. Császár, V. Devi, T. Furtenbacher, J. Harrison, J.-M. Hartmann, A. Jolly, T. Johnson, T. Karman, I. Kleiner, A. Kyuberis, J. Loos, O. Lyulin, S. Massie, S. Mikhailenko, N. Moazzen-Ahmadi, H. Müller, O. Naumenko, A. Nikitin, O. Polyansky, M. Rey, M. Rotger, S. Sharpe, K. Sung, E. Starikova, S. Tashkun, J. V. Auwera, G. Wagner, J. Wilzewski, P. Wcisło, S. Yu, E. J. Zak, The HITRAN2016 molecular spectroscopic database, J. Quant. Spectrosc. Radiat. Transf. (In press, 2017) doi:10.1016/j.jqsrt.2017.06.038.

[197] B. J. Drouin, Private communication (2016).

[198] R. Herman, R. F. Wallis, Influence of vibration-rotation interaction on line intensities in vibration-rotation bands of diatomic molecules, The Journal of Chemical Physics 23 (4) (1955) 637–646. doi:10.1063/1.1742069.

[199] M. Kiseleva, J. Mandon, S. Persijn, J. Petersen, L. Nielsen, F. J. M. Harren, Tractable line strength measurements of methane and carbon dioxide in the near infrared wavelength region at 1.65 μm using cavity ring down spectroscopy, in: 13th ASA-HITRAN conference, Reims, 2016, pp. P1–16.

[200] L. S. Rothman, I. E. Gordon, Y. Babikov, A. Barbe, D. C. Benner, P. F. Bernath, M. Birk, L. Bizzocchi, V. Boudon, L. R. Brown, A. Campargue, K. Chance, E. A. Cohen, L. H. Coudert, V. M. Devi, B. J. Drouin, A. Fayt, J.-M. Flaud, R. R. Gamache, J. J. Harrison, J.-M. Hartmann, C. Hill, J. T. Hodges, D. Jacquemart, A. Jolly, J. Lamouroux, R. J. Le Roy, G. Li, D. A. Long, O. M. Lyulin, C. J. Mackie, S. T. Massie, S. Mikhailenko, H. S. P. Müller, O. V. Naumenko, A. V. Nikitin, J. Orphal, V. Perevalov, A. Perrin, E. R. Polovtseva, C. Richard, M. A. H. Smith, E. Starikova, K. Sung, S. Tashkun, J. Tennyson, G. C. Toon, V. G. Tyuterev,

G. Wagner, The *HITRAN* 2012 molecular spectroscopic database, J. Quant. Spectrosc. Radiat. Transf. 130 (2013) 4 – 50. doi:10.1016/jqsrt.2013.07.002.

[201] A. Pogany, O. Ott, O. Werhahn, V. Ebert, Towards traceability in CO_2 line strength measurements by TDLAS at 2.7 μm, J. Quant. Spectrosc. Radiat. Transf. 130 (2013) 147–157. doi:{10.1016/j.jqsrt.2013.07.011}.

[202] R. Schermaul, R. C. M. Learner, A. A. D. Canas, J. W. Brault, O. L. Polyansky, D. Belmiloud, N. F. Zobov, J. Tennyson, Weak line water vapor spectrum in the regions 13 200 – 15 000 cm^{-1}, J. Mol. Spectrosc. 211 (2002) 169–178.

[203] G. Durry, J. S. Li, I. Vinogradov, A. Titov, L. Joly, J. Cousin, T. Decarpenterie, N. Amarouche, X. Liu, B. Parvitte, O. Korablev, M. Gerasimov, V. Zéninari, Near infrared diode laser spectroscopy of C_2H_2, H_2O, CO_2 and their isotopologues and the application to TDLAS, a tunable diode laser spectrometer for the martian PHOBOS-GRUNT space mission, Appl. Phys. B 99 (2010) 339–351. doi:10.1007/s00340-010-3924-y.

[204] L. S. Rothman, D. Jacquemart, A. Barbe, D. C. Benner, M. Birk, L. R. Brown, M. R. Carleer, C. Chackerian, K. Chance, L. H. Coudert, V. Dana, V. M. Devi, J.-M. Flaud, R. R. Gamache, A. Goldman, J.-M. Hartmann, K. W. Jucks, A. G. Maki, J.-Y. Mandin, S. T. Massie, J. Orphal, A. Perrin, C. P. Rinsland, M. A. H. Smith, J. Tennyson, R. N. Tolchenov, R. A. Toth, J. Vander Auwera, P. Varanasi, G. Wagner, The *HITRAN* 2004 molecular spectroscopic database, J. Quant. Spectrosc. Radiat. Transf. 96 (2005) 139–204.

[205] L. S. Rothman, I. E. Gordon, A. Barbe, D. C. Benner, P. F. Bernath, M. Birk, V. Boudon, L. R. Brown, A. Campargue, J. P. Champion, K. Chance, L. H. Coudert, V. Dana, V. M. Devi, S. Fally, J. M. Flaud, R. R. Gamache, A. Goldman, D. Jacquemart, I. Kleiner, N. Lacome, W. J. Lafferty, J. Y. Mandin, S. T. Massie, S. N. Mikhailenko, C. E. Miller, N. Moazzen-Ahmadi, O. V. Naumenko, A. V. Nikitin, J. Orphal, V. I. Perevalov, A. Perrin, A. Predoi-Cross, C. P. Rinsland, M. Rotger, M. Simeckova, M. A. H. Smith, K. Sung, S. A. Tashkun, J. Tennyson, R. A. Toth, A. C. Vandaele, J. Vander Auwera, The *HITRAN* 2008 molecular spectroscopic database, J. Quant. Spectrosc. Radiat. Transf. 110 (2009) 533–572.

[206] E. Karlovets, A. Campargue, D. Mondelain, S. Kassi, S. Tashkun, V. Perevalov, High sensitivity Cavity Ring Down spectroscopy of 18O enriched carbon dioxide between 5850 and 7000 cm^{-1}: Part IIAnalysis and theoretical modeling of the $^{12}C^{18}O_2$, $^{13}C^{18}O_2$ and $^{16}O^{13}C^{18}O$ spectra, J. Quant. Spectrosc. Radiat. Transf. 136 (2014) 71 – 88. doi:10.1016/j.jqsrt.2013.11.005.

[207] R. Toth, C. Miller, L. Brown, V. M. Devi, D. C. Benner, Line positions and strengths of $^{16}O^{12}C^{18}O$, $^{18}O^{12}C^{18}O$ and $^{17}O^{12}C^{18}O$ between 2200 and 7000 cm^{-1}, J. Mol. Spectrosc. 243 (2007) 43–61. doi:10.1016/j.jms.2007.03.005.

[208] E. V. Karlovets, A. Campargue, D. Mondelain, S. Béguier, S. Kassi, S. A. Tashkun, V. I. Perevalov, High sensitivity cavity ring down spectroscopy of ^{18}O enriched carbon dioxide between 5850 and 7000 cm^1: I. analysis and theoretical modeling of the $^{16}O^{12}C^{18}$ spectrum, J. Quant. Spectrosc. Radiat. Transf. 130 (2013) 116 – 133. doi:10.1016/j.jqsrt.2013.05.019.

[209] S. A. Tashkun, V. I. Perevalov, private communication: Intensities calculated using the effective dipole moment function (2012).

[210] L. S. Rothman, R. L. Hawkins, R. B. Wattson, R. R. Gamache, Energy levels, intensities, and linewidths of atmospheric carbon dioxide bands, J. Quant. Spectrosc. Radiat. Transf. 48 (1992) 537–566. doi:10.1016/0022-4073(92)90119-o.

[211] D. Jacquemart, F. Gueye, O. M. Lyulin, E. V. Karlovets, D. Baron, V. I. Perevalov, Infrared spectroscopy of CO2 isotopologues from 2200 to 7000 cm^{-1}: I—Characterizing experimental uncertainties of positions and intensities, J. Quant. Spectrosc. Radiat. Transf. 113 (2012) 961–975. doi:10.1016/j.jqsrt.2012.02.020.

[212] C. Claveau, J.-L. Teffo, D. Hurtmans, A. Valentin, Infrared fundamental and first hot bands of (OCO)-O^{12}C^{17}O isotopic variants of carbon dioxide, J. Mol. Spectrosc. 189 (1998) 153–195. doi:10.1006/jmsp.1998.7546.

[213] J. W. C. Johns, Absolute intensity and pressure broadening measurements of CO_2 in the 4.3-μm region, J. Mol. Spectrosc. 125 (1987) 442–464. doi:10.1016/0022-2852(87)90109-3.

[214] R. Toth, C. Miller, L. Brown, V. M. Devi, D. C. Benner, Line strengths of $^{16}O^{13}C^{16}O$, $^{16}O^{13}C^{18}$, $^{16}O^{13}C^{17}O$ and $^{18}O^{13}C^{18}O$, between 2200 and 6800 cm^{-1}, J. Mol. Spectrosc. 251 (2008) 64–89. doi:10.1016/j.jms.2008.01.009.

[215] Y. G. Borkov, D. Jacquemart, O. M. Lyulin, S. A. Tashkun, V. I. Perevalov, Infrared spectroscopy of ^{17}O- and ^{18}O-enriched carbon dioxide: Line positions and intensities in the 3200–4700 cm^{-1} region. Global modeling of the line positions of $^{16}O^{12}C^{17}O_2$ and $^{17}O^{12}C^{17}O$, J. Quant. Spectrosc. Radiat. Transf. 137 (2014) 57–76. doi:10.1016/j.jqsrt.2013.11.008.

[216] J. W. C. Johns, J. Vander Auwera, Absolute intensities in CO_2: The $\nu 2$ fundamental near 15 μm, J. Mol. Spectrosc. 140 (1990) 71–102. doi:10.1016/0022-2852(90)90008-e.

[217] J.-L. Teffo, L. Daumont, C. Claveau, A. Valentin, S. A. Tashkun, V. I. Perevalov, Infrared Spectra of the $^{16}O^{12}C^{17}O$ and $^{16}O^{12}C^{18}O$ Species of Carbon Dioxide: The Region 500–1500 cm^{-1}, J. Mol. Spectrosc. 213 (2002) 145–152. doi:10.1006/jmsp.2002.8561.

[218] R. J. Kshirsagar, L. P. Giver, C. Chackerian, L. R. Brown, The rovibrational intensities of the $2\nu 3$ band of at 4639 cm^{-1}, J. Quant. Spectrosc. Radiat. Transf. 61 (1999) 695–701. doi:10.1016/s0022-4073(98)00058-2.

[219] R. A. Toth, Line positions and strengths of CO_2 in the 1200–1430 cm^{-1} region, Appl. Opt. 24 (1985) 261. doi:10.1364/ao.24.000261.

[220] J.-L. Teffo, L. Daumont, C. Claveau, A. Valentin, S. Tashkun, V. Perevalov, Infrared spectra of the and species of carbon dioxide: II. the 1500–3000 cm^{-1} region, J. Mol. Spectrosc. 219 (2003) 271–281. doi:10.1016/s0022-2852(03)00057-2.

[221] C. P. Rinsland, D. C. Benner, Absolute intensities of spectral lines in carbon dioxide bands near 2050 cm^{-1}, Appl. Opt. 23 (1984) 4523. doi:10.1364/ao.23.004523.

[222] C. Claveau, J.-L. Teffo, D. Hurtmans, A. Valentin, R. Gamache, Line positions and absolute intensities in the laser bands of carbon-12 oxygen-17 isotopic species of carbon dioxide, J. Mol. Spectrosc. 193 (1999) 15–32. doi:10.1006/jmsp.1998.7704.

[223] D. Jacquemart, Private communication (2014).

[224] S. Kassi, E. Karlovets, S. Tashkun, V. Perevalov, A. Campargue, Analysis and theoretical modeling of the 18o enriched carbon dioxide spectrum by CRDS near 1.35μm: (i) $^{16}O^{12}C^{18}O$,$^{16}O^{12}C^{17}O$,$^{16}O^{12}C^{16}O$ and $^{16}O^{13}C^{16}O$, J. Quant. Spectrosc. Radiat. Transf. 187 (2017) 414–425. doi:10.1016/j.jqsrt.2016.09.002.

[225] V. M. Devi, C. P. Rinsland, D. C. Benner, Absolute intensity measurements of CO_2 bands in the 2395–2680-cm^{-1} region, Appl. Opt. 23 (1984) 4067. doi:10.1364/ao.23.004067.

[226] C. P. Rinsland, D. C. Benner, V. M. Devi, Measurements of absolute line intensities in carbon dioxide bands near 52 μm, Appl. Opt. 24 (1985) 1644. doi:10.1364/ao.24.001644.

[227] E. V. Karlovets, S. Kassi, S. A. Tashkun, V. I. Perevalov, A. Campargue, High sensitivity cavity ring down spectroscopy of carbon dioxide in the 1.19–1.26μm region, J. Quant. Spectrosc. Radiat. Transf. 144 (2014) 137–153. doi:10.1016/j.jqsrt.2014.04.001.

[228] S. Dobos, G. Winnewisser, F. Kling, J. Mink, Improved spectroscopic constants for $^{14}C\ ^{16}O_2$ obtained from the ν_3 band, Z. Naturforsch 44a (1989) 633–639.

[229] O. Lyulin, E. Karlovets, D. Jacquemart, Y. Lu, A. Liu, V. Perevalov, Infrared spectroscopy of 17o- and 18o-enriched carbon dioxide in the 1700-8300cm-1 wavenumber region, J. Quant. Spectrosc. Radiat. Transf. 113 (17) (2012) 2167–2181. doi:10.1016/j.jqsrt.2012.06.028.

[230] J. Tennyson, S. N. Yurchenko, Laboratory spectra of hot molecules: data needs for hot super-earth exoplanets, Mol. Astrophys. 8 (2017) 1–18. doi:10.1016/j.molap.2017.05.002.

[231] G. Tinetti, T. Encrenaz, A. Coustenis, Spectroscopy of planetary atmospheres in our galaxy, Astron. Astrophys. Rev. 21 (2013) 1–65. doi:10.1007/s00159-013-0063-6.

[232] A. G. Császár, E. Mátyus, L. Lodi, N. F. Zobov, S. V. Shirin, O. L. Polyansky, J. Tennyson, Ab initio prediction and partial characterization of the vibrational states of water up to dissociation, J. Quant. Spectrosc. Radiat. Transf. 111 (2010) 1043–1064.

[233] J. Tennyson, P. F. Bernath, L. R. Brown, A. Campargue, M. R. Carleer, A. G. Császár, L. Daumont, R. R. Gamache, J. T. Hodges, O. V. Naumenko, O. L. Polyansky, L. S. Rothmam, A. C. Vandaele, N. F. Zobov, A. R. Al Derzi, C. Fábri, A. Z. Fazliev, T. Furtenbacher, I. E. Gordon, L. Lodi, I. I. Mizus, IUPAC critical evaluation of the rotational-vibrational spectra of water vapor. Part III. Energy levels and transition wavenumbers for $H_2{}^{16}O$, J. Quant. Spectrosc. Radiat. Transf. 117 (2013) 29–80. doi:10.1016/j.jqsrt.2012.10.002.

[234] M. Birk, G. Wagner, J. Loos, L. Lodi, O. L. Polyansky, A. A. Kyuberis, N. F. Zobov, J. Tennyson, Accurate line intensities for water transitions in the infrared: comparison of theory and experiment, J. Quant. Spectrosc. Radiat. Transf.doi:10.1016/j.jqsrt.2017.03.040.

[235] A. A. Kyuberis, N. F. Zobov, O. V. Naumenko, B. A. Voronin, O. L. Polyansky, L. Lodi, A. Liu, S.-M. Hu, J. Tennyson, Room temperature linelists for deuterated water, J. Quant. Spectrosc. Radiat. Transf.doi:10.1016/j.jqsrt.2017.06.026.

[236] T. Sako, K. Yamanouchi, Algebraic approach to vibrationally highly excited states of SO_2. Vibrational wavefunctions from spectroscopy, Chem. Phys. Lett. 264 (1997) 403–410. doi:10.1016/S0009-2614(96)01346-2.

[237] O. N. Ulenikov, E. S. Bekhtereva, V.-M. Horneman, S. Alanko, , O. V. Gromova, High resolution study of the $3\nu_1$ band of SO_2, J. Mol. Spectrosc. 255 (2009) 111–121. doi:10.1016/j.jms.2009.03.009.

[238] O. N. Ulenikov, G. A. Onopenko, O. V. Gromova, E. S. Bekhtereva, V.-M. Horneman, Re-analysis of the (100), (001), and (020) rotational structure of SO_2 on the basis of high resolution FTIR spectra, J. Quant. Spectrosc. Radiat. Transf. 130 (2013) 220–232. doi:10.1016/j.jqsrt.2013.04.011.

[239] J. Tennyson, Vibration-rotation transition intensities from first principles, J. Mol. Spectrosc. 298 (2014) 1–6. doi:10.1016/j.jms.2014.01.012.

[240] J. Jiang, G. B. Park, R. W. Field, The rotation-vibration structure of the SO_2 $\tilde{C}\ ^1B_2$ state explained by a new internal coordinate force field, J. Chem. Phys. 144 (14) (2016) 144312. doi:10.1063/1.4945621.

[241] S. Tashkun, V. Perevalov, J.-L. Teffo, M. Lecoutre, T. Huet, A. Campargue, D. Bailly, M. Esplin, $^{13}C^{16}O_2$: Global treatment of vibrationalrotational spectra and first observation of the $2v_1 + 5v_3$ and $v_1 + 2v_2 + 5v_3$ absorption bands, J. Mol. Spectrosc. 200 (2000) 162 – 176. doi:http://dx.doi.org/10.1006/jmsp.2000.8057.

[242] B. V. Perevalov, A. Campargue, B. Gao, S. Kassi, S. A. Tashkun, V. I. Perevalov, New CW-CRDS measurements and global modeling of $^{12}C^{16}O_2$ absolute line intensities in the 1.6 μm region, J. Mol. Spectrosc. 252 (2008) 190 – 197. doi:http://dx.doi.org/10.1016/j.jms.2008.08.006.

[243] K. F. Song, S. Kassi, S. A. Tashkun, V. I. Perevalov, A. Campargue, High sensitivity CW-cavity ring down spectroscopy of $^{12}CO_2$ near 1.35 μm (II): New observations and line intensities modeling, J. Quant. Spectrosc. Radiat. Transf. 111 (2010) 332 – 344. doi:10.1016/j.jqsrt.2009.09.004.

[244] X. Huang, D. W. Schwenke, R. S. Freedman, T. J. Lee, Ames-2016 line lists for 13 isotopologues of CO_2: Updates, consistency, and remaining issues, J. Quant. Spectrosc. Radiat. Transf. (2017) –doi:10.1016/j.jqsrt.2017.04.026.

[245] L. E. Snyder, D. Buhl, Observations of radio emission from interstellar hydrogen cyanide, The Astrophysical Journal 163 (1971) L47. doi:10.1086/180664.

[246] T. M. Evans, D. K. Sing, T. Kataria, J. Goyal, N. Nikolov, H. R. Wakeford, D. Deming, M. S. Marley, D. S. Amundsen, G. E. Ballester, J. K. Barstow, L. Ben-Jaffel, V. Bourrier, L. A. Buchhave, O. Cohen, D. Ehrenreich, A. G. Muñoz, G. W. Henry, H. Knutson, P. Lavvas, A. L. des Etangs, N. K. Lewis, M. López-Morales, A. M. Mandell, J. Sanz-Forcada, P. Tremblin, R. Lupu, An ultrahot gas-giant exoplanet with a stratosphere, Nature 548 (7665) (2017) 58–61. doi:10.1038/nature23266.

[247] C. Sousa-Silva, S. N. Yurchenko, J. Tennyson, A computed room temperature line list for phosphine, J. Mol. Spectrosc. 288 (2013) 28–37.

[248] L. K. McKemmish, S. N. Yurchenko, J. Tennyson, ExoMol Molecular linelists – XVIII. The spectrum of Vanadium Oxide, Mon. Not. R. Astron. Soc. 463 (2016) 771–793. doi:10.1093/mnras/stw1969.

[249] A. I. Pavlyuchko, S. N. Yurchenko, J. Tennyson, ExoMol line lists XI: A Hot Line List for nitric acid, Mon. Not. R. Astron. Soc. 452 (2015) 1702–1706. doi:10.1093/mnras/stv1376.

[250] T. E. Odaka, T. Hirano, P. Jensen, An ab initio study of the $a^2\pi$ state and the $a^2\pi \leftarrow x^2\sigma^+$ electronic transition of MgNC, J. Mol. Spectrosc. 211 (1) (2002) 147–161. doi:10.1006/jmsp.2001.8485.

[251] T. E. Odaka, V. V. Melnikov, P. Jensen, T. Hirano, B. Lang, P. Langer, Theoretical study of the double renner effect for a $\pi 2$ MgNC MgCN: Higher excited rovibrational states, J. Chem. Phys. 126 (9) (2007) 094301. doi:10.1063/1.2464094.

[252] V. V. Melnikov, T. E. Odaka, P. Jensen, T. Hirano, The double renner effect in the xa_2' and aa_2' electronic states of HO_2, J. Chem. Phys. 128 (11) (2008) 114316. doi:10.1063/1.2827490.

[253] P. Jensen, M. Brumm, W. Kraemer, P. Bunker, A treatment of the renner effect using the MORBID hamiltonian, J. Mol. Spectrosc. 171 (1995) 31–57. doi:10.1006/jmsp.1995.1101.

[254] T. Hirano, V. Derpmann, U. Nagashima, P. Jensen, Large amplitude bending motion in CsOH, studied through ab initio-based three-dimensional potential energy functions, J. Mol. Spectrosc. 263 (2) (2010) 150–159. doi:10.1016/j.jms.2010.07.009.

[255] I. F. C. Mbapeh, S. C. G. Kempf, P. Jensen, Spectroscopic potential energy surfaces for the 12a′, 22a′, and 12a" electronic states of BeOH, J. Phys. Chem. A 119 (39) (2015) 10112–10123. doi:10.1021/acs.jpca.5b07410.

[256] B. Ostojić, P. Jensen, P. Schwerdtfeger, P. R. Bunker, The predicted spectrum and singlet–triplet interaction of the hypermetallic molecule SrOSr, J. Phys. Chem. A 117 (39) (2013) 9370–9379. doi:10.1021/jp310531s.

[257] S. Carter, N. C. Handy, C. Puzzarini, R. Tarroni, P. Palmieri, A variational method for the calculation of spin-rovibronic energy levels of triatomic molecules with three interacting electronic states, Mol. Phys. 98 (21) (2000) 1697–1712. doi:10.1080/00268970009483375.

[258] T. Taketsugu, K. Ishii, S. Carter, Theoretical determination of the spin-rovibronic spectrum of the a$2\pi\leftarrow$x$2\sigma^+$ electronic transition of MgNC, Chem. Phys. Lett. 380 (1-2) (2003) 213–222. doi:10.1016/j.cplett.2003.09.014.

[259] S. Carter, N. C. Handy, R. Tarroni, A variational method for the calculation of spin–rovibronic energy levels of any triatomic molecule in an electronic triplet state, Mol. Phys. 103 (6-8) (2005) 1131–1137. doi:10.1080/00268970412331332961.

[260] X.-G. Wang, T. Carrington, Jr., A discrete variable representation method for studying the rovibrational quantum dynamics of molecules with more than three atoms, J. Chem. Phys. 130 (2009) 094101. doi:{10.1063/1.3077130}.

[261] J. Tennyson, S. N. Yurchenko, The ExoMol project: Software for computing molecular line lists, Intern. J. Quantum Chem. 117 (2017) 92–103. doi:10.1002/qua.25190.

[262] D. S. Underwood, J. Tennyson, S. N. Yurchenko, X. Huang, D. W. Schwenke, T. J. Lee, S. Clausen, A. Fateev, ExoMol molecular line lists – XIV. the rotation–vibration spectrum of hot SO2, Mon. Not. R. Astron. Soc. 459 (4) (2016) 3890–3899. doi:10.1093/mnras/stw849.

[263] G. A. Worth, Accurate wave packet propagation for large molecular systems: The multi-configuration time-dependent hartree (MCTDH) method with selected configurations, The Journal of Chemical Physics 112 (19) (2000) 8322–8329. doi:10.1063/1.481438.

[264] A. Markmann, G. A. Worth, S. Mahapatra, H.-D. Meyer, H. Köppel, L. S. Cederbaum, Simulation of a complex spectrum: Interplay of five electronic states and 21 vibrational degrees of freedom in $C_5H_4^+$, The Journal of Chemical Physics 123 (20) (2005) 204310. doi:10.1063/1.2104531.

[265] H. Meyer, F. Gatti, G. A. Worth, Multidimensional Quantum Dynamics, Wiley-VCH, 2009.

[266] Q. Meng, H.-D. Meyer, A full-dimensional multilayer multiconfiguration time-dependent hartree study on the ultraviolet absorption spectrum of formaldehyde oxide, J. Chem. Phys. 141 (2014) 124309. doi:10.1063/1.4896201.

[267] T. J. Penfold, G. A. Worth, The photodissociation of ozone: A quasi-classical approach to a quantum dynamics problem, J. Mol. Graph. Mod. 26 (2007) 613–621. doi:10.1016/j.jmgm.2007.01.012.

[268] G. B. Park, J. Jiang, C. A. Saladrigas, R. W. Field, Observation of b_2 symmetry vibrational levels of the SO_2 $\tilde{C}\ ^1B_2$ state: Vibrational level staggering, coriolis interactions, and rotation-vibration constants, J. Chem. Phys. 144 (14) (2016) 144311. doi:10.1063/1.4944924.

[269] C. G. Parigger, J. O. Hornkohl, Computation of AlO B-2 Sigma(+) -¿ X-2 Sigma(+) emission spectra, Spectra Chimica Acta A 81 (2011) 404–411. doi:10.1016/j.saa.2011.06.029.

[270] K. Yamanouchi, M. Okunishi, Y. Endo, S. Tsuchiya, Laser induced fluorescence spectroscopy of the $\tilde{C}\ ^1B_2 \leftarrow \tilde{X}\ ^1A_1$ band of jet-cooled SO_2: rotational and vibrational analyses in the 235-210 nm region, J. Mol. Struct. 352-353 (1995) 541–559. doi:10.1016/0022-2860(95)08835-J.

[271] T. Hirano, U. Nagashima, Ro-vibrational properties of FeCO in the $\tilde{X}^3\sigma^-$ and $\tilde{a}^5\sigma^i$ electronic states: A computational molecular spectroscopy study, J. Mol. Spectrosc. 314 (2015) 35–47. doi:10.1016/j.jms.2015.05.007.

[272] H. Mustroph, Potential-energy surfaces, the Born-Oppenheimer approximations, and the franck-condon principle: Back to the roots, Comput. Phys. Commun. 17 (2016) 2616–2629. doi:10.1002/cphc.201600243.

[273] A. R. Whitehill, C. Xie, X. Hu, D. Xie, H. Guo, S. Ono, Vibronic origin of sulfur mass-independent isotope effect in photoexcitation of SO_2 and the implications to the early earth's atmosphere, Proc. Nat. Acad. Sci. 110 (2013) 17697–17702. doi:10.1073/pnas.1306979110.

[274] E. Klisch, P. Schilke, S. Belov, G. Winnewisser, $^{33}SO_2$: Interstellar identification and laboratory measurements, J. Mol. Spectrosc. 186 (2) (1997) 314–318. doi:10.1006/jmsp.1997.7447.

[275] L. M. Ziurys, The chemistry in circumstellar envelopes of evolved stars: Following the origin of the elements to the origin of life, Proc. Nat. Acad. Sci. 103 (33) (2006) 12274–12279. doi:10.1073/pnas.0602277103.

[276] C. Xie, X. Hu, L. Zhou, D. Xie, H. Guo, Ab initio determination of potential energy surfaces for the first two UV absorption bands of SO_2, J. Chem. Phys. 139 (1) (2013) 014305. doi:10.1063/1.4811840.

[277] D. E. Freeman, K. Yoshino, J. R. Esmond, W. H. Parkinson, High-resolution absorption cross-section measurements of SO_2 at 213-K in the wavelength region 172-240 nm, Planet Space Sci. 32 (1984) 1125–1134. doi:10.1016/0032-0633(84)90139-9.

[278] J. Rufus, G. Stark, P. L. Smith, J. C. Pickering, A. P. Thorne, High-resolution photoabsorption cross section measurements of SO_2, 2: 220 to 325 nm at 295 K, J. Geophys. Res. 108 (2003) 5011. doi:10.1029/2002JE001931.

[279] D. Blackie, R. Blackwell-Whitehead, G. Stark, J. C. Pickering, P. L. Smith, J. Rufus, A. P. Thorne, High-resolution photoabsorption cross-section measurements of SO_2 at 198 K from 213 to 325 nm, J. Geophys. Res. 116 (2011) E03006. doi:10.1029/2010JE003707.

[280] S. O. Danielache, C. Eskebjerg, M. S. Johnson, Y. Ueno, N. Yoshida, High-precision spectroscopy of 32S, 33S, and 34S sulfur dioxide: Ultraviolet absorption cross sections and isotope effects, J. Geophys. Res. 113 (D17). doi:10.1029/2007jd009695.

[281] T. Sako, A. Hishikawa, K. Yamanouchi, Vibrational propensity in the predissociation rate of SO_2 ($\tilde{C}\ ^1B_2$) by two types of nodal patterns in vibrational wavefunctions, Chem. Phys. Lett. 294 (6) (1998) 571–578. doi:10.1016/s0009-2614(98)00922-1.

[282] D. Xie, H. Guo, O. Bludsky, P. Nachtigall, Absorption and resonance emission spectra of SO_2 ($\tilde{X}\ ^1A_1 \rightarrow \tilde{C}\ ^1B_2$) calculated from ab initio potential energy and transition dipole moment sur-

faces, Chem. Phys. Lett. 329 (5-6) (2000) 503–510. doi:10.1016/s0009-2614(00)01049-6.

[283] O. Bludský, P. Nachtigall, J. Hrušák, P. Jensen, The calculation of the vibrational states of SO_2 in the $\tilde{C}\ ^1B_2$ electronic state up to the SO(σ-)+O(3p) dissociation limit, Chem. Phys. Lett. 318 (6) (2000) 607–613. doi:10.1016/s0009-2614(00)00015-4.

[284] J. Kłos, M. H. Alexander, P. Kumar, B. Poirier, B. Jiang, H. Guo, New ab initio adiabatic potential energy surfaces and bound state calculations for the singlet ground $\tilde{X}\ ^1A_1$ and excited $\tilde{C}\ ^1B_2$(21a') states of SO_2, J. Chem. Phys. 144 (17) (2016) 174301. doi:10.1063/1.4947526.

[285] P. Kumar, B. Jiang, H. Guo, J. Kłos, M. H. Alexander, B. Poirier, Photoabsorption assignments for the $\tilde{C}\ ^1B_2 \leftarrow \tilde{X}\ ^1A_1$ vibronic transitions of SO_2, using new ab initio potential energy and transition dipole surfaces, J. Phys. Chem. A 121 (5) (2017) 1012–1021. doi:10.1021/acs.jpca.6b12958.

[286] J. T. Hougen, J. K. G. Watson, Anomalous rotational line intensities in electronic transitions of polyatomic molecules: axis-switching, Can. J. Phys. 43 (2) (1965) 298–320. doi:10.1139/p65-028.

[287] D. M. Jonas, X. Yang, A. M. Wodtke, Axis-switching transitions and the stimulated emission pumping spectrum of HCN, J. Chem. Phys. 97 (4) (1992) 2284–2298. doi:10.1063/1.463120.

[288] G. M. Sando, K. G. Spears, Ab initio computation of the duschinsky mixing of vibrations and nonlinear effects, J. Phys. Chem. A 105 (22) (2001) 5326–5333. doi:10.1021/jp004230b.

[289] P. Meier, G. Rauhut, Comparison of methods for calculating Franck–Condon factors beyond the harmonic approximation: how important are duschinsky rotations?, Mol. Phys. 113 (23) (2015) 3859–3873. doi:10.1080/00268976.2015.1074740.

[290] D. L. Kokkin, T. Ma, T. Steimle, T. J. Sears, Detection and characterization of singly deuterated silylene, SiHD, via optical spectroscopy, J. Chem. Phys. 144 (24) (2016) 244304. doi:10.1063/1.4954702.

[291] X. Huang, D. W. Schwenke, T. J. Lee, Highly accurate potential energy surface, dipole moment surface, rovibrational energy levels, and infrared line list for 32S16O2 up to 8000 cm^{-1}, J. Chem. Phys. 140 (2014) 114311. doi:10.1063/1.4868327.

[292] X. Huang, D. W. Schwenke, T. J. Lee, Empirical infrared line lists for five SO2 isotopologues: (SO2)-S-32/33/34/36-O-16 and (SO2)-S-32-O-18, J. Mol. Spectrosc. 311 (2016) 19–24. doi:10.1016/j.jms.2015.01.010.

[293] E. J. Zak, J. Tennyson, Ro-vibronic transition intensities for triatomic molecules from the exact kinetic energy operator; electronic spectrum for the $\tilde{C}\ ^1B_2 \leftarrow \tilde{X}\ ^1A_1$ transition in SO_2, The Journal of Chemical Physics (In press, 2017).

[294] F.-T. Chau, J. M. Dyke, E. P. F. Lee, D. K. W. Mok, Simulation of CF_2 single vibronic level emissions: Including anharmonic and duschinsky effects, J. Chem. Phys. 115 (13) (2001) 5816–5822. doi:10.1063/1.1398103.

[295] X. Yang, C. A. Rogaski, A. M. Wodtke, Vibrational structure of hydrogen cyanide up to 18 900 cm^{-1} J. Opt. Soc. Am. B 7 (9) (1990) 1835. doi:10.1364/josab.7.001835.

[296] I. Tokue, S. Nanbu, Theoretical studies of absorption cross sections for the $\tilde{C}\ ^1B_2 \leftarrow \tilde{X}\ ^1A_1$ system of sulfur dioxide and isotope effects, The Journal of Chemical Physics 132 (2) (2010) 024301. doi:10.1063/1.3277191.

[297] K. C. Thompson, M. J. T. Jordan, M. A. Collins, Polyatomic molecular potential energy surfaces by interpolation in local internal coordinates, J. Chem. Phys. 108 (20) (1998) 8302–8316. doi:10.1063/1.476259.

[298] B. Parsons, L. J. Butler, D. Xie, H. Guo, A combined experimental and theoretical study of resonance emission spectra of SO_2), Chem. Phys. Lett. 320 (5-6) (2000) 499–506. doi:10.1016/s0009-2614(00)00253-0.

[299] P. C. Ray, M. F. Arendt, L. J. Butler, Resonance emission spectroscopy of predissociating SO_2 $\tilde{C}\ ^1B_2$: Coupling with a repulsive $^1A_1$ state near 200 nm, J. Chem. Phys. 109 (13) (1998) 5221–5230. doi:10.1063/1.477139.

[300] C. Wu, B. W. Yang, F. Z. Chen, D. L. Judge, J. Caldwell, L. M. Trafton, Measurements of high-, room-, and low-temperature photoabsorption cross sections of SO_2 in the 2080- to 2950-Å region, with application to io, Icarus 145 (1) (2000) 289–296. doi:10.1006/icar.1999.6322.

[301] B. Ostojic, P. R. Bunker, P. Schwerdtfeger, A. Gertych, P. Jensen, The predicted infrared spectrum of the hypermetallic molecule caoca in its lowest two electronic states (x)(1)sigma(+)(g); and (a)(3)sigma(+)(u), J. Mol. Struct. 1023 (SI) (2012) 101–107. doi:10.1016/j.molstruc.2012.03.048.

[302] W. Fawzy, M. Heaven, Private communication (2017).

[303] L. Lodi, S. N. Yurchenko, J. Tennyson, The calculated rovibronic spectrum of scandium hydride, ScH, Mol. Phys. 113 (2015) 1559–1575. doi:10.1080/00268976.2015.1029996.

[304] S. N. Yurchenko, A. Blissett, U. Asari, M. Vasilios, C. Hill, J. Tennyson, ExoMol Molecular linelists – XIII. The spectrum of CaO, Mon. Not. R. Astron. Soc. 456 (2016) 4524–4532. doi:10.1093/mnras/stv2858.

[305] S. N. Yurchenko, L. Lodi, J. Tennyson, A. V. Stolyarov, Duo: A general program for calculating spectra of diatomic molecules, Comput. Phys. Commun. 202 (2016) 262–275. doi:10.1016/j.cpc.2015.12.021.

[306] A. Alijah, J. Fremont, V. G. Tyuterev, Quantized nonadiabatic coupling terms of H_3^+, Physical Review A 92 (1). doi:10.1103/physreva.92.012704.

[307] J. M. Brown, A. Carrington, Rotational Spectroscopy of Diatomic Molecules (Cambridge Molecular Science), Cambridge University Press, 2010.

[308] B. Mukherjee, S. Mukherjee, K. R. Shamasundar, S. Adhikari, Beyond Born-Oppenheimer treatment for the construction of triple-sheeted accurate diabatic hamiltonian matrix of F^+H_2 system, Journal of Physics: Conference Series 833 (2017) 012004. doi:10.1088/1742-6596/833/1/012004.

[309] J. W. Demmel, Applied Numerical Linear Algebra, SIAM, 1997.

[310] D. R. Yarkony, Diabolical conical intersections, Reviews of Modern Physics 68 (4) (1996) 985–1013. doi:10.1103/revmodphys.68.985.

[311] C. A. Mead, D. G. Truhlar, Conditions for the definition of a strictly diabatic electronic basis for molecular systems, The Journal of Chemical Physics 77 (12) (1982) 6090–6098. doi:10.1063/1.443853.

[312] B. T. Sutcliffe, The coupling of nuclear and electronic motions in molecules, Journal of the Chemical Society, Faraday Transactions 89 (14) (1993) 2321. doi:10.1039/ft9938902321.

[313] G. A. Meek, B. G. Levine, Wave function continuity and the diagonal Born-Oppenheimer correction at conical intersections, The Journal of Chemical Physics 144 (18) (2016) 184109. doi:10.1063/1.4948786.

[314] R. Requist, F. Tandetzky, E. K. U. Gross, Molecular geometric phase from the exact electron-nuclear factorization, Physical Review A 93 (4). doi:10.1103/physreva.93.042108.

[315] G. Herzberg, H. C. Longuet-Higgins, Intersection of potential energy surfaces in polyatomic molecules, Discussions of the Faraday Society 35 (1963) 77. doi:10.1039/df9633500077.

[316] A. Varandas, J. Tennyson, J. Murrell, Chercher le croisement, Chemical Physics Letters 61 (3) (1979) 431–434. doi:10.1016/0009-2614(79)87143-2.

[317] C. A. Mead, The geometric phase in molecular systems, Reviews of Modern Physics 64 (1) (1992) 51–85. doi:10.1103/revmodphys.64.51.

[318] C. Wittig, Geometric phase and gauge connection in polyatomic molecules, Physical Chemistry Chemical Physics 14 (18) (2012) 6409. doi:10.1039/c2cp22974a.

[319] B. K. Kendrick, J. Hazra, N. Balakrishnan, The geometric phase controls ultracold chemistry, Nature Communications 6 (2015) 7918. doi:10.1038/ncomms8918.

[320] I. G. Ryabinkin, A. F. Izmaylov, Geometric phase effects in dynamics near conical intersections: Symmetry breaking and spatial localization, Physical Review Letters 111 (22). doi:10.1103/physrevlett.111.220406.

[321] I. G. Ryabinkin, L. Joubert-Doriol, A. F. Izmaylov, When do we need to account for the geometric phase in excited state dynamics?, The Journal of Chemical Physics 140 (21) (2014) 214116. doi:10.1063/1.4881147.

[322] X. Huang, D. W. Schwenke, R. S. Freedman, T. J. Lee, Ames-2016 line lists for 13 isotopologues of CO_2 : Updates, consistency, and remaining issues, J. Quant. Spectrosc. Radiat. Transf. (In press, 2017) doi:10.1016/j.jqsrt.2017.04.026.